

Sheffield Hallam University

Laser direct energy deposition – the effect of process parameters on inconel 718

ELKINGTON, Helen

Available from the Sheffield Hallam University Research Archive (SHURA) at:

<http://shura.shu.ac.uk/29924/>

A Sheffield Hallam University thesis

This thesis is protected by copyright which belongs to the author.

The content must not be changed in any way or sold commercially in any format or medium without the formal permission of the author.

When referring to this work, full bibliographic details including the author, title, awarding institution and date of the thesis must be given.

Please visit <http://shura.shu.ac.uk/29924/> and <http://shura.shu.ac.uk/information.html> for further details about copyright and re-use permissions.

Laser Direct Energy Deposition – The Effect of Process Parameters on Inconel 718

Helen Elkington

A thesis submitted in partial fulfilment of the requirements of
Sheffield Hallam University
for the degree of Doctor of Philosophy

September 2021

Candidate Declaration

I hereby declare that:

1. I have not been enrolled for another award of the University, or other academic or professional organisation, whilst undertaking my research degree.
2. None of the material contained in the thesis has been used in any other submission for the academic award.
3. I am aware of and understand the University's policy on plagiarism and certify that this thesis is my own work. The use of all published or other sources of material consulted have been properly and fully acknowledged.
4. The work undertaken towards the thesis has been conducted in accordance with the SHU Principles of Integrity in Research and the SHU Research Ethics Policy.
5. The word count of the thesis is 38,804.

| | |
|---------------------|--|
| Name | Helen Elkington |
| Date | September 2021 |
| Award | PhD |
| Faculty | Materials and Engineering Research Institute |
| Director of Studies | Dr. Stephen Magowan |

Abstract

Laser Direct Energy Deposition (DED-L) is an Additive Manufacturing process which uses a laser beam as an energy source to melt blown metal powder to fabricate components. Complex relationships exist between the process parameters, which means that understanding these relationships, and their effect, is critical in understanding DED-L.

This research investigates DED-L process parameters using a Trumpf 505 DMD system, aiming to determine the effect of altering specific process parameters on the metallurgical and mechanical properties of Inconel 718. Laser power, scan speed, and powder feed rate were first investigated using a Taguchi Design of Experiments. Anisotropy, build direction and a heat-treatment were then examined.

The results demonstrate that the interactions between laser power, scan speed, and powder feed rate must be considered when determining process parameter values. An empirical working envelope of process parameter combinations for fabricating Inconel 718 on the Trumpf 505 DMD system was identified.

For thick wall DED-L parts, changing the process parameters did not have any significant effect on the material properties.

Process parameter combinations were found to be non-transferable between geometries – identical process parameters result in different material properties moving between different geometries. Thus individually built small test samples should not be used as representative of a larger components material properties.

Combining different build directions did not have a negative effect on material properties at the interface between the build directions.

Heat-treating eliminated the columnar dendritic grain structure, reduced Laves phase volume, and increased Vickers Hardness by 55%.

This research adds to previous knowledge of how Inconel 718 behaves following fabrication by DED-L, and aids in understanding material integrity in thick wall DED-L builds. This contributes to improving the viability of using DED-L within industry.

Acknowledgements

I would like to thank my supervisors Dr Stephen Magowan, Dr Quanshun Luo, Professor Alan Smith, and Dr Carl Hauser for their support and guidance over the last few years.

I would also like to thank the National Structural Integrity Research Centre, TWI, and Sheffield Hallam University for enabling me to undertake this research.

And finally the biggest thanks goes to my parents, brothers, family, and friends, for their constant love and support throughout writing this.

Contents

| | |
|--|----|
| List of tables..... | 16 |
| List of figures | 20 |
| List of equations | 35 |
| Nomenclature | 36 |
| Acronyms..... | 37 |
| Chapter 1 – Introduction..... | 38 |
| 1.1 Background | 38 |
| 1.2 Aims and Objectives | 40 |
| 1.3 Novelty of research | 41 |
| Chapter 2 – Literature Review | 42 |
| 2.1 Additive Manufacturing | 42 |
| 2.2 Laser Direct Energy Deposition | 45 |
| 2.2.1 Applications..... | 46 |
| 2.2.1.1 Freeform fabrication | 46 |
| 2.2.1.2 Hybrid manufacture..... | 47 |
| 2.2.1.3 Remanufacture..... | 47 |
| 2.2.1.4 Combining materials | 47 |
| 2.2.2 Environment and Equipment | 48 |
| 2.2.2.1 Powder delivery system..... | 49 |

| | |
|--|----|
| 2.2.2.2 Deposition nozzles | 50 |
| 2.2.2.3 Lasers | 52 |
| 2.2.3 Advantages and disadvantages | 52 |
| 2.2.4 Process parameters | 53 |
| 2.2.4.1 Laser power..... | 54 |
| 2.2.4.2 Scan speed..... | 56 |
| 2.2.4.3 Powder feed rate | 56 |
| 2.2.4.4 Gas flow rate | 57 |
| 2.2.4.5 Laser profile..... | 58 |
| 2.2.4.6 Deposit dilution..... | 59 |
| 2.2.4.7 Build strategy | 60 |
| 2.2.4.8 Powder..... | 62 |
| 2.2.5 Process parameter optimisation | 63 |
| 2.2.6 Processing defects..... | 64 |
| 2.2.6.1 Porosity | 65 |
| 2.2.6.2 Cracking..... | 66 |
| 2.2.6.3 Residual stress..... | 67 |
| 2.2.6.4 Distortion..... | 67 |
| 2.2.6.5 Anisotropy | 68 |
| 2.3 Microstructure..... | 69 |

| | |
|---|----|
| 2.3.1 Grain morphology | 73 |
| 2.3.1.1 Secondary Dendrite Arm Spacing..... | 76 |
| 2.3.2 Microstructural phases | 78 |
| 2.4 Heat-treatments | 78 |
| 2.4.1 Pre-heat | 79 |
| 2.4.2 Post-heat..... | 79 |
| 2.4.3 Annealing | 79 |
| 2.4.4 Solution treatment | 80 |
| 2.4.5 Ageing | 80 |
| 2.4.6 Quenching..... | 80 |
| 2.4.7 Hot isostatic pressing | 80 |
| 2.5 Metallurgical and Mechanical Analysis | 81 |
| 2.5.1 Fractography | 82 |
| 2.6 Nickel | 86 |
| 2.6.1 Nickel alloys | 86 |
| 2.7 Inconel 718..... | 89 |
| 2.7.1 Inconel 718 phases | 91 |
| 2.7.2 γ -phase | 97 |
| 2.7.3 γ' -phase and γ'' -phase..... | 97 |
| 2.7.4 δ -phase | 98 |

| | |
|---|-----|
| 2.7.5 Carbides..... | 98 |
| 2.7.6 Laves phase | 100 |
| 2.7.7 Inconel 718 DED-L microstructure | 101 |
| 2.7.7.1 Inconel 718 DED-L phases..... | 102 |
| 2.7.8 Inconel 718 DED-L mechanical properties | 103 |
| 2.7.9 Inconel 718 heat-treatments | 105 |
| 2.8 Design of Experiments..... | 107 |
| 2.9 Summary | 109 |
| Chapter 3 – Methodology | 111 |
| 3.1 Stages of work..... | 111 |
| 3.2 Materials | 112 |
| 3.2.1 Powder composition | 112 |
| 3.2.2 Substrate composition..... | 114 |
| 3.3 DED-L system set-up..... | 115 |
| 3.3.1 Equipment calibration..... | 116 |
| 3.3.1.1 Laser power calibration..... | 116 |
| 3.3.1.2 Nozzle set-up and calibration | 118 |
| 3.3.1.3 Adjustment of focusing optics and powder stream | 118 |
| 3.3.1.4 Aligning deposition nozzle to the laser beam | 119 |
| 3.3.1.5 Powder feed rate calibration..... | 120 |

| | |
|--|-----|
| 3.4 Specimen manufacture | 120 |
| 3.4.1 Specimen dimensions | 120 |
| 3.4.2 Process parameters | 123 |
| 3.4.2.1 Stage 1 | 125 |
| 3.4.2.2 Stage 2, Stage 3, and Stage 4 | 128 |
| 3.4.2.3 Stage 5 | 128 |
| 3.4.3 Determining track separation and z-increment | 128 |
| 3.4.4 Heat-treatment..... | 129 |
| 3.5 Powder capture efficiency | 130 |
| 3.6 Metallographic and mechanical analysis | 131 |
| 3.6.1 Specimen analysis preparation | 133 |
| 3.6.1.1 Stage 1 | 133 |
| 3.6.1.2 Stage 2 | 134 |
| 3.6.1.3 Stage 3 | 134 |
| 3.6.1.4 Stage 4 | 135 |
| 3.6.1.5 Stage 5 | 135 |
| 3.6.2 Optical Light Microscopy | 135 |
| 3.6.2.1 Secondary Dendrite Arm Spacing..... | 138 |
| 3.6.3 Scanning Electron Microscopy | 139 |
| 3.6.4 Tensile testing..... | 141 |

| | |
|--|-----|
| 3.6.5 Vickers Hardness | 143 |
| 3.6.5.1 Microhardness | 144 |
| Chapter 4 – Results | 146 |
| 4.1 Stage 1 – Investigation of key process parameters using a Taguchi DOE approach | 146 |
| 4.1.1 Optical Light Microscopy | 151 |
| 4.1.1.1 Secondary Dendrite Arm Spacing..... | 156 |
| 4.1.2 Scanning Electron Microscopy | 157 |
| 4.1.3 Tensile Testing | 166 |
| 4.1.3.1 Fractography | 172 |
| 4.1.4 Vickers Hardness | 177 |
| 4.1.5 Powder capture efficiency..... | 181 |
| 4.2 Stage 2 – Investigation into anisotropy within a single DED-L part | 182 |
| 4.2.1 Optical Light Microscopy | 182 |
| 4.2.2 Scanning Electron Microscopy | 186 |
| 4.2.3 Tensile Testing | 188 |
| 4.2.3.1 Fractography | 190 |
| 4.2.4 Vickers Hardness | 193 |
| 4.3 Stage 3 – Investigation into the effect of build direction on metallurgical and mechanical properties..... | 195 |
| 4.3.1 Optical Light Microscopy | 195 |

| | |
|--|-----|
| 4.3.2 Scanning Electron Microscopy | 201 |
| 4.3.3 Tensile Testing | 205 |
| 4.3.3.1 Fractography | 206 |
| 4.3.4 Vickers Hardness | 209 |
| 4.4 Stage 4 – Investigation into the effect of an interface using multiple build directions on metallurgical and mechanical properties | 211 |
| 4.4.1 Optical Light Microscopy | 211 |
| 4.4.2 Scanning Electron Microscopy | 212 |
| 4.4.3 Tensile Testing | 214 |
| 4.4.3.1 Fractography | 215 |
| 4.4.4 Vickers Hardness | 217 |
| 4.5 Stage 5 – Investigation into the effect of a heat-treatment on metallurgical properties and Vickers Hardness | 219 |
| 4.5.1 Optical Light Microscopy | 219 |
| 4.5.2 Scanning Electron Microscopy | 220 |
| 4.5.3 Vickers Hardness | 222 |
| Chapter 5 – Discussion | 224 |
| 5.1 Using a Taguchi DOE for the DED-L process | 224 |
| 5.1.1 Determining process parameters for stage 2, 3, and 4 | 225 |
| 5.2 Sample defects..... | 227 |
| 5.3 Sample microstructure | 228 |

| | |
|--|-----|
| 5.3.1 Grain morphology | 229 |
| 5.3.2 Microstructural phases | 231 |
| 5.3.2.1 The γ -matrix..... | 232 |
| 5.3.2.2 Laves phase | 233 |
| 5.3.2.3 γ'' -phase | 234 |
| 5.3.2.4 Al-oxide inclusions | 234 |
| 5.3.2.5 Carbides | 235 |
| 5.3.2.6 Phase distribution..... | 235 |
| 5.3.3 Track (yz-plane) and layer (xz-plane) microstructure..... | 236 |
| 5.3.4 Stage 1 – comparison of parameter sets | 238 |
| 5.3.4.1 Nb-rich phase | 238 |
| 5.3.4.2 Secondary Dendrite Arm Spacing..... | 239 |
| 5.3.5 Stage 1 – comparison of built sample size | 240 |
| 5.3.5.1 Nb-rich phase | 241 |
| 5.3.5.2 Secondary Dendrite Arm Spacing..... | 241 |
| 5.3.6 Stage 2 – microstructure anisotropy within a single part | 241 |
| 5.3.7 Stage 3 – effect of build direction on microstructure | 242 |
| 5.3.8 Stage 4 – effect of an interface on microstructure..... | 243 |
| 5.3.9 Stage 5 – effect of a heat-treatment on microstructure..... | 244 |
| 5.4 Tensile properties..... | 245 |

| | |
|--|-----|
| 5.4.1 Stage 1 – comparison of parameter sets | 252 |
| 5.4.2 Stage 1 – comparison of tensile specimen location | 253 |
| 5.4.3 Stage 2 – comparison of tensile specimen orientation..... | 254 |
| 5.4.4 Stage 3 – effect of build direction on tensile strength | 255 |
| 5.4.5 Stage 4 – effect of an interface on tensile strength | 255 |
| 5.4.6 Fracture mode | 256 |
| 5.5 Vickers Hardness | 259 |
| 5.5.1 Stage 1 – comparison of parameter sets | 259 |
| 5.5.2 Stage 1 – comparison of built sample sizes | 260 |
| 5.5.3 Stage 2 – comparison of individual planes | 262 |
| 5.5.4 Stage 3 – effect of build direction on Vickers Hardness | 262 |
| 5.5.5 Stage 4 – effect of an interface on Vickers Hardness | 264 |
| 5.5.6 Stage 5 – effect of a heat-treatment on Vickers Hardness | 264 |
| 5.6 Powder capture efficiency | 264 |
| 5.7 Energy density, mass density, and specific energy density | 265 |
| Chapter 6 – Conclusions | 269 |
| 6.1 Findings | 269 |
| 6.1.1 Process parameter optimisation | 269 |
| 6.1.2 Microstructure | 270 |
| 6.1.2.1 Laser power, scan speed, and powder feed rate | 270 |

| | |
|--|-----|
| 6.1.2.2 Build geometry | 271 |
| 6.1.2.3 Incorporating an interface..... | 271 |
| 6.1.2.4 Heat-treatment | 271 |
| 6.1.3 Mechanical properties | 271 |
| 6.1.3.1 Laser power, scan speed, and powder feed rate | 271 |
| 6.1.3.2 Build geometry | 272 |
| 6.1.3.3 Incorporating an interface..... | 272 |
| 6.1.2.4 Heat-treatment | 272 |
| 6.2 Limitations | 272 |
| 6.3 Future work..... | 273 |
| 6.3.1 Residual stress analysis..... | 273 |
| 6.3.2 Process parameter optimisation | 273 |
| 6.3.3 Geometrical variation | 274 |
| 6.3.4 Heat-treatments..... | 274 |
| 6.3.5 Layer and track interfaces..... | 275 |
| References | 276 |
| Appendices..... | 303 |
| Appendix 1 – Stage 1 melt pool diameter, track separation and z-increment for each process parameter set..... | 303 |
| Appendix 2 – Previous process parameter combinations on the Trumpf 505 DMD system. | 304 |

| | |
|--|-----|
| Appendix 3 – Raw grain boundary measurement data. | 306 |
| Appendix 4 – Raw SDAS data. | 307 |
| Appendix 5 – Raw tensile data. | 308 |
| Appendix 6 – Raw macrohardness data. | 309 |
| Appendix 7 – Raw microhardness data. | 310 |

List of tables

| | |
|--|----|
| Table 1: Categories and examples of AM technologies (ASTM International, 2013)..... | 43 |
| Table 2: Properties used to reflect DED-L component quality. | 54 |
| Table 3: Parameter influence on deposit properties, derived from findings of studies mentioned (Dass & Moridi, 2019; Fotovvati, Wayne, Lewis, & Asadi, 2018; Liu, et al., 2019; Ludovico, Angelastro, & Campanelli, 2010; Mahamood, Akinlabi, & Owolabi, 2017; Mahamood & Akinlabi, 2015; Mahamood & Akinlabi, 2014). | 63 |
| Table 4: The arrangement of atoms within common crystal structures in metals/alloys. | 70 |
| Table 5: The role of some alloying elements within Nickel (Donachie & Donachie, 2002; Reed, 2006). | 88 |
| Table 6: Chemical composition for Inconel 718 (ASTM International, 2018; SAE International, 2016), the tensile properties pre (a) and post (b) heat-treatment (SAE International, 2016), and Vickers Hardness following solution annealing (c), and solution annealing and ageing (d) (SAE International, 2016)..... | 90 |
| Table 7: Inconel 718 phases, their crystal structures and chemical formulas. | 92 |
| Table 8: Inconel 718 solidification stages, showing precipitation temperature and phase change. L is the material in molten liquid state. Adapted from DuPont, Notis, Marder, Robino, and Michael (1998) and Knorovsky, Cieslak, Headley, Romig, and Hammetter (1989)..... | 93 |
| Table 9: Images from the literature containing examples of phases present within Inconel 718. | 96 |

| | |
|--|-----|
| Table 10: Common carbides present in Ni-alloys (M represents a metal atom). | 99 |
| Table 11: Examples of Laves composition obtained using EDX analysis. (2014) | 101 |
| Table 12: Inconel 718 heat-treatments..... | 105 |
| Table 13: An outline of each aim for the five stages of work within this study. | 111 |
| Table 14: The composition and size of the Inconel 718 powder used to manufacture samples within this work. This was determined according to ASTM E1019 (a) and ASTM E1097 (b). ASTM F3055 standard for AM using Inconel 718 is shown for comparison. | 113 |
| Table 15: The composition of Stainless steel 304L according to ASTM A240. | 114 |
| Table 16: The number of specimens and their dimensions for each stage of work..... | 121 |
| Table 17: Previous process parameter sets used for Inconel 718 on the Trumpf DED 505 system (TWI Technology Centre, 2019). | 124 |
| Table 18: The process parameter values determined to be used for each level within the Taguchi DOE..... | 126 |
| Table 19: The Taguchi orthogonal array for each test run process parameter combination and the run order. A run was also done using the maximum value of process parameters. | 127 |
| Table 20: The process parameters used for stages 2, 3, and 4. | 128 |
| Table 21: The heat-treatment applied to Stage 5 samples. | 130 |
| Table 22: Table outlining composition of etchants considered for use within this work..... | 137 |

| | |
|---|-----|
| Table 23: The settings used to create EDX maps using Aztec software. | 140 |
| Table 24: The energy density, mass density, and specific energy density for each parameter set. These have been ranked from highest (1) to lowest (10). | 146 |
| Table 25: Images of the small and large blocks for parameter sets 4, 5, 9, and 10. Large block build times are shown (to the nearest 10 minutes). | 150 |
| Table 26: Mean values for porosity of the small and large blocks. Standard deviation is shown. | 151 |
| Table 27: Mean grain width values for the large blocks. | 155 |
| Table 28: Mean values for SDAS for the small and large blocks. Standard deviation is shown. | 156 |
| Table 29: Values for the percentage of white present, obtained by binarising SEM images (dimensions 100 μm \times 120 μm) of samples. | 160 |
| Table 30: Table containing the element wt% for the powder pre-DED-L, and for the EDX analysis performed. | 162 |
| Table 31: Mean values obtained for 0.2% proof stress and UTS through tensile testing. Standard deviation is shown. | 166 |
| Table 32: Mean values obtained for elongation through tensile testing. Standard deviation is shown. | 167 |
| Table 33: The difference in 0.2% proof and UTS values moving between individual tensile specimen test results. H1 and V1 are used as the baseline for plotting values. | 169 |
| Table 34: Mean values obtained for Vickers macro/microhardness. Standard deviation is shown. | 177 |

| | |
|--|-----|
| Table 35: Values obtained for powder input, block weight, and calculated process efficiency for each large block..... | 181 |
| Table 36: The EDX point analysis results for Figure 98. | 187 |
| Table 37: Mean values obtained from tensile testing. Values for standard deviation are shown..... | 189 |
| Table 38: Mean values obtained for Vickers macro/microhardness. Standard deviation values are shown. | 194 |
| Table 39: The EDX point analysis results for the following figures of SEM images. | 202 |
| Table 40: Mean values obtained from tensile testing. Standard deviation is shown. | 205 |
| Table 41: Mean values obtained for Vickers macro/microhardness for each plane of the horizontal and vertical samples are shown. Standard deviation values are shown. | 210 |
| Table 42: Mean values obtained for tensile testing, including standard deviation values. | 214 |
| Table 43: Mean values obtained for Vickers macrohardness testing, including standard deviation values. | 217 |
| Table 44: Table containing the element wt% for the powder pre-DED-L, and for the EDX analysis performed. | 221 |
| Table 45: Mean values obtained for Vickers macro/microhardness of heat-treated samples. Standard deviation is shown. | 222 |
| Table 46: The four process parameter sets which were successful in building, and the values used to fabricate specimens for stages 2, 3 and 4. Energy density, mass density and specific energy density are shown..... | 226 |

List of figures

| | |
|---|----|
| Figure 1: Schematic showing how subtractive manufacturing removes material from feedstock, whilst AM builds up material (3dexter, 2018). | 38 |
| Figure 2: Overview of DED-L parameters. | 39 |
| Figure 3: Schematic of DED-L, depicting the nozzle, laser, and substrate. | 46 |
| Figure 4: An example of how a powder feed system works in DED-L..... | 49 |
| Figure 5: Photographs of a conical flow (left) and 3-jet (right) nozzle and their powder streams (Fraunhofer ILT, 2018)..... | 51 |
| Figure 6: The nozzle types A) conical, B) multi-jet, C) a side-feed nozzle. | 52 |
| Figure 7: The effect of increasing laser power on the melt-pool, resulting in a keyhole forming..... | 55 |
| Figure 8: Schematic of the effect on track height when powder feed rate is increased. Cross sections of individual tracks on substrate. | 57 |
| Figure 9: Schematic showing how identical laser spot sizes can be achieved at positive and negative laser standoffs. | 58 |
| Figure 10: Using a cross section to calculate dilution..... | 59 |
| Figure 11: Inter-track porosity – pores between tracks formed due to excessive track spacing. | 60 |
| Figure 12: Common toolpath patterns used in DED-L; raster (a); bi-directional (b); offset (c & d); fractal (e) (Shamsaei, Yadollahi, Bian, & Thompson, 2015). 61 | |
| Figure 13: Scanning electron micrograph of GA powder (a) and PREP powder (b) (Ahsan, Pinkerton, Moat, & Shackleton, 2011). Examples of satellites within the GA powder are indicated..... | 62 |

| | |
|---|----|
| Figure 14: Optical micrograph of process-induced porosity (irregular) and gas porosity (spherical) (Sames, List, Pannala, Dehoff, & Babu, 2016). | 65 |
| Figure 15: Solidification cracking along the solidification grain boundary (SGB) of a single deposited Inconel 718 track (Alizadeh-Sh, Marashi, Renjarnodeh, Shoja-Razavi, & Oliveira, 2020). | 66 |
| Figure 16: Stages of solidification resulting in grain formation. a) Crystal nucleation, b & c) increase in crystal number and grain growth, d) grains and grain boundaries as seen under a microscope (NDT Resource Centre, 2018). | 71 |
| Figure 17: Schematic of typical columnar grain structure formed during DED-L. Grains cross multiple layers, extending towards the laser. | 72 |
| Figure 18: The effect of temperature gradient (G) and growth rate (R) on microstructure (Mao, et al., 2002). | 73 |
| Figure 19: Schematic showing three approaches to quantify SDAS. 1 and 2 use variations of the linear intercept method, 3 uses the distance between two SDA. L refers to length. | 77 |
| Figure 20: The linear intercept method approach which Vandersluis and Ravindran (2017) determined most accurate for determining SDAS. L refers to length. | 78 |
| Figure 21: Tensile specimens which have fractured through ductile and brittle fracture mechanisms (Enomoto, 2017). | 82 |
| Figure 22: Schematic of brittle and ductile fracture failure mechanisms. Brittle fracture occurs perpendicular to the applied load, no deformation is present. Ductile fracture shows evidence of deformation. | 83 |
| Figure 23: The fracture surface of a copper tensile specimen containing equiaxed dimples. (Gabriel, 1987). | 84 |
| Figure 24: Mechanisms involved in ductile fracture. | 85 |

| | |
|---|-----|
| Figure 25: Fracture surface of a Nickel 201 specimen. Ledge-like features (cleavage facets) and dimples are indicated. (ASM International, 1987). | 85 |
| Figure 26: Transformation-time-temperature diagram for wrought Inconel 718 (Oradei-Basile & Radavich, 1991). | 93 |
| Figure 27: SEM images of as-deposited Inconel 718, solution treated, solution treated and aged, and direct aged (Sreekanth, Hurtig, Joshi, & Andersson, 2021). GB = grain boundary. | 107 |
| Figure 28: Schematic of a "black box" process model which can be used to describe DOE theory. | 108 |
| Figure 29: Secondary electron SEM images of the Inconel 718 powder used within this work. The size of some particles is shown. | 114 |
| Figure 30: Example of the stainless steel 304L substrate used within this work. | 115 |
| Figure 31: The Trumpf DMD 505 system used for this work. Key parts are labelled. Powder feeders are not shown. | 116 |
| Figure 32: The equipment used for laser power calibration – an OPHIR thermal power sensor (left) and OPHIR NOVA remote meter (right). | 117 |
| Figure 33: Power requested plotted against the power recorded at the workpiece for requested powers from 400 W to 1500 W. A linear relationship between the two variables was observed. | 118 |
| Figure 34: Schematic showing how the human eye is used to observe the powder focus point and laser beam to ensure correct alignment. | 119 |
| Figure 35: The dimensions of the two blocks manufactured for each set of process parameters in Stage 1. | 121 |
| Figure 36: The dimensions of the block built for Stage 2. | 122 |

| | |
|---|-----|
| Figure 37: The dimensions and orientation of blocks for Stage 3. These dimensions were also used for Stage 4 blocks. | 122 |
| Figure 38: The position of the laser in relation to the block for the first section and second section of deposition. The laser was kept in the same orientation whilst the block was orientated 90°. | 123 |
| Figure 39: Schematic of a bi-directional scan pattern that was used to manufacture test specimens. | 125 |
| Figure 40: Schematic of a deposited track illustrating step 2 of determining track separation and z-increment. | 128 |
| Figure 41: Schematic of a 1-layer 6-track deposit illustrating step 4 of determining track separation and z-increment. | 129 |
| Figure 42: Schematic of a 2-layer 6-track/5-track deposit illustrating step 5 of determining track separation and z-increment. | 129 |
| Figure 43: The equipment used to prepare samples for examination – manual grinding wheels (left) and automatic polisher (right). | 132 |
| Figure 44: Three of the EDM sectioned blocks mounted in VARI-SET 20 powder cold mount using 30 mm mounts. | 132 |
| Figure 45: The location of where the tensile test specimens were taken from for the larger block in Stage 1. The area in the middle was used for metallurgical analysis and hardness testing. | 133 |
| Figure 46: Schematic showing how the block was split into tensile test specimens (yellow) orientated in different directions. The material not used for the tensile test specimens' blocks was EDM'd into the small blocks. Drawing is not to scale. | 134 |
| Figure 47: Schematic of one tensile test specimen per sample. Vertical (V) and horizontal (H). | 135 |

| | |
|--|-----|
| Figure 48: The Olympus BX60 optical microscope and Leica DFC450 5-megapixel digital camera used for OLM..... | 136 |
| Figure 49: Schematic of a dendrite showing the length and SDA to be used. . | 138 |
| Figure 50: The FEI Quanta 650 SEM used. | 139 |
| Figure 51: An example of an SEM image of an un-etched sample (Stage 1, set 4)..... | 141 |
| Figure 52: A drawing of the dimensions of the tensile test specimens used in this work in accordance with standard ASTM E8..... | 142 |
| Figure 53: The Instron Universal Testing Machine (Model 3369) and Instron Video Extensometer AVE2 used for testing Stage 1 tensile specimens. | 142 |
| Figure 54: The Mitutoyo HV-100 hardness testing machine used for taking hardness readings. | 143 |
| Figure 55: The Wilsons VH3300 hardness machine used for taking microhardness readings of the samples..... | 144 |
| Figure 56: The single-track deposits and melt runs for each parameter set. ... | 147 |
| Figure 57: Optical micrograph of the single track deposited for parameter set 2. Poor deposit-substrate fusion can be seen. | 148 |
| Figure 58: The partially built set 8 small block. A burn mark from the laser can be seen..... | 149 |
| Figure 59: An optical micrograph used for set 5 porosity measurements. Larger pores are indicated. | 151 |
| Figure 60: Optical micrograph of the xz-plane of set 5 large. Grains can be seen to extend through multiple layers (indicated in yellow). | 152 |

Figure 61: Higher magnification optical micrograph of the xz-plane of set 5 large. The meeting point between layers can be clearly seen, highlighted by a variation in structure as phases in the upper portion of the previous layer have been refined during the deposition of the subsequent layer. 153

Figure 62: Optical micrograph of the yz-plane of set 9 large. Grains can be seen to extend through multiple tracks. 153

Figure 63: Higher magnification optical micrograph of the yz-plane of set 4 large. The meeting point between tracks can be seen, indicated by the yellow dashed lines. 154

Figure 64: Optical micrographs of the xy-plane of set 10 large. The meeting point between tracks is indicated by the yellow dashed line. 154

Figure 65: Example of micrograph used for calculating average grain width for large block 5. 155

Figure 66: Graph displaying the mean values for SDAS for the small and large blocks. Standard deviation error bars are shown. 157

Figure 67: Examples of the optical micrographs used for measuring SDAS. ... 157

Figure 68: Secondary electron SEM images of the yz-planes of the small blocks. An example of the bright phase (Laves phase) is indicated on each SEM image. 158

Figure 69: Secondary electron SEM images of the yz-planes of the large blocks. An example of the bright phase (Laves phase) is indicated on each SEM image. 159

Figure 70: Secondary electron SEM image of the xy-plane of set 10 large. The previously deposited track and subsequently deposited track are indicated. A more regular/consistent pattern of the white phase is present within the region of the previously deposited track that is adjacent to the subsequently deposited track. 161

Figure 71: Secondary electron SEM image of the xz-plane of set 4 large, showing the phases which are present within the samples. The corresponding EDX spectra can be found in Table 30. 163

Figure 72: Secondary electron SEM image of the xz-plane of set 5 large. The layers are indicated. The right-hand image is an SEM image at a higher magnification, showing that the white phase is present at the point of layers meeting. 163

Figure 73: Secondary electron SEM image of the yz-plane of set 10 small. 4 phases that are present within the sample are indicated by the arrows. 1 indicates the matrix; 2 the white phase; 3 the phase surrounding the white phase; 4 the phase within the white phase; 5 a dark precipitate or void. 164

Figure 74: Backscatter electron SEM image of the yz-plane of set 9 small. 4 phases that are present within the sample are indicated by the arrows. 1 indicates the matrix; 2 the white phase; 3 the phase surrounding the white phase; 4 the phase within the white phase; 5 a dark precipitate or void. 165

Figure 75: EDX maps of the SEM image in Figure 74. Elemental segregation can be seen to have occurred. 165

Figure 76: Graph showing the mean values obtained for 0.2% proof stress. Standard deviation error bars are shown. Values for untreated wrought Inconel 718 are included for comparison. 167

Figure 77: Graph showing the mean values obtained for UTS. Standard deviation error bars are shown. Values for untreated wrought Inconel 718 are included for comparison. 168

Figure 78: Graph showing the mean values obtained for elongation during tensile testing. Standard deviation error bars are shown. 168

Figure 79: Graph displaying the difference in 0.2% proof stress value for horizontal tensile test specimens, moving from the top of the large DED-L block to the bottom. All number 1 tensile samples lie at 0 MPa. 170

Figure 80: Graph displaying the difference in 0.2% proof stress value for vertical tensile test specimens, moving from the outer of the large DED-L block to the middle. All number 1 tensile samples lie at 0 MPa. 170

Figure 81: Graph displaying the difference in UTS value for horizontal tensile test specimens, moving from the top of the large DED-L block to the bottom. 171

Figure 82: Graph displaying the difference in UTS value for vertical tensile test specimens, moving from the outer of the large DED-L block to the middle. 171

Figure 83: Secondary electron SEM image of the fracture surface of tensile specimen H2 from set 10 large. This horizontal fracture surface is rough and jagged. 173

Figure 84: Secondary electron SEM image of the fracture surface of tensile specimen V2 from set 10 large. This vertical fracture surface is rough and jagged but flatter towards the centre than the previously shown Horizontal tensile specimen fracture surface. 173

Figure 85: Secondary electron SEM images of tensile specimen 10H2. An equiaxed dimple rupture network can be seen. Step-like features, tearing ridges and an Al-oxide are labelled. 174

Figure 86: Secondary electron SEM images of tensile specimen 4H2. A crack, shear deformation, step-like features, microvoid coalescence, tearing ridges and an Al-oxide are labelled. 175

Figure 87: Secondary electron SEM image of tensile specimen 9H2. A crack, adjacent shear deformation, and step-like features are labelled. 175

| | |
|---|-----|
| Figure 88: Secondary electron SEM image of tensile specimen 4V2. An equiaxed dimple rupture network containing microvoid coalescence (labelled) can be seen. Tearing ridges and an Al-oxide are labelled. | 176 |
| Figure 89: Secondary electron SEM images of tensile specimen 5V2. An equiaxed dimple rupture network containing microvoid coalescence is seen. A crack, Al-oxide and possible inclusion are labelled. | 176 |
| Figure 90: Graph showing mean Vickers macrohardness (HV_{10}) and microhardness ($HV_{0.5}$) for the small and large blocks. Standard deviation error bars are shown. | 178 |
| Figure 91: Microhardness maps plotted for each of the small blocks (cross section in the yz-plane)..... | 179 |
| Figure 92: Microhardness maps plotted for each of the large blocks (cross section in the yz-plane)..... | 180 |
| Figure 93: Optical micrograph of a 3-dimensional section of the sample. Differences between all three planes can be seen. | 182 |
| Figure 94: Optical micrograph of the xz-plane where grains (outlined in blue) grew upwards through multiple layers (indicated by the yellow lines). | 183 |
| Figure 95: Optical micrograph of the xz-plane where grains (outlined in blue) grew upwards through multiple layers (indicated by the yellow lines) in a zig-zag pattern. | 184 |
| Figure 96: Optical micrograph of the yz-plane. Track meeting points can be seen. Heat-affected regions where phase refinement has occurred is shown. | 185 |
| Figure 97: Higher magnification optical micrograph of the xz-plane. A variation in phase distribution can be seen moving across the heat-affected region. Possible phases – Ni-rich solid solution and precipitates – are indicated. | 186 |

| | |
|---|-----|
| Figure 98: Secondary electron SEM image of the xy-plane showing the white phase and small precipitate. | 187 |
| Figure 99: Secondary electron SEM image of the yz-plane where the white phase can be seen to have segregated. EDX maps of a smaller region of the image are shown..... | 188 |
| Figure 100: Schematic showing the locations of the tensile specimens with regards to the laser and scan path direction. | 188 |
| Figure 101: Graph displaying the mean results obtained for UTS and 0.2% proof stress. Standard deviation error bars are shown. Values for untreated wrought Inconel 718 are shown for comparison..... | 189 |
| Figure 102: Graph showing mean elongation values obtained during tensile testing for samples..... | 190 |
| Figure 103: Secondary electron SEM image of a sample 1 fracture surface. and a higher magnification SEM image showing cracks in the sample surface..... | 191 |
| Figure 104: Higher magnification secondary electron SEM image of a sample 2 fracture surface. A network of equiaxed dimples containing microvoid coalescence is present. Step-like features, and tearing ridges (formed in uniform lines) are shown. | 192 |
| Figure 105: Higher magnification secondary electron SEM image of a sample 3 fracture surface. Step-like features can be seen on the left image. The right image shows microvoid coalescence, a tearing ridge, and an Al-oxide. | 192 |
| Figure 106: Schematic showing the location for where Vickers hardness measurements were taken from relative to the laser and scan path direction. | 193 |
| Figure 107: Graph showing the mean values obtained for Vickers macrohardness (HV ₁₀) and microhardness (HV _{0.5}) testing. Standard deviation error bars are shown. | 194 |

| | |
|---|-----|
| Figure 108: Optical micrograph of a 3-dimensional section of the vertical sample. Differences between the xy-plane and the other two planes (xz and yz) can be seen..... | 196 |
| Figure 109:Optical micrograph of a 3-dimensional section of the horizontal sample. Differences between all three planes can be observed. | 196 |
| Figure 110: Optical micrograph of the horizontal sample xz-plane. Deposited layers are visible and indicated by yellow lines. Grains are outlined in blue and extend through multiple layers. | 197 |
| Figure 111: Optical micrograph of the vertical sample yz-plane (comparable to xz-plane). Deposited layers are visible and indicated by yellow lines. Grains are outlined in blue and extend through multiple layers and across tracks. | 198 |
| Figure 112: Optical micrograph of the horizontal sample xy-plane where two tracks overlap (indicated in yellow). A darker region containing refined phases can be seen in the heat-affected region. | 199 |
| Figure 113: Optical micrograph of the vertical sample yz-plane (comparable to xz-plane). Tracks can be clearly differentiated. A dendritic structure can be seen. Layers are indicated in yellow..... | 199 |
| Figure 114: Optical micrograph of the horizontal xy-plane. A dendritic structure can be seen. Possible phases are indicated – Ni-rich solid solution and precipitates..... | 200 |
| Figure 115: Optical micrograph of the vertical yz-plane. A dendritic structure can be seen. Possible phases are indicated – Ni-rich solid solution and precipitates. | 201 |
| Figure 116: Secondary electron SEM image of horizontal xz-plane showing the discontinuous network of the bright phase. Spectrums of this phase were taken. | 202 |

Figure 117: Secondary electron SEM image of vertical yz-plane showing the continuous network of the bright phase. Spectrums of this phase and the matrix were taken.....203

Figure 118: Secondary electron SEM image of a region within the vertical xz-plane (comparable to yz-plane) used for EDX mapping and the corresponding EDX maps obtained.....204

Figure 119: Graph showing the mean values obtained for UTS and 0.2% proof stress. Standard deviation error bars are shown. Values for untreated wrought Inconel 718 are shown for comparison.....205

Figure 120: Graph showing the mean values obtained for elongation. Standard deviation error bars are shown.206

Figure 121: Secondary electron SEM image of a fracture surface of a horizontal tensile specimen.207

Figure 122: Secondary electron SEM image of a fracture surface of a vertical tensile specimen. A region where external contamination following fracture occurred is shown.207

Figure 123: A higher magnification secondary electron SEM of the fracture surface of a horizontal tensile specimen. Examples of microvoid coalescence, step-like features and Al-oxide inclusion are indicated. Tearing ridges can be seen to have formed uniform lines.....208

Figure 124: A higher magnification secondary electron SEM of the fracture surface of a vertical tensile specimen. An equiaxed dimple rupture network can be seen. Examples of microvoid coalescence, tearing ridges (formed randomly), and fragments of Laves are indicated.209

Figure 125: Graph displaying the mean Vickers macrohardness (HV_{10}) and microhardness ($HV_{0.5}$) values for each plane of the horizontal and vertical samples. Standard deviation error bars are shown.210

Figure 126: Optical micrograph of the interface between build direction 1 and build direction 2. The deposited layers and tracks can be distinguished.211

Figure 127: A higher magnification optical micrograph of the interface between build direction 1 and build direction 2. A crack can be observed to extend to the interface from direction 1 deposited material.212

Figure 128: Secondary electron SEM image of the interface between build direction 1 and build direction 2. A bright phase can be seen to form a continuous network in build direction 2, whilst being more homogeneously spread in build direction 1.213

Figure 129: A high magnification secondary electron SEM image of the bright phase present within the sample.213

Figure 130: Graph displaying the mean UTS and 0.2% proof stress values obtained from tensile testing. Standard deviation error bars are shown. Untreated wrought Inconel 718 values are shown for comparison.214

Figure 131: The fractured tensile specimens. The interface was aligned to fall at the midpoint of the specimen gage.215

Figure 132: Secondary electron SEM image of a fracture surface of one of the tensile specimens.216

Figure 133: Higher magnification secondary electron SEM images of the fracture surface. The yellow boxed image on the left corresponds to the box in the previous figure. The blue boxed image on the right corresponds to the blue box in the image on the left. Examples of observable features are indicated on the images.216

Figure 134: Graph displaying mean Vickers macrohardness (HV_{10}) values obtained. Standard deviation error bars are shown.217

Figure 135: Graph showing average microhardness moving across the interface. The interface is at 0 mm. Standard deviation error bars are shown.218

Figure 136: Optical micrograph showing a microhardness indent directly on the interface (at 0 mm).....218

Figure 137: Optical micrograph of Stage 1 set 4 large block, showing examples of grain boundaries, γ -phase and precipitates.219

Figure 138: Secondary electron SEM image of heat-treated large block 4 yz-plane. The bright phase which was previously present within Stage 1 untreated samples is indicated.220

Figure 139: Higher magnification Secondary electron SEM image of the bright phase in heat-treated large block 4 yz-plane.221

Figure 140: Graph displaying mean values for Vickers macrohardness (HV_{10}) and microhardness ($HV_{0.5}$) of heat-treated samples. Results from Stage 1 large blocks are shown to enable a comparison. Standard deviation is shown.223

Figure 141: Schematic showing how grain-growth would form in a continuous diagonal direction if the same x-direction (in this case the positive x-direction) was used for all layers.231

Figure 142: Schematic of the re-melted and heat-affected regions induced when a new layer is deposited onto a previous layer. Diagram is not to scale.236

Figure 143: Graph displaying SDAS plotted against 0.2% proof stress for the Stage 1 tensile samples. Standard deviation is shown.246

Figure 144: Graph showing average grain width plotted against 0.2% proof stress for Stage 1 samples. Standard deviation is shown.247

Figure 145: Schematic of how grains lay within tensile specimens taken perpendicular to (left: horizontal), and specimens taken parallel to (right:

vertical), grain growth. Grains are indicated by blue and orange and are not to scale.248

Figure 146: Plot of layer thickness against 0.2% proof stress (MPa) for Stage 1, 2, and 3 samples. Standard deviation is shown.....250

Figure 147: Graph displaying specific energy density plotted against scan speed to show where a working envelope of successful parameter sets lies for the Trumpf 505 DMD system for Inconel 718 (those from previous work are shown in Appendix 2).267

List of equations

| | |
|--|-----|
| Equation 1: Equation for calculating dilution (Dass & Moridi, 2019). | 59 |
| Equation 2: The Hall-Petch equation for the relationship between strength and grain boundaries. | 75 |
| Equation 3: Equation to calculate SDAS. | 77 |
| Equation 4: Equation for calculating energy density. | 125 |
| Equation 5: Equation for calculating mass density. | 126 |
| Equation 6: Equation for calculating specific energy density. | 126 |
| Equation 7: Calculation for powder input using the powder feed rate and the time to build the sample. | 130 |
| Equation 8: Calculation for powder input using the total mass of powder per unit length and the total distance of the scan path for the sample. | 130 |
| Equation 9: Calculation for powder capture efficiency using the powder input as calculated according to Equation 1 and Equation 2 and the weight of the final sample. | 130 |
| Equation 10: Equation to calculate secondary dendrite arm spacing. | 138 |
| Equation 11: Empirical formula for the working envelope presented in Figure 147, and thus the range for x and y values. | 268 |
| Equation 12: Empirical working envelope formula, and thus the range for specific energy density (x) and scan speed (y) values. | 270 |

Nomenclature

δ – delta

γ – gamma

γ' – gamma prime

γ'' – gamma double prime

μ – mu

σ – stress

Acronyms

AM – Additive Manufacture

ANOVA – Analysis of Variance

APA – Advanced Plasma Atomisation

BSE – Back Scatter Electron

CAD – Computer-Aided-Design

DED-L – Laser Direct Energy Deposition

DOE – Design Of Experiments

FCC – Face Centred Cubic

GA – Gas Atomised

HAZ – Heat-Affected Zone

PREP – Plasma Rotating Electron Process

SDA – Secondary Dendrite Arm

SDAS – Secondary Dendrite Arm Spacing

Chapter 1 – Introduction

This chapter contains an overview of the research. Firstly, Additive Manufacturing (AM), Laser Direct Energy Deposition (DED-L), and Inconel 718 are introduced. This is followed by a description of the aims and objectives.

1.1 Background

Additive Manufacturing (AM) processes use the addition of material to build components. They allow components to be created, altered, or repaired wasting minimal material as compared to conventional subtractive manufacturing methods such as grinding, turning, drilling, and milling, where the desired shape is achieved through removing material from the feedstock. Figure 1 demonstrates the difference between subtractive manufacturing and AM.

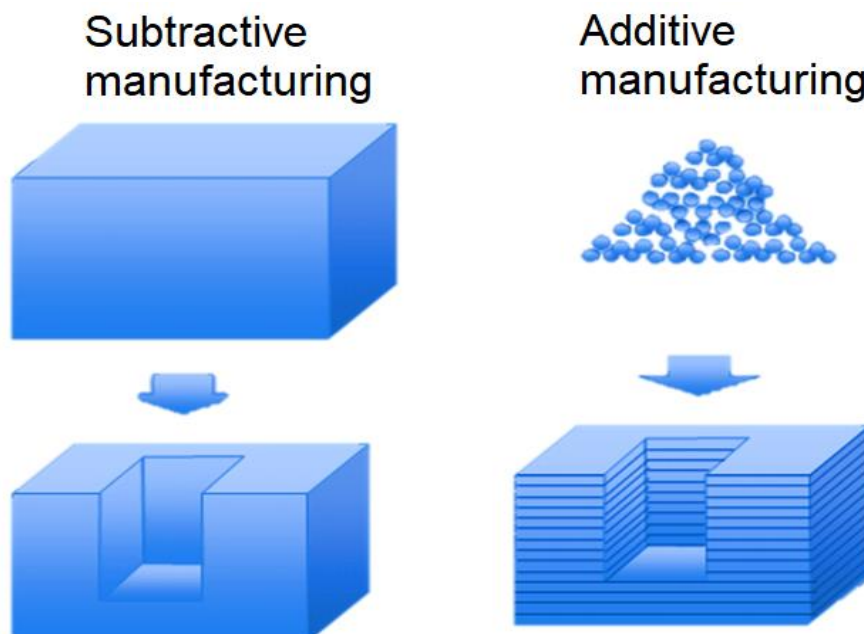


Figure 1: Schematic showing how subtractive manufacturing removes material from feedstock, whilst AM builds up material (3dexter, 2018).

Some of advantages which AM offers over conventional manufacturing methods include: reduced material costs, reduced waste, reduced energy costs,

increased process efficiency, and reduced number of manufacturing steps and lead times.

Laser Direct Energy Deposition (DED-L) is an AM process which utilises a laser to create a molten pool in a metallic substrate. An inert gas is used to blow metal powder into this melt-pool via a nozzle. Upon interaction with the melt-pool and laser beam, the powder melts and binds to the substrate or previously deposited material. As the laser continues to move along its projected toolpath the deposited material cools and solidifies.

Numerous process parameters are involved within DED-L. These can be varied to alter the process outcome. As complex relationships exist between the process parameters, small variations in these can result in significant changes to the deposited material microstructure and properties. Thus, an understanding of the relationships present, and their effect, is critical in understanding DED-L. Figure 2 contains an overview of some parameters involved in DED-L.

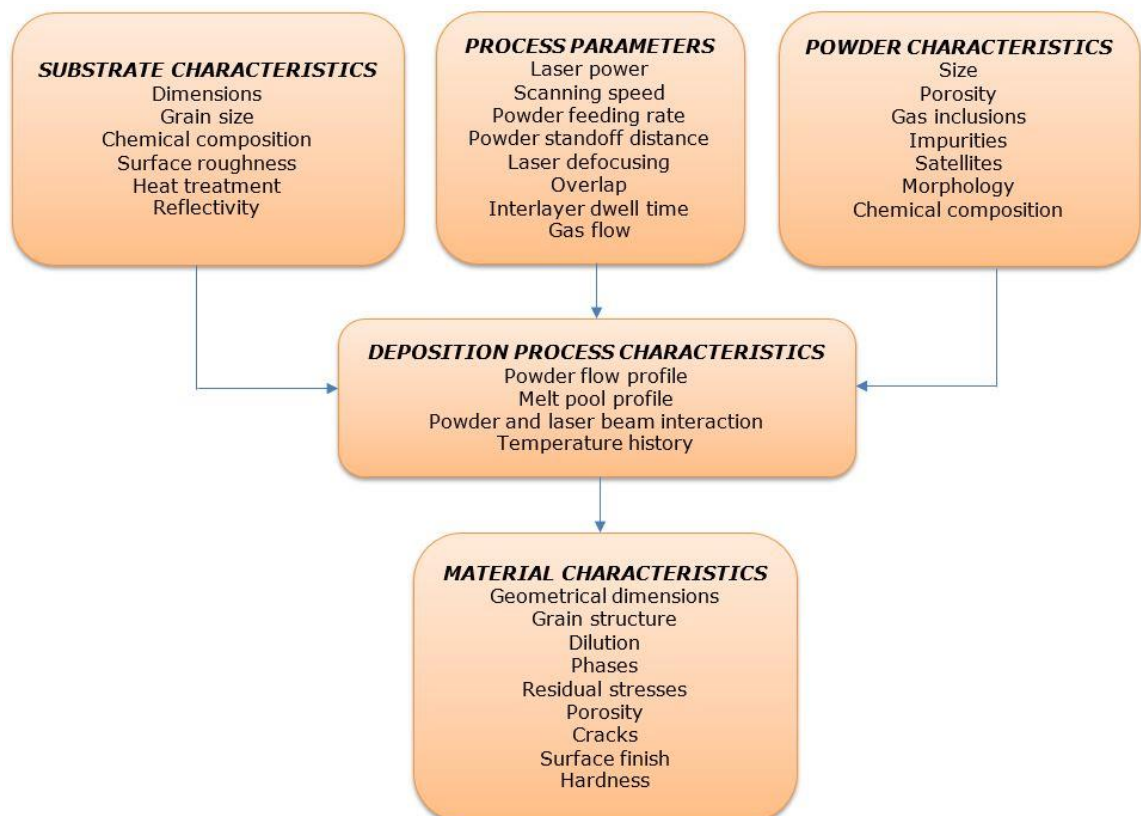


Figure 2: Overview of DED-L parameters.

DED-L has already proved to be successful in decreasing a components weight, reducing multi-part components to a single component, and repairing high value worn-out parts previously considered irreparable.

Due to the advantages that DED-L offers to the aerospace industry, a material often utilised for aerospace components has been used within this this work – Inconel 718. Inconel 718 is typically used in aerospace applications owing to its ability to retain its mechanical properties when subjected to elevated temperatures for prolonged periods of time. Common applications include jet engines and gas turbine operations. It also displays excellent weldability, making it extremely suitable for DED-L.

1.2 Aims and Objectives

This research set out to investigate DED-L process parameters, aiming to determine the effect of altering specific process parameters on the metallurgical and mechanical properties of Inconel 718.

To meet this the following objectives were defined:

- 1) Carry out a review of existing literature surrounding the research topic.
- 2) Use a Taguchi Design of Experiments to investigate three key process parameters and establish process parameter values to be used for the subsequent stages of work.
- 3) Build a single DED-L test specimen to examine anisotropy.
- 4) Build DED-L test specimens with identical geometries using different build directions.
- 5) Build DED-L test specimens using two deposition directions to create an interface within the build.

- 6) Establish the effect of a heat-treatment on the microstructure and Vickers Hardness.

1.3 Novelty of research

The novelty of this research lies in its demonstration of non-transferability of process parameter sets between different geometries. A working envelope of successful process parameter combinations for using a CO₂ laser to fabricate Inconel 718 parts using DED-L is identified. The results show that changing process parameters for fabricating thick wall DED-LB parts may not have a critical effect on the material properties, but that the build direction chosen to fabricate a part does. The effect that incorporating an interface (formed by using two different build directions) within a DED-LB build has on material properties is also demonstrated. This research adds to previous knowledge of how Inconel 718 behaves following fabrication by DED-LB, and aids in understanding material integrity in thick wall DED-LB builds. This will contribute to improving the viability of DED-LB for use within industry.

Chapter 2 – Literature Review

This chapter reviews the literature surrounding the research area to provide a context for the research, illustrate its relevance to industry, and explore previous work within this field. Topics covered include the DED-L process, material analysis, and Nickel superalloy – Inconel 718.

2.1 Additive Manufacturing

Additive Manufacturing (AM) refers to the set of processes which use a Computer-Aided-Design (CAD) file to build components via layer-wise addition. The CAD drawing is approximated by triangles and sliced into multiple layers, with each slice containing the information for it to be printed (Zhang & Jung, 2018).

Multiple AM technologies capable of producing functional components are available, these can be split into 7 categories and rely on different power sources (Table 1). Those associated with metal materials use a feedstock in the form of wire or powder.

| Category | Power Source | Example Technologies |
|----------------------------|----------------------------|--|
| Directed Energy Deposition | Laser Beam | Laser Metal Deposition Electronic Beam Welding |
| Sheet Lamination | Laser Beam | Laminated Object Manufacturing |
| Powder Bed Fusion | High-powered Laser Beam | Selective Laser Sintering Selective Laser Melting |
| | Electron Beam | Electron Beam Melting |
| Vat Photo-polymerization | Ultraviolet Laser | Stereo-lithography |
| Material Extrusion | Thermal Energy | Fused Deposition Modelling |
| Binder Jetting | Thermal Energy | Indirect Inkjet Printing |
| Material Jetting | Thermal Energy/Photocuring | Polyjet/Inkjet Printing |

Table 1: Categories and examples of AM technologies (ASTM International, 2013)

AM offers many benefits over conventional manufacturing. Waste is minimal, improving material efficiency and reducing associated material costs (Emmelmann, Sander, Kranz, & Wycisk, 2011). Energy costs are reduced, for example metal powder feedstock can be directly produced from molten metal, eliminating the requirement for rolling or forging (Ngo, Kashani, Imbalzano, Nguyen, & Hui, 2018). The need for tooling modification or die manufacture is eliminated. Time to manufacture is decreased as products can move almost directly from design to production via CAD data (Ngo, Kashani, Imbalzano, Nguyen, & Hui, 2018). Alterations or significant changes can be carried out to component design through changing the CAD model.

As AM builds a component layer by layer it is possible to produce complex internal features using fewer production steps. Assemblies formed from multiple parts can be produced as a single integrated component, eliminating the need for parts to be joined, and potentially reducing weight, improving strength, and reducing costs (Lindemann & Jahnke, 2017). By using finite element analysis during the design process, components can be designed to use the minimum amount of material possible, reducing weight, whilst maintaining the required strength (Emmelmann, Herzog, & Kranz, 2017). AM processes can also be used in the repair of complex components.

Over the last decade an increased focus has been placed on AM as a field of research, especially with regards to the aerospace, nuclear and automotive industries (Yusuf, Cutler, & Gao, 2019; Leal, et al., 2017; Hiser, Schneider, Audrain, & Hull, 2020). The U.S Department of Energy (2012) reported that a potential 75% to 98% reduction in energy consumption could be achieved by switching from conventional manufacturing methods to AM. However more research and development is needed before AM can replace conventional manufacturing techniques. Currently it is largely regarded as a method to complement conventional manufacturing methods, with potential to increase component value – for instance through its capacity for part customisation and reductions in waste.

Through AM, design engineers are provided with increased freedom to explore component designs, altering them to optimise performance and reduce weight. For the aerospace industry this is desirable as reductions in component weight reduce fuel consumption. £350-£550 per kg of weight saved per year is commonly quoted, this can lead to huge cost savings across an aircraft's service life (Reinforced Plastics, 2014). Weight reductions in aerospace components using AM have already been witnessed. GE aviation adopted AM for producing their LEAP engine fuel nozzles. These previously consisted of 21 separate pieces, with 19 nozzles required per engine. Using AM they are produced as a single component, five-times more durable than their non-printed counterpart and 25% lighter (GE Aviation, 2013).

Lockheed Martin showed that using AM brackets within their joint strike fighter plane reduced manufacturing costs by 50% and the buy-to-fly ratio (the ratio of the weight of raw material used to manufacture a part to the weight of the final part (Saha, 2016)) from 33:1 to almost 1:1 (Dehoff, Tallman, Duty, & Blue, 2013). A 30% reduction in manufacturing costs was demonstrated by the US Air Force research laboratory whilst integrating AM into aero-engine casing production, also reducing component weight (Kinsella, 2008). These examples all demonstrate how AM is already benefitting the aerospace industry.

2.2 Laser Direct Energy Deposition

Laser Direct Energy Deposition (DED-L) uses a laser beam as an energy source to heat and create a melt-pool onto a metallic substrate. Using an inert gas, metal powder is blown into this melt-pool via a nozzle, aligned to the laser to optimise powder capture. Upon interaction with the melt-pool this powder melts, forming a deposit which fusion-bonds to the substrate (Gu, 2015). This deposit solidifies as the laser beam continues along its projected toolpath, forming a track of raised material in its wake. Through layering and overlapping tracks it is possible to form raised surface features on a substrate to near-net-shape (Zhong, Pirch, Gasser, Poprawe, & Schleifenbaum, 2017). By having

control over the laser and nozzle each layer can be developed with precise accuracy (Gu, 2015). Figure 3 shows a basic schematic of DED-L.

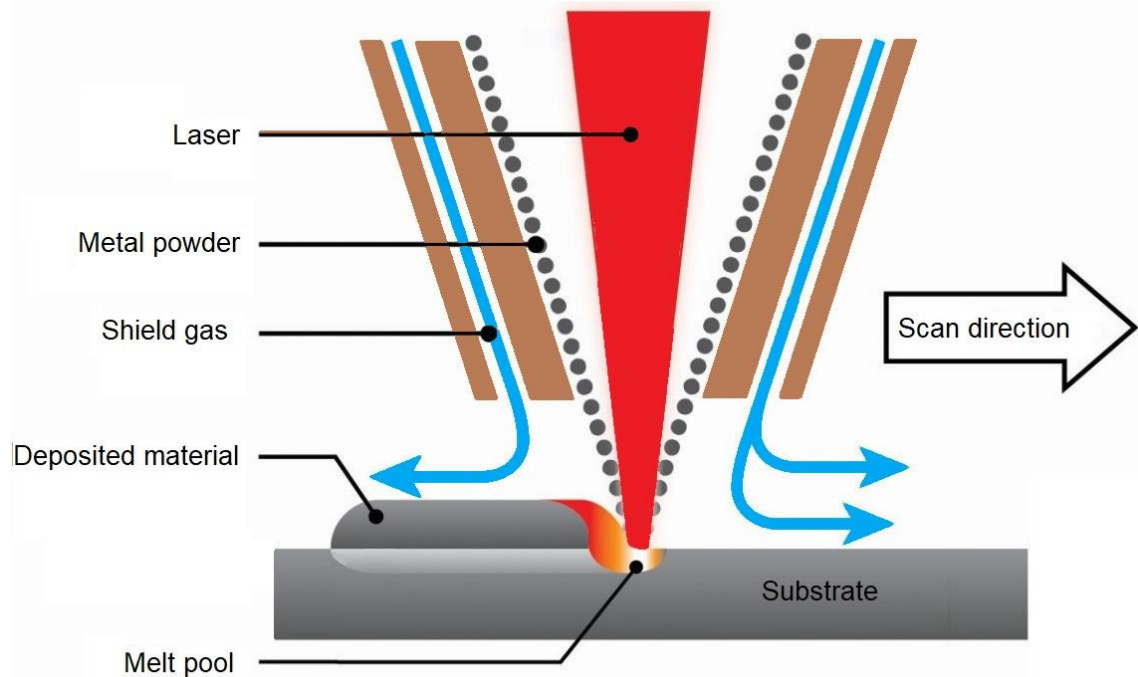


Figure 3: Schematic of DED-L, depicting the nozzle, laser, and substrate.

2.2.1 Applications

DED-L can be used to manufacture freestanding components, repair high value worn out parts, and to add new material onto existing components.

2.2.1.1 Freeform fabrication

Freeform fabrication provides a potential route for manufacturing components which require the properties or efficiency that DED-L can achieve. A fully net finish is unattainable for some applications, for example the surface of a deposited part may be too rough meaning post-processing is necessary to obtain the desired surface finish (Zhang & Jung, 2018). It can be difficult to produce overhangs and complex internal features, with support material required to successfully manufacture these structures (Milewski, 2017). This support material must support the melt-pool formed by the laser, otherwise the

deposition process will become unstable and the deposit geometry will deteriorate. Whilst 3-axis manipulation can be used to successfully build simple solid components with low angle side-walls (Kianian, 2017), advances in 5-axis configurations are enabling more complex components to be formed. This is because the two rotational axes allow the angle of the workpiece relative to the laser head to be manipulated. This ensures the melt-pool remains supported and that gravity does not alter the powder stream.

2.2.1.2 Hybrid manufacture

DED-L can be integrated with conventional subtractive manufacturing to form a hybrid system. This can eliminate unnecessary or expensive steps. For example where a forged billet of material must go through multiple stages to refine the components shape and features (U.S Department of Energy, 2012), DED-L can be used to add the features onto the basic component shape. This reduces the number of steps within the manufacturing process, saving time and costs (Zhang & Jung, 2018).

2.2.1.3 Remanufacture

Part repair and reconditioning can be performed via DED-L. This is useful for expensive components such as turbine blades, where repair costs less than replacement, extending component lifetime and reducing overall maintainance costs (Gregori & Bertaso, 2007). This method has proved successful for repairing single crystal nickel superalloy components, as DED-L can maintain the single crystal structure (Gaumann, Bezencon, Canalis, & Kurz, 2001; Gregori & Bertaso, 2007).

2.2.1.4 Combining materials

Functionally graded materials have gradual variations in microstructure or material composition along a specific dimension. DED-L can accomplish this as powder composition can be altered as the component is built layer by layer, providing almost total control over the changing gradient of the component.

Scwendner et al. (2001) suggest that this can be done by using separate powder feeders to simultaneously inject the powder in its desired proportions into the melt-pool. This enables components to be tailored to meet specific purposes or varying material properties across a component (Brueckner, Seidei, Lopez, & Willner, 2017; Santos, Shiomi, Osakada, & Laoui, 2006).

In-situ alloying can be accomplished with DED-L. Different powder materials are mixed within an integrated powder-mixing chamber prior to deposition. The resultant material deposited will have a composition equal to the sum of the individual powder feedstocks used (Brueckner, Seidei, Lopez, & Willner, 2017). However, variations in powder morphology and densities, and vibrations within the powder feed system can cause powders to segregate, causing uncontrollable variations in composition (Ludovico, Angelastro, & Campanelli, 2010).

2.2.2 Environment and Equipment

Maintaining the correct environment is essential during DED-L. At elevated temperatures many metals are highly reactive with oxygen and nitrogen, forming oxides and nitrides (Katayama, 2013). These are undesirable and often detrimental to the material, therefore exposure to these should be prevented. To do this an inert atmosphere is created inside the machine/deposition chamber, or a gas is used to shield the powder from the atmosphere. This gas is typically argon or helium (Ruiz, Cortina, Arrizubieta, & Aitzol, 2018).

To achieve an inert environment the machine/deposition chamber is sealed and filled with gas to reduce oxygen levels to below 10 ppm. However, maintenance of a totally inert environment can be difficult, timely, and costly (Katayama, 2013). This can be avoided by using an open atmosphere system with a shielding gas. The gas is pumped around the deposition head to protect the melt-pool and deposit from reacting with the atmosphere (Ruiz, Cortina, Arrizubieta, & Aitzol, 2018). It also assists in preventing powder particles from deflecting from the substrate and damaging the nozzle. However, the shielding

gas is limited to the area over which the nozzle is located, therefore as the deposition head continues along its toolpath the deposited material remains at a high temperature and can oxidise. Another alternative for smaller scale DED-L is to use a gas-filled bag which encompasses the laser, nozzle, and entire deposit.

2.2.2.1 Powder delivery system

DED-L powder feeders control the supply of powder to the nozzle. This is done using a hopper containing powder to supply powder into a slot cut into a rotating disc. Powder enters the disc powder slot and is carried to an outlet leading to the powder nozzle, as shown in Figure 4.

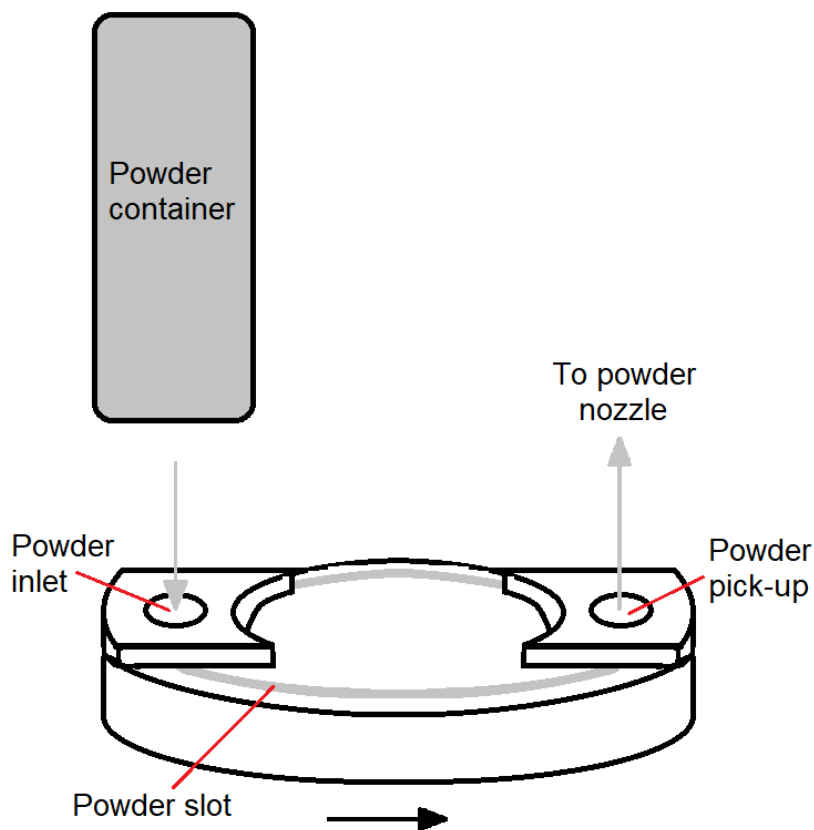


Figure 4: An example of how a powder feed system works in DED-L.

Powder slot size and powder outlet size affect powder feed rate. By adjusting the rotation speed of the disc, powder feed rate can be controlled, with faster

rotational speeds increasing the powder feed rate. The powder hopper is maintained at a positive pressure by an inert carrier gas (argon or helium). The pressure causes powder to be ejected from the rotating disc powder slot through the outlet port, then through anti-static polymer tubing to the deposition nozzle. The carrier gas then transports the powder to the melt-pool. This inert gas also prevents powder oxidation occurring as the powder interacts with the melt-pool and laser (Cortina, Arrizubieta, Ruiz, Lamikiz, & Ukar, 2018).

2.2.2.2 Deposition nozzles

Most DED-L systems use a deposition nozzle positioned coaxial to the laser beam, allowing the laser beam to pass through an aperture in the nozzle centre. This allows movement in any direction as the powder can enter the melt-pool from any angle.

Continuous, or conical flow coaxial nozzles are comprised of two truncated cones concentrically mounted, one within another, to form a narrow annulus between the inner and outer cones. By injecting powder into the upper of this annulus at several locations the pressure of the gas forces the powder to the opening at the thinner end of the cone. Upon exiting the nozzle the powder forms a hollow cone which reaches a focal point at a distance from the nozzle tip – known as powder standoff (Arrizubieta, Ruiz, Martinez, Ukar, & Lamikiz, 2017). An extremely fine powder focus can be achieved through controlling the gas flow rate, annulus gap, and lateral cone position. This enables fine features to be produced. Excessive heating, such as from repelled partially melted powder particles (spatter), can damage conical nozzles. Thus conical nozzles should not be used in conjunction with extremely high laser powers as overheating and melting may occur. The thin cone edges can easily deform if the nozzle and workpiece collide, resulting in turbulence and powder scattering, reducing process efficiency.

Where high laser powers are required multi-stream/jet coaxial nozzles may be more suitable. These are produced from a single block of material, and are

thicker, thus less sensitive to heat. Powder delivery channels are drilled into these nozzles at a fixed angle. This results in the powder converging and intersecting to form a powder focus a set distance from the nozzle tip. However this nozzle creates a coarser non-circular powder focus, resulting in a larger powder spot size and lower deposition efficiency (Arrizubieta, Ruiz, Martinez, Ukar, & Lamikiz, 2017).

These differences affect powder efficiency. Zhong et al. (2017) determined powder efficiency to be 11.5% greater using a conical nozzle compared to a 3-jet nozzle. Figure 5 shows the two nozzle types.

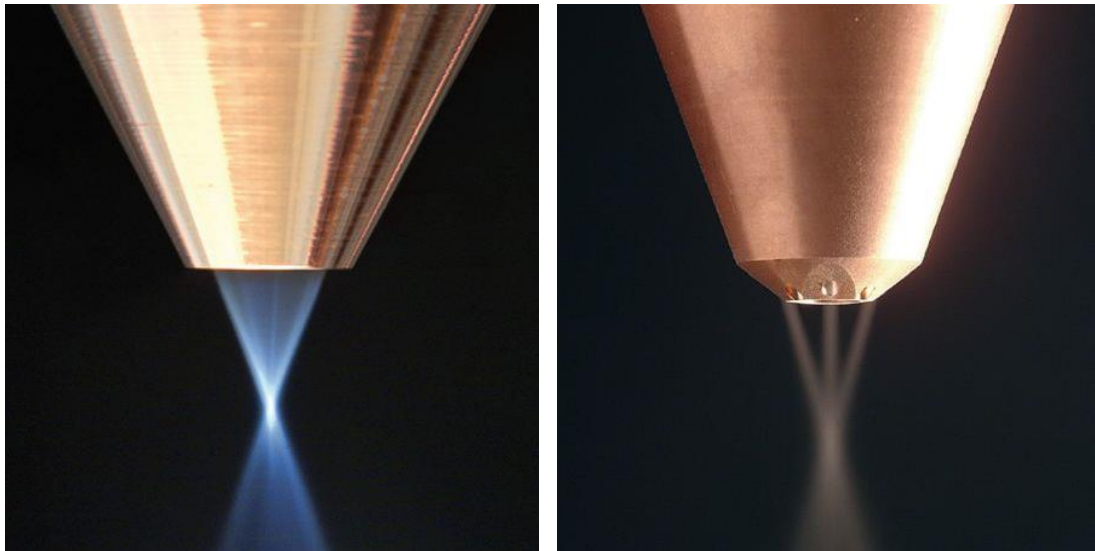


Figure 5: Photographs of a conical flow (left) and 3-jet (right) nozzle and their powder streams (Fraunhofer ILT, 2018).

For applications requiring a single direction of deposition – such as cladding constantly rotating shafts – side-feed nozzles can be used. As the single stream of powder enters the leading edge of the melt-pool at an optimum angle and position, good deposition efficiency and deposit quality are guaranteed (Arrizubieta, Ruiz, Martinez, Ukar, & Lamikiz, 2017). Figure 6 depicts the three nozzle types.

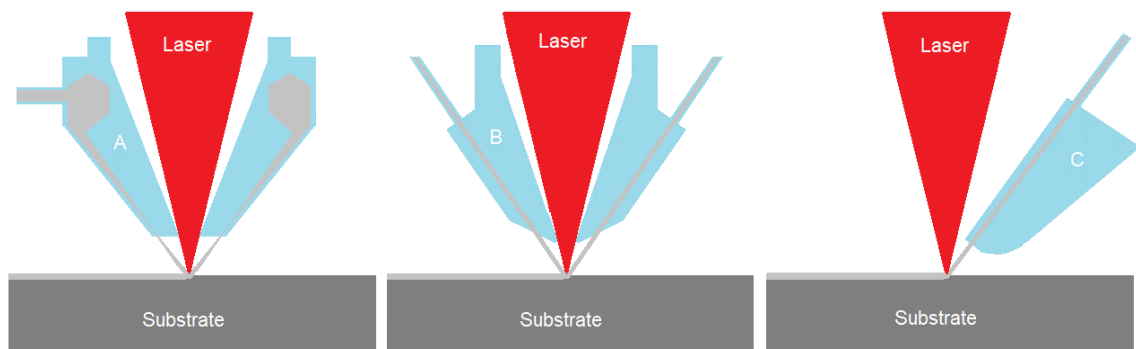


Figure 6: The nozzle types A) conical, B) multi-jet, C) a side-feed nozzle.

2.2.2.3 Lasers

Common lasers used for DED-L are semiconductor diode lasers, CO₂ lasers (wavelength: 10.6μm) or solid state Nd:YAG lasers (wavelength: 1.06μm). Lasers may be continuous wave or pulsed, varying in characteristics such as maximum power output and wavelength. All provide heat as an energy source for melting powder. Presently the majority of DED-L systems use CO₂ lasers due to their higher efficiency, lower cost, and easier maintenance than Nd:YAG lasers (Ludovico, Angelastro, & Campanelli, 2010).

2.2.3 Advantages and disadvantages

DED-L presents capabilities for fabrication, repairs, and surfacing. As the number of steps within the manufacturing process can be reduced, and multiple parts can be constructed within the same build, production times, material waste and thus costs can be decreased. Extremely accurate and fine features can be produced using this process.

Presently the costs associated with DED-L equipment are high, likely discouraging adoption within industry (Lindemann & Jahnke, 2017). Construction of a final component can be slow compared to conventional production methods if low deposition rates are required, limiting the applications where DED-L could be economically viable. Complex components with overhangs or internal cavities can be difficult to fabricate, and as only a near-

net-shape surface finishes can be obtained post-processing is often required to achieve the desired surface finish and geometric accuracy of a part.

Powder quality also varies. Variations in powder particle size, morphology, atomisation method and chemical composition contribute to poor repeatability in component material properties, despite maintaining identical processing parameters (Hu, Mei, & Kovacevic, 2002). This decreases confidence in the technology as outcomes can be uncertain. In addition to this a full understanding of the effect of deposition process parameters on material properties has not yet been realised.

2.2.4 Process parameters

Process parameters are variables which can be changed, altering the process. An overview of DED-L parameters is presented in Figure 2. Complex relationships exist between DED-L process parameters and the deposited materials properties (Segerstark, Andersson, & Svensson, 2014; Zhang & Jung, 2018). Process parameters affect the melt-pool characteristics, which regulates material fusion and the microstructure (Segerstark, Andersson, & Svensson, 2014). DED-L process parameters are typically determined by depositing numerous individual tracks using different process parameters combinations – this is a lengthy process, and what may produce a good quality track deposit does not guarantee the same quality in a larger build.

Due to non-linear relationships between process parameters and properties, slight changes in process parameters can result in large changes to material properties (Vetter, Engel, & Fontaine, 1994). Accurate control of these is therefore essential to obtain repeatable and predictable results. Table 2 contains properties which may be used to judge component quality.

| Mechanical | Geometrical | Metallurgical | Chemical |
|-------------------|--------------------|----------------------|----------------------|
| Toughness | Surface roughness | Grain size | Corrosion resistance |
| Tensile strength | Deposit dimensions | Microstructure | Homogeneity |
| Hardness | | Porosity | |
| Residual stress | | Cracking | |
| Wear resistance | | | |

Table 2: Properties used to reflect DED-L component quality.

2.2.4.1 Laser power

Laser power refers to the optical power output of a laser beam or average power of a pulsed or modulated laser. Deposition efficiency, surface finish, and the dimensions of a deposited track are significantly affected by laser power. Insufficient laser power does not provide enough energy to melt the powder or adequately fuse the deposited material, resulting in a poor deposit density (Mahamood & Akinlabi, 2015; Petrat, Brunner-Schwer, Graf, & Rethmeier, 2019). Greater laser powers can improve surface finish quality, reduce porosity, and increase dilution as more energy is available for powder melting (Mahamood & Akinlabi, 2014; Mahamood, Akinlabi, & Owolabi, 2017).

Liu et al. (2019) use Inconel 718 to show that increasing laser power increases melt-pool temperature. The melt-pool temperature of the first layer is the lowest, increasing non-linearly as further layers are deposited due to heat accumulation. This increase in melt-pool temperature is finite, reaching a point where it no longer increases.

Ocylok et al. (2014) state that there is a linear (straight-line) relationship between laser power and melt-pool dimensions. Heat accumulation within the substrate also affects melt-pool dimensions. If heat loss is rapid and there is little heat stored within the substrate, the melt-pool width decreases. If heat loss is slow and the substrate is storing a large amount of heat, the melt-pool width increases (Ludovico, Angelastro, & Campanelli, 2010).

Excessive laser powers can cause melt-pool vaporisation, subsequently increasing power absorption and causing a keyhole to form – where the melt-pool extends deeper into the substrate or material being deposited onto (Figure 7). This indicates that the relationship between laser power and melt-pool size is linear to a point before diverging due to vaporisation.

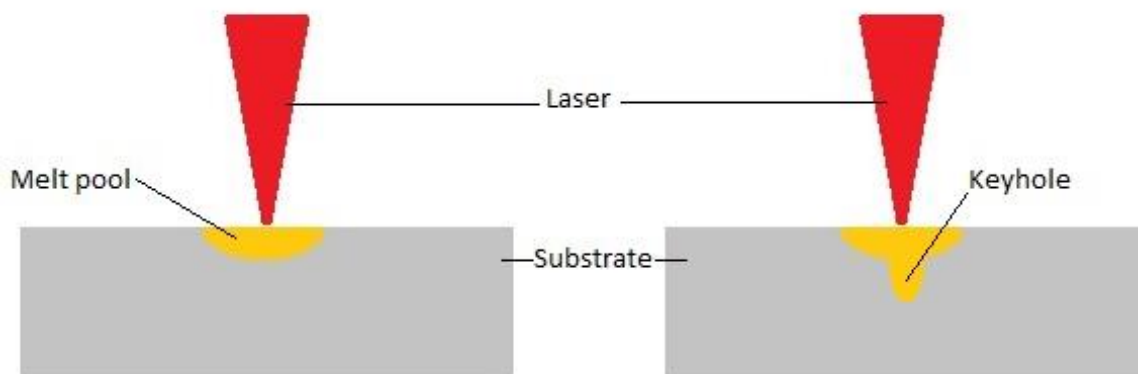


Figure 7: The effect of increasing laser power on the melt-pool, resulting in a keyhole forming.

Vaporisation results in melt-pool instability. When high laser powers result in high energy densities, spattering may occur, where liquid metal is ejected from the melt-pool (Zhang, Cao, Wanjara, & Medraj, 2013). Plasma may form, disturbing the powder flow. Plasma is an ionised gas formed when a gas is heated to the extent that atoms collide with each other, knocking electrons off

one another (Goldston & Rutherford, 1995). When using CO₂ lasers for welding, plasma formation is usually seen in powers exceeding 3kW (Laserline Technical, 2010). This may be akin to the effects seen in DED-L.

2.2.4.2 Scan speed

Scan speed is the speed that the laser moves along the toolpath. By increasing the scan speed, the time required to build a component can be reduced. However, this reduces the laser-material interaction time and can have an adverse effect on component quality (Mahamood & Akinlabi, 2015; Ludovico, Angelastro, & Campanelli, 2010). Powder particles may not fully melt or fuse, increasing porosity (Mahamood & Akinlabi, 2015). Alternatively, deposited layers may not achieve the desired thickness, or the height may vary between a component's edges and centre (Ludovico, Angelastro, & Campanelli, 2010).

Slower scan speeds increase laser-material interaction time ensuring powder particles melt, reducing porosity. However heat can accumulate in the material quicker.

2.2.4.3 Powder feed rate

Powder feed rate is the mass of powder per unit time exiting the nozzle. Multiple studies have demonstrated the importance of powder feed rate and its interaction with laser power. Mahamood and Akinlabi (2015) observed that increasing powder feed rate from 2 g/min to 4 g/min at a fixed laser power (from 1.8 kW to 3.0 kW) reduced melt efficiency –the laser power was insufficient to melt the powder. This increased porosity within the deposit. Greater surface roughness was noted under increased powder feed rates (Mahamood, Akinlabi, & Owolabi, 2017).

Ocylok et al. (2014) suggest that an increase in powder feed rate lowers the fraction of the laser available to interact with the substrate. Thus, assuming melt-pool width remains constant, track height will increase (Figure 8) and substrate penetration depth decrease. This has the effect of decreasing dilution (Mahamood, Akinlabi, & Owolabi, 2017).

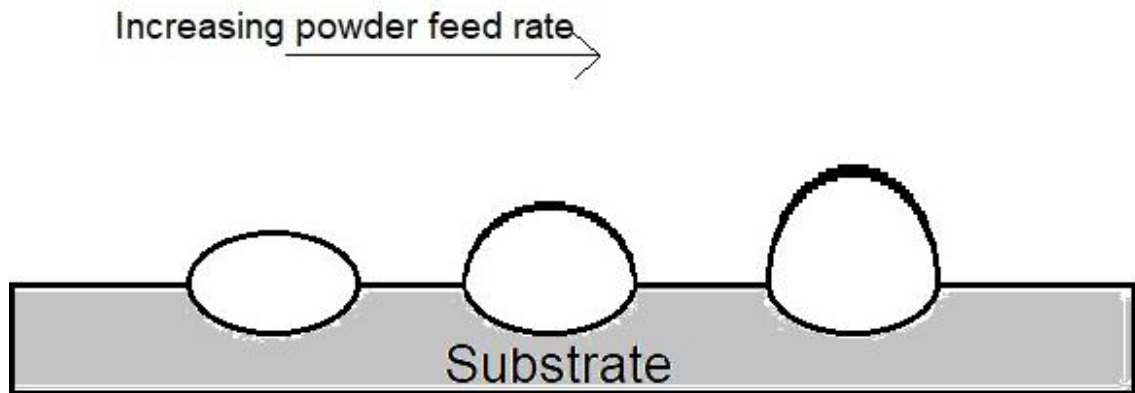


Figure 8: Schematic of the effect on track height when powder feed rate is increased. Cross sections of individual tracks on substrate.

A lower powder feed rate increases laser-substrate interaction, increasing penetration depth, melt efficiency and improving surface finish (Mahamood, Akinlabi, & Owolabi, 2017). However too little powder can result in keyhole formation as less energy from the laser is absorbed by the powder, and is therefore absorbed by the substrate (Matsunawa, Kim, Seto, & Mizuntani, 1998).

2.2.4.4 Gas flow rate

Gas flow rate is the volume of gas which exits the DED-L nozzle per unit time. Shielding gas flow rate and carrier gas flow rate take on individual values which can be different. Both flow rates affect the DED-L deposit. A high shielding gas flow rate can decrease efficiency by interfering with powder focus and increase gas entrapment, hence porosity (Ng, Jafors, Bi, & Zheng, 2009). Shah et al. (2010) showed that increasing carrier gas flow rates led to deeper melt-pools with reduced diameters, possibly due to increased powder particle velocity caused by the increase in gas flow rate.

2.2.4.5 Laser profile

The laser profile consists of the beam diameter and shape. Beam spot size/diameter can be altered by changing the distance between the substrate and the laser. Laser standoff refers to the point where the laser beam converges prior to diverging again. Identical laser spot sizes can be achieved at a positive and a negative laser standoff (Figure 9).

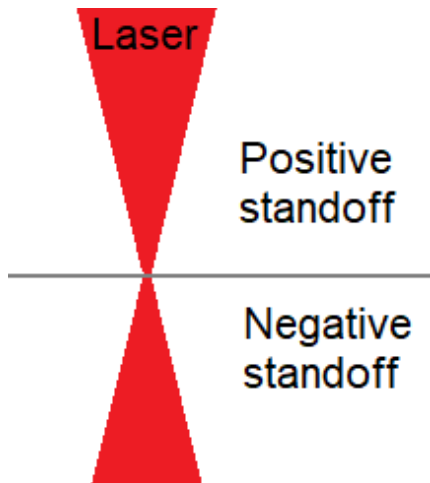


Figure 9: Schematic showing how identical laser spot sizes can be achieved at positive and negative laser standoffs.

Spot size ultimately determines the width of the track deposited, dictating the minimum size of features which can be achieved. A positive laser standoff distance is frequently used in DED-L as it means that the spot size grows into the material, reducing keyhole formation.

By reducing the spot diameter, the intensity of the laser power at that point increases, whilst the powder capture area of the melt-pool decreases, potentially reducing efficiency and build rate. Energy density is increased, resulting in potential vaporisation and excessive penetration (Matsunawa, Kim, Seto, & Mizuntani, 1998). However finer features can be created. Through using a large spot size in conjunction with a high laser power, a broad, shallow melt-pool can be created with a high powder capture area – potentially increasing process efficiency (Fotovvati, Wayne, Lewis, & Asadi, 2018).

2.2.4.6 Deposit dilution

Dilution is the mixing proportion of substrate to the region of deposited material (Yorserkani, Khajepour, & Corbin, 2005), and is more simply explained using Figure 10 and Equation 1.

Using a cross section of the deposited material, measurements of the area of deposit lying above the substrate surface and the melted material lying below can be taken, these measurements can be input into Equation 1 to obtain a value for dilution (Dass & Moridi, 2019; Yorserkani, Khajepour, & Corbin, 2005).

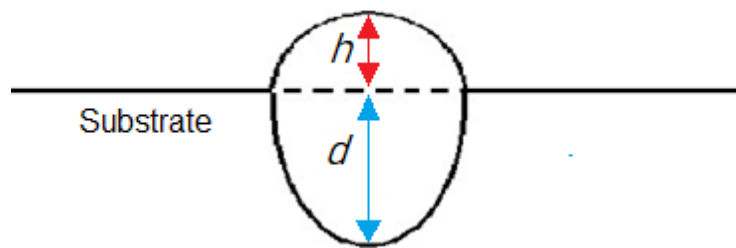


Figure 10: Using a cross section to calculate dilution.

$$D = \frac{d}{h + d} \times 100$$

Equation 1: Equation for calculating dilution (Dass & Moridi, 2019).

Where:

D = Dilution (%)

d = Depth of melt-pool below substrate surface (mm)

h = Height of material deposited above substrate surface (mm)

A greater value of h can be achieved by a lower energy input or higher powder feed rate, linking to a low dilution and lack of fusion between layers. A greater value of d corresponds to a higher energy input or lower powder feed rate, and can cause keyhole formation (Dass & Moridi, 2019).

2.2.4.7 Build strategy

Build strategy includes the deposition toolpath, the overlap between adjacent deposited tracks, and the z-increment between successive layers. Too little spacing between tracks can result in the tracks building on top of each other, creating a deposited layer with inconsistent thickness. It can also cause excessive re-melting of the adjacent track, and excessive heat input into the substrate (Bartolo, et al., 2013). If the spacing is too large, the surface of the deposited layer will be uneven – comprising of parallel grooves and ridges which can cause inter-track porosity (Figure 11) and fusion defects (Kao & Prinz, 1998).

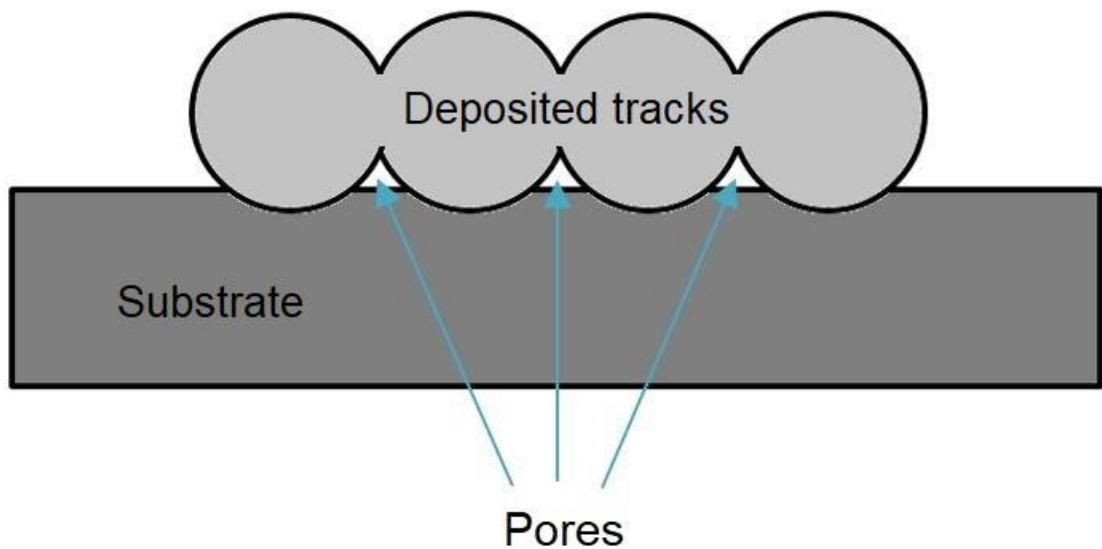


Figure 11: Inter-track porosity – pores between tracks formed due to excessive track spacing.

The height increment (z-increment) between successive layers is often established using trial runs to determine deposition layer height. As deposition layer height is geometry dependent, this value varies and is usually greater when fabricating thin walled sections (Qi, Azer, & Singh, 2010).

Four common toolpath patterns used to build DED-L parts include raster, bi-directional, offset (inward or outward) and fractal (Jin, He, & Fu, 2013; Yu, et al., 2011) (Figure 12).

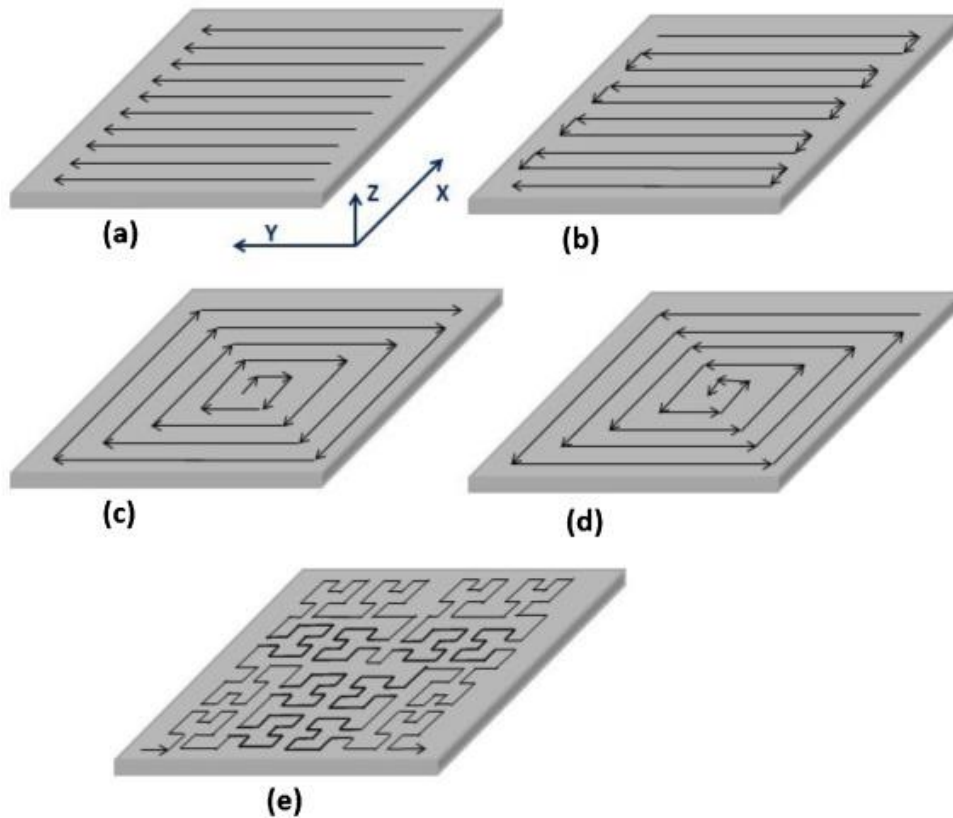


Figure 12: Common toolpath patterns used in DED-L; raster (a); bi-directional (b); offset (c & d); fractal (e) (Shamsaei, Yadollahi, Bian, & Thompson, 2015).

The geometrical and mechanical properties of fabricated parts are influenced by the toolpath used (Beuth & Klingbeil, 2001). Discontinuity is present within all toolpath patterns shown. This can result in excess powder being deposited at turn points, creating an uneven surface (Routhu, 2010). By using an appropriate toolpath, residual stresses and distortion can be minimised. Fractal and offset patterns increase geometric accuracy and use less energy, however raster is the most commonly used due to ease of implementation (Yu, et al., 2011). Use of a cross-directional raster toolpath (rotating 90° between each layer) results in the same material properties in the x-direction and y-direction (Kobryn & Semiatin, 2001).

Build orientation also influences material properties. Specimens deposited in the direction parallel to tensile specimen length via raster or bi-directional toolpaths have been found to exhibit greater tensile strength than those with layers deposited perpendicular to tensile specimen length (Zhang J. , 2004; Alcisto, et al., 2011). The different cooling rates experienced between these two

deposition orientations influences the microstructure, hence mechanical properties (Blackwell, 2005).

2.2.4.8 Powder

The powder used for DED-L can be produced via different methods. Gas Atomisation (GA) and Plasma Rotation Electrode Processes (PREP) are typically used, with quality varying between suppliers and manufacturing method. Advanced Plasma Atomisation (APATM) is used by AP&C to manufacture powder for AM. APATM feeds the raw material in wire form into an atomisation unit, where plasma melts the wire and atomises the molten material into spherical powder (GE Additive, 2017).

GA powder is cheaper than PREP and APATM powder. However satellites – powder particles stuck together – are common in GA powder. GA powder also has greater variation in morphology and may contain hollow particles which contribute to porosity (Xu, Ding, Ganguly, & Williams, 2019). PREP powder has a more spherical morphology, a higher density, and lower satellite content than GA powder. APATM powder also has a highly spherical morphology, high density, flowability, purity, and very low levels of porosity (GE Additive, 2017). Figure 13 shows GA powder, including satellites, compared to PREP powder.

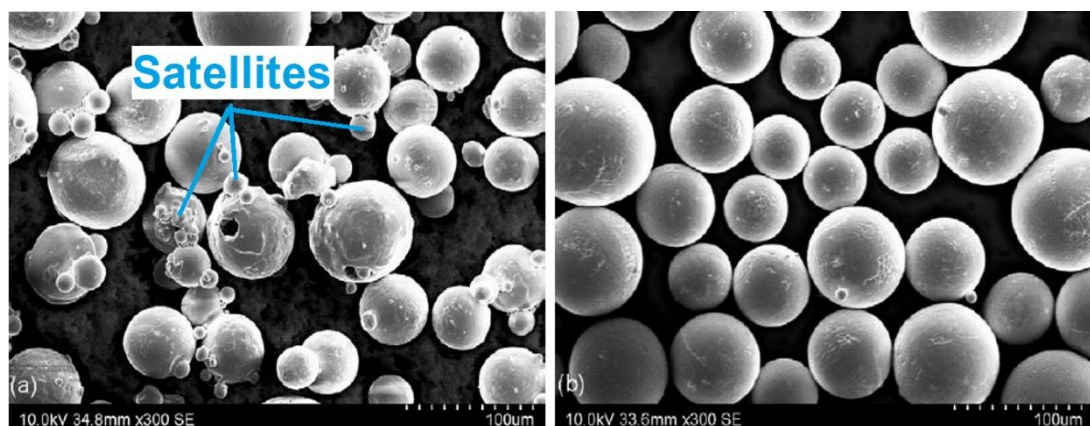


Figure 13: Scanning electron micrograph of GA powder (a) and PREP powder (b) (Ahsan, Pinkerton, Moat, & Shackleton, 2011). Examples of satellites within the GA powder are indicated.

Powder is classified by particle size distribution, for example 25 µm - 45 µm or 45 µm - 90 µm, as to obtain a specific individual powder particle size would be time-consuming and costly. This size variation, and variations which occur in powder composition and shape, contribute to disparity within material properties. However production of continually perfectly spherical particles is difficult. Greater sphericity of powder particles improves powder flowability and promotes uniform melting.

2.2.5 Process parameter optimisation

Table 3 shows a summary of the influence of several process parameters.

| | Parameter (effect on property as increased) | | | |
|---------------------|--|-------------------|-------------------------|----------------------|
| Property | Laser power | Scan speed | Powder feed rate | Spot diameter |
| Penetration | ↑ | ↓ | ↓ | ↓ |
| Hardness | ↓ | ↑ | ↑ | ↑ |
| Dilution | ↑ | ↓ | ↓ | ↓ |
| Track height | ↓ | ↓ | ↑ | ↓ |

Table 3: Parameter influence on deposit properties, derived from findings of studies mentioned (Dass & Moridi, 2019; Fotovvati, Wayne, Lewis, & Asadi, 2018; Liu, et al., 2019; Ludovico, Angelastro, & Campanelli, 2010; Mahmood, Akinlabi, & Owolabi, 2017; Mahmood & Akinlabi, 2015; Mahmood & Akinlabi, 2014).

Adjustments must be made to process parameters to maintain a consistent deposition process – however there are currently no quantitative studies which indicate optimal control parameters as a result of the complex underlying

physics of the process. Due to heat conduction from newly deposited layers to previously deposited layers (Dinda, K, & Mazumder, 2010), and heat accumulation which occurs during building, maintaining constant process parameters does not generate a uniform thermal history throughout the deposited part (Bi, Gasser, Wissenbach, Drenker, & Popraw, 2006; Song, Bagavath-Singh, Dutta, & Mazumder, 2021).

Energy per unit length, which is calculated using laser power and scan speed is frequently used as a comparative factor in DED-L. Powder per unit length, calculated using powder feed rate and scan speed has also been considered to an extent. Petrat et al. (2019) combined laser power, scan speed, and powder feed rate to obtain mass energy (Joules/g), and demonstrate that a constant mass energy (obtained by varying laser power, scan speed, and powder feed rate) results in different microstructures and track geometries. They suggest that future work using mass energy to evaluate process parameters should be performed.

Process parameters affect the microstructure, and thus mechanical properties, making process parameter optimisation important in minimising defects (Mazzucato, Forni, Valente, & Cadoni, 2021). Optimal process parameters are typically determined through extensive test runs which can be time-consuming and incur significant costs. Due to the interactions between process parameters, development of a general, comprehensive methodology for DED-L process optimisation is challenging. Models have been created which define multiple critical parameters, however these are defined independently of one another, neglecting the complex relationships which are present between them (Thompson, Bian, Shamsaei, & Yadollahi, 2015).

2.2.6 Processing defects

Processing defects include porosity, cracks, residual stress, distortion, and anisotropy. These are influenced by the thermal cycling and heat build-up within the deposit (Segerstark, Andersson, & Svensson, 2014).

2.2.6.1 Porosity

Porosity occurs due to vaporisation of elements (Hashmi, Batalha, Tyne, & Yilbas, 2014), solidification shrinkage, or rapid solidification providing insufficient time for gas to escape (Mahamood, Akinlabi, Shukla, & Pityana, 2014). Inter-track porosity can also form (Figure 11). Pores can act as sites for crack initiation (Shamsaei, Yadollahi, Bian, & Thompson, 2015). Figure 14 shows process-induced pores from lack of fusion, and gas porosity caused by gas trapped within the powder.

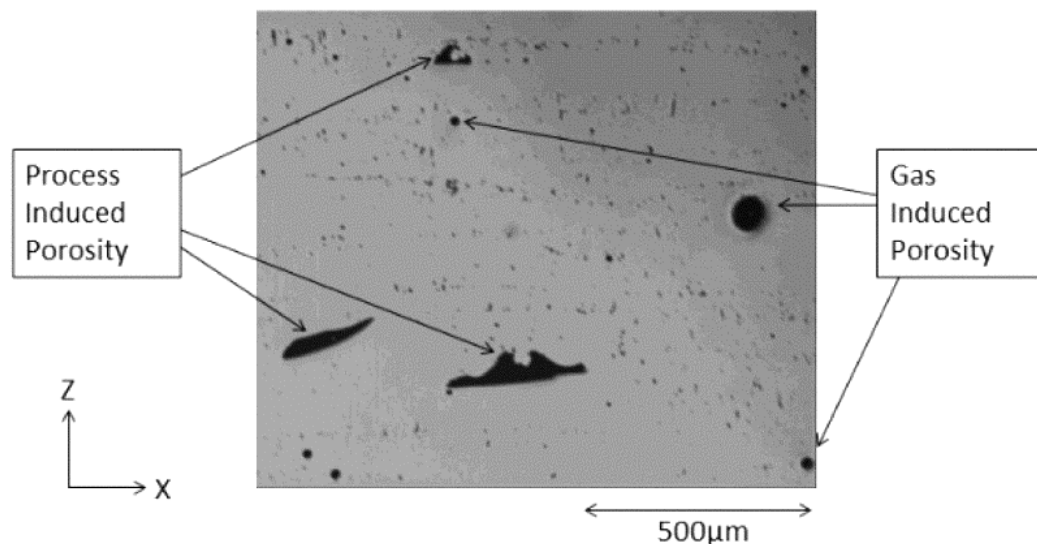


Figure 14: Optical micrograph of process-induced porosity (irregular) and gas porosity (spherical) (Sames, List, Pannala, Dehoff, & Babu, 2016).

Mahamood et al. (2014) observed pore size to vary depending on the cause of porosity. They suggest that un-melted powder porosity produces smaller pores as pore size is limited by powder particle size, whereas pores formed from gas entrapment are larger and more variable in size. They demonstrated that combining lower scan speeds with higher laser powers can reduce porosity levels, as the increased interaction time and slower solidification rate ensured powder melting, and that gas could escape the melt-pool prior to solidification. They observed no porosity in samples manufactured using 800 W laser power and 0.005 m/s scan speed.

The interaction between powder particle size and laser power affects porosity. Smaller particles heat up faster than larger particles, increasing the probability that they are completely molten when entering the melt-pool. Larger particles which are not fully molten are more likely to contain gas inclusions which cannot escape (Segerstark, Andersson, & Svensson, 2014).

2.2.6.2 Cracking

Cracks can develop via multiple mechanisms, with each melting and solidification step during DED-L allowing material shrinkage, liquation, and elemental segregation to occur.

As the material solidifies, changes in volume can cause solidification cracks (Brueckner, Seidei, Lopez, & Willner, 2017). Figure 15 shows an example of solidification cracking in Inconel 718.

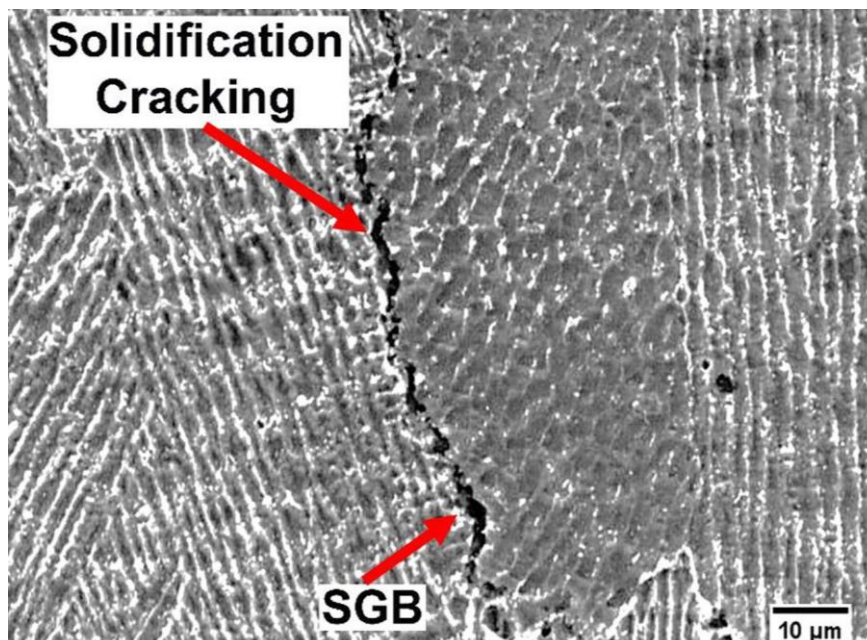


Figure 15: Solidification cracking along the solidification grain boundary (SGB) of a single deposited Inconel 718 track (Alizadeh-Sh, Marashi, Renjbarnodeh, Shoja-Razavi, & Oliveira, 2020).

Differences in solid and liquid phase zones can cause liquation cracks. Chen et al. (1998) reported that Heat-Affected Zone (HAZ) liquation cracks are affected by scan speed and heat input – higher scan speeds and heat inputs increased crack length. Elements or constituents within an alloy can segregate during

solidification due to their different melting points, providing potential weak points for crack initiation (Amine, Newkirk, & Liou, 2014).

Segerstark et al. (2018) determined cracking susceptibility to increase under a lower powder feed rate, and higher laser power and scan speeds. Cracks predominantly propagated perpendicular to the substrate and were located close to the centre of the deposited tracks. Klimova-Korsmik et al. (2016) also observed fewer cracks in Ni-alloy deposited using lower scan speeds, and found that cracks initiated during cooling.

2.2.6.3 Residual stress

Residual stress is the stress within a body in equilibrium, at rest, and at uniform temperature in the absence of external and mass forces (ASTM International, 2009). Despite DED-L considered to be a “low heat input” process compared to others, such as arc welding (Bian, Shamsaei, & Usher, 2017), the rapid substrate melting and repetitive heating can result in high thermal gradients and thus residual stresses (Pirch, et al., 2018). Residual stress can cause cracking, distortion, and reduce component strength and lifetime, (Kamara, Marimuthu, & Li, 2011; Lawrence & Waugh, 2014; Beuth & Klingbeil, 2001).

During DED-L the high energy intensity of the laser heats the material rapidly causing it to expand – this is thermal expansion. The expansion is restrained by the surrounding material which is at a lower temperature. This results in compressive stress forming at the heated zone. When the energy/heat source is removed the heated zone begins to cool and shrink. This shrinkage is partly restrained by the plastic strain formed previously during the heating stage. The result is tensile residual stress in the heated zone which is balanced by a surrounding compressive zone (Mercelis & Kruth, 2006).

2.2.6.4 Distortion

Distortion, which is described as the deviation of a part from its actual dimension or shape, can occur during or following DED-L. This can deteriorate

a components functionality, potentially rendering it unusable (Li, Liu, X, & Gua, 2018).

As thermal gradients form, and cooling and heating rates vary throughout a component, the uneven heat dispersion causes distortion. This can be reduced by controlling cooling rates (Shamsaei, Yadollahi, Bian, & Thompson, 2015). Higher laser powers and slower scan speeds, hence larger heat input, have been linked to increased distortion (Amine, Newkirk, & Liou, 2014).

Distortion can take multiple forms, such as contraction upon cooling. It can be non-uniform throughout a component, such as when bowing occurs non-coincidentally with the neutral axis. As distortion is governed by material contraction and expansion, the coefficient of thermal expansion is key in determining the stresses which are generated during DED-L and hence distortion (Smallman & Ngan, 2014). Materials with higher coefficients of thermal expansion are more likely to suffer from distortion.

2.2.6.5 Anisotropy

Anisotropy describes the variation in material properties between different directions. This relates to the microstructure. As multiaxial loading is common in many industrial applications, elimination or minimisation of anisotropy is essential. Anisotropy has been noted within DED-L deposits, attributed partly to local process variations and differences in inter-track and inter-layer bonding (Kobryn & Semiatin, 2001). Directional columnar grain growth is proposed to be the main cause of anisotropy in DED-L builds (Mostafa, Rubio, Brailovski, Jahazi, & Medraj, 2017).

DED-L anisotropy is affected by build orientation and fabrication direction (Kobryn & Semiatin, 2001; Shamsaei, Yadollahi, Bian, & Thompson, 2015). This varies according to component geometry and the build strategy used. The heterogeneous cooling induced by various laser toolpaths leads to different microstructures forming, causing variation in mechanical properties. A review by Dass & Moridi (2019) on DED-L found that greater cooling times between

adjacent tracks and successive layers promotes homogenous properties, reducing anisotropy.

2.3 Microstructure

The microstructure of a material refers to the grain structure which is visible under an optical or electron microscope. Final deposit microstructure is predominantly determined by the chemical composition of the depositing material used, the solidification rates, and any further exposure to temperature of the deposit during manufacture and subsequent processing (ASM International, 1993; Optomec, 2016). This microstructure governs the materials mechanical properties.

As solidification of the deposited molten metal commences in DED-L, nucleation occurs at the solid-liquid interface. Individual crystals grow around these solid nuclei. These crystals can vary in crystalline structure or atomic arrangement, influencing properties. This variation is material dependent as only certain structures are possible within different materials. Previous studies on welding show that heterogenous nucleation, surface nucleation, grain separation and dendrite (defined in section 2.3.1) breakages enable new grain nucleation (Kou, 2003). These mechanisms are also found during DED-L (Jelvani, Razavi, Barekat, Dehnavi, & Erfanmanesh, 2019). External factors such as un-melted powder and impurities also contribute to the formation of new nuclei (Li, et al., 2018). Table 4 shows the atomic arrangement of common crystalline structures.

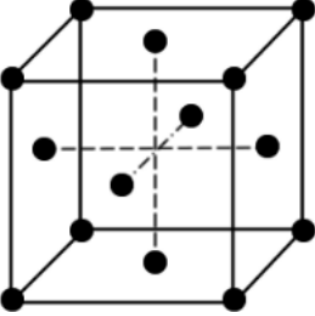
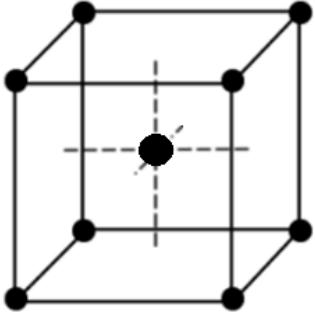
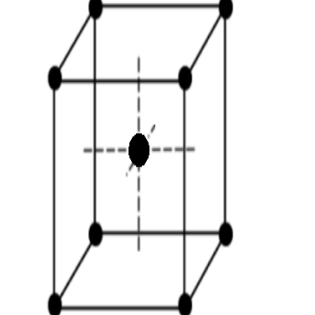
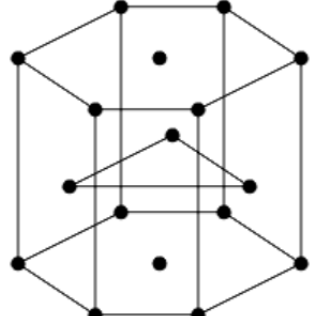
| Structure | Description | Image |
|--------------------------------|--|---|
| Face-centered cubic (FCC) | Cube with atoms on each corner and face centres. |  |
| Body-centered cubic (BCC) | Cube with atoms on each corner and one in the cube centre. |  |
| Body-centered tetragonal (BCT) | Cuboid with atoms on each corner and one in the cuboid centre. |  |
| Hexagonally close packed (HCP) | Three layers of atoms. The top and bottom layers contain 7 atoms each: one at the centre of the face and others at the corners. The middle layer contains 3 atoms. |  |

Table 4: The arrangement of atoms within common crystal structures in metals/alloys.

As the number of crystals increases, grains are formed which grow independently of each other. This creates the grain structure, which can consist of various grain types and sizes. Where grains growing in different orientations meet, grain boundaries are formed. These create a continuous network within the disrupted structure, acting to hinder dislocation movement, reduce metal ductility and increase strength. This often results in the metal acting differently at grain boundaries. Figure 16 demonstrates grain and grain boundary formation.

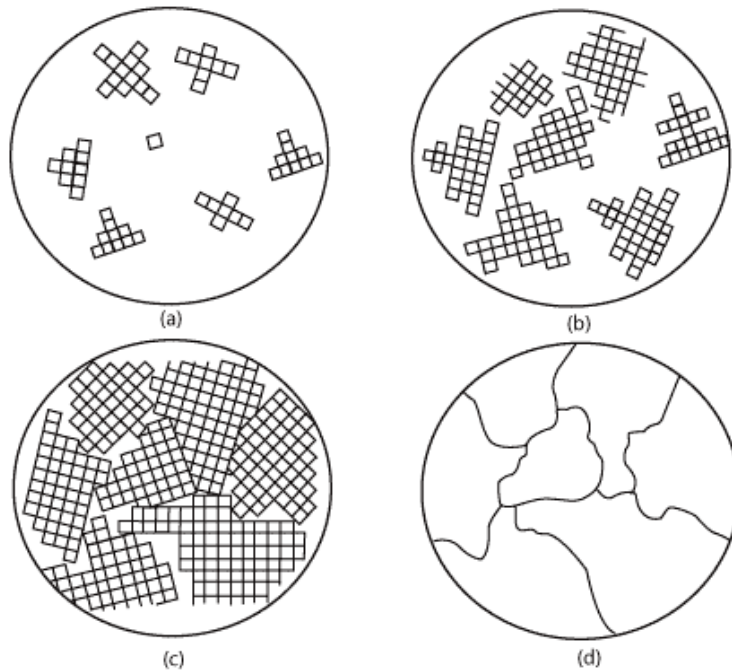


Figure 16: Stages of solidification resulting in grain formation. a) Crystal nucleation, b & c) increase in crystal number and grain growth, d) grains and grain boundaries as seen under a microscope (NDT Resource Centre, 2018).

DED-L parts have a different microstructure compared to their wrought counterpart due to their different thermal history (Xu, Ding, Ganguly, & Williams, 2019). As successive layers are deposited, the previously deposited material is re-melted, allowing grains to continue to grow through consecutive layers. Different layers experience different thermal history's (Li, et al., 2018), resulting in a complex microstructural evolution (Wei, Knapp, Mukherjee, & DebRoy, 2019). Figure 17 contains a schematic of the typical columnar microstructure formed during DED-L.

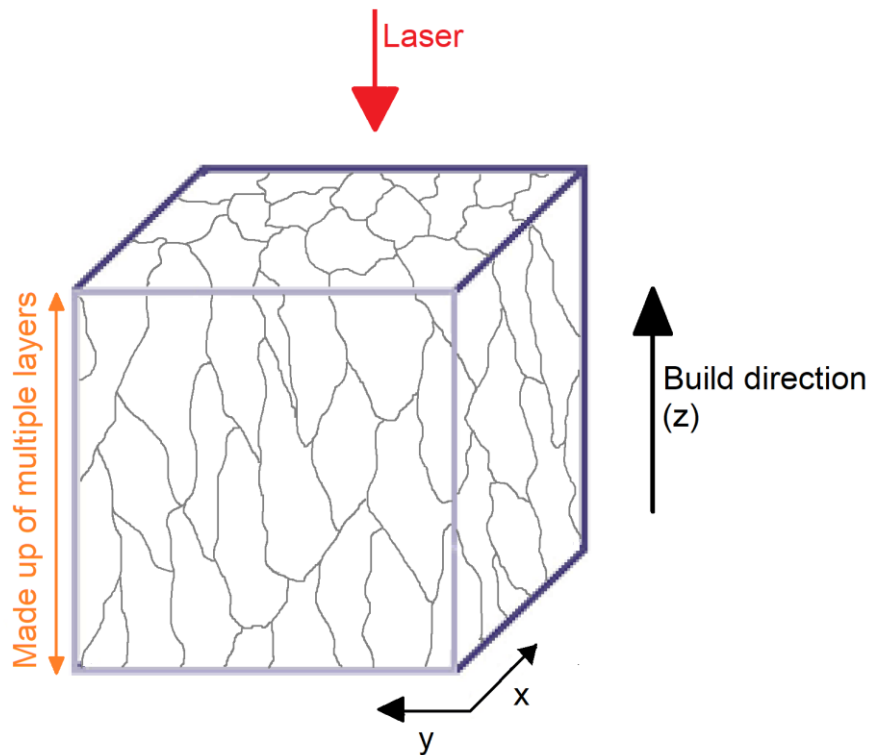


Figure 17: Schematic of typical columnar grain structure formed during DED-L. Grains cross multiple layers, extending towards the laser.

Microstructure morphology varies moving upwards through the layers of a DED-L deposit. This is due to the substrate that is being deposited onto initially acting as a heat-sink for the first few deposited layers. In a continuous DED-L build this results in a higher cooling rate initially compared to later on in the process, as the increasing number of deposited layers causes heat to build up within the deposited material, decreasing the cooling rate (Kim, Cong, Zhang, & Liu, 2017; Bennett, et al., 2018).

As numerous process parameters impact the thermal cycle, predicting microstructural features and their dependence on process parameters is a challenge. Multiple studies have demonstrated that the thermal history of a component significantly affects microstructural homogeneity and mechanical properties (Bontha, Klingbeil, Kobryn, & Fraser, 2006; Mazumder, Dutta, Kikuchi, & Ghosh, 2000; Sanchez Amaya, Amaya-Vazquez, & Botana, 2013).

2.3.1 Grain morphology

Grain morphology refers to the size and shape of the grains which make up the microstructure. The grain morphology of a deposited part is determined by the temperature gradient (G) and the growth/solidification rate (R) (Wei, Mazumber, & BedRoy, 2015; Mao, et al., 2002). Optimal G and R values vary according to part geometry, part purpose, material properties, and process parameters (Selcuk, 2011; Vilar, 2001).

Different G and R values result in three major structure grain morphologies: columnar (elongated grain morphology), columnar-equiaxed, and equiaxed (isotropic grain morphology – equal dimensions in all directions).

Microstructures may be planar (high G and low R), cellular, columnar dendritic or equiaxed dendritic (low G and high R) (Selcuk, 2011). The transformation from columnar to equiaxed grain morphology is promoted by higher solidification rates (Bontha, Klingbeil, Kobryn, & Fraser, 2006). A cellular structure is generated when the crystals grow in columns. If secondary arms, called dendrites, form the structure is said to be dendritic (Smallman & Ngan, 2014). Figure 18 demonstrates the influence of G and R on microstructure.

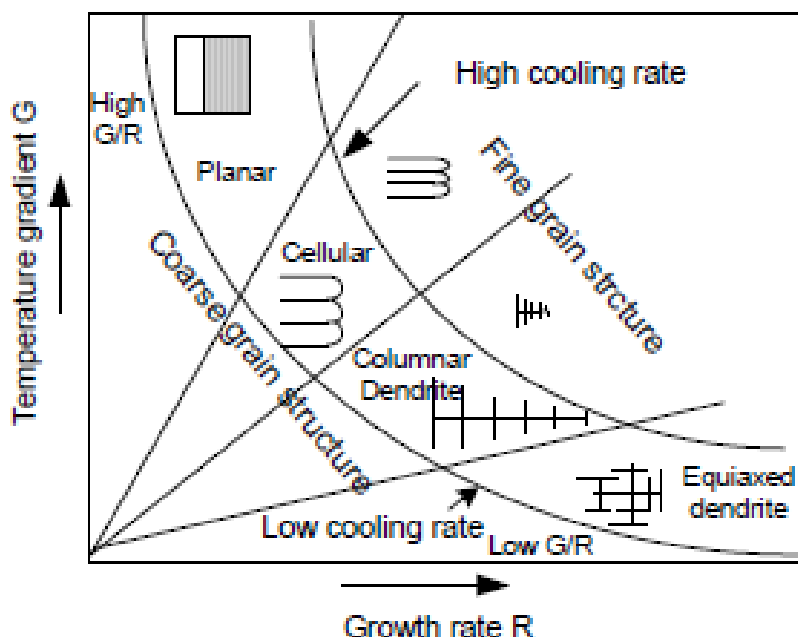


Figure 18: The effect of temperature gradient (G) and growth rate (R) on microstructure (Mao, et al., 2002).

The nature of the grains, including composition and grain size, determines overall mechanical behaviour. As G and R values vary spatially, grain morphology can vary throughout a component (Wei, Mazumber, & BedRoy, 2015). In DED-L, single grains can run through several layers of the deposited material, and columnar grains may grow throughout the entire length of a part (Li, et al., 2018). Finer microstructures produced through greater solidification and cooling rates tend to contain more grains and grain boundaries compared to coarse microstructures, resulting in superior material properties such as increased strength (Selcuk, 2011). This is due to the rapid solidification minimising the opportunity for grain growth (Everton, Hirsch, Stravroulakis, Leach, & Clare, 2016).

Saboori et al. (2017) found that during DED-L, columnar grains form at the bottom of the melt-pool due to the high thermal gradient and cooling induced by the substrate. Moving upward through the melt-pool the thermal gradient and cooling rate decrease resulting in equiaxed grain formation at the top of the melt-pool. As consecutive tracks or layers are deposited these equiaxed grains partially re-melt and act as nuclei for epitaxial grain growth, resulting in the formation of columnar grain morphology (Wei, Knapp, Mukherjee, & DebRoy, 2019; Jinoop, Paul, & Bindra, 2019). The size of solidified grains largely depends upon the previous layers' grain size.

Previous research has shown that columnar grain growth occurs in the direction opposite to the largest thermal gradient, in the case of DED-L this is towards the laser (Yang, Du, & Chang, 2018; Mostafa, Rubio, Brailovski, Jahazi, & Medraj, 2017). Gaumann et al. (2001) observed that a lower scan speed promoted columnar grain formation, attributed to a decreased solidification rate.

The coarse columnar grain morphology which forms due to the repeated thermal cycling alters mechanical properties compared to the materials wrought or cast counterpart (Kim, Cong, Zhang, & Liu, 2017). Columnar microstructures are more susceptible to solidification cracking than fine equiaxed microstructures (Kou, 2003) due to increased segregation during solidification

and poor accommodation of strain (Dye, Hunziker, & Reed, 2001). The higher density slip bands in finer microstructures promote resistance to crack initiation. However, they also promote of a flatter crack path which results in a reduced resistance to crack propagation than coarse microstructures with rougher crack paths.

Equiaxed grain formation is favoured as homogenous material properties can be obtained throughout a component, improving the predictability of mechanical properties. However for the repair of single crystal or directionally-solidified alloy components, epitaxial columnar grains of the same orientation as that of the base metal are preferred. This is due to their better performance in situations where greater mechanical properties can be obtained in a single direction (Versnyde & Shank, 1970).

Grain size determines the maximum slip band length, hence its effect on strength. The smaller the grain size the less the repulsion stress experienced from a grain boundary dislocation, thus the greater the applied stress required to propagate dislocations within the material (Whang, 2011). As strength increases ductility decreases, resulting in a trade-off between the properties (Selcuk, 2011).

The Hall-Petch equation (Equation 2) considers the relationship between strength and grain size, regardless of other microstructural parameters.

$$\sigma_y = \sigma_0 + \frac{K}{\sqrt{d}}$$

Equation 2: The Hall-Petch equation for the relationship between strength and grain boundaries.

Where:

σ_y = Yield strength

σ_0 = Material constant – grain interior resistance to deformation

K = Material constant – strengthening coefficient

d = Mean grain size

This equation is largely used for wrought alloys, requiring modification or an alternative method of quantification for more complex microstructures containing dendrites, secondary phases, or intermetallic phases.

2.3.1.1 Secondary Dendrite Arm Spacing

For materials containing dendritic structures, Secondary Dendrite Arm Spacing (SDAS), which relates to localised solidification rate, is the microstructural feature most frequently considered akin to wrought material grain size (Ghassemali, Riestra, Bogdanoff, Kumar, & Seifeddine, 2017).

Formation of dendritic structures signifies elemental segregation. This is dependent on the cooling rate, and is characterised by a gradient in composition between the dendrite core and its periphery, arising during non-equilibrium solidification (Radhakrishna & Prasad Rao, 1997; Zhang, Yao, & Jyoti, 2011).

A finer dendritic structure reduces SDAS, this is associated with faster solidification and has been observed to correlate with increased strength and hardness (Vandersluis & Ravindran, 2017; Chen & Mazumber, 2017). Amine, Newkirk and Liou (2014) found SDAS to increase with increasing laser power when other process parameters were kept constant, supporting that quicker solidification decreases SDAS. They also observed increased SDAS to correlate to greater hardness.

SDAS is generally measured on micrographs using the “linear intercept method”. This involves drawing a straight line along a primary dendrite arm and counting the number of secondary dendrite arms (SDA) which intersect this line (Vandersluis & Ravindran, 2017). However there is variation in how this technique has been applied in research. Figure 19 shows various examples of how this technique has been adapted.

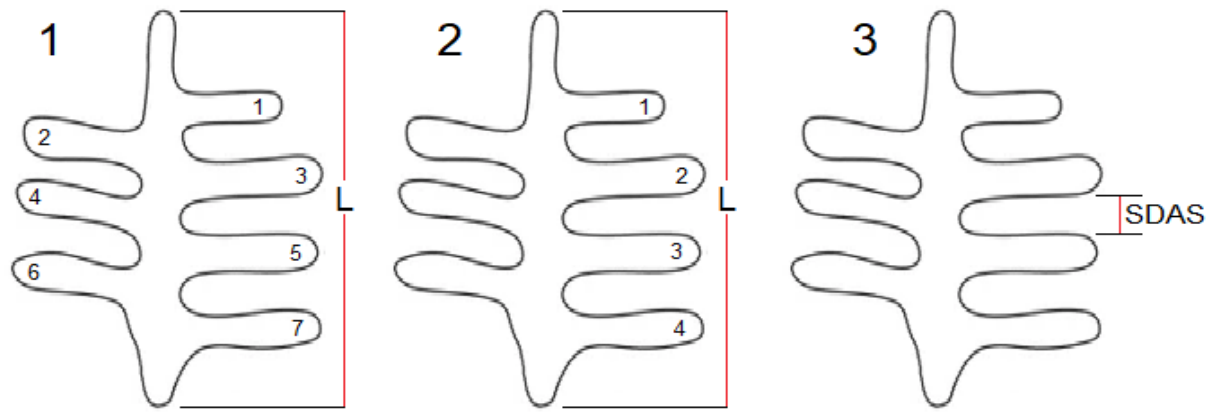


Figure 19: Schematic showing three approaches to quantify SDAS. 1 and 2 use variations of the linear intercept method, 3 uses the distance between two SDA. L refers to length.

Approach 1 uses the full length of the primary dendrite arm and counts the SDA on both sides of this whilst approach 2 counts the SDA on only one side. The following equation is then used to calculate SDAS.

$$SDAS = \frac{L}{N - 1}$$

Equation 3: Equation to calculate SDAS.

Where:

L = Length

N = Number of SDA

Alternatively the distance between adjacent SDA may be measured (Figure 19, approach 3).

A comparison of five common methods was carried out by Vandersluis and Ravindran (2017). They determined that using the length between the centre points of the topmost and bottommost SDA on one side and counting that sides number of SDA to be most consistent in determining SDAS (Figure 20).

Equation 3 is then applied.

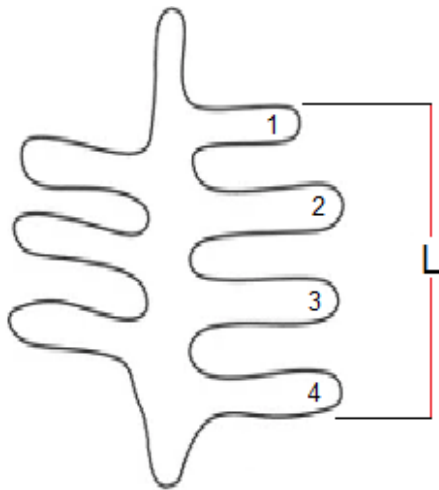


Figure 20: The linear intercept method approach which Vandersluis and Ravindran (2017) determined most accurate for determining SDAS. L refers to length.

This approach was determined most accurate as dendrite asymmetry did not influence this method and the primary lengths used are restricted to where the SDA were measured.

2.3.2 Microstructural phases

Microstructures can consist of several different phases. Each phase has its own unique chemical composition and/or structure. They form according to the materials chemical composition and thermal history. Exposure to certain conditions, such as high temperatures or rapid cooling, can cause phase transformations within the metal. Transformations may occur whilst the metal remains in solid state, these are allotropic transformations. Material properties are determined by the phases present, their proportions, and their spatial arrangement.

2.4 Heat-treatments

Heat-treatments use heating or cooling to alter or refine a materials microstructure (Dempster, Forgings, & Wallis, 2016; American Machine Tools, 2012). Undesirable phases which are detrimental to mechanical properties can

be removed, second-phase particles – such as carbides or intermetallic phases – can be dissolved or redistributed, and desirable phases can be precipitated (Dempster, Forgings, & Wallis, 2016).

Heat-treatment temperatures and times depend on the material, and the structure developed during prior mechanical and thermal operations. Heat-treatments can be used before or during DED-L (pre-heat), or after DED-L (post-heat).

2.4.1 Pre-heat

Prior to deposition the substrate to be deposited onto is heated to a specific temperature. This reduces the temperature gradient between the substrate, the deposited material, and the laser. This lowers the cooling rate, producing a more ductile metallurgical structure with greater cracking resistance and increases the length of time for entrapped gas to diffuse out (Totten, 2007).

2.4.2 Post-heat

Following deposition, the temperature is slowly lowered to encourage even cooling of the component. This reduces the cooling rate and can reduce distortion, crack propagation, and crack development (Totten, 2007).

2.4.3 Annealing

Annealing involves heating to a high temperature for a set time during which recrystallisation and/or phase transformation occurs, prior to cooling slowly (American Machine Tools, 2012). This softens the alloy, and often reduces the yield and tensile strength, but increases ductility. Post-annealing of an as-deposited part can reduce residual stress by 70% (Shiomi, Osakada, Nakamura, Yamashita, & Abe, 2004).

2.4.4 Solution treatment

Solution treatment involves heating the material to a suitably high temperature to dissolve soluble elements/constituents. The material is held at this temperature prior to rapid cooling to prevent the dissolved constituent(s) from re-precipitating (American Machine Tools, 2012). This process is often followed by ageing.

2.4.5 Ageing

In ageing or precipitation hardening the material is held at a temperature lower than any previous solution treatment temperature for a period of time prior to cooling. Double-ageing involves holding the material at a second lower temperature following part cooling from the initial ageing temperature. This is utilised to produce the desired size and distribution of precipitates throughout the material, enabling increases in yield and tensile strength. El-Bagoury & Ramadan (2012) observed Inconel 718 hardness to increase when subjected to ageing following solution treatment.

2.4.6 Quenching

Quenching is the process of rapidly cooling from a high temperature by submersion in a quenching medium, for example oil, water, or brine (American Machine Tools, 2012), and can be used to prevent undesirable phase transformations (Liscic, Tensi, Canale, & Totten, 2010).

2.4.7 Hot isostatic pressing

Hot isostatic pressing (HIP) utilises high pressure in conjunction with temperature. The component is surrounded by a gaseous medium – typically argon – and a high pressure and temperature are simultaneously applied. This consolidates the material, densifying the component and reducing porosity (Kobryn & Semiatin, 2003).

2.5 Metallurgical and Mechanical Analysis

Metallurgical analysis is the study of a materials microstructure and is crucial for understanding its mechanical properties. Analytical techniques include Optical Light Microscopy (OLM) and Scanning Electron Microscopy (SEM). To carry out these techniques effectively samples must be prepared correctly. This includes using grinding and polishing wheels to get a deformation free surface for examination. For OLM and SEM, chemical etching can be used to highlight the sample features at microscopic level (Vander Voort, 2004). This technique involves applying an etchant (chemical) to the sample surface which selectively corrodes some of the phases present. This occurs due to compositional variation, meaning that corrosion rates vary when exposed to the etchant (Vander Voort, 2004). Etching enables microstructures to be examined in more detail, providing an insight into material properties. Etchants can expose the shape and size of grains, metallic phases, and indicate material uniformity.

Mechanical analysis and testing should be performed in adherence to any relevant technical industry standards. These standards contain mandatory requirements and establish uniform technical criteria, methods, and processes. Minimum values for mechanical properties are also found within these standards.

Mechanical properties refers to a materials measurable reaction to an applied force, for example tensile strength or hardness. Tensile testing provides information regarding the strength and ductility of a material under uniaxial tensile stresses (Kuhn & Medlin, 2000). Hardness is a materials ability to resist deformation, determined through measuring surface resistance to indentation (ASM International, 1999). A positive correlation has been noted between the hardness and tensile properties of metals – greater hardness relates to greater yield strength and UTS (Pavlina & Tyne, 2008; ASTM International, 2020).

2.5.1 Fractography

Fractography can be performed following tensile testing. This is the study of the fracture surface to determine the type of fracture and point that failure initiated. It includes investigation into the mechanism of crack initiation and propagation and linking this to the microstructure.

Failure can occur via brittle or ductile fracture failure mechanism, each of which is identifiable by characteristics visible on the fracture surface (Gilbertson & Zipp, 1981). Fracture surfaces can display a mixed-mode failure mechanism (brittle-to-ductile or ductile-to-brittle), exhibiting features from both fracture modes. Fracture can initiate at an internal defect – such as an inclusion or void – or exterior surface, and can be metallurgical or geometric (Becker, 2002).

Examples of a ductile and brittle fracture surface are shown in Figure 21.

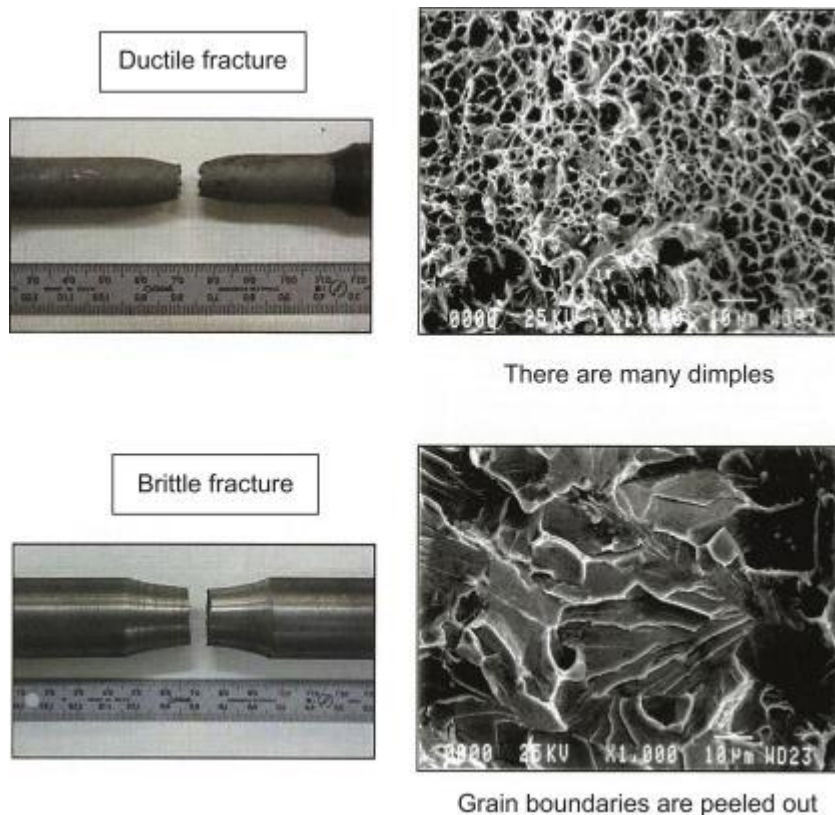


Figure 21: Tensile specimens which have fractured through ductile and brittle fracture mechanisms (Enomoto, 2017).

Brittle fracture occurs by two methods: cleavage fracture, which occurs across crystallographic planes resulting in distinct ledges, or intergranular fracture, a low energy failure that occurs along grain boundaries. Brittle fracture surfaces form perpendicular to the applied load, with no prior deformation evident (Becker, 2002).

Ductile fracture is characterised by significant plastic deformation prior to fracture, shear lips on the fracture surface. Ductile fractures typically exhibit a “cup and cone” appearance (Vander Voort, 1987).

Figure 22 shows a schematic of brittle and ductile fracture failure mechanisms. This highlights the lack of deformation in brittle fracture compared to ductile, and that brittle fracture occurs perpendicular to the force. Whilst in ductile fracture the force applied to the tensile specimen causes plastic deformation and elongation, resulting in necking (Becker, 2002; Vander Voort, 1987).

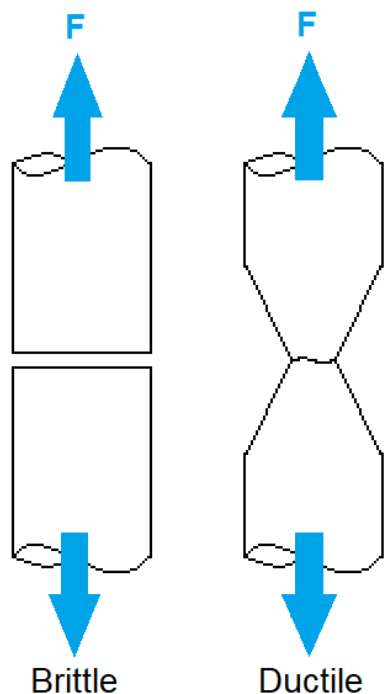


Figure 22: Schematic of brittle and ductile fracture failure mechanisms. Brittle fracture occurs perpendicular to the applied load, no deformation is present. Ductile fracture shows evidence of deformation.

Tiny voids – microvoids – form, these grow and coalesce into larger voids – known as microvoid coalescence (Gilbertson & Zipp, 1981). This is the dominant mechanism in ductile fracture. As the voids separate at the fracture surface a dimpled texture is created. When separation occurs perpendicular to the fracture plane it results in round dimples, called equiaxed microvoids (Kerlins & Phillips, 1987). Figure 23 shows a fracture surface containing equiaxed dimples.

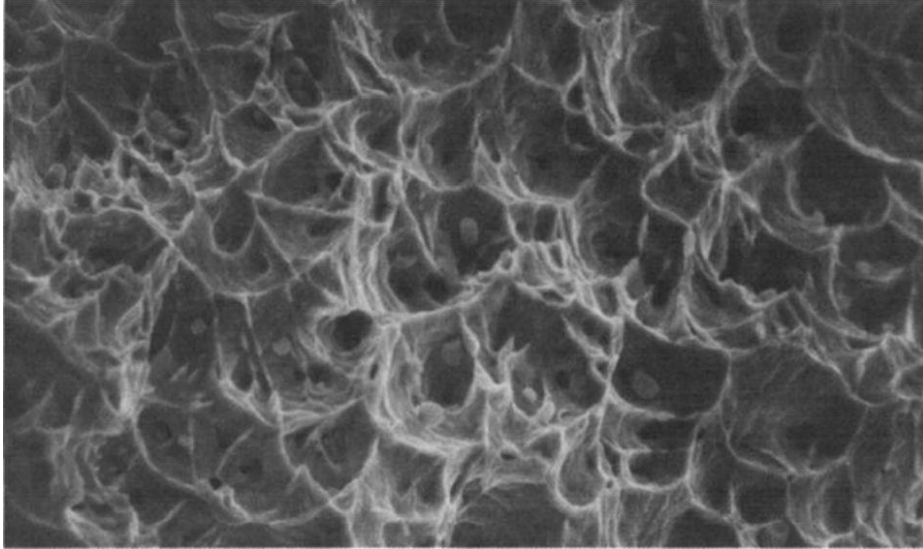
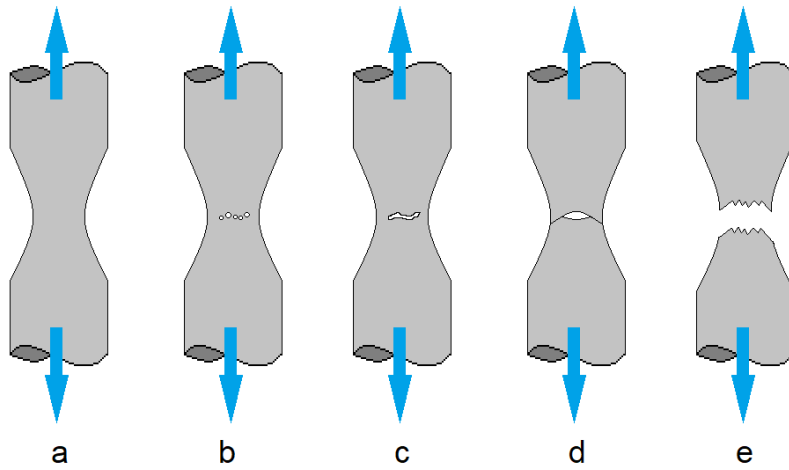


Figure 23: The fracture surface of a copper tensile specimen containing equiaxed dimples. (Gabriel, 1987).

If microvoid coalescence occurs adjacent to a grain boundary, or if voids form within grain boundaries this is known as dimpled intergranular fracture. Figure 24 shows the mechanisms involved in ductile fracture.



- a) Necking
- b) Formation of microvoids
- c) Coalescence of microvoids to form a crack
- d) Crack propagation by shear deformation
- e) Fracture (Cup-and-cone fracture)

Figure 24: Mechanisms involved in ductile fracture.

Figure 25 shows a mixed-mode fracture surface. Cleavage facet and dimples are visible.

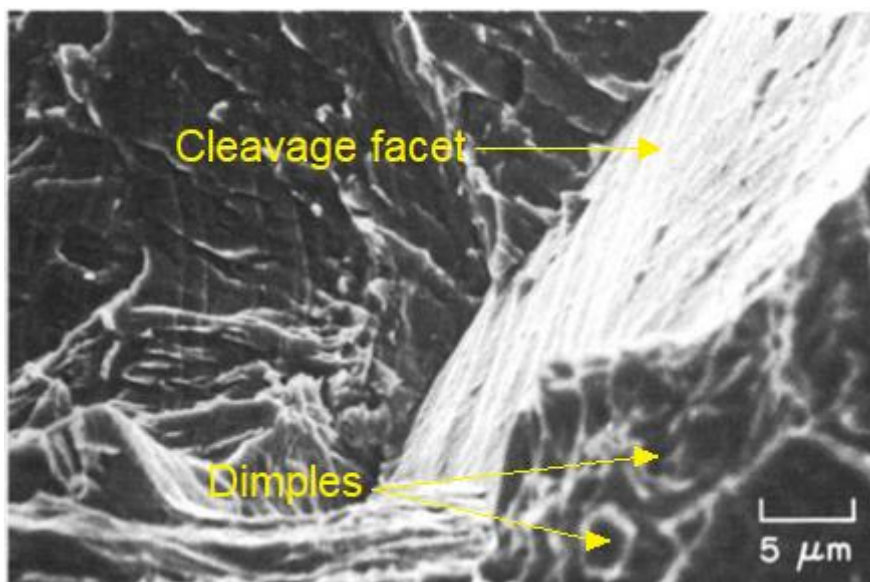


Figure 25: Fracture surface of a Nickel 201 specimen. Ledge-like features (cleavage facets) and dimples are indicated. (ASM International, 1987).

Microstructural features associated with dendritic solidification such as columnar grains and interdendritic phases also influence fracture appearance (Becker, 2002). Preferential phase precipitation at grain boundaries can cause weakening or embrittlement. Weakened grain boundaries are at risk of decohesion, resulting in intergranular fracture, which exhibits a rocky appearance (Lampman, 2002). Segregation of elements or inclusions within the microstructure also affect fracture.

2.6 Nickel

Nickel (Ni) is a ferromagnetic material which displays no allotropic transformation and undergoes no phase changes during cooling to room temperature. It can form solid solutions with numerous metals – a solid solution is formed by mixing a solvent (a perfect crystalline element, in this case Ni) with a solute (a foreign element/impurity). Nickel is often combined with other elements to produce alloys.

2.6.1 Nickel alloys

Ni-alloys are widely used in the aero-industry as they retain their mechanical properties in elevated temperatures for prolonged time periods and display high corrosion resistance in liquid and gaseous environments (Goodfellow, et al., 2018).

Ni-alloys can be solid solution strengthened or precipitation hardened (Reed, 2006). Solid solution strengthening relies on the difference in size between the Ni-alloy matrix and alloying/solute elements. This distorts the atomic structure impeding the movement of atoms and dislocation motion through the material – increasing strength. Precipitation hardening occurs when an alloying element exceeds its solubility within the alloy matrix, hence precipitates form. These precipitates block or slow down dislocation movement, improving strength.

Composition is carefully controlled, with each elemental addition serving a specific purpose, for example to improve different material properties (Donachie & Donachie, 2002). Elements are also added to aid precipitation hardening or solid solution strengthening phases forming. Table 5 describes the function of commonly added elements in Ni-alloys:

| Element | Principle function(s) |
|------------------------|---|
| Nickel (Ni) | Forms matrix; precipitation hardening phases |
| Aluminium (Al) | Precipitation hardener; promotes oxidation resistance |
| Chromium (Cr) | Solid solution strengthener; promotes corrosion and oxidation resistance |
| Iron (Fe) | Solid solution strengthener; affects formation of precipitation hardeners |
| Molybdenum (Mo) | Solid solution strengthener; affects formation of precipitation hardeners |
| Niobium (Nb) | Precipitation hardener; forms secondary phases |
| Titanium (Ti) | Precipitation hardener |

Table 5: The role of some alloying elements within Nickel (Donachie & Donachie, 2002; Reed, 2006).

2.7 Inconel 718

Inconel 718 – a precipitation hardened alloy – is commonly used in DED-L due to its excellent weldability (Zhong, Kittel, Gasser, & Schleigenbau, 2019). It displays high tensile, yield, and creep-rupture properties at elevated temperatures (~700°C) (High Temp Metals, 2015), thus common applications include jet engines and gas turbine operations (AZO Materials, 2008).

Composition according to ASTM B637-18 and the tensile properties pre^(a) and post^(b) heat-treatment (SAE International, 2016) are shown (Table 6). Vickers Hardness following solution annealing^(c), and both solution annealing and ageing^(d) (SAE International, 2016) are also displayed.

| | | |
|--|--------------------------------|-------------------------------------|
| Chemical composition limits (%) | Ni | 50-55 |
| | Cr | 7-21 |
| | Mo | 2.8-3.3 |
| | Fe | Remainder |
| | Al | 0.2-0.8 |
| | Ti | 0.6-1.15 |
| Mechanical properties | 0.2% proof stress (MPa) | 725 ^a 1034 ^b |
| | UTS (MPa) | 1035 ^a 1275 ^b |
| | Elongation (%) | 30 ^a 12 ^b |
| | Vickers Hardness | 246 ^c 385 ^d |

Table 6: Chemical composition for Inconel 718 (ASTM International, 2018; SAE International, 2016), the tensile properties pre (a) and post (b) heat-treatment (SAE International, 2016), and Vickers Hardness following solution annealing (c), and solution annealing and ageing (d) (SAE International, 2016).

Several studies have been carried out researching the material properties of DED-L Inconel 718. These largely focus on single track and thin wall deposits. Limited studies investigate larger, thick wall builds. Due to the low thermal conductivity of Inconel 718, heat dissipation during building larger thick walls will be compromised as compared to building thinner structures, increasing heat accumulation (Careri, et al., 2021).

2.7.1 Inconel 718 phases

Current data regarding Inconel 718 phase formation largely relates to cast materials. Although some comparisons can be made between cast Inconel 718 and DED-L Inconel 718, the non-equilibrium thermal cycling which occurs during DED-L means that a true comparison is difficult (Radhakrishna & Prasad Rao, 1997).

The microstructure of Inconel 718 can contain several phases. This includes the matrix γ -phase, and secondary phases; γ' , γ'' , δ , MC carbides (where M is a metal), and Laves (Carlson & Radavich, 1989). Table 7 summarises the crystal structures and chemical formulas of these phases.

| Phase | Crystal Structure | Chemical Formula |
|--------------|--------------------------|--|
| γ | Face-centered cubic | Ni |
| γ' | Body-centered tetragonal | $\text{Ni}_3(\text{Al/Ti})$ |
| γ'' | Face-centered cubic | Ni_3Nb |
| δ | Orthorhombic | Ni_3Nb |
| MC | Cubic | $(\text{Nb/Ti})\text{C}$ |
| Laves | Hexagonal | $(\text{Ni/Fe/Cr})_2(\text{Nb/Mo/Ti})$ |

Table 7: Inconel 718 phases, their crystal structures and chemical formulas.

Phases form according to the temperature and time, this can be illustrated in a Time-Temperature-Transformation (TTT) diagram. TTT diagrams can be used to predict which phases may be present within a material according to its thermal history, and to determine suitable heat-treatments for the material (Dempster, Forgings, & Wallis, 2016). Figure 26 shows the TTT diagram for wrought Inconel 718.

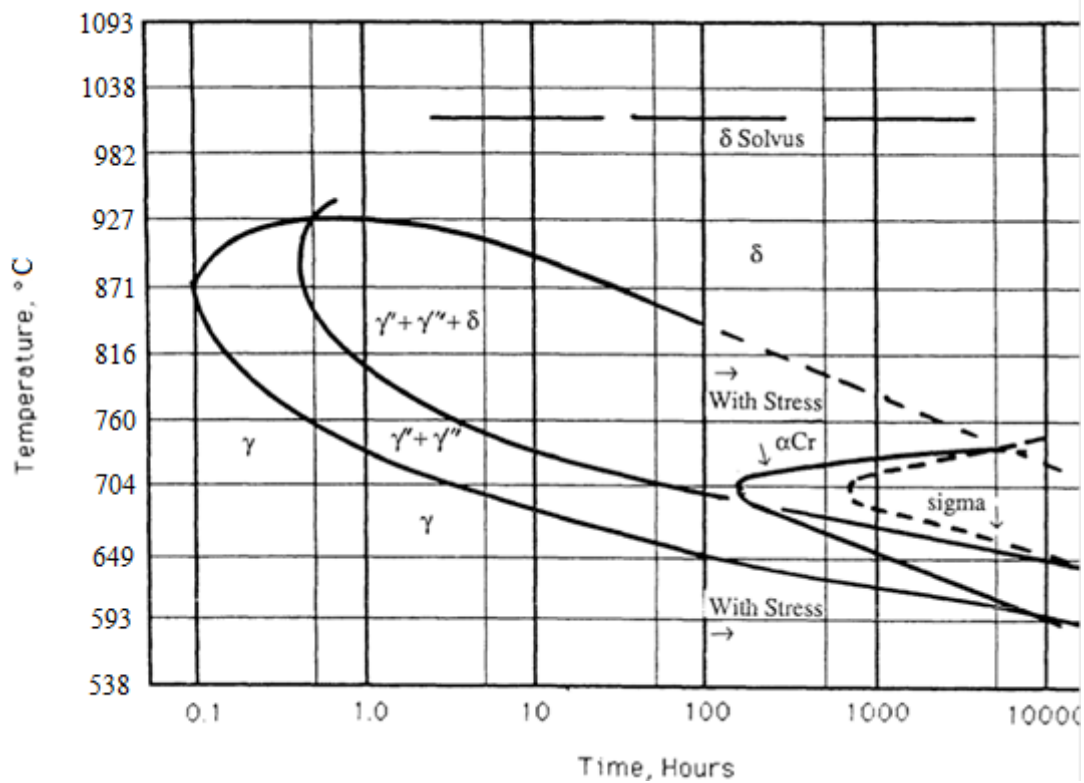


Figure 26: Transformation-time-temperature diagram for wrought Inconel 718 (Oradei-Basile & Radavich, 1991).

The solidification stages of Inconel 718 during cooling to room temperature can be simplified as follows (Table 8).

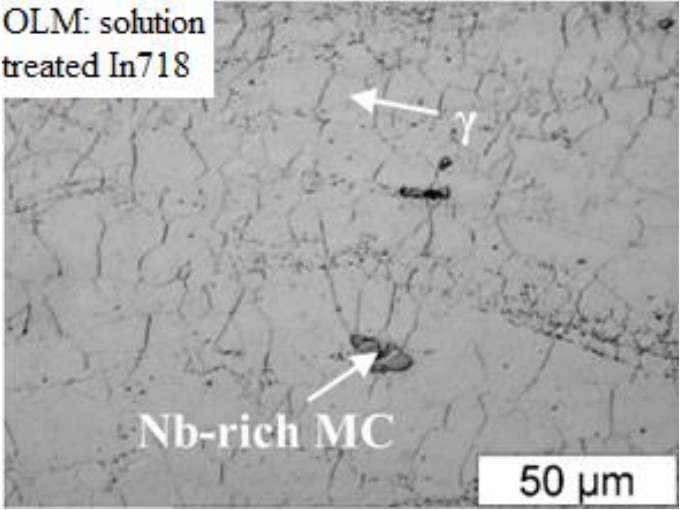
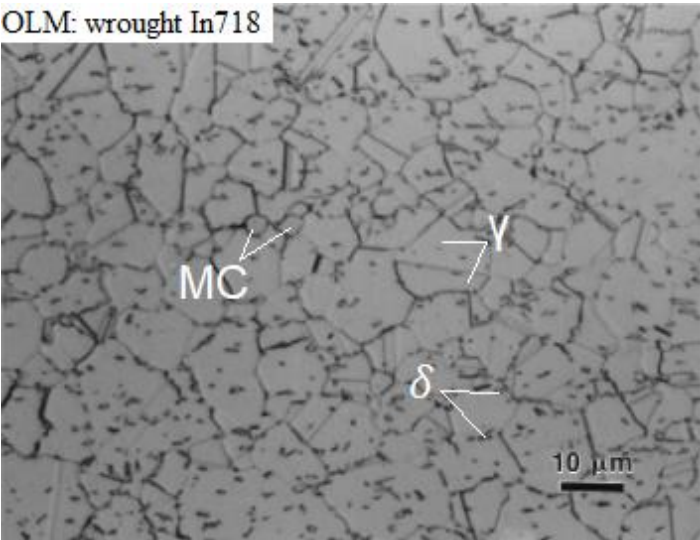
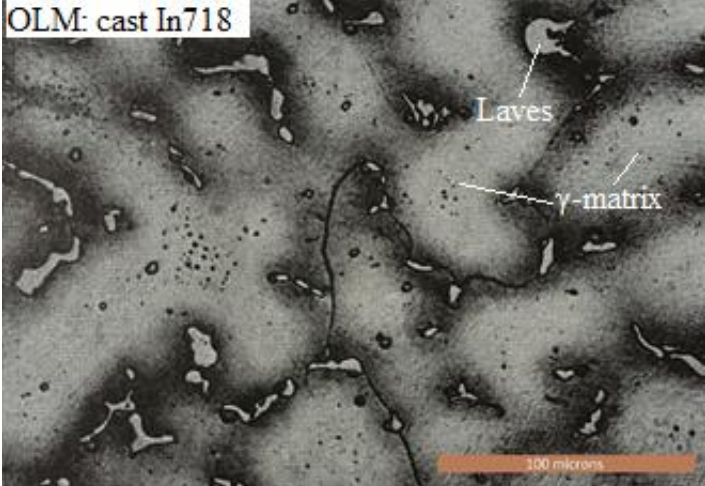
| Temperature of precipitation (°C) | Phase change |
|-----------------------------------|-----------------------------------|
| ~1340 | L→ γ |
| ~1270 | L→ γ +MC |
| ~1160 | L→ γ +Laves |
| ~1145 | γ → δ |
| ~1000 | γ → γ' + γ'' |

Table 8: Inconel 718 solidification stages, showing precipitation temperature and phase change. L is the material in molten liquid state. Adapted from DuPont, Notis, Marder, Robino, and Michael (1998) and Knorovsky, Cieslak, Headley, Romig, and Hammett (1989).

A eutectic reaction is a 3-phase reaction whereby a liquid transforms to two solid phases concurrently (Smallman & Ngan, 2014). This occurs at specific compositions and temperatures. Two eutectic reactions occur during the non-equilibrium solidification of Inconel 718. These depend on solidification conditions and degree of elemental segregation (Shi, Duan, Yang, Gua, & Gua, 2018).

According to solidification theory (DuPont, Notis, Marder, Robino, & Michael, 1998; Knorovsky, Cieslak, Headley, Romig, & Hammett, 1989), primary γ -dendrites form first, whilst Nb and C begin to segregate due to their low maximum solubility in the molten liquid (Ding, et al., 2015; Shi, Duan, Yang, Gua, & Gua, 2018). As solidification progresses, Nb and C segregate further until reaching their maximum solubilities within the γ -matrix. This gives rise to γ and MC (largely NbC) formation through a eutectic reaction, consuming most available C. The remaining liquid continues to solidify, forming γ -dendrites. A secondary eutectic reaction then occurs, forming γ and Laves (Kim, Cong, Zhang, & Liu, 2017). This Laves phase forms in interdendritic regions due to element segregation. At $\sim 1145^{\circ}\text{C}$ δ -phase precipitation occurs, and at $\sim 1000^{\circ}\text{C}$ γ' -phase and γ'' -phase precipitation.

Inconel 718 phases can be observed and identified using OLM and SEM. Table 9 shows images of Inconel 718 phases from the literature.

| | |
|--|--|
| <p>(Zhang, Cao, Wanjara, & Medraj, 2013)</p> | <p>OLM: solution treated In718</p>  <p>γ</p> <p>Nb-rich MC</p> <p>50 μm</p> |
| <p>(Vander Voort, 2004)</p> | <p>OLM: wrought In718</p>  <p>MC</p> <p>γ</p> <p>δ</p> <p>10 μm</p> |
| <p>(ASM Committee on Metallography, 1972)</p> | <p>OLM: cast In718</p>  <p>Laves</p> <p>γ-matrix</p> <p>100 microns</p> |

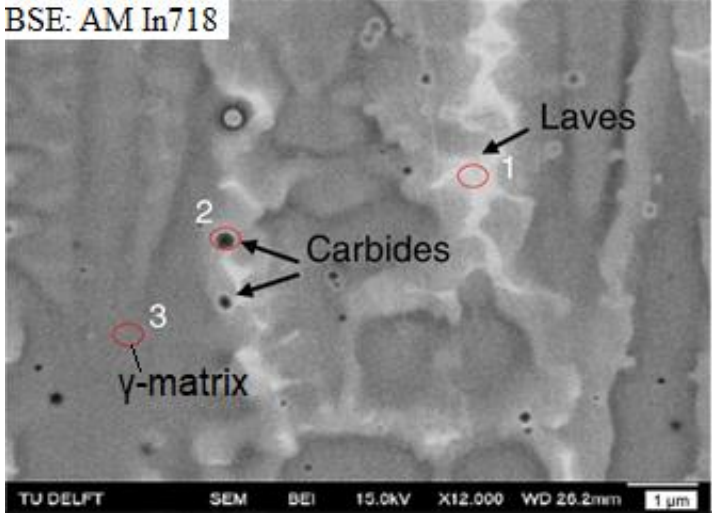
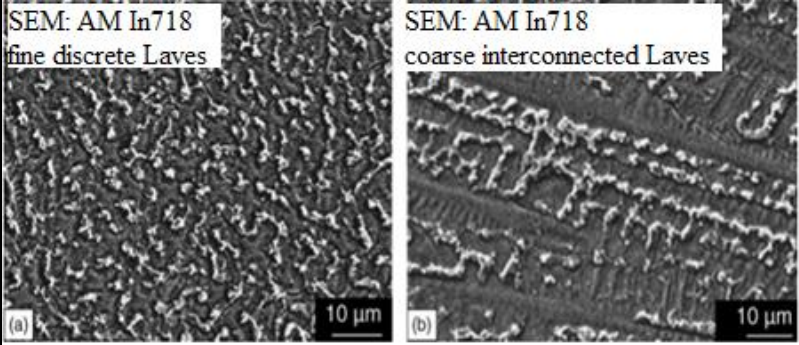
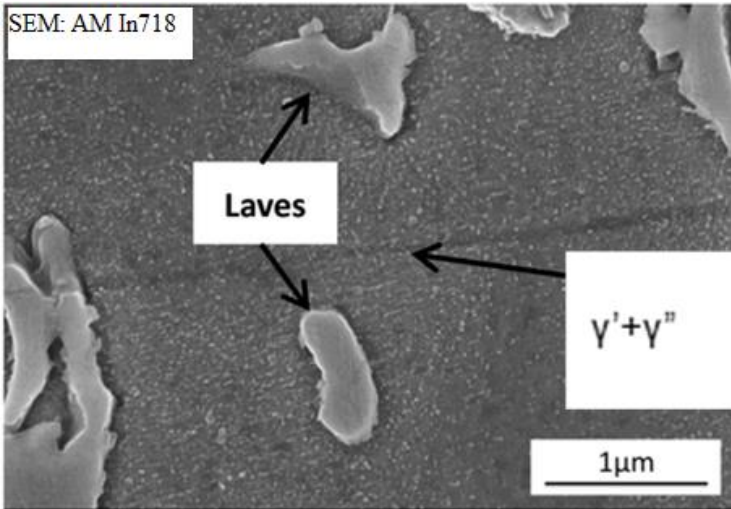
| | |
|---|--|
| <p>(Popvich, et al., 2017)</p> |  |
| <p>(Ram, Reddy, Rao, Reddy, & Sundar, 2005)</p> |  |
| <p>(Sui, et al., 2017)</p> |  |

Table 9: Images from the literature containing examples of phases present within Inconel 718.

2.7.2 γ -phase

γ -phase primarily consists of Ni and forms the alloy matrix. Ni has an FCC structure, and by substituting the Ni atoms with other solute elements, such as Cr, Fe, and Mo, this phase can be strengthened – solid solution strengthening (Goodfellow, et al., 2018).

2.7.3 γ' -phase and γ'' -phase

γ' -phase and γ'' -phase are the main strengthening phases within Ni-alloys, with γ' precipitating quicker. These strengthen the material through precipitation hardening – with their ability to impede dislocation motion partially dictated by phase precipitate size and volume. Greater volume fractions of these improve strength (Zhang, Cao, Wanjara, & Medraj, 2013). Precipitation of these phases is primarily determined by Nb content and temperature exposure.

In Inconel 718, Al, Ti and Nb are rejected by the solidifying dendrites into the surrounding liquid (Porter & Easterling, 1991), causing compositional variation. The rejection of elements results in interdendritic regions and grain boundaries containing greater volumes of the rejected elements, this can contribute to γ' precipitation within the interdendritic regions. This is followed by the formation of γ'' , the primary strengthening phase of Inconel 718.

γ' is largely responsible for the elevated temperature strength and creep resistance within Ni-alloys (Carlson & Radavich, 1989). As alloying elements continue to partition to γ' during solidification, γ' precipitates grow larger, increasing their hardening effect.

γ'' is unstable when exposed to temperatures exceeding 650°C for prolonged periods of time, decomposing to γ' (from 650°C to 850°C) and δ -phase (from 750°C to 1000°C).

2.7.4 δ -phase

δ -phase has the same composition as γ'' , precipitating mainly at grain boundaries (Azadian, Wei, & Warren, 2004; Sundararaman, Mukhopadhyay, & Banerjee, 1988). δ precipitation occurs heterogeneously in the temperature range of 750°C to 1000°C (Azadian, Wei, & Warren, 2004; Sundararaman, Mukhopadhyay, & Banerjee, 1988).

Although more thermodynamically stable than γ'' , δ precipitation is slow, following γ'' precipitation below 900°C (Azadian, Wei, & Warren, 2004). δ is detrimental to strength and toughness at large volume fractions and when it forms continuously at grain boundaries (Gleeson, 2008). Its presence suggests reduced hardenability as its formation depletes γ'' volume (Azadian, Wei, & Warren, 2004).

2.7.5 Carbides

Carbides typically precipitate at grain boundaries, causing pinning. Pinning prevents dislocation movement, increasing the force required for a dislocation to move, thus strengthening the material. Pinning also reduces grain coarsening and boundary migration at elevated temperatures (Song K. , 2008). Carbides can form continuous films at grain boundaries reducing alloy ductility and acting as crack propagation pathways (Sims, Stoloff, & Hagel, 1987; Singh Handa, 2013).

Carbide formation is heterogenous (Donachie & Donachie, 2002), with carbide type dependent on alloy composition and thermal history (Sims, Stoloff, & Hagel, 1987; Singh Handa, 2013). Table 10 shows common carbides found in Ni-alloys.

| Carbide | Description |
|--------------------------------|--|
| MC | High temperature carbide, forms first from molten state. Coarse random globular/blocky/script structure. Decomposes at elevated temperatures. (Donachie & Donachie, 2002) |
| M ₆ C | Intermediate temperature carbide. Complex cubic structure. Forms when Mo & W content exceeds 6-8at%. |
| M ₂₃ C ₆ | Forms during low temperature heat-treatment, especially when alloy Cr content is moderate to high. May form during MC decomposition or by reacting with matrix residual carbons. |

Table 10: Common carbides present in Ni-alloys (M represents a metal atom).

Carbon is almost insoluble in Inconel 718 γ -phase, segregating during solidification to react with active metal elements (e.g. Ti/Nb), forming MC carbides (Chen, Lee, Jo, Choe, & Lee, 1998; Mitchell, 2010). In Inconel 718 most carbon is bound within this type of carbide, largely NbC (Sundararaman, Mukhopadhyay, & Banerjee, 1997). NbC formation is aided by Nb segregation during solidification. Small proportions of Ti are often found in carbide peripheral regions (Mitchell, 2010). NbC formation at grain boundaries in Inconel 718 has been associated with γ' and γ'' free areas near these boundaries (Sundararaman, Mukhopadhyay, & Banerjee, 1997).

MC carbides are stable when held for short periods above 1100°C, remaining unaltered in morphology. However, following long exposure times at elevated temperatures – such as during heat-treatment or service – they can decompose to form M₂₃C₆ and M₆C (Dempster, Forgings, & Wallis, 2016; Donachie & Donachie, 2002).

2.7.6 Laves phase

As Laves phase forms, Ni, Nb, Mo and Ti are consumed, depleting the matrix of these elements. This reduces the volume of γ' and γ'' that can form, reducing their precipitation effect (Carlson & Radavich, 1989; Darolia, Lahrman, Field, & Sisson, 1988).

Laves formation is affected by carbon content, Nb segregation, and time exposed to high temperatures (Schirra, Caless, & Hatala, 1991). The repetitive re-melting that occurs in DED-L provides multiple opportunities for Nb to segregate from the matrix. Antonsson and Fredriksson (2005) found that, in Inconel 718, Nb content within the interdendritic liquid must exceed 20 wt% for Laves to form. Greater Nb segregation results in greater volumes of Laves forming.

Laves forms within interdendritic regions due to alloying element segregation during solidification, appearing as globular aggregates under the SEM (Schirra, Caless, & Hatala, 1991). Finer solidified dendritic structures mean finer interdendritic regions, thus finer Laves particles, whilst columnar dendritic solidification produces strongly aligned interdendritic regions, resulting in extended chains of interconnecting Laves particles (Xiao, et al., 2016).

The size, network, and continuity of Laves affects mechanical properties (Manikandan, Sivakumar, Rao, & Kamaraj, 2015; Mazzucato, Forni, Valente, & Cadoni, 2021). Laves is considered detrimental to mechanical properties, with studies showing that a 'weak-zone' forms between the matrix and Laves. It also acts as a preferential site for crack initiation and propagation (Schirra, Caless, & Hatala, 1991; Darolia, Lahrman, Field, & Sisson, 1988). It is suggested that a Laves content exceeding 2-3wt% can reduce strength by 20% and plasticity by 60% (Popovich, et al., 2017).

Sui et al. (2017) however, show Laves can act as a hardening phase in Inconel 718 DED-L parts when its presence is controlled, finding as-built specimens to

display greater hardness as compared to wrought Inconel 718 at room temperature.

To mitigate elemental segregation, and subsequent formation of Laves, it is suggested that process conditions such as heat input, cooling rate and thermal gradients should be controlled (Radhakrishna & Prasad Rao, 1997). A higher cooling rate reduces Nb and Mo segregation during solidification (Shi, Duan, Yang, Gua, & Gua, 2018), preventing Laves from forming (Bambach, Sizova, Silze, & Schnick, 2018).

Table 11 contains Energy Dispersive X-ray (EDX) analysis of Laves phase performed in previous studies.

| Authors | Element wt% | | | | | | |
|-----------------------------------|-------------|------|------|------|------|-----|-----|
| | Ni | Fe | Cr | Nb | Mo | Ti | Al |
| (Ardila, et al., 2014) | 47.4 | 15.1 | 17.4 | 10.6 | 3.4 | 1.2 | 0.6 |
| (Schirra, Caless, & Hatala, 1991) | 32.5 | 13.9 | 12.7 | 27.3 | 12.5 | 0.7 | - |

Table 11: Examples of Laves composition obtained using EDX analysis.

2.7.7 Inconel 718 DED-L microstructure

The dominant microstructure obtained for DED-L Inconel 718 consists of columnar dendrites elongated in the direction towards the heat source – essentially consisting of γ -dendrites and interdendritic Laves (Jelvani, Razavi, Barekat, Dehnavi, & Erfanmanesh, 2019; Smith, et al., 2016; Zhao, Chen, Lin, & Huang, 2008; Zhang Q. , Zhang, Zhuang, Lu, & Yao, 2020; Mantri, et al., 2021).

Long et al. (2016) varied laser power and scan speed to maintain constant energy densities for depositing single tracks of Inconel 718. They reported an equiaxed dendritic microstructure at a laser power of 1000 W and scan speed of 2 mm/s, and a columnar dendritic microstructure at a laser power of 3000 W, scan speed 6 mm/s. This shows that energy density alone cannot be used to predict the microstructure formed by DED-L.

Petrat et al. (2019) observed higher laser power to result in grains extending across multiple layers, whilst a low power increased cooling rates and limited directional growth across multiple layers. Guévenoux et al. (2020) found that by incorporating a delay between depositing layers, grain growth across layers was reduced.

Jelvani et al. (2019) observed a columnar dendritic microstructure at laser powers 150 W and 200 W, and equiaxed dendritic at 250 W and 300 W. Alhuzaim, Imbrogno and Attallah (2021) found a lower heat input to produce columnar grains with less Nb segregation, whilst a higher heat input produced equiaxed grains and promoted Nb segregation. Pinkerton and Li (2004) found columnar grain size to vary according to laser power when depositing a single layer, increasing from 200 μm at 800 W to 500 μm at 1200 W. Zhang, Yao and Jyoti (2011) also observed grain size to increase with increased incident energy.

Yuan et al. (2018) and Liu et al. (2019) observed decreasing laser power to decrease primary dendrite spacing, resulting in a finer structure.

2.7.7.1 Inconel 718 DED-L phases

DED-L Inconel 718 has been identified to consist of a γ -matrix containing Laves and carbides (Yuan, et al., 2018; Zhang Q. , Zhang, Zhuang, Lu, & Yao, 2020). Laves forms irregularly, with morphology differing between laser powers (Zhu, Xu, & Gu, 2018).

Li et al. (2020) observed Laves within interdendritic regions, with γ' and γ'' distributed non-uniformly around Laves. This corresponds to observations by Stevens et al. (2017), who identified interdendritic Mo-rich and Nb-rich eutectic products surrounded by γ'' , whilst dendrite cores contained less Mo and Nb than nominal composition.

Stevens et al. (2017) observed a difference in the concentration of Laves between deposited track centres and edges, making individual layers and tracks clearly visible. Measurements of Laves and carbide proportions were 3.58% for the upper region of a deposited track and 1.46% for the edge. Li et al. (2020) also observed distinct layers, caused by the different microstructures found in the track edges (planar interface growth) compared to other areas (dendritic growth). Zhang et al. (2013) suggest that the thermal cycling caused by the successive deposition of layers has a heat-treating effect on some regions of the microstructure, possibly dissolving Laves within regions.

This uneven precipitation of phases is attributed to the variations in thermal cycling and solidification affecting elemental segregation, resulting in microstructural inconsistency throughout DED-L parts.

2.7.8 Inconel 718 DED-L mechanical properties

Zhong et al. (2016) found significant levels of porosity in as-deposited Inconel 718, resulting in poor mechanical properties. Anisotropy was observed, this was attributed to the orientation of the columnar grains which formed. HIP was used to reduce the porosity of the deposits, and a homogenisation heat-treatment used to transform the columnar grains to equiaxed, thereby removing anisotropy. They also found that Laves which had predominantly precipitated within interdendritic regions was dissolved via solution heat-treatment, improving mechanical properties.

Yuan et al. (2018) also observed anisotropy within samples. The columnar grains which formed in the direction parallel to the laser resulted in a lower

strength in this direction, and greater strength in the scan path direction – perpendicular to grain growth. Fracture surfaces were a mixed-mode of ductile and brittle fracture failure mechanisms.

Zhang et al. (2020) attribute the lower tensile strength in as-deposited Inconel 718 to the Laves formed, as it consumes strengthening elements. They observed fractures to primarily extend along the interfaces between the γ -matrix and Laves. Witzel et al. (2011) also attribute lower tensile strength to Laves formation. They show that higher laser powers increase dendrite arm spacing and the Nb concentration within Laves. Liu et al. (2020) suggest that Laves promotes micropores forming. These facilitate crack initiation and growth, lowering tensile strength.

Microhardness variation throughout DED-L components has been noted in several materials, including Inconel 718. Microhardness has been observed to decrease moving from the first deposited layer upwards towards the middle region of the build, prior to increasing moving upwards towards the final deposited layer (Costa, Vilar, Reto, & Deus, 2005; Zheng, Zhou, Schoenung, & Lavernia, 2008; Tian, et al., 2014). This inhomogeneity between layers is attributed to cooling rate variability, and slower solidification of the middle region.

Zhang et al. (2013) found that Vickers Hardness of DED-L Inconel 718 could be increased by ~ 200 HV₁ (as-deposited, 291 HV₁; heat-treated, 490 HV₁) by solution treatment and ageing. They attribute the lower hardness of the as-deposited material to the the formation of Laves, and the thermal cycling that occurs during DED-L.

A study on the effect of specific energy density (Joules/g) on Inconel 718 microstructure varied laser power, powder feed rate, and scan speed to obtain identical specific energy densities for manufacturing samples (Petrat, Brunner-Schwer, Graf, & Rethmeier, 2019). They found similar hardness values between samples and within individual samples (260 HV₁ ± 10 HV₁). The sample built

using the greatest laser power decreased in hardness towards the upper layers, this was attributed to larger grains spreading across several layers in this region.

2.7.9 Inconel 718 heat-treatments

Heat-treatments are usually required for DED-L Inconel 718 to optimise properties due to its anisotropic behaviour and absence of strengthening phases (Xu, Ding, Ganguly, & Williams, 2019; Careri, et al., 2021). The heat-treatments homogenise the microstructure and dissolve detrimental phases, such as Laves and carbides, formed during fabrication (Ma, Wang, & Zeng, 2015; Parimi, Ravi, Clark, & Attallah, 2014; Zhong, Gasser, Kittel, Wissenbach, & Poprawe, 2016; Manikandan, Sivakumar, & Kamaraj, 2019; Radhakrishna & Prasad Rao, 1997). Many Inconel 718 heat-treatments consist of a solution treatment followed by ageing. Table 12 contains examples of heat-treatments.

| | |
|---|--|
| <p>AMS 5663 (SAE International, 2016)</p> | <p>1) Solution anneal; 980°C/1hr, air/argon cool. 2) Ageing treatment; hold at 720°C/8hr, furnace cool to 620°C/2hr, hold at 620°C/8hr, air/argon cool.</p> |
| <p>AMS 5664 (SAE International, 2017)</p> | <p>1) Solution anneal; 1065°C/1hr, air/argon cool. 2) Ageing treatment; hold at 760°C/10hr, furnace cool to 650°C/2hr, hold at 650°C/8hr, air/argon cool.</p> |
| <p>AMS 5383 (SAE International, 2018)</p> | <p>1) Homogenisation treatment; 1100°C/1hr, air cool. 2) Solution treatment ; 980°C/1hr, air cool. 3) Double ageing treatment; 720°C/8hr, furnace cool, 620°C/8hr, air cool.</p> |

Table 12: Inconel 718 heat-treatments.

NbC is often observed in as-deposited Inconel 718, this has a dissolution temperature of 1176°C, therefore temperatures exceeding this are required to dissolve this carbide (Knorovsky, Cieslak, Headley, Romig, & Hammetter, 1989). As Laves is often present within cast and wrought Inconel 718 (Radavich, 2004), most Inconel 718 heat-treatments are designed to dissolve Laves (observed to dissolve from ~980°C in laser AM Inconel 718 (Cao, Bai, Liu, Hou, & Guo, 2020; Fayed, et al., 2021)). This releases Nb back into the γ -matrix making it available for γ'' precipitation during ageing. Yuan et al. (2018) observed Inconel 718 anisotropy to be significantly reduced following heat-treatment.

Liu et al. (2020) found Laves dissolution to vary between heat-treatments. Solution treating at 1020°C (for 0.5h, 1h, 2h, or 4h) dissolved the Nb within the thinner regions of Laves first, resulting in necking, and the breakdown of Laves into large granules. Ageing at 890°C/9h resulted in δ forming which cut across the Laves, this was followed by solution treating at 1020°C (for 0.5h, 1h, 2h, or 4h) during which Nb dissolved and Laves was broken into small granules. Both heat-treatments were followed with an ageing treatment: 720°C/8h- furnace cooled to 620°C, then 620°C/8h- air cooled. Ageing followed by solution treating reduced Laves volume significantly more than solution treating.

Examination of the effects of solution treatment, solution treatment and ageing, and direct ageing on DED-L Inconel 718 was performed by Sreekanth et al. (2021) as follows; solution treatment: 954°C/1hr- air cooled; ageing: 718°C/8hr- furnace cooled at 56°C/hr to 621°C, then 621°C/8hr- air cooled.

Figure 27 contains SEM images of the as-deposited material, and heat-treated samples. Laves volume decreases following heat-treatment, whilst δ forms in the solution treated samples.

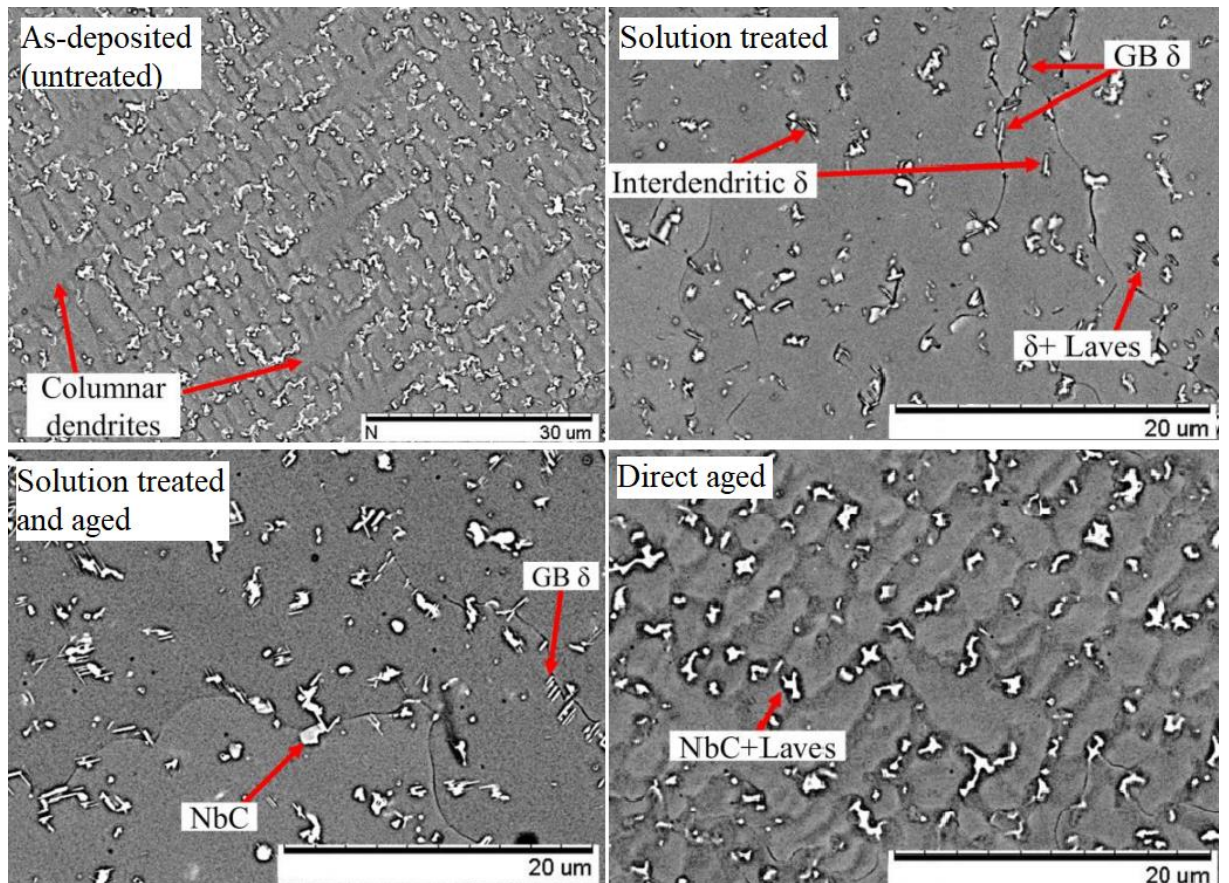


Figure 27: SEM images of as-deposited Inconel 718, solution treated, solution treated and aged, and direct aged (Sreekanth, Hurtig, Joshi, & Andersson, 2021). GB = grain boundary.

2.8 Design of Experiments

Design of Experiments (DOE) is a statistical technique which uses a minimum number of experiments to obtain the maximum amount of information (Park, 2007).

A “black box” process model concept can be used to describe DOE theory (Figure 28). The model has several controlled inputs (factors), continuous and discrete uncontrollable inputs (factors), and one or more measurable outputs (responses) (Montgomery, 1984; Park, 2007).

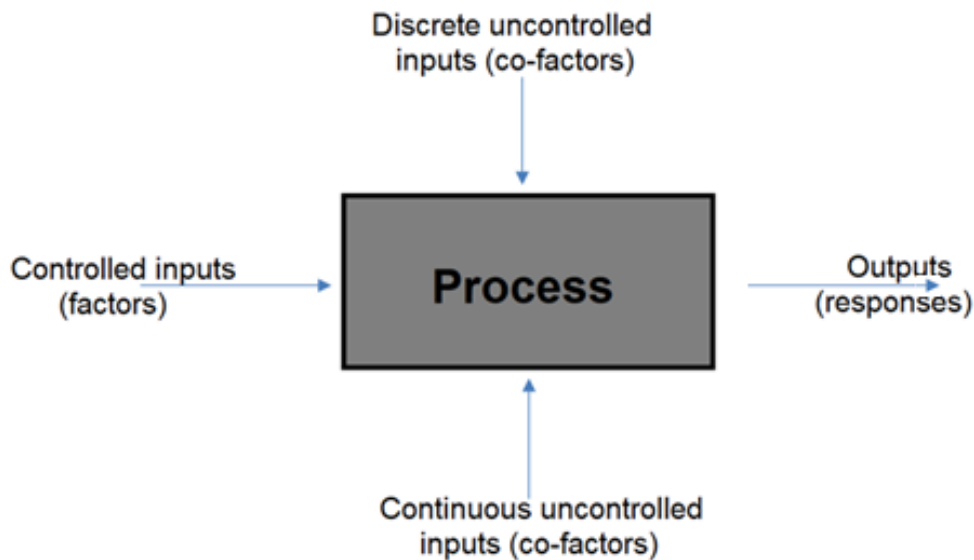


Figure 28: Schematic of a "black box" process model which can be used to describe DOE theory.

From the experimental data an approximate empirical model linking the inputs and outputs can be determined. This aids in understanding and predicting relationships between the inputs and outputs, and can reveal any trends present. This can assist in optimising the process under investigation.

The following considerations should be made prior to using a DOE methodology (Montgomery, 1984; Park, 2007; Anderson & Whitcomb, 2000):

- 1) Capability of measurement systems for responses – the methods and tools used to measure the generated responses must be able to measure the changes and differentiate between results accurately.
- 2) Process stability – control runs should be made at the “standard” process condition at the start and end of the experiment. Plots of the control run outcomes will indicate any intrinsic scatter of the process.
- 3) Response approximation by simple polynomial models – the outputs over the experimental range must be continuous and smooth. This is due to the approximating polynomials which fit to the data assuming a smooth curving response surface, hence a sudden drop in response value would be missed.

- 4) Residual behaviour – “residuals” are the deviation of the observed results from the predicted responses, thus are estimates of experimental error. These can be regarded variations unexplained by the fitted model. Residuals are a type of error; thus it can be assumed that they would be close to normal and freely distributed with a mean of 0 and some constant variance.

Taguchi DOE is a fractional factorial DOE often used in analysing manufacturing processes, and has been used to examine laser AM process parameters (Izabi, Farzaneh, Gibson, & Rolfe, 2017; Lee, 2008; Paul, et al., 2007; Sun & Hao, 2021). These designs approximate the effect of factors on the response mean and variation. Factor levels are weighted equally allowing each factor to be individually evaluated (Anderson & Whitcomb, 2000). The number of runs for a Taguchi DOE is significantly less compared to a full factorial design. For example, if 3 factors are used at 3 levels a full factorial design would use $3^3 = 27$ runs, whereas a Taguchi DOE reduces this to 9 runs.

The results obtained by a Taguchi DOE are typically analysed using a method such as Analysis of Variance (ANOVA). Through ANOVA, an understanding of how significant variables, or parameters, affect the process can be obtained. The variable/parameter which is most influential to the process can be determined, in addition to the influence of interactions between variables/parameters (Anderson & Whitcomb, 2000).

2.9 Summary

DED-L is an AM process that utilises a laser beam and material in powder form to create components. Complex relationships exist between DED-L process parameters, affecting the material properties of the deposit/build. These relationships, and their effect on material properties, are not yet fully understood. To move forward in using DED-L within industry to produce components a deeper understanding of the process parameters, the relationships between them, and their effect on material properties is essential.

Few studies have been carried out to understand the combined effect of process parameters. Those that have suggest that the relationships between laser power, scan speed, and powder feed rate should be further investigated.

As laser power is the source of energy it could be assumed that this parameter has the greatest impact on the microstructure. However, interactions with powder feed rate and scan speed mean that the total heat provided by the laser does not reach the substrate/previously deposited material.

Powder feed rate plays a key role in influencing how much heat from the laser reaches the substrate/ previously deposited material as higher powder feed rates mean more of the heat is absorbed by the powder, whilst lower powder feed rates allow more of the heat from the laser to penetrate the melt-pool.

Scan speed affects the time for the laser to interact with the material. A faster scan speed reduces the interaction time between the laser and the material, whilst a slower scan speed increases interaction time.

Use of Inconel 718 for DED-L has been broadly researched due to its widespread use within industries – particularly aerospace. Its excellent material properties and weldability mean that recognising how this material behaves following DED-L fabrication, and how DED-L can be optimised accordingly, will benefit multiple industries.

Chapter 3 – Methodology

This chapter contains the methodology used for this research. First the different stages which form this work are defined. The materials and DED-L system used are then presented. This is followed by an outline of how the specimens were manufactured. Finally, the analytical techniques are presented.

3.1 Stages of work

The experimental work within this study has been split into 5 stages. Table 13 outlines each stage of work and its aim.

| Stage | Aim |
|--------------|--|
| 1 | Use a Taguchi Design Of Experiments to investigate three key DED-L process parameters for thick wall builds using a Trumpf DMD 505 system and a CO ₂ laser. |
| 2 | Examine anisotropy present within a single DED-L built part. |
| 3 | Investigate the effect of using different build directions to manufacture parts with identical geometries. |
| 4 | Investigate the effect of an interface when using multiple DED-L deposition directions to build one part. |
| 5 | Investigate the effect of a heat-treatment on the microstructure and Vickers hardness. |

Table 13: An outline of each aim for the five stages of work within this study.

3.2 Materials

3.2.1 Powder composition

Inconel 718 powder produced using advanced plasma atomisation (APA™) by AP&C (GE Additive) was used to manufacture samples. Powder composition was measured by the manufacturer (Table 14). This composition was determined using thermal conductivity detection according to standard ASTM E1019 (ASTM International, 2018) to measure carbon, oxygen and nitrogen proportions. Other element concentrations were determined through direct current plasma atomic emission spectrometry according to standard ASTM E1097 (ASTM International, 2017).

| | | | |
|---|---|-------|---------------------|
| Inconel 718 powder particle size | 25-45 µm (93.4% – measured by manufacturer) | | |
| Element | ASTM F3055 (%) | | Measured (%) |
| | min. | max. | |
| Carbon, max.^(a) | - | 0.8 | 0.05 |
| Manganese, max.^(b) | - | 0.35 | 0.02 |
| Silicon, max.^(b) | - | 0.35 | 0.05 |
| Phosphorus, max.^(b) | - | 0.015 | 0.005 |
| Sulphur, max.^(a) | - | 0.015 | <0.001 |

| | | | |
|--|---------------|---------------|-----------------|
| Chromium, range^(b) | 17 | 21 | 18.3 |
| Cobalt, max.^(b) | - | 1 | <0.1 |
| Molybdenum, range^(b) | 2.8 | 3.3 | 2.97 |
| Niobium & Tantalum, range^(b) | 4.75 | 5.50 | 5.08 |
| Titanium, range^(b) | 0.65 | 1.15 | 0.95 |
| Aluminium, range^(b) | 0.2 | 0.8 | 0.52 |
| Iron^(b) | Remainder | | 18.768 (+/-0.1) |
| Copper, max.^(b) | - | 0.3 | <0.1 |
| Nickel, range^(b) | 50 | 55 | 53.15 |
| Boron, max.^(b) | - | 0.006 | 0.005 |
| Oxygen^(a) | Not specified | Not specified | 0.016 |
| Nitrogen^(a) | Not specified | Not specified | 0.015 |

Table 14: The composition and size of the Inconel 718 powder used to manufacture samples within this work. This was determined according to ASTM E1019 (a) and ASTM E1097 (b). ASTM F3055 standard for AM using Inconel 718 is shown for comparison.

Figure 29 shows SEM images of the powder, demonstrating particle sphericity and size. Several particles can be seen to exceed 45 μm .

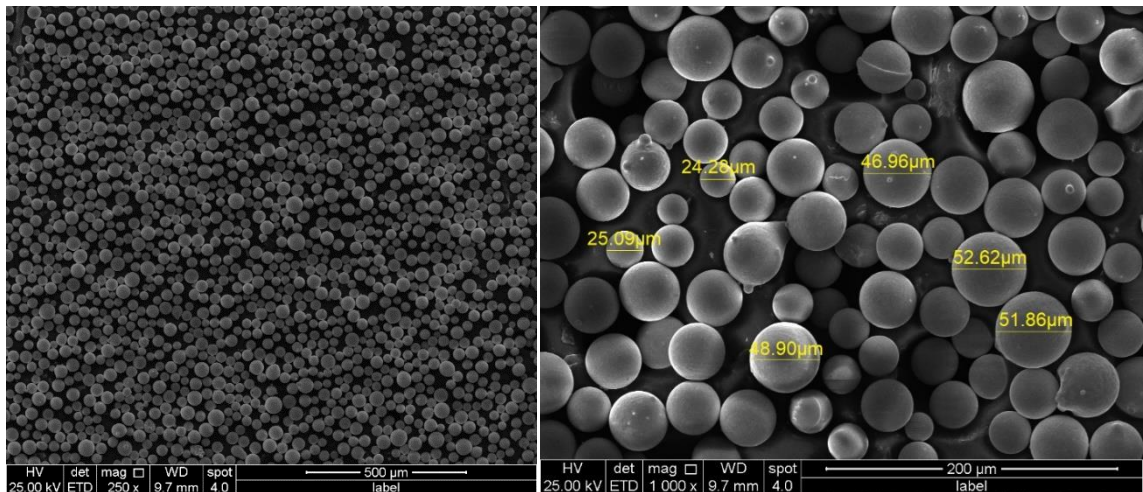


Figure 29: Secondary electron SEM images of the Inconel 718 powder used within this work. The size of some particles is shown.

3.2.2 Substrate composition

Stainless steel 304L with a milled surface was used as the substrate for depositing test specimens onto. This had the following composition, in line with ASTM A240 (ASTM International, 2019) (Table 15):

| Element maximum/range (wt%) | | | | | | | |
|-----------------------------|------|----|-------|------|-----------|------|-----|
| C | Si | Mn | P | S | Cr | Ni | N |
| 0.03 | 0.75 | 2 | 0.045 | 0.03 | 17.5-19.5 | 8-12 | 0.1 |

Table 15: The composition of Stainless steel 304L according to ASTM A240.

A different substrate material to the powder could be used, as during deposition of the first layer of material there is very little dilution from the substrate material into the deposited material. Where this dilution is present it does not extend further than the first two layers and therefore would not influence the results of this study.

The minimum dimensions of the substrates used were 300 mm × 300 mm × 25 mm to enable secure fixture during deposition (Figure 30).

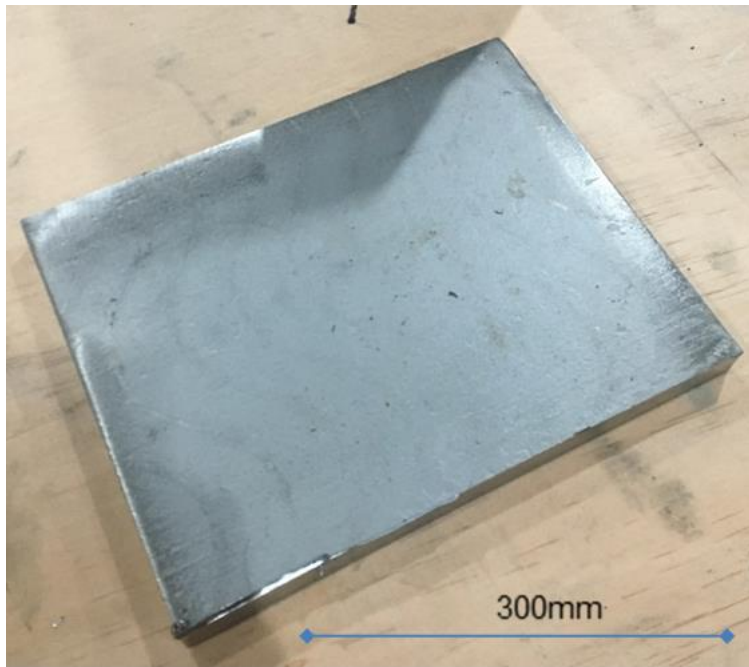


Figure 30: Example of the stainless steel 304L substrate used within this work.

3.3 DED-L system set-up

A Trumpf DMD 505 system (Figure 31) comprised of the following was used to manufacture specimens:

- A Trumpf 1.8 kW HQ CO₂ laser (10.6 μm wavelength, Gaussian energy distribution).
- A 5-axis single cantilever Cartesian gantry system with a processing envelope of 2.00 m (x) × 1.10 m (y) × 0.75 m (z).
- A Sinumerik 840D Siemens controller.
- A Sulzer-Metco twin-10C powder feeder with 1.5 litre capacity per hopper.
- A 50 mm coaxial powder feed nozzle.

- 100% Argon was used as the nozzle shielding gas and powder carrier gas.

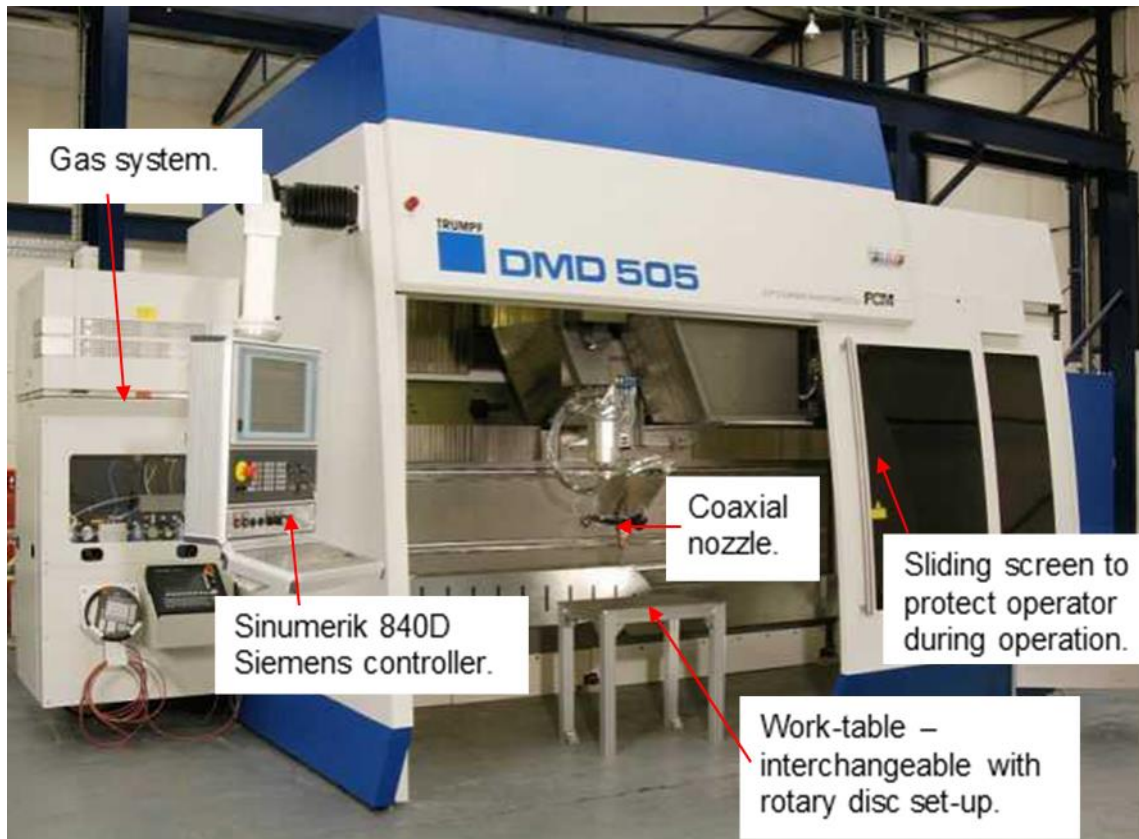


Figure 31: The Trumpf DMD 505 system used for this work. Key parts are labelled. Powder feeders are not shown.

3.3.1 Equipment calibration

3.3.1.1 Laser power calibration

There are several components between the laser source and workpiece, these create losses in the amount of energy which reaches the workpiece. As the beam in a CO₂ laser is produced by running electricity through a gas-filled tube, the quality and mixture of this gas is important in producing optimal energy output. This gas cannot be checked and changed daily therefore calibration of the laser power output is vital.

Issues can arise within the optics that cause more significant and unpredictable losses in laser energy. These can occur when contaminating dust and particles

enter the system and settle on the optical mirrors and lenses. Therefore these were kept as clean as possible.

To ensure the required laser power is reaching the workpiece a power meter can be used to measure laser power output at the workpiece. This measured value can then be compared to the input laser power that was requested.

An OPHIR thermal power sensor and OPHIR NOVA remote meter were used to carry out power calibration at the start of each day (Figure 32). When taking measurements the laser was emitted for 1 minute to allow the measurement to stabilise before recording the value.



Figure 32: The equipment used for laser power calibration – an OPHIR thermal power sensor (left) and OPHIR NOVA remote meter (right).

By plotting recorded power output against the requested power in a graph it can be predicted what power to request to get the desired power at the workpiece. This was done using requested powers from 400 W to 1800 W in 100 W increments (Figure 33). A linear relationship can be observed. This was expected and corresponds to a 15% loss in energy between the laser and output.

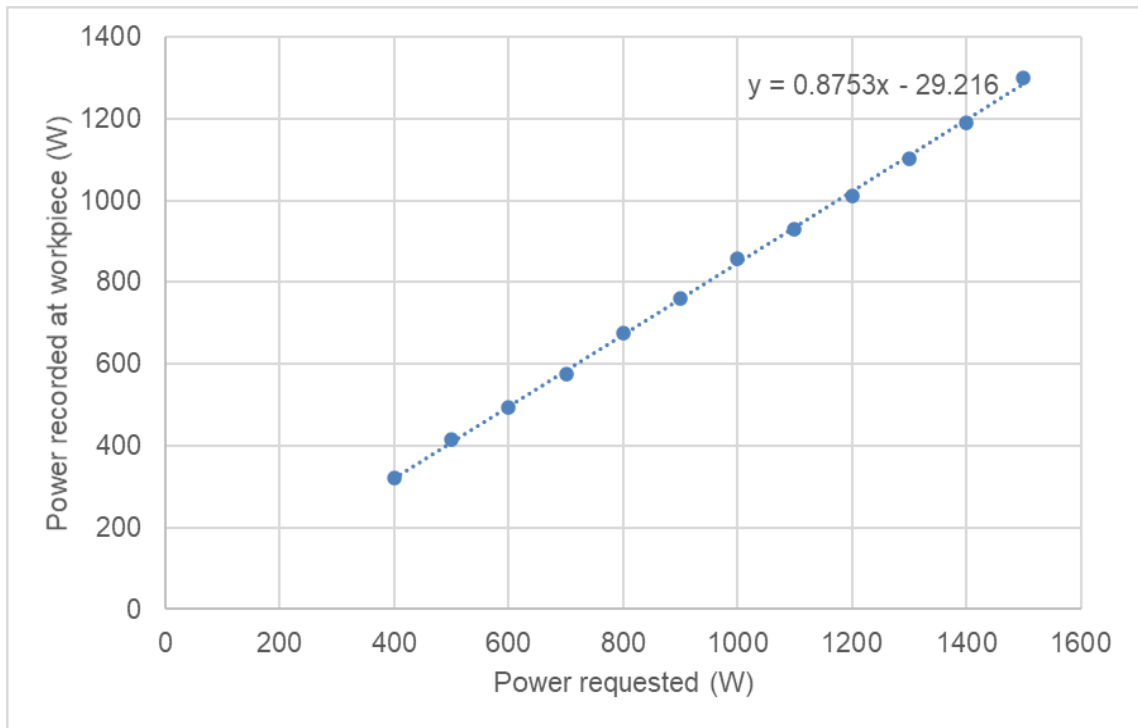


Figure 33: Power requested plotted against the power recorded at the workpiece for requested powers from 400 W to 1500 W. A linear relationship between the two variables was observed.

3.3.1.2 Nozzle set-up and calibration

The interaction between the powder and melt-pool is critical in DED-L. For optimum results, the correct set-up of the deposition nozzle is essential. The nozzle should be aligned laterally and vertically to the coaxial laser beam to obtain the correct relationship between laser spot size, melt-pool size, and powder feed focus size. Optimising these interactions can maximise powder capture efficiency, and support a stable, omnidirectional process.

3.3.1.3 Adjustment of focusing optics and powder stream

By altering the distance of the focusing optics with regards to the workpiece the spot size can be changed within the limitations of the equipment. Spot size limitations for the equipment used within this work are from 0.3 mm to 2.0 mm. Altering the spot size is done through moving the deposition head vertically until the correct distance for the required spot size is reached, this is checked by using a beam profiler. Alternatively, a set distance for the focusing optics from the workpiece can be chosen for carrying out deposition work.

To keep the focal point of the powder stream focused at the workpiece surface the nozzle is retracted or extended. As the powder focal length is a known distance from the nozzle tip (11 mm for the nozzle used within this work) a gauge block was used to set this distance.

3.3.1.4 Aligning deposition nozzle to the laser beam

Alignment of the deposition nozzle to the laser beam is critical to ensure maximum powder capture and melting. This uses a HeNe laser which is optically visible as red light and follows an identical path to the CO₂ laser. By turning on the HeNe laser, the carrier gas, and powder feeder on, it can be checked if the laser beam passes through the powder focus point. This is done by human eye, observing the powder focus point from two perpendicular positions (Figure 34).

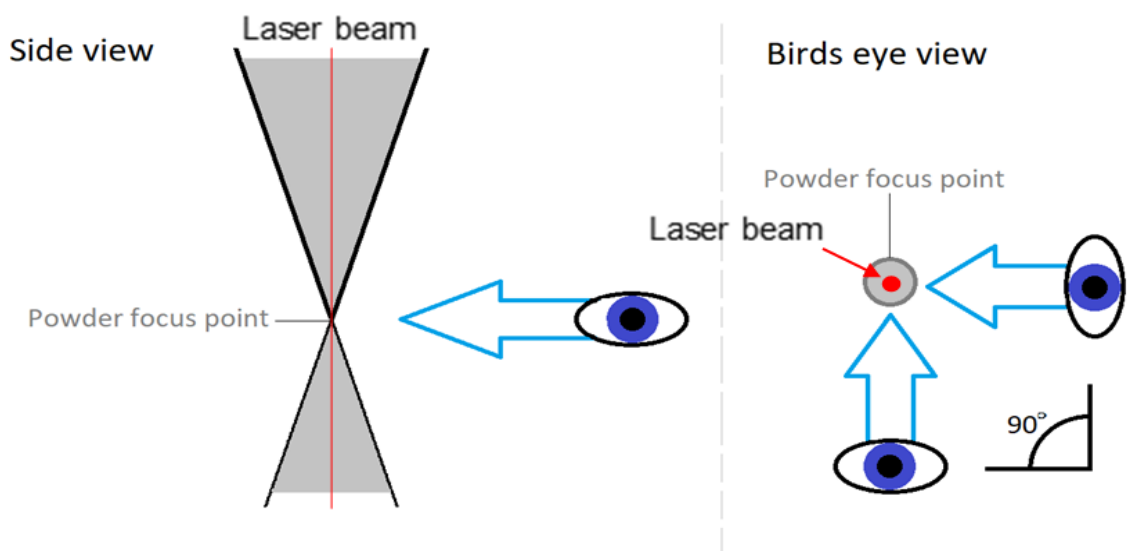


Figure 34: Schematic showing how the human eye is used to observe the powder focus point and laser beam to ensure correct alignment.

The position of the nozzle is adjusted with regards to the laser beam using an XY micro-adjustment positioner above the nozzle to ensure the laser passes through the powder focus point.

3.3.1.5 Powder feed rate calibration

Measurements of powder mass flow rate for the Sulzer-Metco twin-10C powder feeder fitted with a grooved disc (groove dimensions: 5 mm width × 0.6 mm depth) used for this work were taken. A combination of the groove dimensions, disc rotation speed (revolutions per minute (RPM)), and powder density dictate the powder flow rate. Using calibrated digital scales, a beaker was weighed, and weight noted. The beaker was then placed under the deposition nozzle and the powder feeder was turned on for 120 seconds. Argon carrier gas was delivered at 3.5 L/min throughout calibration. The powder exiting the nozzle was captured in the beaker, weighed, and beaker weight subtracted from this value to obtain a measurement of total powder deposited through the nozzle during the set time period. This was done three times and an average taken to ensure consistency. This method provided an average powder feed rate as it does not measure any variation in powder flow which can occur, and is difficult to measure.

3.4 Specimen manufacture

A post-heat-treatment was used for Stage 5 of work. No pre/post-heat-treatments were applied to any other specimens. There was no dwell time between depositing adjacent tracks or subsequent layers. The substrates to be deposited onto were clamped to the DED-L systems rotary table.

3.4.1 Specimen dimensions

Table 16 shows the number of specimens, and their dimensions, to be built for the five stages of work.

| Stage | Number of specimens | Dimensions (mm) (l × w × h) |
|-------|---|-----------------------------|
| 1 | 10 | 50 × 15 × 20 |
| | 10 | 140 × 25 × 65 |
| 2 | 1 | 75 × 80 × 75 |
| 3 | 8 | 110 × 20 × 20 |
| 4 | 4 | 110 × 20 × 20 |
| 5 | N/A – machined sections from Stage 1 specimens were used. | |

Table 16: The number of specimens and their dimensions for each stage of work.

Figure 35, Figure 36, and Figure 37 show schematic drawings of the test specimens.

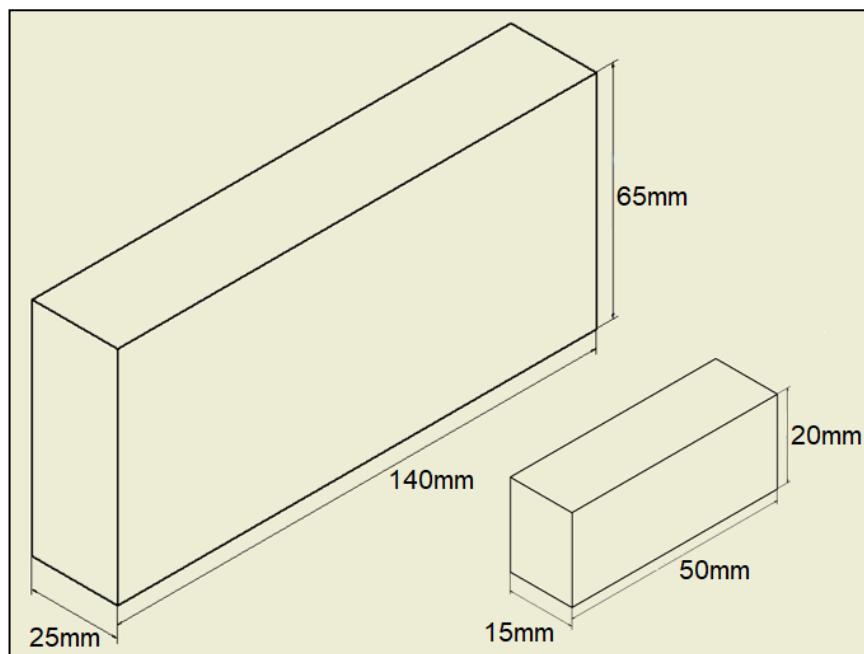


Figure 35: The dimensions of the two blocks manufactured for each set of process parameters in Stage 1.

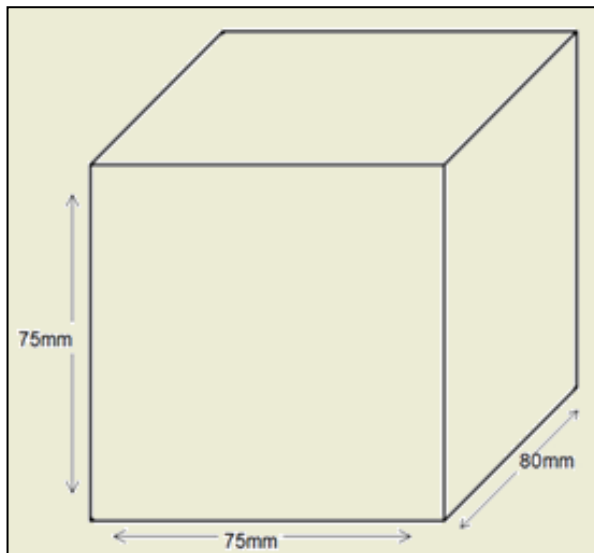


Figure 36: The dimensions of the block built for Stage 2.

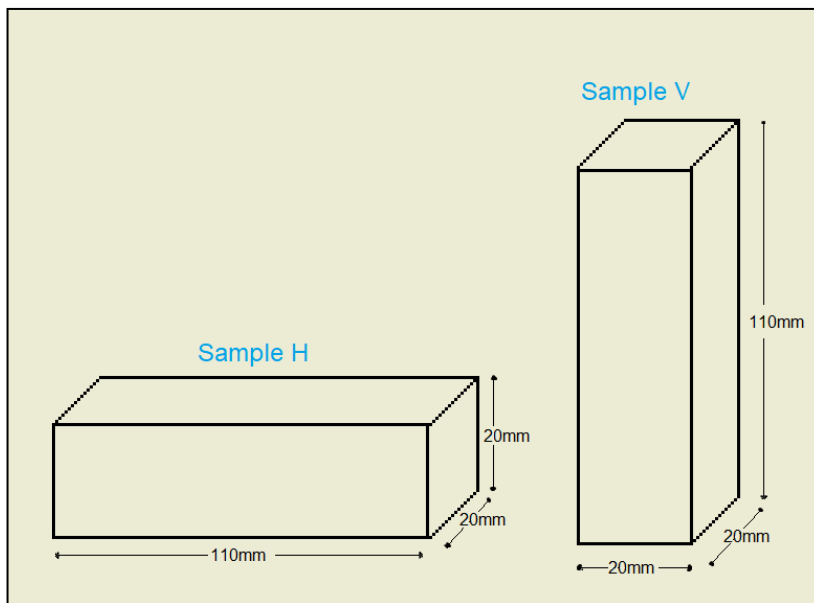


Figure 37: The dimensions and orientation of blocks for Stage 3. These dimensions were also used for Stage 4 blocks.

For Stage 3, four samples had the long edge (110 mm) aligned parallel to the substrate (sample H) whilst the other four had the long edge perpendicular to the substrate (sample V). A 90° rotation of the laser scan path was used between each layer for building sample V test specimens to minimise rounding of edges.

For Stage 4 two build directions were used to manufacture specimens. 55 mm × 20 mm × 20 mm was deposited with the laser positioned perpendicular to the substrate (with the 55 mm parallel to the substrate). This was then removed from the substrate using a bandsaw. The deposit was then rotated 90° to deposit another 55 mm × 20 mm × 20 mm onto the end face of the first build. Figure 38 depicts how the orientation of the block with regards to the laser was changed between build directions.

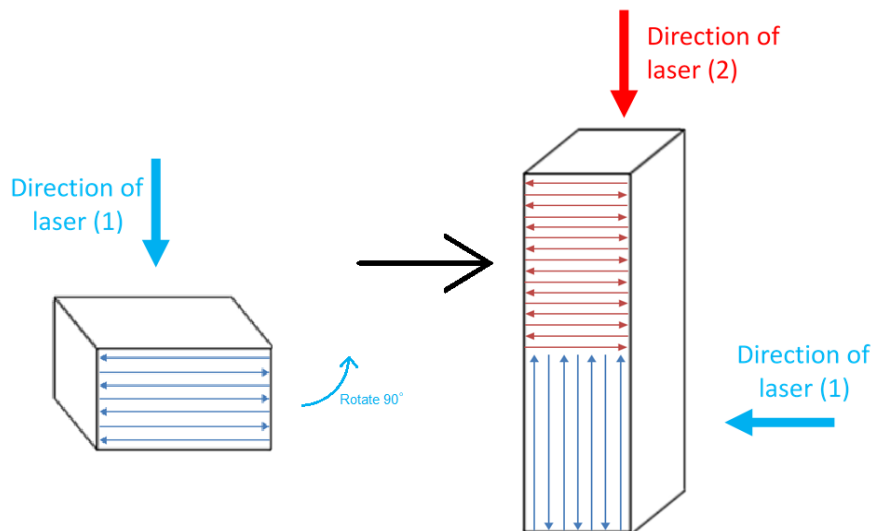


Figure 38: The position of the laser in relation to the block for the first section and second section of deposition. The laser was kept in the same orientation whilst the block was orientated 90°.

3.4.2 Process parameters

Process parameters from previous work carried out by TWI on the Trumpf DMD 505 system using Inconel 718 were collated (Table 17). These were used to determine the flow rates for carrier and shielding gas – 3.5 L/min and 4.0 L/min respectively and were kept constant throughout all stages of work. These process parameters were also used to determine the range to be tested for laser power, scan speed, and powder feed rate within Stage 1 of work.

| Laser power (W) | Scan speed (mm/min) | Powder feed rate (g/min) | Spot size (mm) | Nozzle gas (L/min) | Carrier gas (L/min) |
|------------------------|----------------------------|---------------------------------|-----------------------|---------------------------|----------------------------|
| 285 | 1000 | 1.75 | 0.3 | 3 | 3 |
| 565 | 905 | 2 | 1 | 3.5 | 3 |
| 590 | 650 | 1.7 | 0.9 | 3.5 | 3 |
| 675 | 900 | 3.2 | 1.2 | 4 | 3.5 |
| 675 | 800 | 2.5 | 0.9 | 3 | 3 |
| 765 | 660 | 3 | 1.6 | 4 | 3.5 |
| 840 | 660 | 3 | 1.8 | 4 | 3.5 |
| 1030 | 700 | 2.5 | 1.6 | 3.5 | 3 |
| 1060 | 675 | 3 | 1.8 | 4 | 3.5 |
| 1300 | 660 | 3.5 | 2 | 4 | 3.5 |

Table 17: Previous process parameter sets used for Inconel 718 on the Trumpf DED 505 system (TWI Technology Centre, 2019).

The distance of the focusing optics from the workpiece was kept constant for all specimens within this work, this was 387 mm, meaning that spot size was also constant. To minimise powder wastage and production time, a bi-directional scan pattern was used to manufacture test specimens (Figure 39).



Figure 39: Schematic of a bi-directional scan pattern that was used to manufacture test specimens.

3.4.2.1 Stage 1

Three process parameters were identified as critical in affecting the microstructure and mechanical properties of the part based on previous literature, these were laser power, scan speed, and powder feed rate (Segerstark, Andersson, & Svensson, 2014; Zhang & Jung, 2018; Zhang, Zhang, & Liu, 2012; Fotovvati, Wayne, Lewis, & Asadi, 2018; Mahamood & Akinlabi, 2015; Mahamood, Akinlabi, & Owolabi, 2017; Mahamood, Akinlabi, Shukla, & Pityana, 2014). These parameters have been identified as key due to their significant effect on the heat input – a factor which is crucial to microstructure formation and thus mechanical properties. Laser power, scan speed, and powder feed rate can be linked using the following equations for energy density, mass density and specific energy density as follows:

$$\text{Energy density (Joules/mm}^3\text{)} = \frac{\text{Laser power (W)}}{\text{Scan speed (mm/s)} * \text{Spot area (mm}^2\text{)}}$$

Equation 4: Equation for calculating energy density.

$$\text{Mass density (g/mm}^3\text{)} = \frac{\text{Powder feed rate (g/s)}}{\text{Scan speed (mm/s)} * \text{Spot area (mm}^2\text{)}}$$

Equation 5: Equation for calculating mass density.

$$\text{Specific energy density (Joules/g)} = \frac{\text{Laser power (W)}}{\text{Powder feed rate (g/s)}}$$

Equation 6: Equation for calculating specific energy density.

Laser power, scan speed, and powder feed rate were used at three values. Minitab software (Minitab, LLC, 2021) was used to generate the combination of parameter values and build order – this is the order for specimens to be manufactured in and is randomised to reduce the effect that variation in external factors such as atmospheric temperature may have on results.

Table 18 shows the values to be used for laser power, scan speed, and powder feed rate within the Taguchi DOE for Stage 1, whilst Table 19 shows the Taguchi orthogonal array of parameter combinations and the build order for specimens.

| Level | Laser power (W) | Scan speed (mm/min) | Powder feed rate (g/min) |
|--------------|------------------------|----------------------------|---------------------------------|
| Low | 800 | 500 | 1.8 |
| Middle | 1050 | 750 | 2.9 |
| High | 1300 | 1000 | 4.0 |

Table 18: The process parameter values determined to be used for each level within the Taguchi DOE.

| Set number | Laser power (W) | Scan speed (mm/min) | Powder feed rate (g/min) | Build order |
|-------------------|------------------------|----------------------------|---------------------------------|--------------------|
| 1 | 800 | 500 | 1.8 | 8 |
| 2 | 800 | 750 | 2.9 | 1 |
| 3 | 800 | 1000 | 4.0 | 7 |
| 4 | 1050 | 500 | 2.9 | 4 |
| 5 | 1050 | 750 | 4.0 | 5 |
| 6 | 1050 | 1000 | 1.8 | 9 |
| 7 | 1300 | 500 | 4.0 | 6 |
| 8 | 1300 | 750 | 1.8 | 3 |
| 9 | 1300 | 1000 | 2.9 | 2 |
| 10 | 1300 | 1000 | 4.0 | 10 |

Table 19: The Taguchi orthogonal array for each test run process parameter combination and the run order. A run was also done using the maximum value of process parameters.

Melt-pool diameter, track separation, and z-increment varied between the combinations of process parameters, these are detailed in Appendix 1.

3.4.2.2 Stage 2, Stage 3, and Stage 4

Based on the results obtained from Stage 1, the following process parameters were used for Stage 2, Stage 3, and Stage 4 (Table 20). The determination of these process parameters is discussed later, in section 5.1.1.

| Laser power (W) | Spot diameter (mm) | Scan speed (mm/min) | Powder feed rate (g/min) | Track separation (mm) | z-increment (mm) |
|------------------------|---------------------------|----------------------------|---------------------------------|------------------------------|-------------------------|
| 995 | 2 | 675 | 3 | 1.2 | 0.45 |

Table 20: The process parameters used for stages 2, 3, and 4.

3.4.2.3 Stage 5

The sections used for Stage 5 were obtained from Stage 1 specimens, thus the process parameters are the same.

3.4.3 Determining track separation and z-increment

The following method was used to determine the track separation and z-increment for each set of process parameters for building the specimens within this work:

- 1) Deposit a single track approximately 50 mm in length.
- 2) Measure the track width (Figure 40).

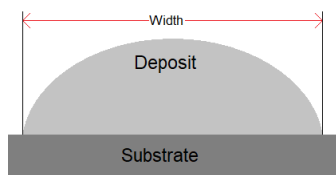


Figure 40: Schematic of a deposited track illustrating step 2 of determining track separation and z-increment.

- 3) Use $\frac{2}{3}$ of this width as the value for track separation to build a 1-layer, 6-track deposit.
- 4) Measure the height of this deposit (Figure 41).

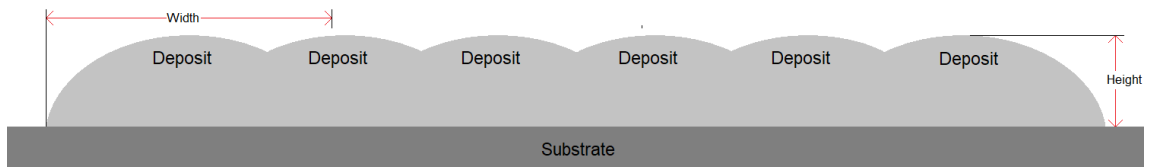


Figure 41: Schematic of a 1-layer 6-track deposit illustrating step 4 of determining track separation and z-increment.

- 5) Use this height as the z-increment for building a 2-layer, 6-track/5-track deposit (using the same track separation as for the 1-layer, 6-track deposit).
- 6) Measure the total height and the widths of individual second layer tracks for the 2-layer, 6-track/5-track deposit (Figure 42).

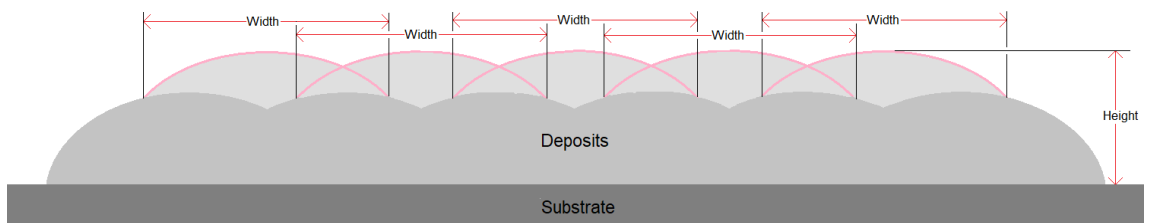


Figure 42: Schematic of a 2-layer 6-track/5-track deposit illustrating step 5 of determining track separation and z-increment.

- 7) Use $\frac{2}{3}$ of the average of these widths as the value for track separation to build test specimens.
- 8) Subtract the recorded value of the 1-layer deposit from the total height of the 2-layer, 6-track/5-track deposit. This gives the z-increment to be used to build test specimens.

3.4.4 Heat-treatment

The following heat-treatment (AMS 5663) was applied for Stage 5 using a Nabertherm 30-3000°C industrial furnace. This heat-treatment was chosen to avoid opening the furnace at a temperature greater than 1000°C to air cool.

| | |
|---|--|
| <p>AMS 5663</p> <p>(SAE International, 2016)</p> | <p>1) Solution Anneal at 980°C for 1 hour, air cool.</p> <p>2) Ageing treatment; hold at 720°C 8 hours, furnace cool to 620°C in 2 hours, hold at 620°C for 8 hours, air cool.</p> |
|---|--|

Table 21: The heat-treatment applied to Stage 5 samples.

3.5 Powder capture efficiency

Powder capture efficiency was calculated for the Stage 1 large blocks. This was done using two approaches to calculate the powder input, and hence the expected weight of the blocks.

Approach 1 (Equation 7), using the time the block took to build:

$$\text{Powder input (kg)} = \frac{\text{Powder feed rate (g/min)} * \text{time to build (minutes)}}{1000}$$

Equation 7: Calculation for powder input using the powder feed rate and the time to build the sample.

Approach 2 (Equation 8), using the total scan path distance for building the block:

$$\text{Powder input (kg)} = \frac{\text{Mass per unit length (g/mm)} * \text{scan path distance (mm)}}{1000}$$

Equation 8: Calculation for powder input using the total mass of powder per unit length and the total distance of the scan path for the sample.

These values were used in conjunction with the final weight of the block to calculate powder capture efficiency (Equation 9):

$$\text{Powder capture efficiency (\%)} = \frac{\text{Powder input (kg)}}{\text{Final block weight (kg)}} \times 100$$

Equation 9: Calculation for powder capture efficiency using the powder input as calculated according to Equation 1 and Equation 2 and the weight of the final sample.

The final weight of the block was determined by weighing the substrate before deposition, then weighing the substrate with the deposited block attached after deposition. These weights were measured to the closest gram. The value of the substrate was subtracted from the second value to obtain the weight of the block.

3.6 Metallographic and mechanical analysis

Specimens were analysed in their as-deposited state for all stages except for Stage 5. All specimens were removed from the substrate using a bandsaw. Cross sections of the single deposited tracks, the 1-layer 6-track, and the 2-layer 6-track/5-track deposits were taken by using a metallurgical cutting wheel to cut perpendicular to the direction of track deposit. These were mounted in MetPrep Ltd VARI-SET 20 powder cold mount using 30 mm mounts. These samples were then prepared for examination using standard metallurgical preparation techniques. This included using manual grinding wheels with grit paper of P60 up to P4000 grits followed by automatic polishers to a 1 μm diamond polish (Figure 43).



Figure 43: The equipment used to prepare samples for examination – manual grinding wheels (left) and automatic polisher (right).

Tensile specimens were machined from samples according to section 3.5.4, whilst electrical discharge machining (EDM) was used to cut small blocks – minimum dimensions 15 mm × 15 mm × 5 mm – from specimens for OLM, SEM, EDX analysis and microhardness testing. This size block was used as a minimum as it could be mounted comfortably within a 30 mm mount whilst still providing a good-sized area for analysis. This machining method was used to avoid any metallurgical damage and minimise contamination to samples. The EDM blocks were mounted and prepared as previously outlined for the single tracks (Figure 44).



Figure 44: Three of the EDM sectioned blocks mounted in VARI-SET 20 powder cold mount using 30 mm mounts.

3.6.1 Specimen analysis preparation

3.6.1.1 Stage 1

Six tensile specimens were taken from each large block, three in the direction parallel to the substrate (H) and three perpendicular to the substrate (V) (Figure 45).

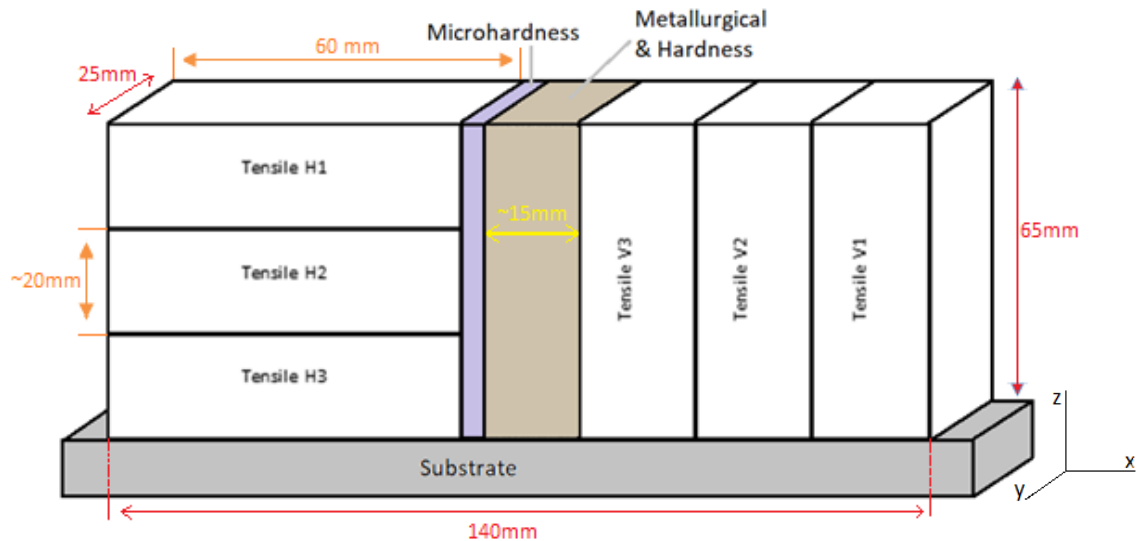


Figure 45: The location of where the tensile test specimens were taken from for the larger block in Stage 1. The area in the middle was used for metallurgical analysis and hardness testing.

For the large test specimen blocks, three blocks with minimum dimensions 15 mm × 15 mm × 5 mm were sectioned using the EDM process in three orientations and prepared for metallurgical analysis. Hardness readings were taken from the 15 mm × 15 mm × 5 mm block removed from the mid-section of the large block which corresponded to the yz-plane. A cross section of the small block was used for metallurgical analysis and hardness testing. Microhardness readings were taken for the entire height of the manufactured blocks, both small and large.

3.6.1.2 Stage 2

Nine tensile specimens were machined from the block, three orientated parallel to the x-axis, three to the y-axis and three to the z-axis. Three blocks with minimum dimensions 15 mm × 15 mm × 5 mm were sectioned using the EDM process in the three orientations and prepared for metallurgical analysis and hardness testing. This is indicated in Figure 46.

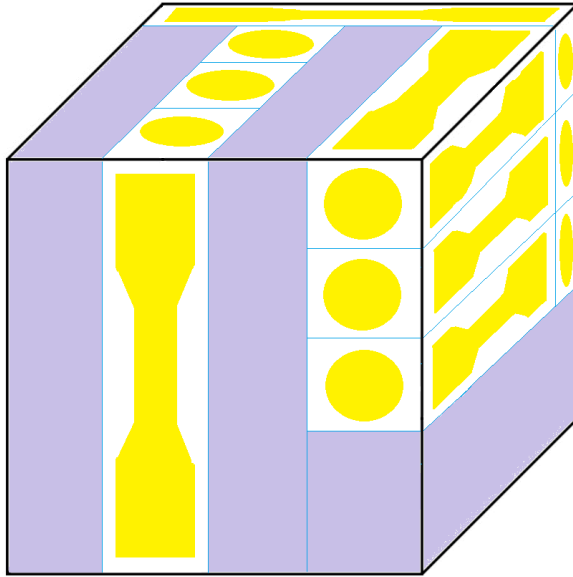


Figure 46: Schematic showing how the block was split into tensile test specimens (yellow) orientated in different directions. The material not used for the tensile test specimens' blocks was EDM'd into the small blocks. Drawing is not to scale.

3.6.1.3 Stage 3

Tensile specimens were machined from six of the oblong samples (three of each build orientation), one tensile specimen per sample as per Figure 47. Three blocks with minimum dimensions 15 mm × 15 mm × 5 mm were sectioned using the EDM process in the three orientations and prepared for metallurgical analysis and hardness testing.

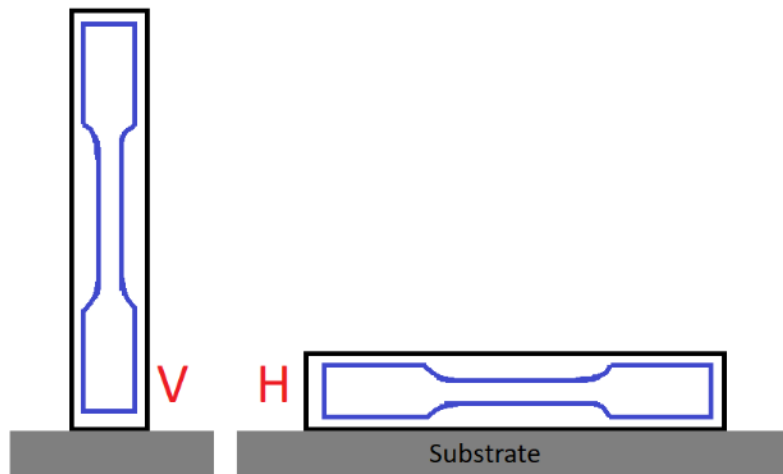


Figure 47: Schematic of one tensile test specimen per sample. Vertical (V) and horizontal (H).

3.6.1.4 Stage 4

Tensile specimens were machined from three samples. Three blocks with minimum dimensions 15 mm × 15 mm × 5 mm were sectioned using the EDM process at the location of the interface and prepared for metallurgical analysis and hardness testing. Blocks were taken at the location of the interface to investigate the interface itself.

3.6.1.5 Stage 5

The 15 mm × 15 mm × 5 mm blocks which corresponded to the yz-plane taken from the mid-section of the large block in Stage 1 (see section 3.6.1) were subject to the heat-treatment outlined in Table 21 prior to preparation for metallurgical analysis and hardness testing. No tensile testing was performed for Stage 5.

3.6.2 Optical Light Microscopy

OLM was conducted using an Olympus BX60 optical microscope and Leica DFC450 5-megapixel digital camera (Figure 48).



Figure 48: The Olympus BX60 optical microscope and Leica DFC450 5-megapixel digital camera used for OLM.

Measurements of the single tracks deposited prior to specimen manufacture were taken using OLM. These were taken of height and width. These measurements were used to determine the track separation and z-increment values for specimen manufacture (outlined in section 3.4.3). Tracks were also checked for evidence of porosity, cracks and to ensure adequate fusion was obtained.

Following surface preparation of EDM samples, optical examination was undertaken using a microscope to check for evidence of defects including porosity, cracks, or segregation both before and after etching. Prior to etching, porosity measurements were taken from 3 different fields per sample at 10x magnification, measuring an area of 1.29 mm² for pores larger than 1.5 µm. This magnification was used as it was determined to be adequate for viewing pores within the material and pores are unlikely to be smaller than 1.5 µm. This

was done using ImageJ software to binarise the image, the two colours (white being the polished metal, and black being artefacts – including pores) are then used to generate a percentage which can be correlated to porosity. As cracks and other possible artefacts also result in a difference in colour, their presence within porosity measurements must be accounted for. This is done by measuring the area of the crack/artefact and subtracting this value from the porosity value.

Glyceregia, Kalling's No. 2 reagent, and Marble's reagent were considered for immersion etching. Table 22 shows their compositions.

| Etchant | Composition |
|--|--|
| Glyceregia (reveals general structure (Vander Voort, 2004)) | 15ml HCl + 10ml glycerol + 5 ml HNO ₃ |
| Kalling's No. 2 reagent (reveals general structure (Vander Voort, 2004)) | 5g CuCl ₂ + 100ml HCl + 100ml C ₂ H ₆ O |
| Marble's reagent (reveals general structure (Vander Voort, 2004)) | 10g CuSO ₄ + 50ml HCl + 50ml H ₂ O |

Table 22: Table outlining composition of etchants considered for use within this work.

Immersion etching using Kalling's No. 2 reagent was found to produce the best results. This etchant attacks intermetallic phases rendering them largely unobservable, whilst darkening carbide phases. Samples were immersed in the etchant for 30 seconds immediately after their final 1 µm diamond polish. They were observed for signs of the grain structure being revealed during this time. Following the 30 second period samples were examined under an optical microscope to check if the grain structure was visible. If further etching was

required, the sample was re-immersed for 5 second periods until the grain structure was suitably revealed.

3.6.2.1 Secondary Dendrite Arm Spacing

Secondary Dendrite Arm Spacing (SDAS) was used as the quantitative measure for the Stage 1 DOE. This was to be used as for dendritic microstructures this feature is considered most akin to grain size within wrought material microstructures (Ghassemali, Riestra, Bogdanoff, Kumar, & Seifeddine, 2017) and hence can relate to material properties. The average grain width of 10 adjacent grains within a sample was measured in the yz-plane for Stage 1 large blocks to examine for any relation to tensile properties.

SDAS is calculated using the following (Equation 10; Figure 49). This can be subjective as dendrites may not always be clear. Hence one operator may interpret dendrites differently to others, and as such the measurements are subject to possible human error. To reduce this error all measurements were taken by the same operator on the same day, using the same microscope and magnification. Multiple measurements were also taken. Six SDAS measurements were taken in the middle region of the yz-plane of samples for each parameter set to obtain a mean. SDAS was not measured in Stage 2, 3, 4, or 5.

$$SDAS = \frac{L}{N - 1}$$

Equation 10: Equation to calculate secondary dendrite arm spacing.

Where:

L = Length

N = Number of SDA

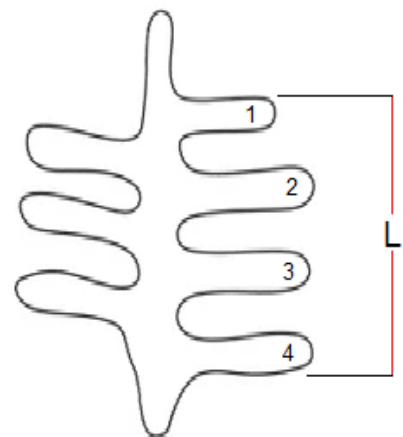


Figure 49: Schematic of a dendrite showing the length and SDA to be used.

3.6.3 Scanning Electron Microscopy

A FEI Quanta 650 FEG SEM (Figure 50) was used to examine and image the etched samples at a higher resolution than OLM. This allowed further interrogation of microstructural phases and features that were unobservable under OLM.



Figure 50: The FEI Quanta 650 SEM used.

20 kV or 25 kV with a spot size of 4.5 were selected as the most appropriate beam settings for the material as images with a good quality resolution could be obtained. Back Scattered Electron (BSE) images were taken to show variation in elemental composition. Using Oxford Instruments Aztec software, EDX maps were created to investigate elemental distribution. These were taken using the following settings (Table 23).

| Setting | Value |
|------------------------------------|--------------|
| Resolution | 256 |
| Frame count | 3 |
| Number of channels | 2048 |
| Process time | 4 |
| Pixel dwell time (μs) | 20000 |
| Binning factor | 2 |

Table 23: The settings used to create EDX maps using Aztec software.

Multiple EDX point analyses were also used to investigate sample composition at different points. The acquisition time for these was 60 seconds.

Un-etched samples were not examined under the SEM as features could not be as fully distinguished as when etched – Figure 51 shows an SEM image of un-etched Stage 1 set 4 where lighter and darker areas were partially visible. EDX analysis was performed on these but did not reveal any correlation to composition variation.

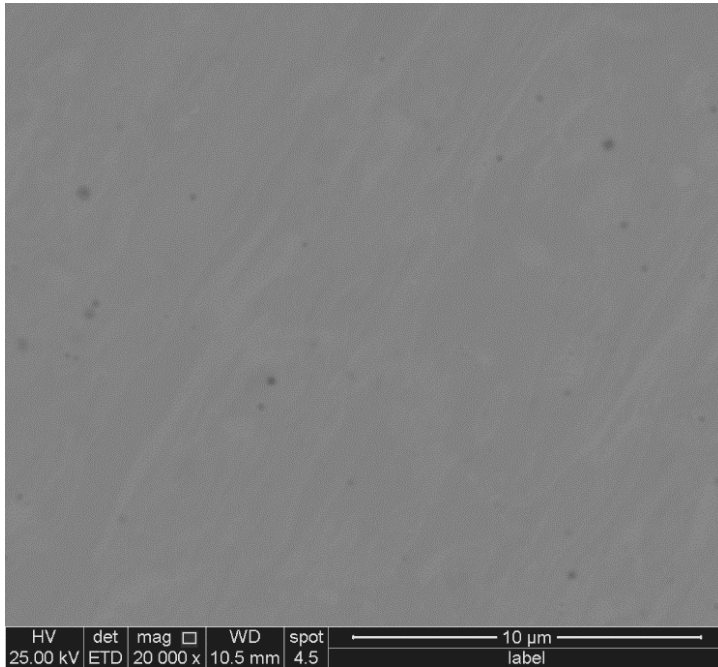


Figure 51: An example of an SEM image of an un-etched sample (Stage 1, set 4).

3.6.4 Tensile testing

Dumbbell tensile test specimens with dimensions according to Figure 52 were machined and tested at room temperature according to ASTM E8 standard at a cross head speed of 1 mm/min. An Instron Universal Testing Machine (Model 3369) and Instron Video Extensometer AVE2 (Figure 53) were used for testing Stage 1 samples, and a MTS Criterion Model 45 tensile test machine and Epsilon Model 3542 extensometer were used for testing Stages 2, 3, and 4 samples. Both tensile test machines and extensometers were calibrated, therefore the difference in machines should not affect the results.

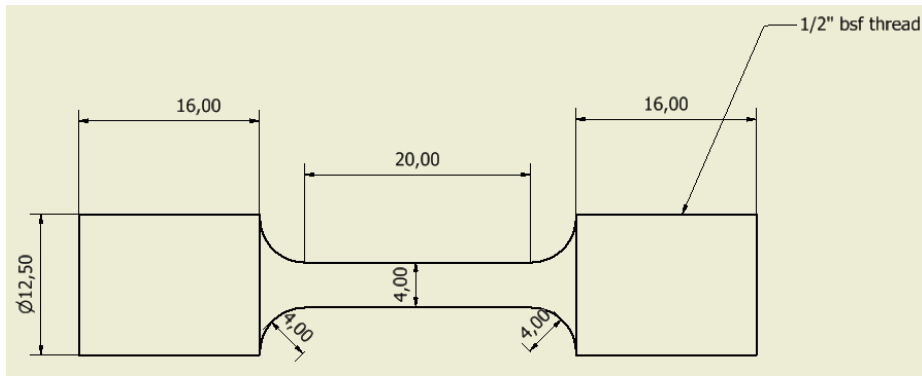


Figure 52: A drawing of the dimensions of the tensile test specimens used in this work in accordance with standard ASTM E8

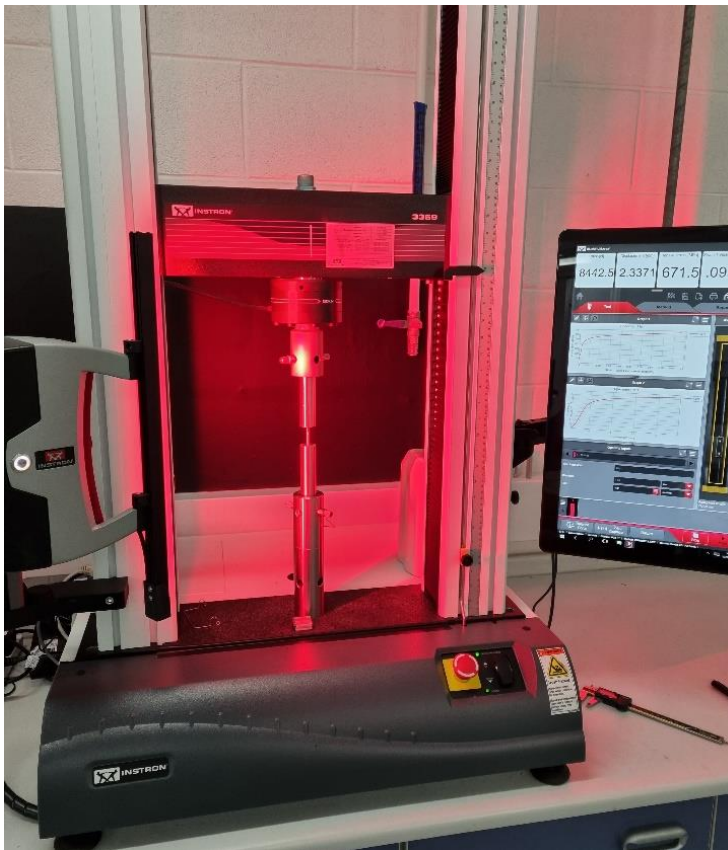


Figure 53: The Instron Universal Testing Machine (Model 3369) and Instron Video Extensometer AVE2 used for testing Stage 1 tensile specimens.

The results from these tests are shown in comparison to standard untreated wrought Inconel 718 0.2% proof stress (725 MPa) and UTS (1035 MPa) values (SAE International, 2016).

Following tensile testing, fractography was carried out using the OLM and SEM to determine the mode of fracture. Fracture surfaces were visually examined for signs of oxidation – indicated by the presence of a blue tinge on the fracture face surface (Li, et al., 2018)

3.6.5 Vickers Hardness

Following surface preparation as detailed in section 3.5 a Mitutoyo HV-100 hardness testing machine (Figure 54) was used to take macrohardness readings of the sample. This was conducted to standard BS EN ISO 6507-1:2005.

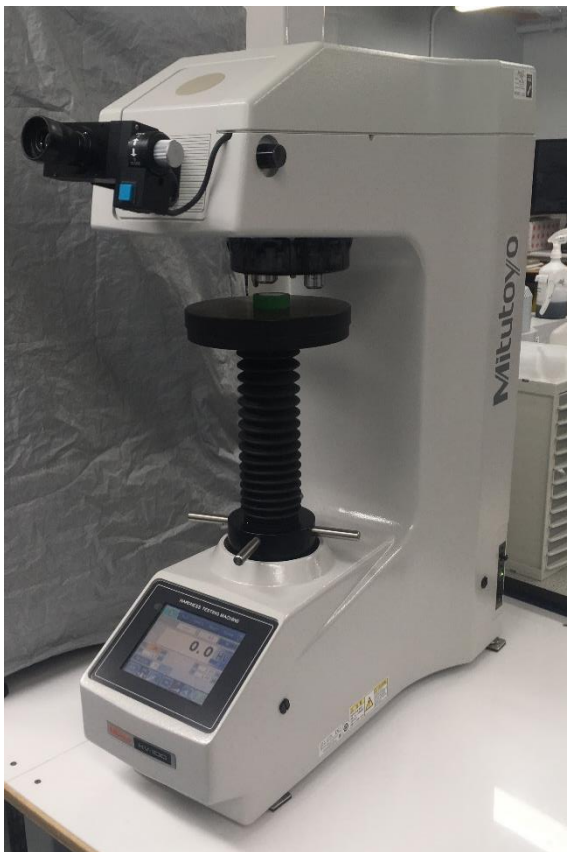


Figure 54: The Mitutoyo HV-100 hardness testing machine used for taking hardness readings.

A load of 10 kgf was used with a dwell time of 15 s. 10 kgf was decided upon based on values used in previous literature (Tucho, Cuviller, Sjolyst-Kverneland, & Hansen, 2017; Sutton, Herderick, Thodla, Ahlfors, & Ramirez, 2019; Zhou, Mehta, McWilliams, Cho, & Sohn, 2019) for Inconel 718. Indents

were measured using a microscope built into the machine. Twelve measurements were taken for each sample to obtain a mean value.

For Stage 4, four measurements were taken in build directions 1, four in build direction 2, and four along the interface.

3.6.5.1 Microhardness

As DED-L is a process which can result in variation at a microscopic level, Vickers microhardness measurements were taken in addition to Vickers macrohardness to see if any variation was present between the two.

Following surface preparation as for OLM, a Wilsons VH3300 hardness machine (Figure 55) was used to take microhardness readings of the sample. This was conducted to standard BS EN ISO 6507-1:2005.



Figure 55: The Wilsons VH3300 hardness machine used for taking microhardness readings of the samples.

Microhardness 0.5 kgf was used with a dwell time of 15 s. 0.5 kgf was established through taking four microhardness measurements at different loads (0.2 kgf – 1 kgf), then plotting the average for each load in a graph (hardness against load). The lowest load in the region where hardness was constant with load (i.e. the plateau/flat section of the graph) is the load deemed to be most suitable for measurements. This value is also used in other studies measuring Inconel 718 microhardness (Kim, Cong, Zhang, & Liu, 2017; Mandal, Lalvani, Watt, Conway, & Tuffs, 2020; Cortina, Arrizubieta, Ruiz, Lamikiz, & Ukar, 2018). Indents were measured using a built-in microscope. The number of microhardness measurements per sample were taken as following:

- Stage 1 small blocks – an oblong matrix of 12 × 17 points spaced 1 mm apart.
- Stage 1 large blocks – an oblong matrix of 20 × 50 points spaced 1 mm apart.
- Stage 2, Stage 3, and Stage 5 cut sections, (minimum 15 mm × 15 mm × 5 mm) – a square matrix of 6 by 6 points spaced 1 mm apart.
- Stage 4 – an oblong matrix of 16 × 16 points spaced 0.5 mm apart. Mean values were calculated according to the distance of a row of points with regards to the interface of the build directions. Eight readings were also taken directly on the point of the interface.

Chapter 4 – Results

This chapter presents the results from this study. Each stage of work is presented individually in its own sub-section.

4.1 Stage 1 – Investigation of key process parameters using a Taguchi DOE approach

Table 24 shows the energy density, mass density, and specific energy density for each parameter set. These values have been ranked from highest (1) to lowest (10).

| Set | Energy density | | Mass density (x 10 ⁻³) | | Specific energy density (x 10 ⁴) | |
|-----|----------------------|------|---------------------------------------|------|--|------|
| | (J/mm ³) | Rank | (g/mm ³) | Rank | (J/g) | Rank |
| 1 | 129.2 | 1 | 4.8 | 2 | 2.7 | 4 |
| 2 | 72.8 | 3 | 4.4 | 3 | 1.7 | 8 |
| 3 | 75.5 | 2 | 6.3 | 1 | 1.2 | 10 |
| 4 | 55.2 | 4 | 2.5 | 5 | 2.2 | 5 |
| 5 | 45.1 | 7 | 2.9 | 4 | 1.6 | 9 |
| 6 | 53.1 | 5 | 1.5 | 8 | 3.5 | 2 |
| 7 | 42.9 | 8 | 2.2 | 6 | 2.0 | =6 |
| 8 | 48.6 | 6 | 1.1 | 10 | 4.3 | 1 |
| 9 | 33.4 | 9 | 1.2 | 9 | 2.7 | 3 |
| 10 | 30.7 | 10 | 1.6 | 7 | 2.0 | =6 |

Table 24: The energy density, mass density, and specific energy density for each parameter set. These have been ranked from highest (1) to lowest (10).

Figure 56 shows the single-track deposits and melt runs for each parameter set. A melt run uses the same parameters as for depositing, but the powder feeder is kept off, so no powder is deposited. Little to no penetration was observed for set 1, 2, and 3 melt runs.

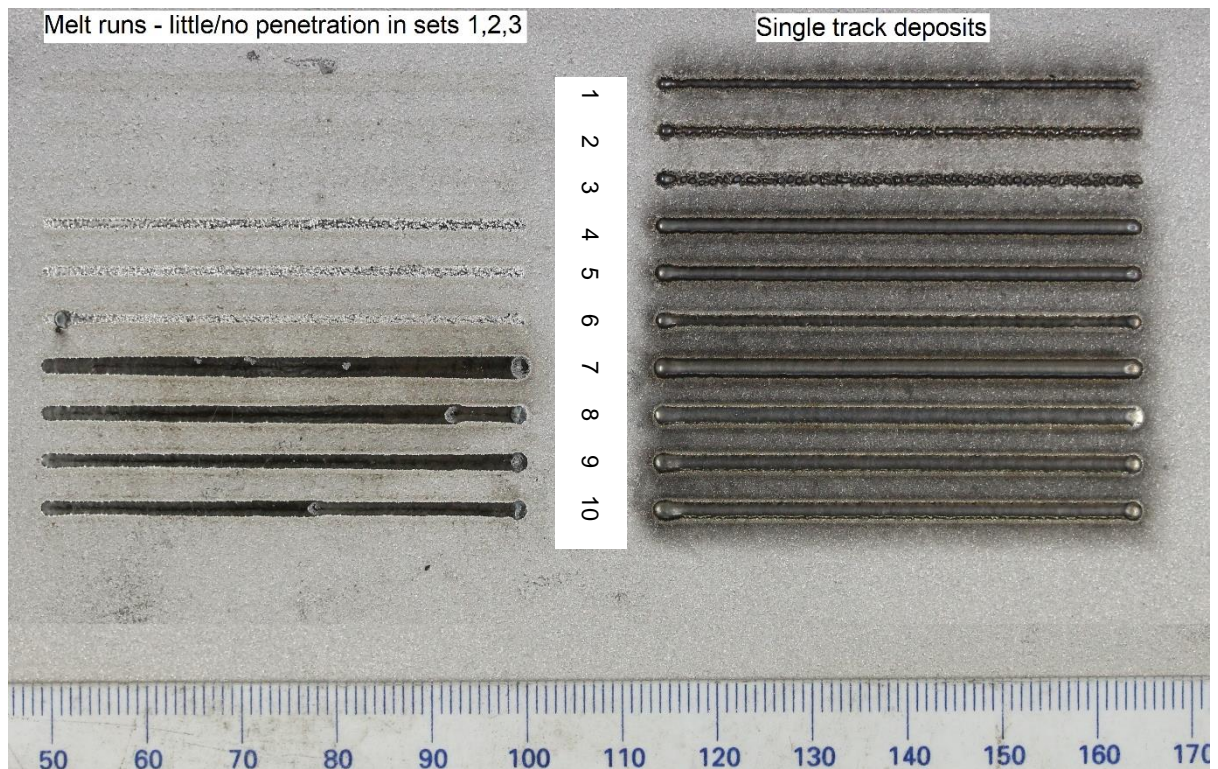


Figure 56: The single-track deposits and melt runs for each parameter set.

The single tracks were deposited according to the Taguchi orthogonal array. Set 1, 2, and 3 single tracks were very narrow (track 1 width: 0.973 mm, track 2 width: 1.058 mm, track 3 width: N/A) with very little penetration into the substrate below. This is due to their low laser power value. They were deemed unsuitable for building the multi-track, multi-layer blocks due to the length of time that each block would have taken to build, and the volume of powder that may have been wasted (not captured in the melt-pool). This indicates that a sufficiently high laser power is essential for a high quality deposit.

Figure 57 shows the poor bonding between the deposit and substrate for set 2. After cooling, sections of the track deposited for set 3 detached from the

substrate meaning no measurements could be taken for this track. This links to the high mass density and low specific energy density of set 3 (Table 24).

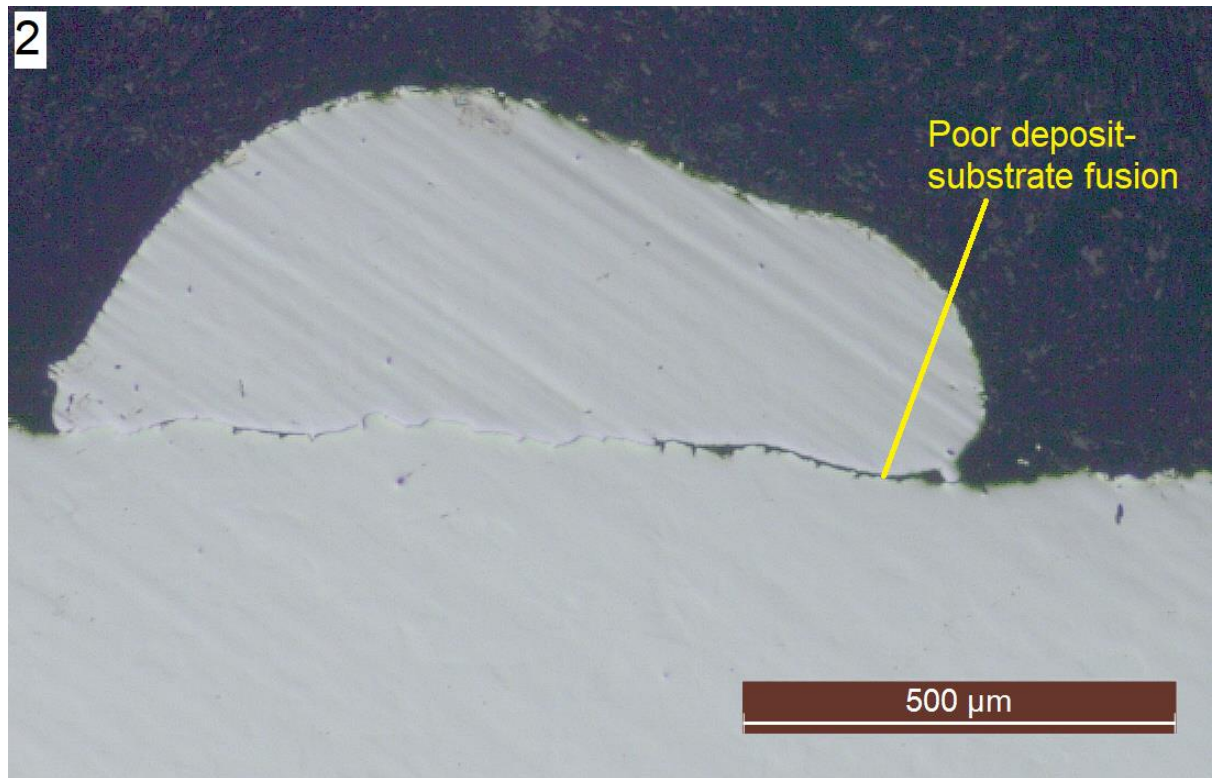


Figure 57: Optical micrograph of the single track deposited for parameter set 2. Poor deposit-substrate fusion can be seen.

2-layer, 6-track/5-track deposits were manufactured for the seven remaining sets of parameters (4 to 10). During this, set 6 was observed to dome significantly at the edges of the sample. As the tracks were also narrow (1.23 mm) it was rendered unsuitable for building larger blocks. As set 6 used the highest scan speed and lowest powder feed rate the narrow track relates to the low powder feed rate. Whilst depositing the initial layers for the small block using set 7 parameters, large amounts of reflection and spatter from the workpiece was seen, therefore this parameter set was not used moving forward in the work as it would have been dangerous and damaged the laser.

Parameter set 8 used the lowest powder feed rate and highest laser power, and had the lowest mass density and highest specific energy density. Whilst building the small block, large amounts of reflection and spatter were observed, and irreversible damage occurred to the protective lens in the laser. This may be due to plasma formation despite the laser power being below what would typically be seen to induce plasma forming. For this reason, a large block using this parameter set was not built. Figure 58 shows the partially built set 8 small block where a burn mark from the laser can be seen.

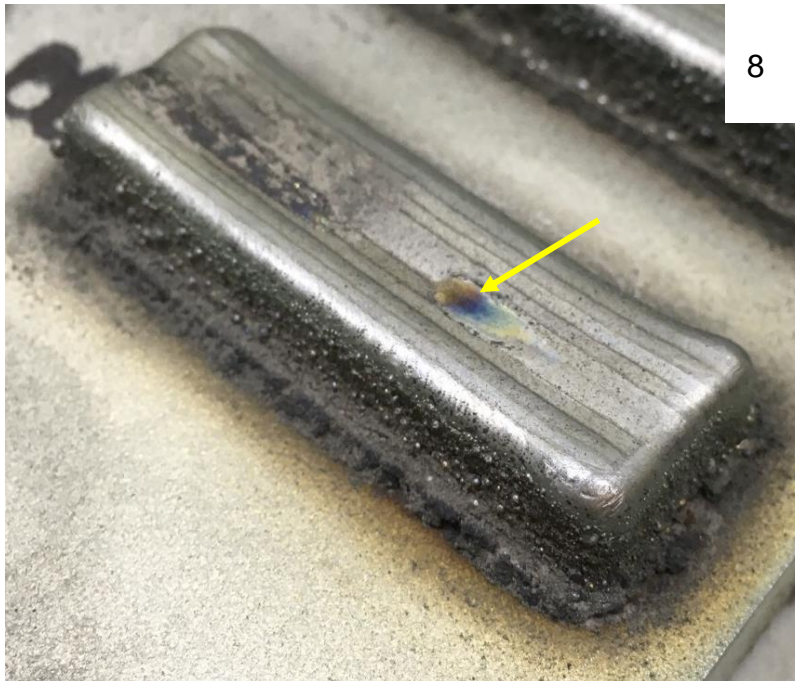


Figure 58: The partially built set 8 small block. A burn mark from the laser can be seen.

As reflection and spatter were common between set 7 and set 8, this indicates that when the laser power is increased to the highest value, a low scan speed or low powder feed rate result in the overmelting of powder and previously deposited material, causing the process to become unstable.

Table 25 contains images of the small blocks and large blocks for the remaining parameter sets (4, 5, 9, 10). The time taken to build large blocks is shown.

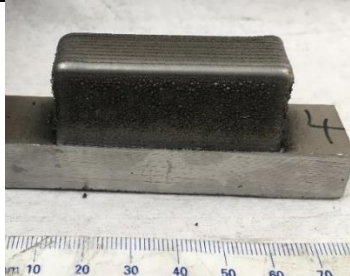

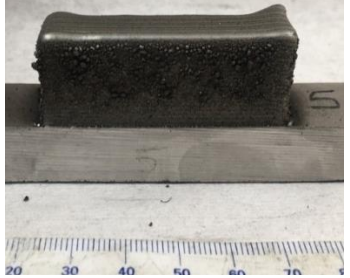


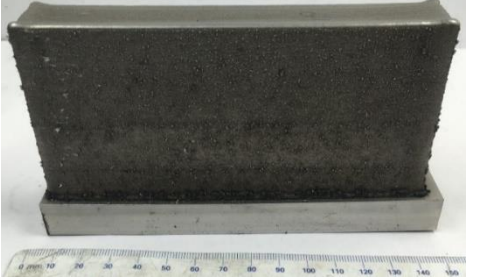
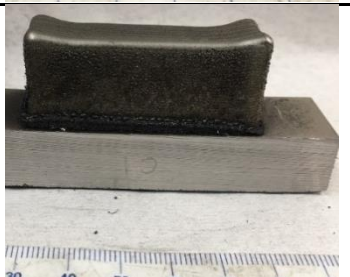
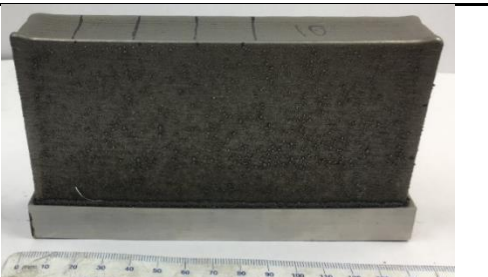
| # | Small block | Large block | Large block build time (minutes) |
|----|---|--|----------------------------------|
| 4 |  A small, dark, rectangular block with a slightly curved top surface, resting on a wooden base. A ruler is visible below it, showing markings from 10 to 70. |  A large, dark, rectangular block with a slightly curved top surface, resting on a wooden base. A ruler is visible below it, showing markings from 0 to 150. | 840 |
| 5 |  A small, dark, rectangular block with a slightly curved top surface, resting on a wooden base. A ruler is visible below it, showing markings from 20 to 70. |  A large, dark, rectangular block with a slightly curved top surface, resting on a wooden base. A ruler is visible below it, showing markings from 0 to 150. | 600 |
| 9 |  A small, dark, rectangular block with a slightly curved top surface, resting on a wooden base. A ruler is visible below it, showing markings from 0 to 90. |  A large, dark, rectangular block with a slightly curved top surface, resting on a wooden base. A ruler is visible below it, showing markings from 0 to 150. | 630 |
| 10 |  A small, dark, rectangular block with a slightly curved top surface, resting on a wooden base. A ruler is visible below it, showing markings from 30 to 90. |  A large, dark, rectangular block with a slightly curved top surface, resting on a wooden base. A ruler is visible below it, showing markings from 0 to 150. | 550 |

Table 25: Images of the small and large blocks for parameter sets 4, 5, 9, and 10. Large block build times are shown (to the nearest 10 minutes).

4.1.1 Optical Light Microscopy

OLM found specimens to display no visible evidence of cracks prior to etching. Porosity results for the small and large blocks which could be built are shown in Table 26. Porosity was observed in all samples, and lay within a narrow range. Figure 59 shows an example of an image used for porosity measurements. Pores are a mix of speherical and irregularly shaped.

| Set | Porosity (%) | | | |
|-----|--------------|----------|-------------|----------|
| | Small block | Std dev. | Large block | Std dev. |
| 4 | 0.20 | 0.15 | 0.18 | 0.012 |
| 5 | 0.18 | 0.12 | 0.14 | 0.013 |
| 9 | 0.10 | 0.02 | 0.11 | 0.009 |
| 10 | 0.17 | 0.09 | 0.06 | 0.002 |

Table 26: Mean values for porosity of the small and large blocks. Standard deviation is shown.

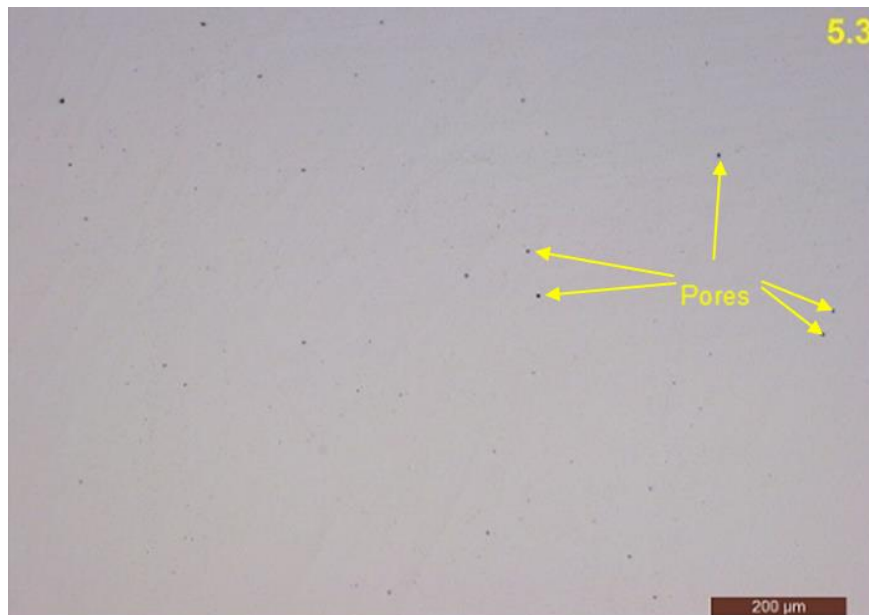


Figure 59: An optical micrograph used for set 5 porosity measurements. Larger pores are indicated.

OLM of etched samples revealed the microstructure to vary between the three planes for all large block samples. Individual deposited layers and tracks were visible, these are indicated by the yellow dashed lines on Figure 60. Grains within a newly deposited layer grew from the existing grains of the former layers, without new nuclei forming – the former layer provided parent grains for the epitaxial growth into the new layer. This resulted in a unidirectional microstructure, with columnar grains elongating upwards towards the laser, and most grain boundaries laying parallel to the growth direction. A difference in contrast is present in these images at the meeting point between adjacent tracks and layers.

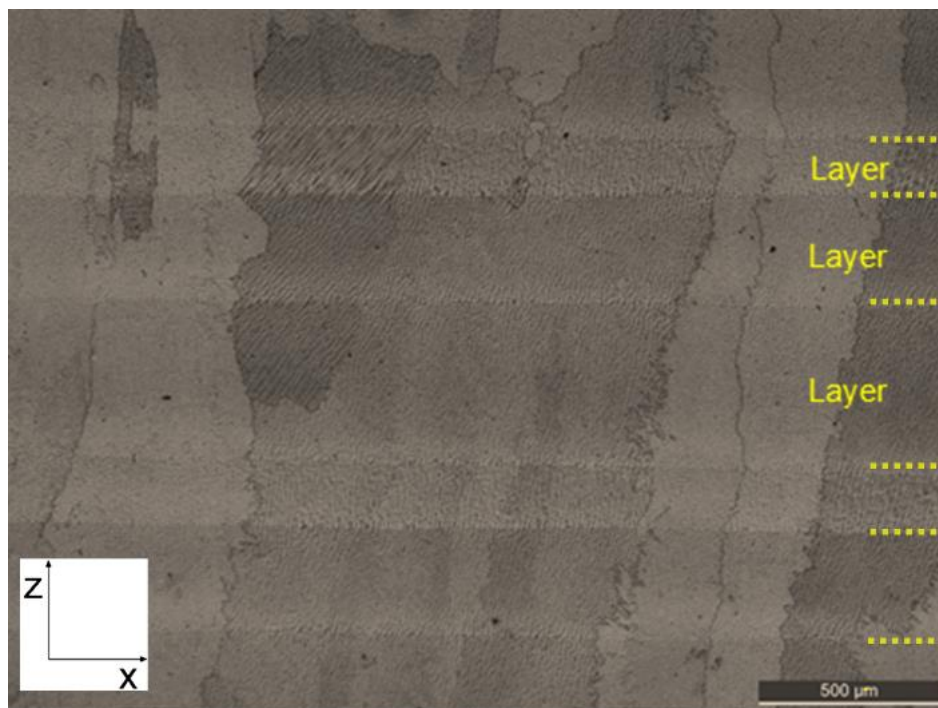


Figure 60: Optical micrograph of the xz-plane of set 5 large. Grains can be seen to extend through multiple layers (indicated in yellow).

Under higher magnification a variation in structure can be observed at this meeting point, with refinement of phases seen to have occurred in the area adjacent to the subsequently deposited layer or track (Figure 61, Figure 62, Figure 63, Figure 64). This corresponds to the region that has been heat-affected during the deposition of subsequent material.

It is likely that the light regions visible in the etched samples are Ni-rich solid solution (γ -phase), whilst the darker regions are precipitates, such as carbides and Laves phase.

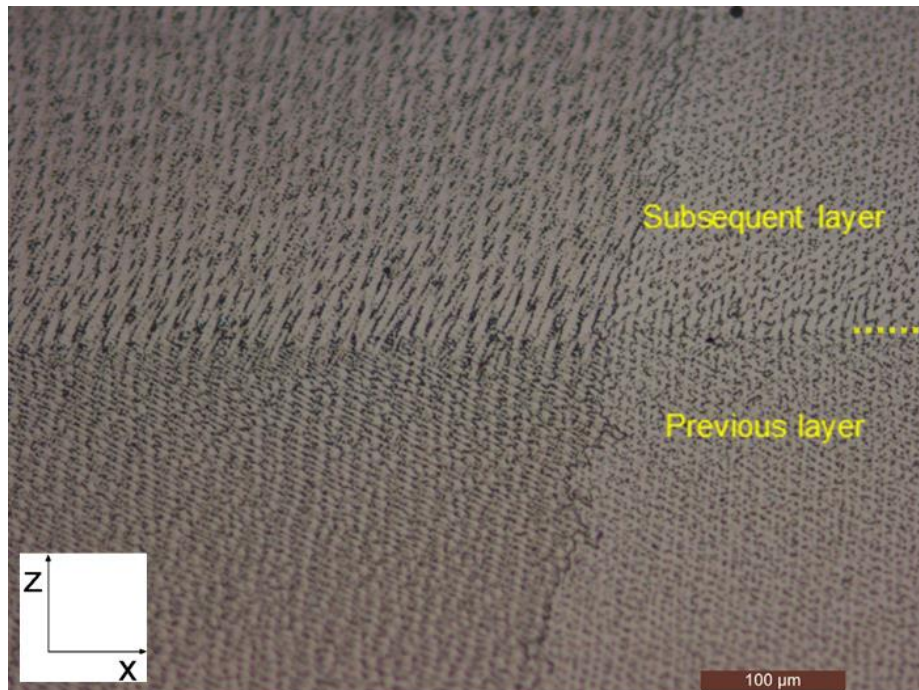


Figure 61: Higher magnification optical micrograph of the xz-plane of set 5 large. The meeting point between layers can be clearly seen, highlighted by a variation in structure as phases in the upper portion of the previous layer have been refined during the deposition of the subsequent layer.



Figure 62: Optical micrograph of the yz-plane of set 9 large. Grains can be seen to extend through multiple tracks.

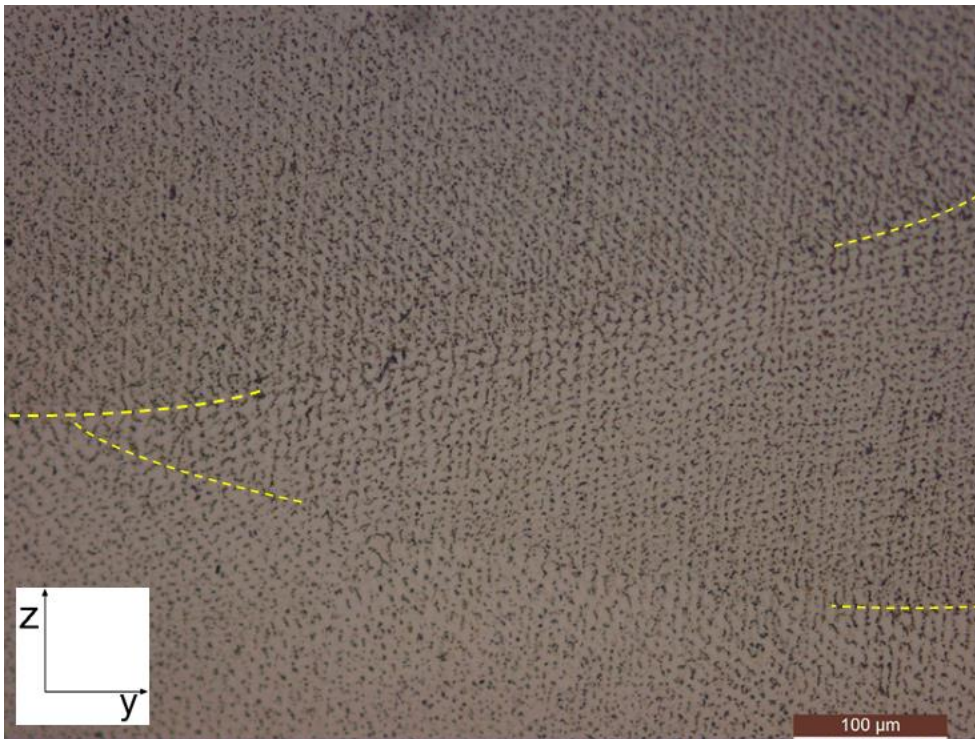


Figure 63: Higher magnification optical micrograph of the yz -plane of set 4 large. The meeting point between tracks can be seen, indicated by the yellow dashed lines.

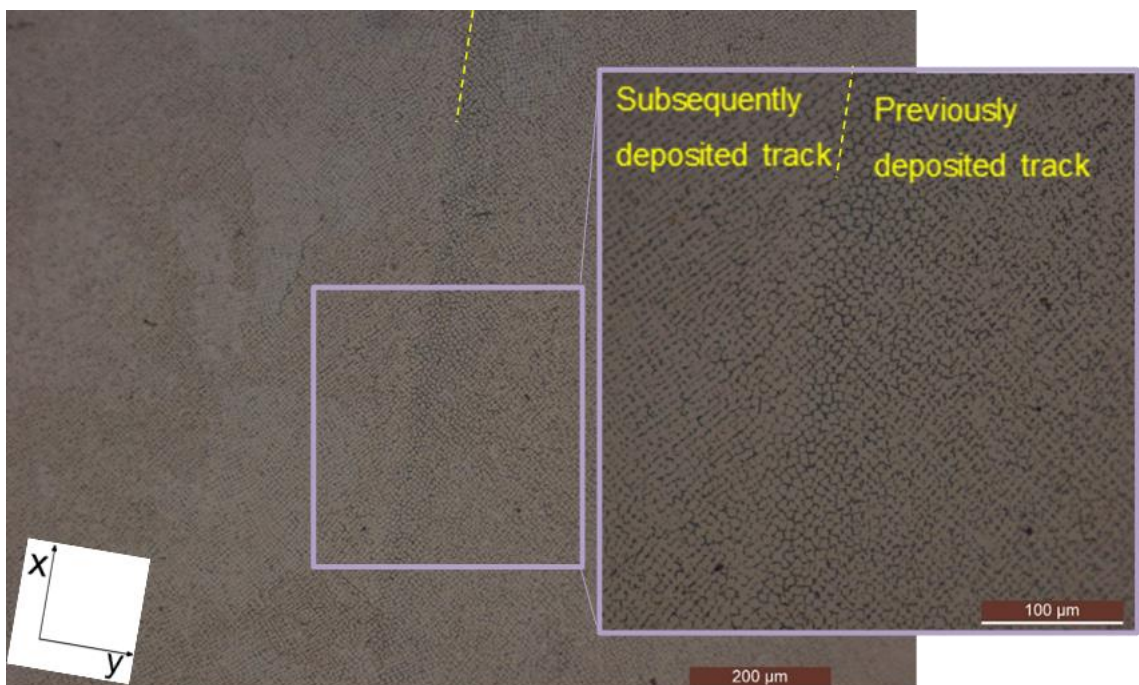


Figure 64: Optical micrographs of the xy -plane of set 10 large. The meeting point between tracks is indicated by the yellow dashed line.

Figure 65 shows an example of an image used for grain width measurements. Mean values for each sample are shown in Table 27.

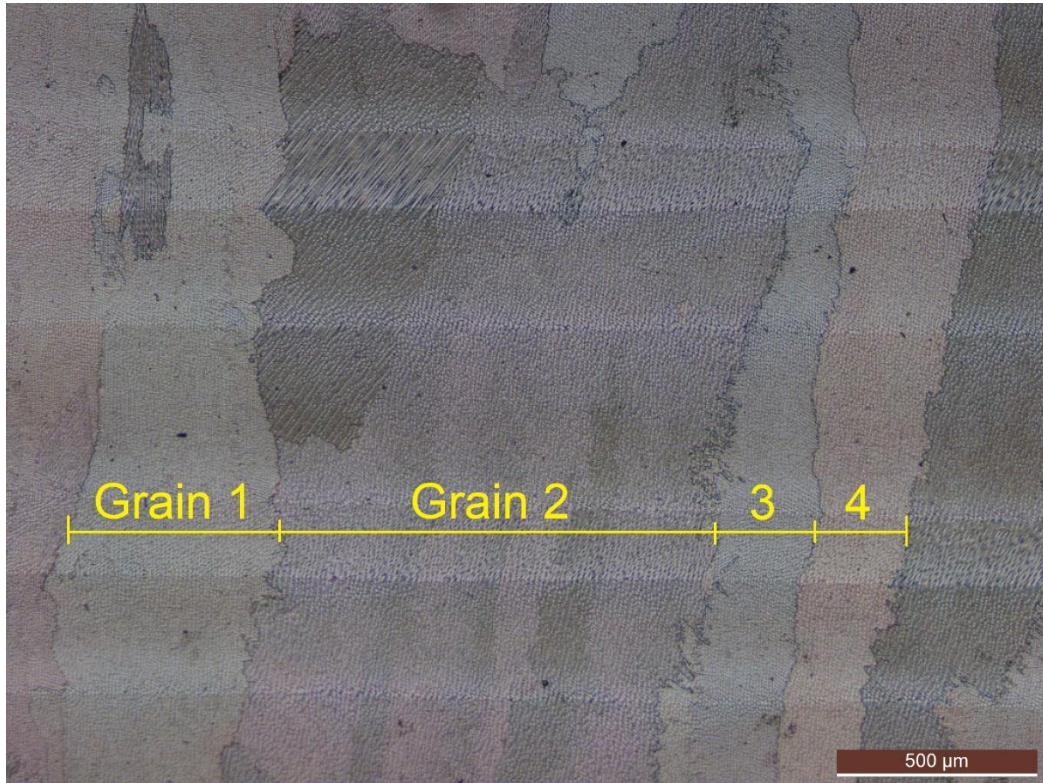


Figure 65: Example of micrograph used for calculating average grain width for large block 5.

| Set | Grain width (μm) | Std dev. |
|------------|-------------------------|-----------------|
| 4 | 297 | 28.5 |
| 5 | 301 | 39.6 |
| 9 | 317 | 38.6 |
| 10 | 298 | 36.9 |

Table 27: Mean grain width values for the large blocks.

4.1.1.1 Secondary Dendrite Arm Spacing

Mean SDAS for the parameter sets are shown in Table 28 and Figure 66. Significant differences between small and large block SDAS were present in all sets apart from set 5. Within small blocks, significant differences were present between the averages obtained for small block 4 and small block 9, and between small block 5 and small block 9. No significant difference was present between large blocks. Examples of images used for these measurements are shown in Figure 67.

| | Small block | | Large block | |
|------------|--|-----------------|--|-----------------|
| Set | SDAS (μm) | Std dev. | SDAS (μm) | Std dev. |
| 4 | 8.33 | 0.50 | 11.39 | 2.23 |
| 5 | 9.83 | 1.15 | 11.27 | 4.55 |
| 9 | 6.58 | 0.97 | 12.21 | 2.90 |
| 10 | 8.10 | 1.00 | 12.24 | 1.89 |

Table 28: Mean values for SDAS for the small and large blocks. Standard deviation is shown.

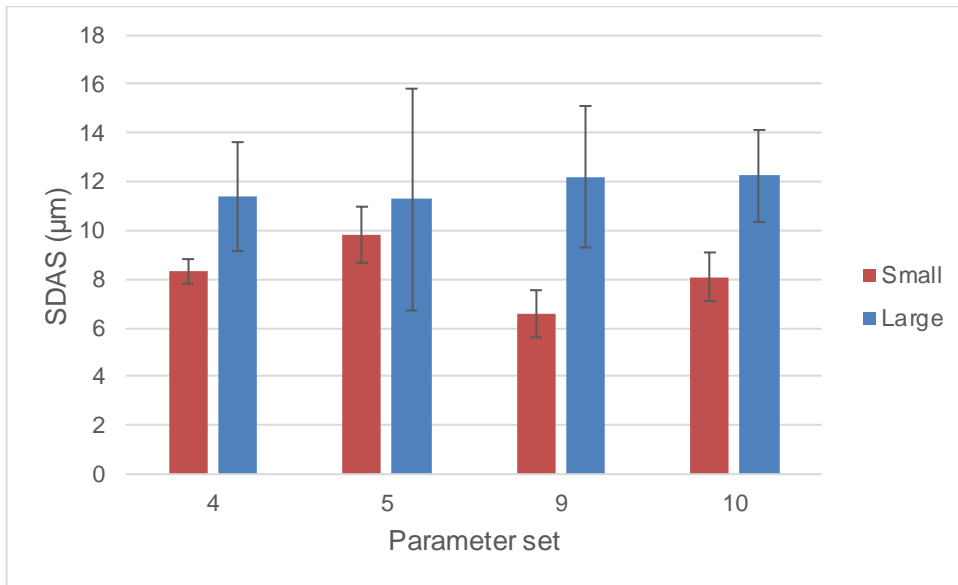


Figure 66: Graph displaying the mean values for SDAS for the small and large blocks. Standard deviation error bars are shown.



Figure 67: Examples of the optical micrographs used for measuring SDAS.

4.1.2 Scanning Electron Microscopy

A bright phase (later identified as Laves phase) was present in all samples, these were seen to aggregate in continuous and discontinuous networks. Continuous networks of Laves extending in the direction of the laser were more dominant in small blocks, being most apparent in set 10 small. In large blocks

this phase is less continuous, and in set 5 large it is spread uniformly. Figure 68 and Figure 69 contain SEM images of the samples for comparison.

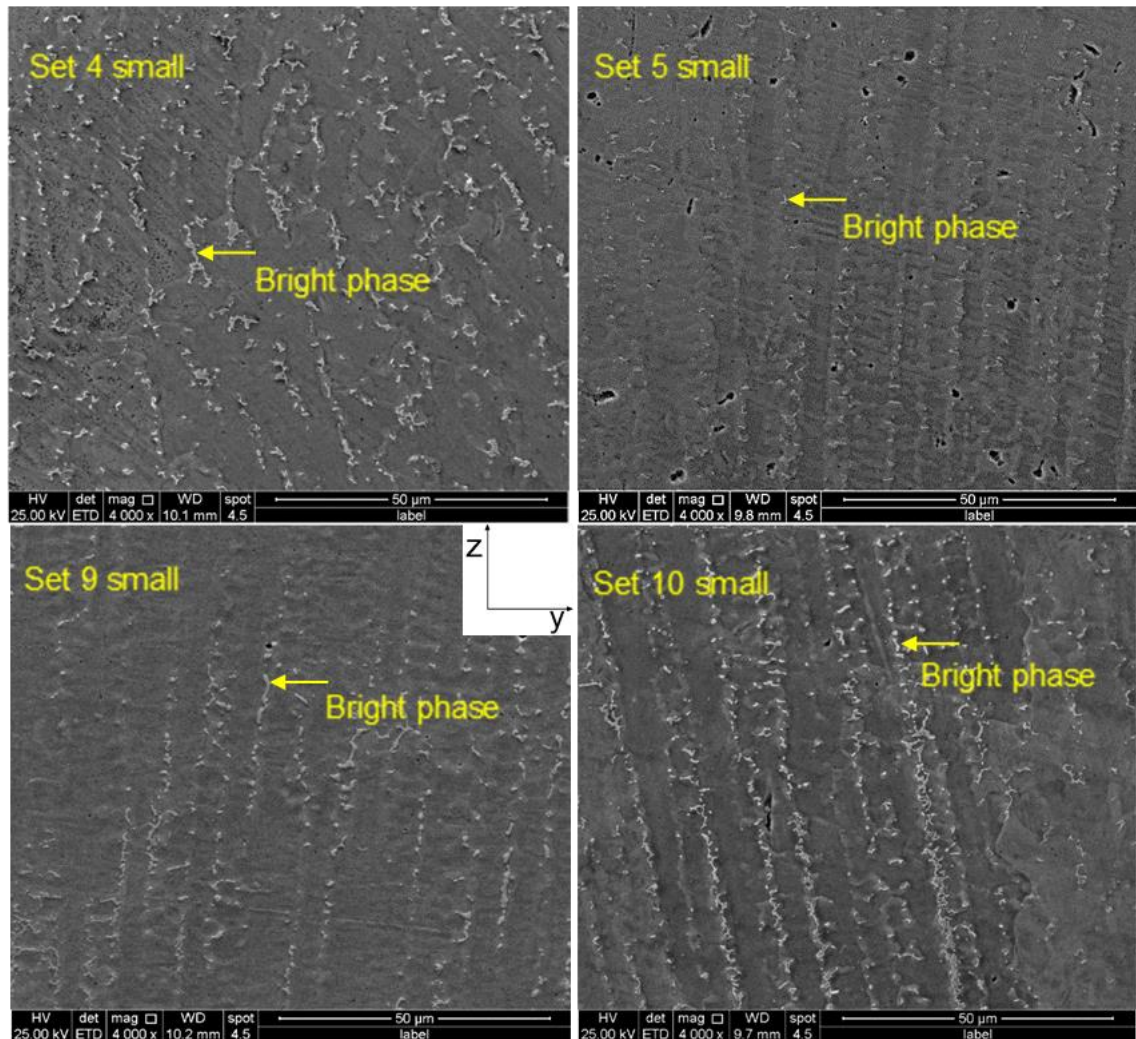


Figure 68: Secondary electron SEM images of the yz-planes of the small blocks. An example of the bright phase (Laves phase) is indicated on each SEM image.

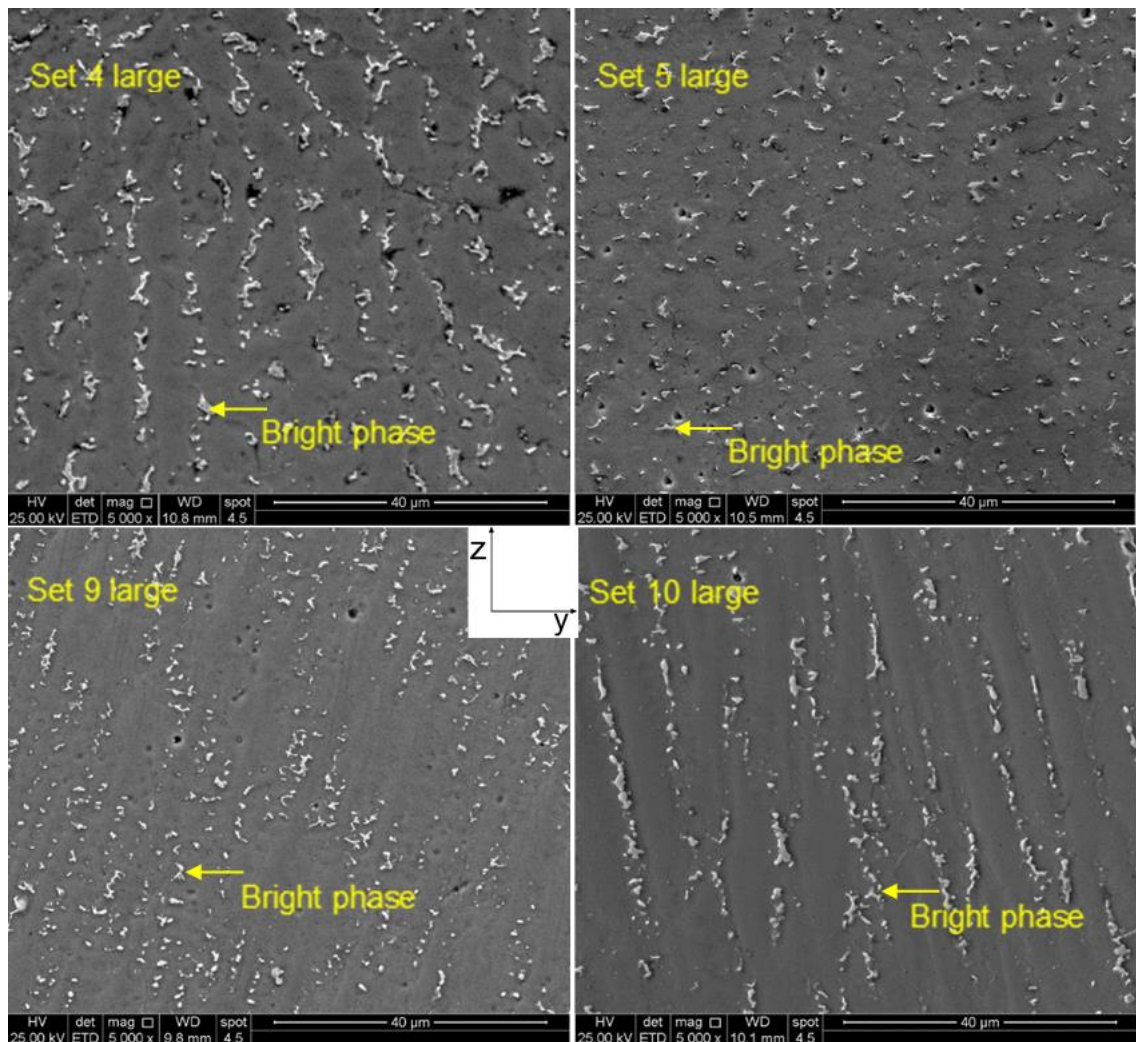


Figure 69: Secondary electron SEM images of the yz-planes of the large blocks. An example of the bright phase (Laves phase) is indicated on each SEM image.

Greater volumes of this phase were present within the large blocks than their corresponding small block. This was confirmed by binarising SEM images, of dimensions $100\ \mu\text{m} \times 120\ \mu\text{m}$, and measuring the percentage of white within the samples. This corresponds to the Nb-rich phase – determined to be Laves phase. Results are presented in Table 29.

| Sample | % white | |
|---------------|----------------|--------------|
| | Small | Large |
| 4 | 2.68 | 6.64 |
| 5 | 1.31 | 5.90 |
| 9 | 1.21 | 10.20 |
| 10 | 3.26 | 5.34 |

Table 29: Values for the percentage of white present, obtained by binarising SEM images (dimensions 100 μm \times 120 μm) of samples.

Figure 70 shows the region where two adjacent tracks meet. The heat-affected region where the subsequently deposited track has altered the previously deposited track displays a more consistent pattern of the bright phase.

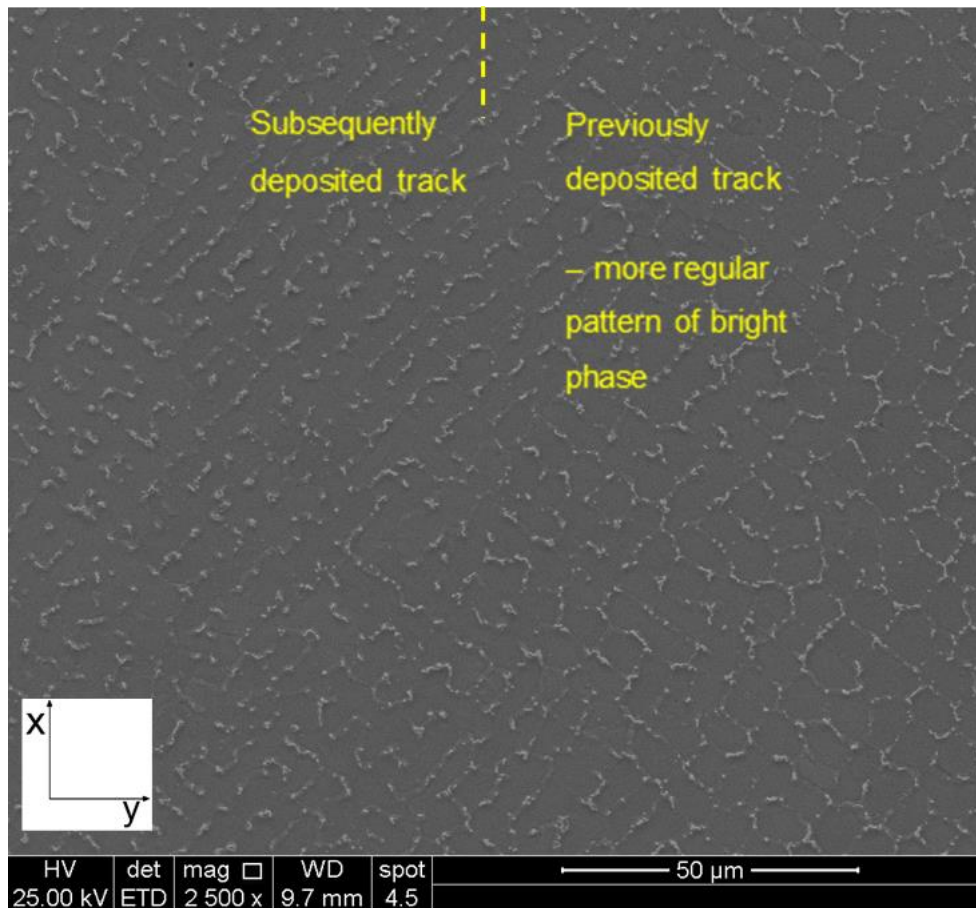


Figure 70: Secondary electron SEM image of the xy-plane of set 10 large. The previously deposited track and subsequently deposited track are indicated. A more regular/consistent pattern of the white phase is present within the region of the previously deposited track that is adjacent to the subsequently deposited track.

At least five phases are visible in the samples. This is demonstrated in Figure 71) A grey matrix, a white globular phase, a darker phase surrounding the white phase, dark precipitates, and small round light precipitates. EDX analysis was performed on each of these phases.

The matrix (Figure 71 Spectrum 1; Figure 72 Spectrum 6) was found to contain less Nb and greater Cr than the Inconel 718 powder used for manufacture (Table 30). The white phase was high in Nb (Figure 71 Spectrum 2, 3, 4; Figure 72 Spectrum 7), whilst the small round precipitates were found to be high in Al and also contain greater Ti (Figure 71 Spectrum 5; Figure 72 Spectrum 8). An increase in the white phase can be seen where layers meet (Figure 72).

| | Element Wt% | | | | | | |
|-------------------|-------------|-------|-------|------|------|------|------|
| | Ni | Fe | Cr | Nb | Mo | Ti | Al |
| Powder | 53.15 | 18.80 | 18.30 | 5.08 | 2.97 | 0.95 | 0.52 |
| Spectrum 1 | 52.4 | 19.6 | 19.5 | 4.2 | 2.9 | 1.0 | 0.4 |
| Spectrum 2 | 38.7 | 15.2 | 16.0 | 23.2 | 2.8 | 3.4 | 0.6 |
| Spectrum 3 | 34.1 | 13.4 | 14.1 | 35.1 | - | 2.9 | 0.4 |
| Spectrum 4 | 46.5 | 14.3 | 14.7 | 18.3 | 4.4 | 1.4 | 0.4 |
| Spectrum 5 | 44.8 | 18.1 | 17.8 | 4.7 | 2.3 | 4.9 | 7.3 |
| Spectrum 6 | 53.2 | 20.9 | 19.7 | 2.6 | 2.4 | 0.7 | 0.5 |
| Spectrum 7 | 45.5 | 14.1 | 14.7 | 19.2 | 4.6 | 1.4 | 0.5 |
| Spectrum 8 | 43.2 | 17.2 | 16.8 | 6.7 | 2.5 | 5.8 | 7.9 |

Table 30: Table containing the element wt% for the powder pre-DED-L, and for the EDX analysis performed.

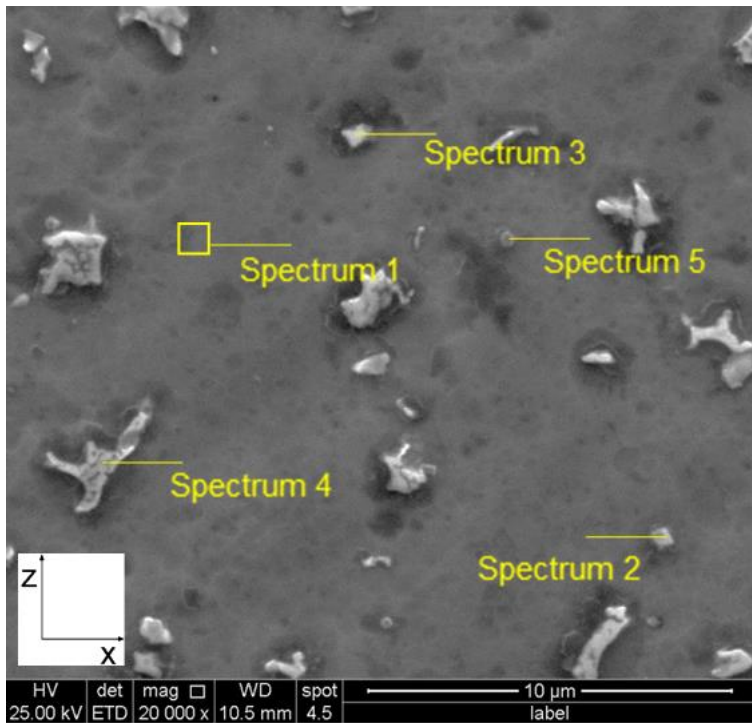


Figure 71: Secondary electron SEM image of the xz-plane of set 4 large, showing the phases which are present within the samples. The corresponding EDX spectra can be found in Table 30.

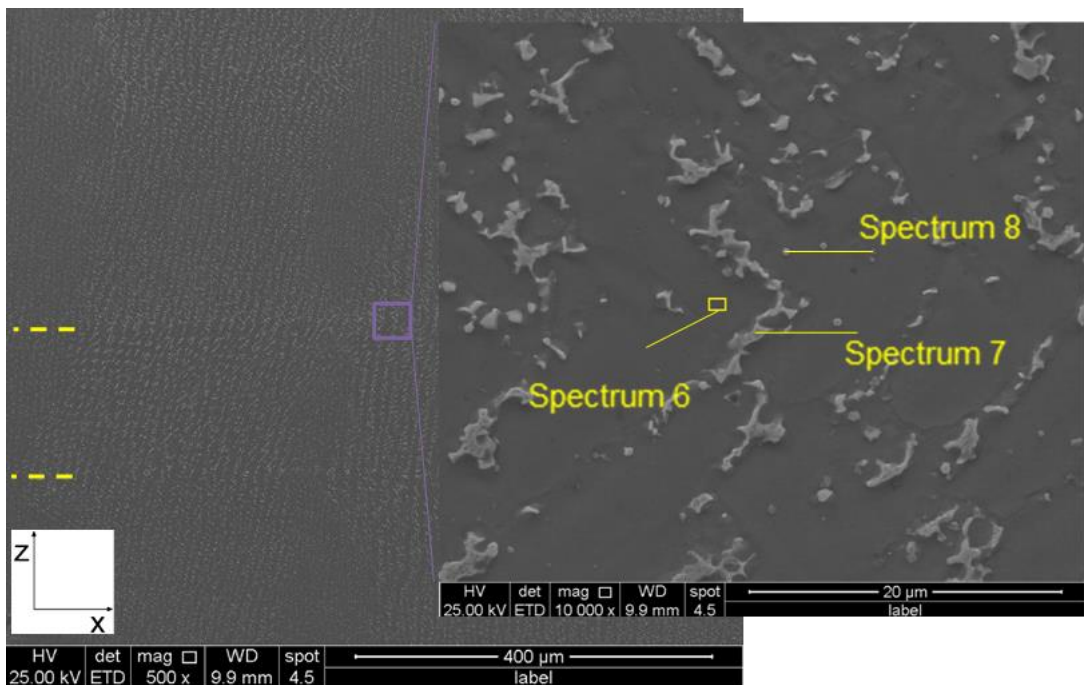


Figure 72: Secondary electron SEM image of the xz-plane of set 5 large. The layers are indicated. The right-hand image is an SEM image at a higher magnification, showing that the white phase is present at the point of layers meeting.

The dark phase surrounding the white phase was more visible in small blocks 4, 9, and 10. Dark regions contained within the white phase are also present. These are indicated in Figure 73 and Figure 74 – a backscatter image. Arrow 1 indicates the matrix; 2 the white phase; 3 the phase surrounding the white phase; 4 the phase within the white phase; 5 a dark precipitate or void. EDX maps corresponding to the backscatter image are shown (Figure 75).

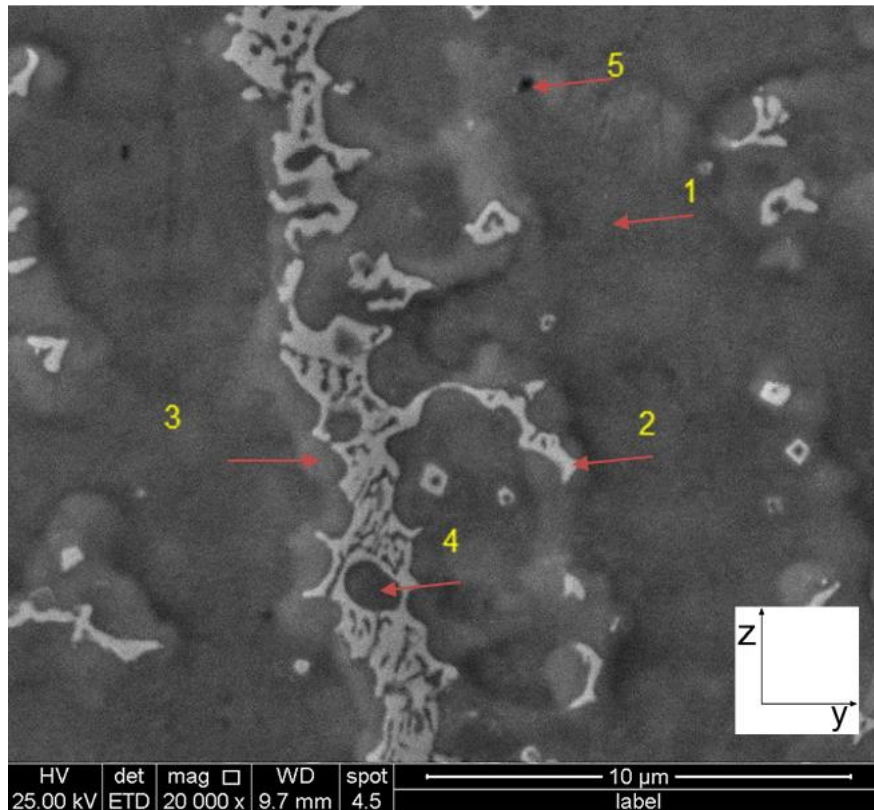


Figure 73: Secondary electron SEM image of the yz-plane of set 10 small. 4 phases that are present within the sample are indicated by the arrows. 1 indicates the matrix; 2 the white phase; 3 the phase surrounding the white phase; 4 the phase within the white phase; 5 a dark precipitate or void.

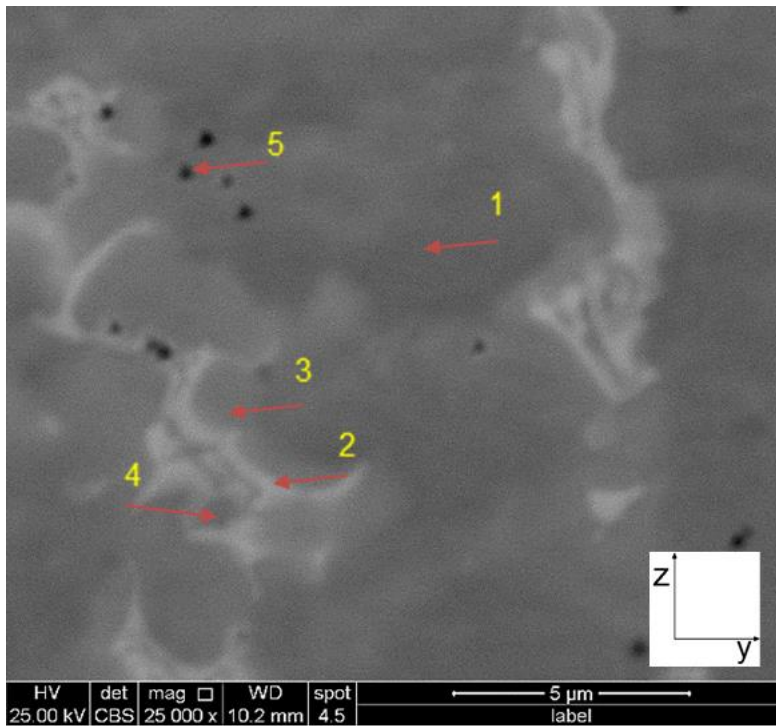


Figure 74: Backscatter electron SEM image of the yz-plane of set 9 small. 4 phases that are present within the sample are indicated by the arrows. 1 indicates the matrix; 2 the white phase; 3 the phase surrounding the white phase; 4 the phase within the white phase; 5 a dark precipitate or void.

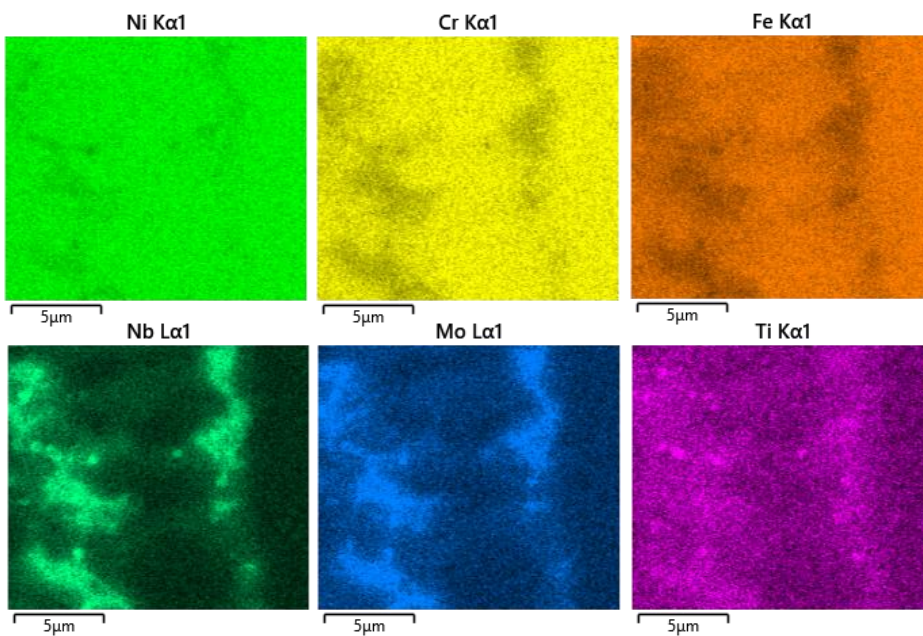


Figure 75: EDX maps of the SEM image in Figure 74. Elemental segregation can be seen to have occurred.

4.1.3 Tensile Testing

Results for tensile tests are displayed in Table 31, Table 32, Figure 76, Figure 77, and Figure 78. All results are valid as they show small values of standard deviation. The location of tensile specimens taken relative to the laser and scan path direction is shown previously, in Figure 45. Horizontal tensile values were significantly greater than vertical tensile values, indicating orientation of tensile specimen strongly influences tensile properties. Other significant differences can also be seen within the graphs.

| Set | 0.2% proof stress (MPa) | | | | UTS (MPa) | | | |
|-----------|-------------------------|----------|----------|----------|------------|----------|----------|----------|
| | Horizontal | Std dev. | Vertical | Std dev. | Horizontal | Std dev. | Vertical | Std dev. |
| 4 | 700 | 27.9 | 497 | 9.7 | 927 | 65.4 | 741 | 16.4 |
| 5 | 614 | 27.1 | 482 | 17.0 | 959 | 17.1 | 786 | 9.9 |
| 9 | 595 | 23.2 | 472 | 12.6 | 920 | 5.8 | 814 | 3.3 |
| 10 | 595 | 22.0 | 462 | 9.3 | 957 | 18.8 | 804 | 3.8 |

Table 31: Mean values obtained for 0.2% proof stress and UTS through tensile testing. Standard deviation is shown.

| Set | Elongation (%) | | | |
|-----|----------------|----------|----------|----------|
| | Horizontal | Std dev. | Vertical | Std dev. |
| 4 | 11.3 | 3.4 | 38.7 | 5.5 |
| 5 | 22.6 | 3.1 | 35.5 | 2.6 |
| 9 | 25.0 | 1.4 | 37.2 | 2.2 |
| 10 | 31.3 | 2.9 | 39.9 | 2.3 |

Table 32: Mean values obtained for elongation through tensile testing. Standard deviation is shown.

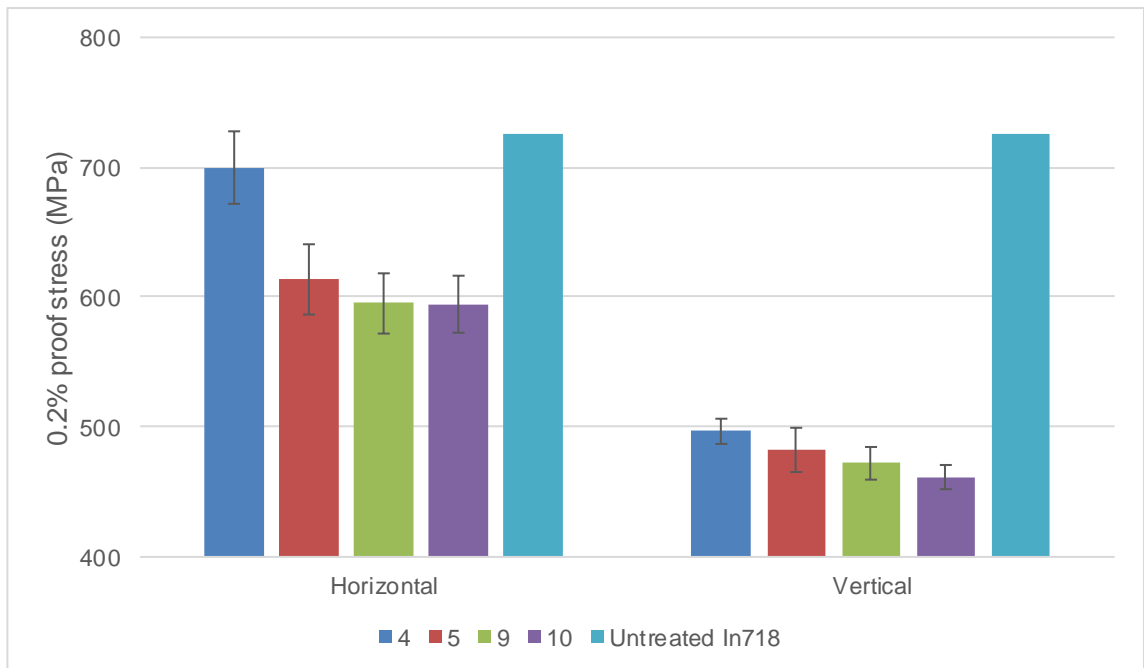


Figure 76: Graph showing the mean values obtained for 0.2% proof stress. Standard deviation error bars are shown. Values for untreated wrought Inconel 718 are included for comparison.

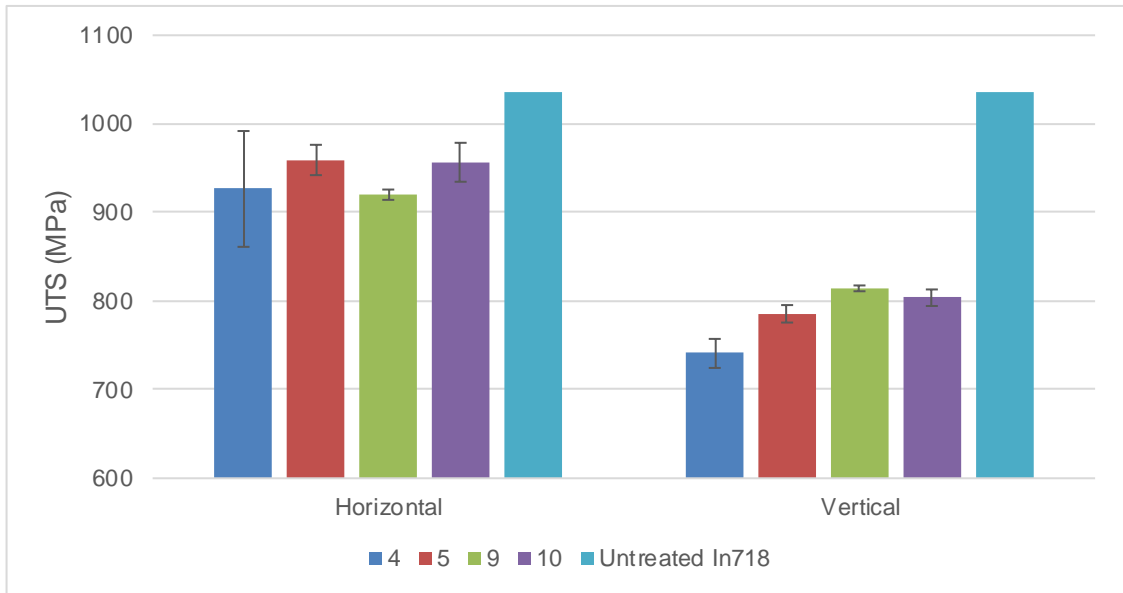


Figure 77: Graph showing the mean values obtained for UTS. Standard deviation error bars are shown. Values for untreated wrought Inconel 718 are included for comparison.

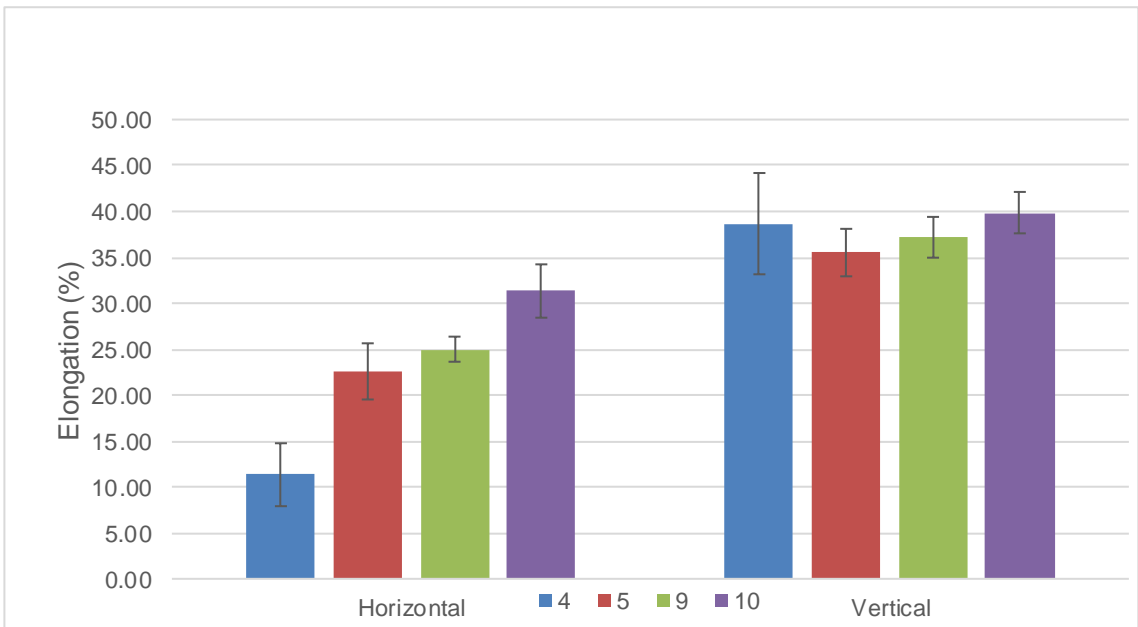


Figure 78: Graph showing the mean values obtained for elongation during tensile testing. Standard deviation error bars are shown.

The difference in 0.2% proof stress and UTS values moving between individual results for the horizontal and vertical tensile tests are shown in Table 33. This is to compare how the location of test specimen may have influenced strength. These values are less reliable as they refer to individual tensile specimens. H1 to H2 to H3 moves down the DED-L block, whilst V1 to V2 to V3 moves across from the outside edge to the middle of the block. 0.2% proof stress for horizontal tensile specimens is consistently greatest for specimen H3, with a possible decline in the middle H2 region (Figure 79). For all vertical specimens except set 9, 0.2% proof stress is greatest for V3, the middle region of the block (Figure 80). No consistent pattern can be seen for UTS when plotted graphically (Figure 81, Figure 82). H1 and V1 act as a baseline (0) for comparison of other tensile specimen values to.

| Set | 0.2% proof stress difference (MPa) | | | | UTS difference (MPa) | | | |
|-----------|------------------------------------|-------|-------|-------|----------------------|-------|-------|-------|
| | H1→H2 | H1→H3 | V1→V2 | V1→V3 | H1→H2 | H1→H3 | V1→V2 | V1→V3 |
| 4 | +27 | +68 | -10 | +13 | +144 | -133 | -31 | -6 |
| 5 | -7 | +53 | -32 | +8 | +9 | +31 | +5 | +18 |
| 9 | -12 | +42 | -23 | -29 | +2 | +11 | +1 | -7 |
| 10 | -22 | +31 | +9 | +23 | -26 | +46 | +9 | -5 |

Table 33: The difference in 0.2% proof and UTS values moving between individual tensile specimen test results. H1 and V1 are used as the baseline for plotting values.

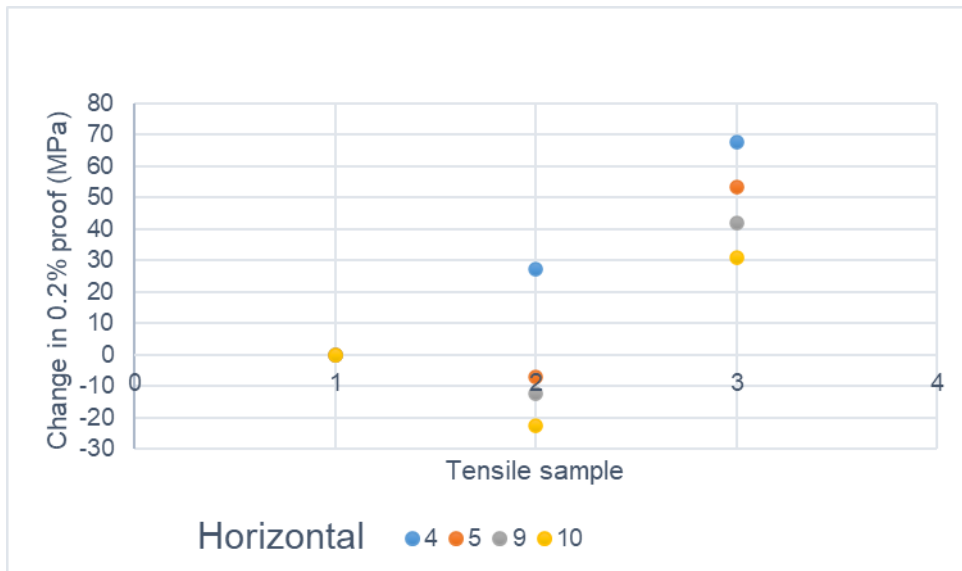


Figure 79: Graph displaying the difference in 0.2% proof stress value for horizontal tensile test specimens, moving from the top of the large DED-L block to the bottom. All number 1 tensile samples lie at 0 MPa.

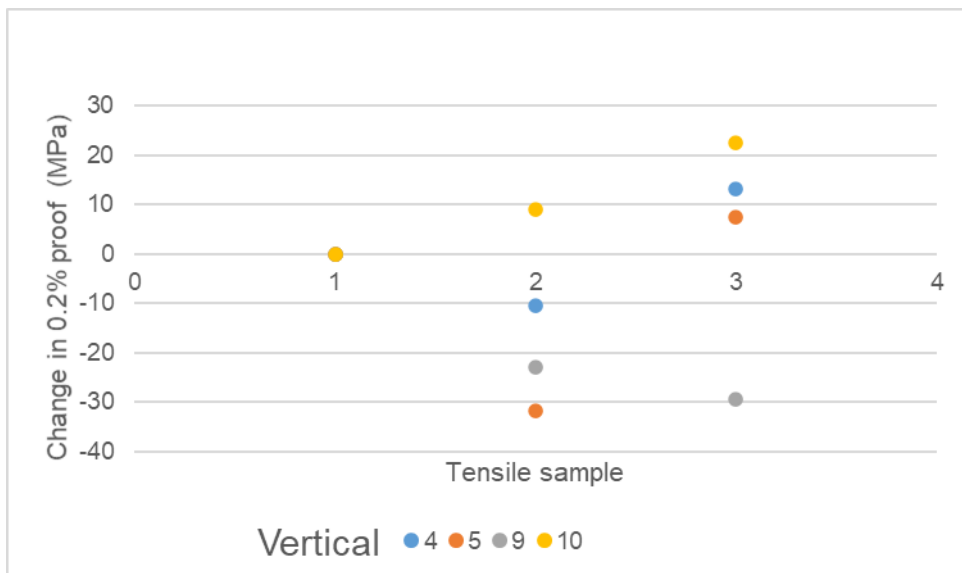


Figure 80: Graph displaying the difference in 0.2% proof stress value for vertical tensile test specimens, moving from the outer of the large DED-L block to the middle. All number 1 tensile samples lie at 0 MPa.

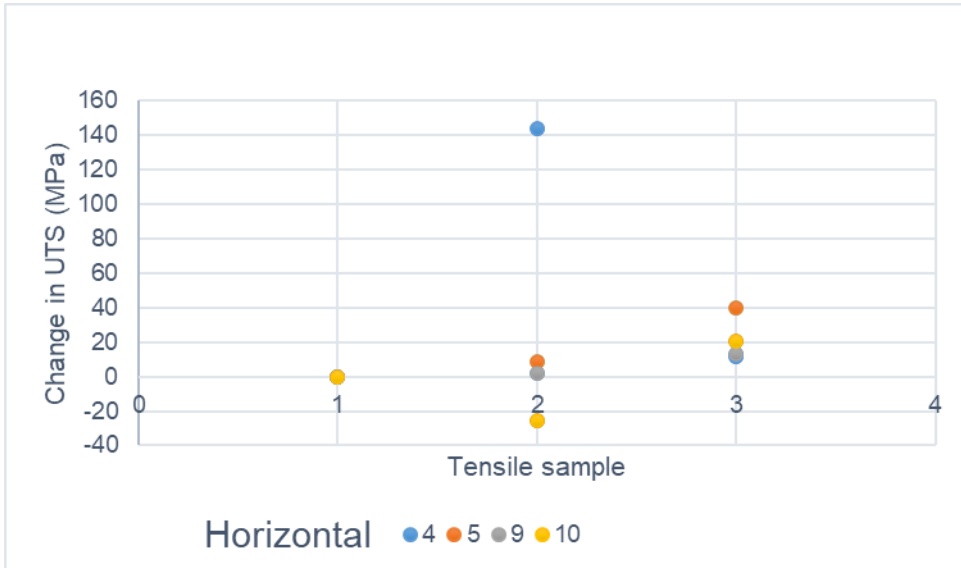


Figure 81: Graph displaying the difference in UTS value for horizontal tensile test specimens, moving from the top of the large DED-L block to the bottom.

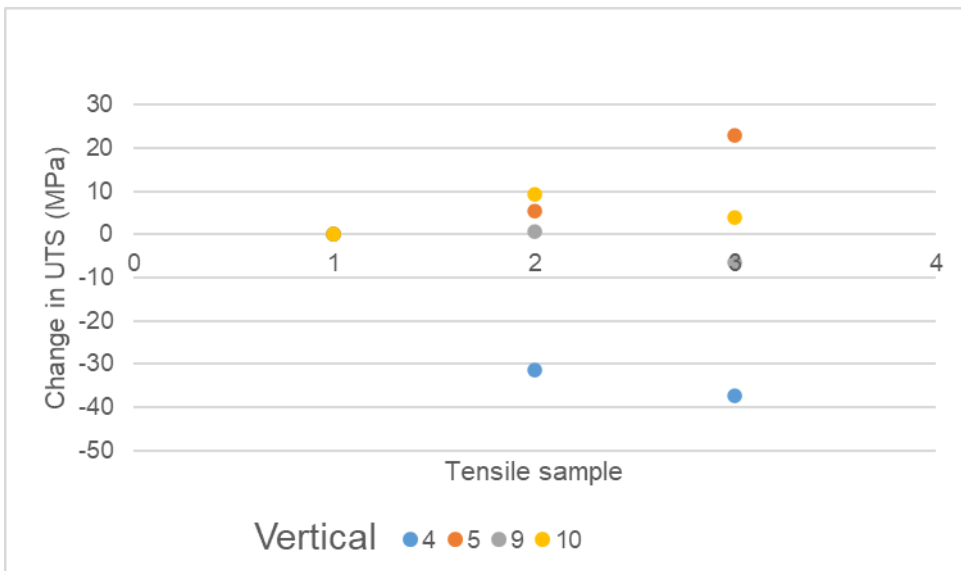


Figure 82: Graph displaying the difference in UTS value for vertical tensile test specimens, moving from the outer of the large DED-L block to the middle.

4.1.3.1 Fractography

Visual examination of fracture faces for all tensile specimens found no presence of oxidation following tensile testing. The cross sectional area of the fractured specimen decreased as the gauge length of the tensile specimen elongated. Plastic deformation was observable on the outside surface of the specimen and shear lips on the fracture surface could be seen (Figure 83, Figure 84).

At lower magnification, all specimens have a jagged appearance, with horizontal fracture surfaces appearing more jagged than vertical fracture surfaces, which have a flatter appearance towards the specimen centre. Coarse intergranular regions with step-like features, and dimpled regions are observable.

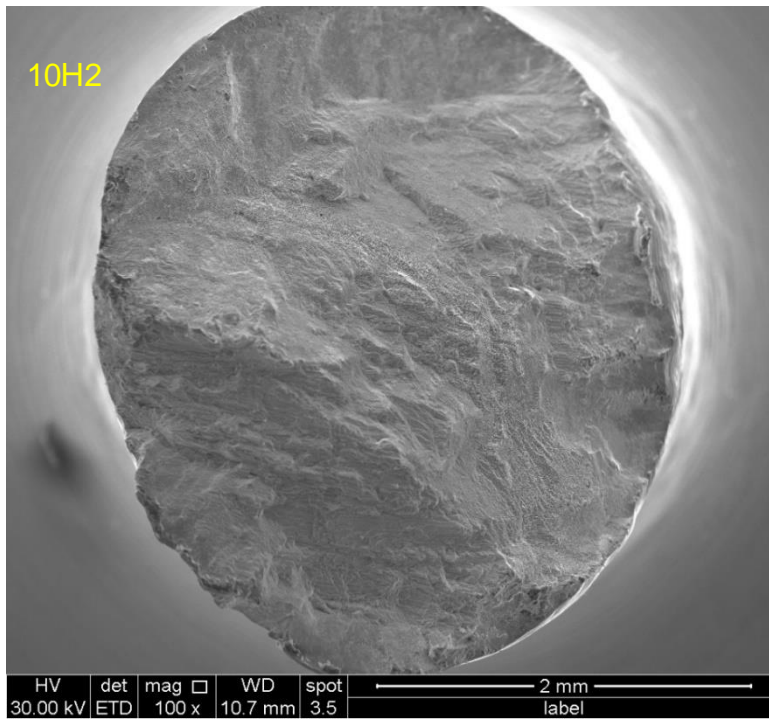


Figure 83: Secondary electron SEM image of the fracture surface of tensile specimen H2 from set 10 large. This horizontal fracture surface is rough and jagged.

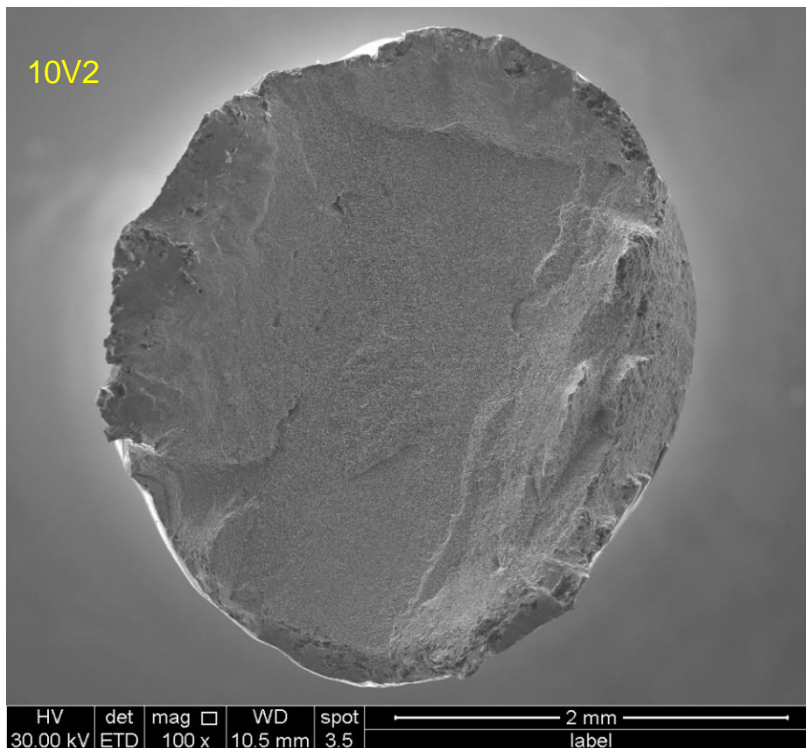


Figure 84: Secondary electron SEM image of the fracture surface of tensile specimen V2 from set 10 large. This vertical fracture surface is rough and jagged but flatter towards the centre than the previously shown Horizontal tensile specimen fracture surface.

Under higher magnification, features observed across the fracture face include step-like features, tearing ridges, microvoid coalescence, Al-oxide inclusions (confirmed by EDX analysis), cracks, and shear deformation. These are indicated in Figure 85, Figure 86, Figure 87, Figure 88, and Figure 89.

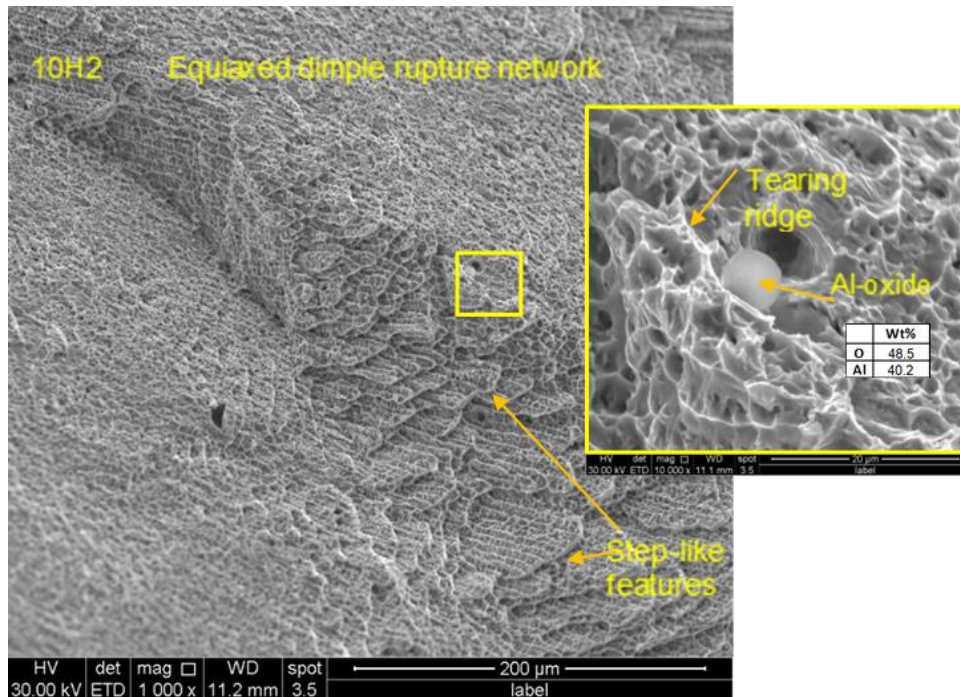


Figure 85: Secondary electron SEM images of tensile specimen 10H2. An equiaxed dimple rupture network can be seen. Step-like features, tearing ridges and an Al-oxide are labelled.

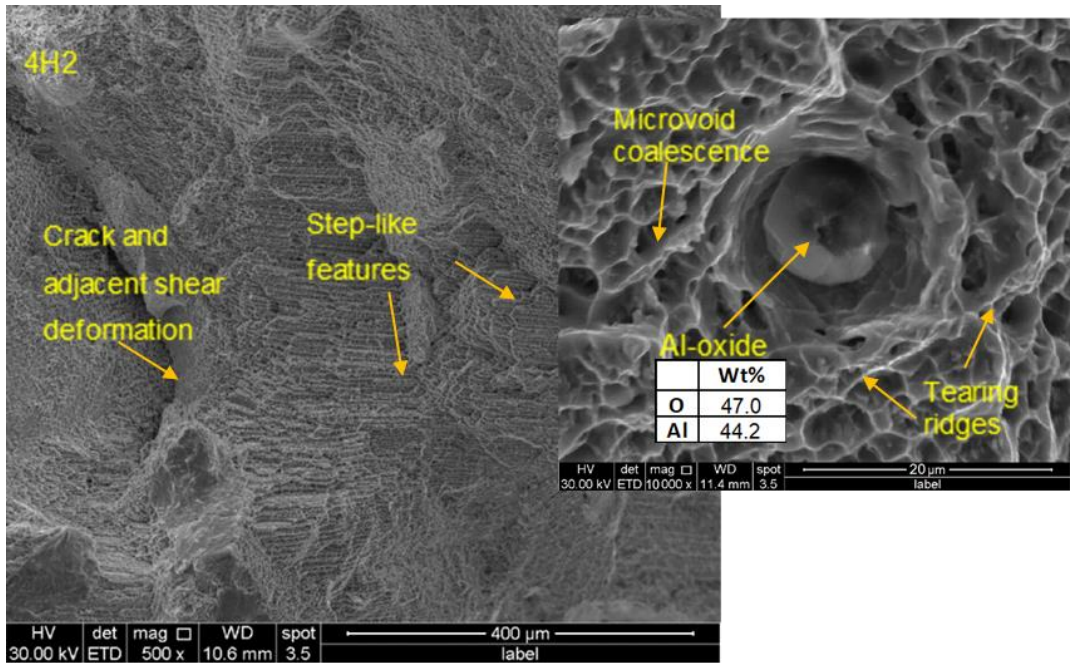


Figure 86: Secondary electron SEM images of tensile specimen 4H2. A crack, shear deformation, step-like features, microvoid coalescence, tearing ridges and an Al-oxide are labelled.

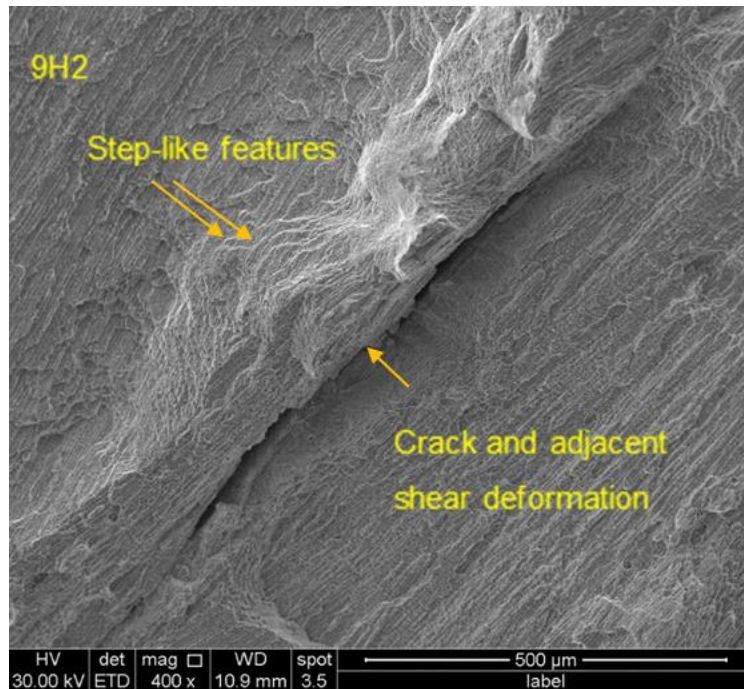


Figure 87: Secondary electron SEM image of tensile specimen 9H2. A crack, adjacent shear deformation, and step-like features are labelled.

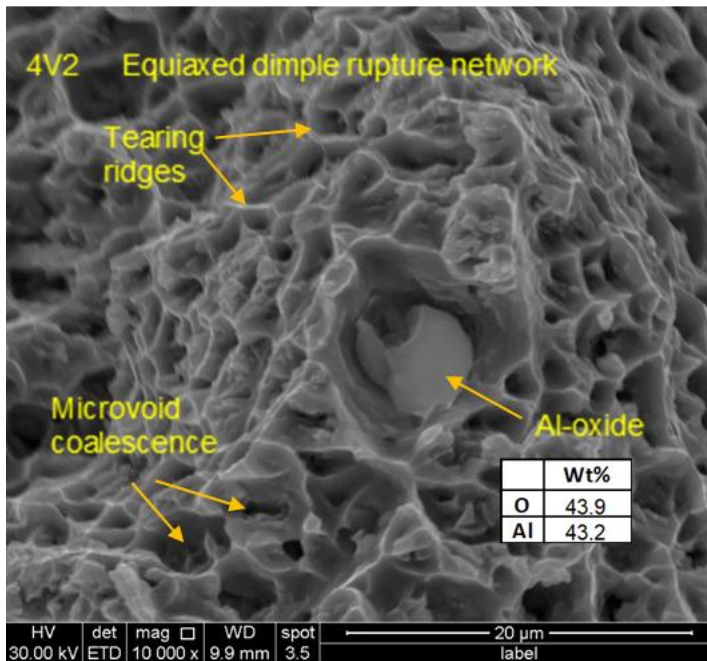


Figure 88: Secondary electron SEM image of tensile specimen 4V2. An equiaxed dimple rupture network containing microvoid coalescence (labelled) can be seen. Tearing ridges and an Al-oxide are labelled.

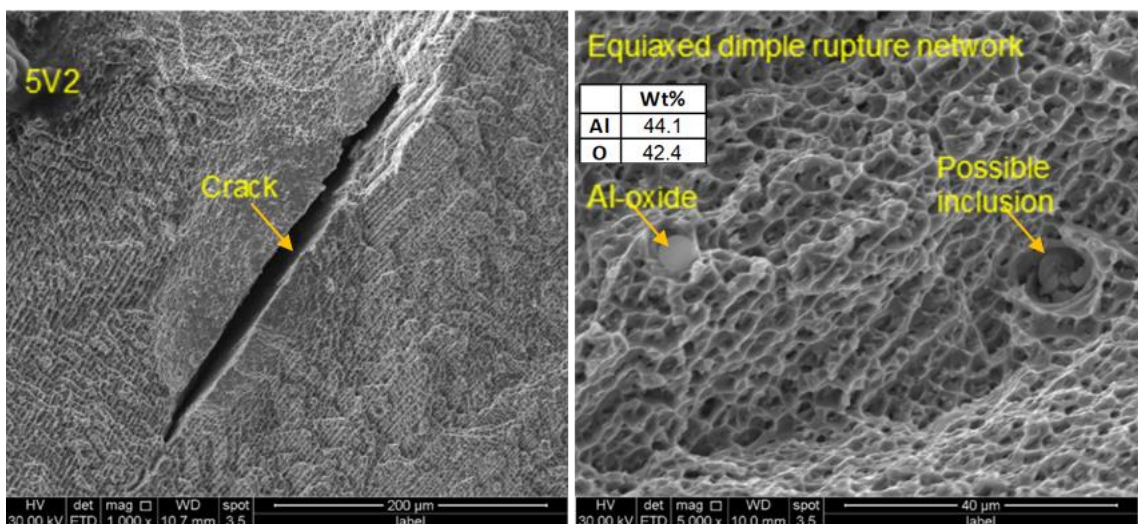


Figure 89: Secondary electron SEM images of tensile specimen 5V2. An equiaxed dimple rupture network containing microvoid coalescence is seen. A crack, Al-oxide and possible inclusion are labelled.

4.1.4 Vickers Hardness

Mean macrohardness and microhardness results, and standard deviation for the sample sets are shown in Table 34 and Figure 90. All results are valid as they show small values of standard deviation. Small block macrohardness was lower than small block microhardness, with the most notable difference present in set 4. Apart from set 5, small block macro/microhardness values were greater than values obtained for the large blocks. All values exceed standard Vickers Hardness for solution annealed Inconel 718 (246 HV) but are below solution annealed and aged Inconel 718 (385 HV) – except for small block microhardness which takes a value of 385 HV_{0.5}.

| | Small block | | | | Large block | | | |
|-----|-----------------------------------|----------|------------------------------------|----------|-----------------------------------|----------|------------------------------------|----------|
| Set | Macrohardness (HV ₁₀) | Std dev. | Microhardness (HV _{0.5}) | Std dev. | Macrohardness (HV ₁₀) | Std dev. | Microhardness (HV _{0.5}) | Std dev. |
| 4 | 304 | 10.0 | 385 | 39.3 | 282 | 8.3 | 271 | 9.8 |
| 5 | 274 | 6.4 | 299 | 20.0 | 278 | 6.1 | 274 | 13.3 |
| 9 | 307 | 7.3 | 344 | 27.5 | 288 | 4.4 | 266 | 8.4 |
| 10 | 308 | 13.2 | 333 | 32.0 | 285 | 10.1 | 265 | 8.1 |

Table 34: Mean values obtained for Vickers macro/microhardness. Standard deviation is shown.

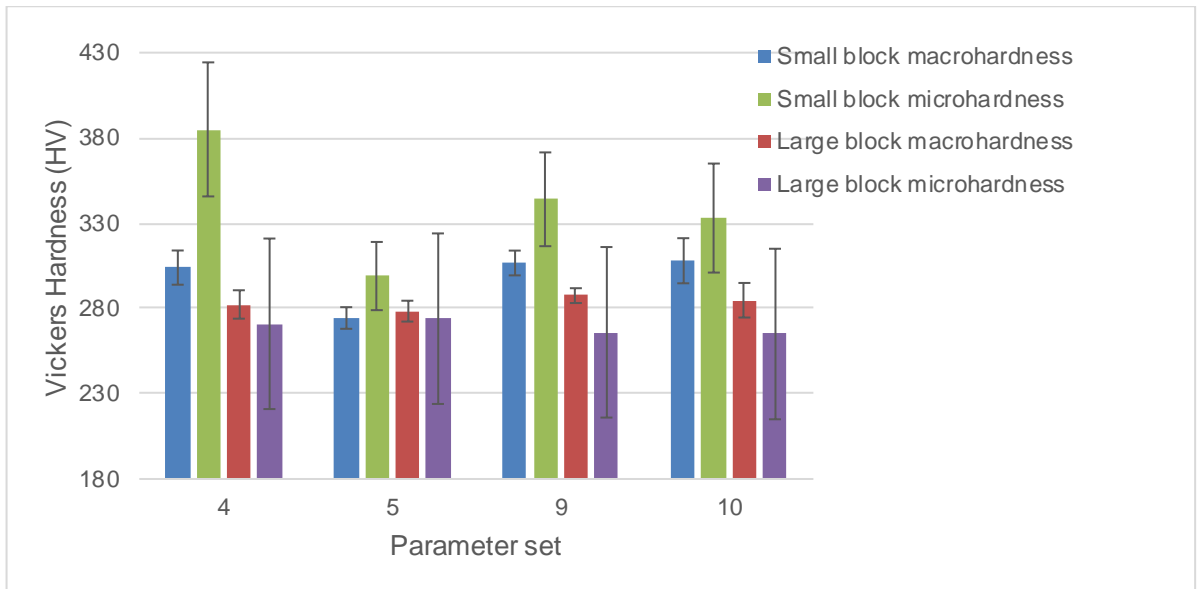


Figure 90: Graph showing mean Vickers macrohardness (HV_{10}) and microhardness ($HV_{0.5}$) for the small and large blocks. Standard deviation error bars are shown.

Microhardness maps for the cross sections of the small and large blocks are shown in Figure 91 and Figure 92. These maps show some variation between the small blocks for the four parameter sets, variation in microhardness within a sample map can also be seen. Less variation in values can be seen in the map for set 5 small and set 10 large.

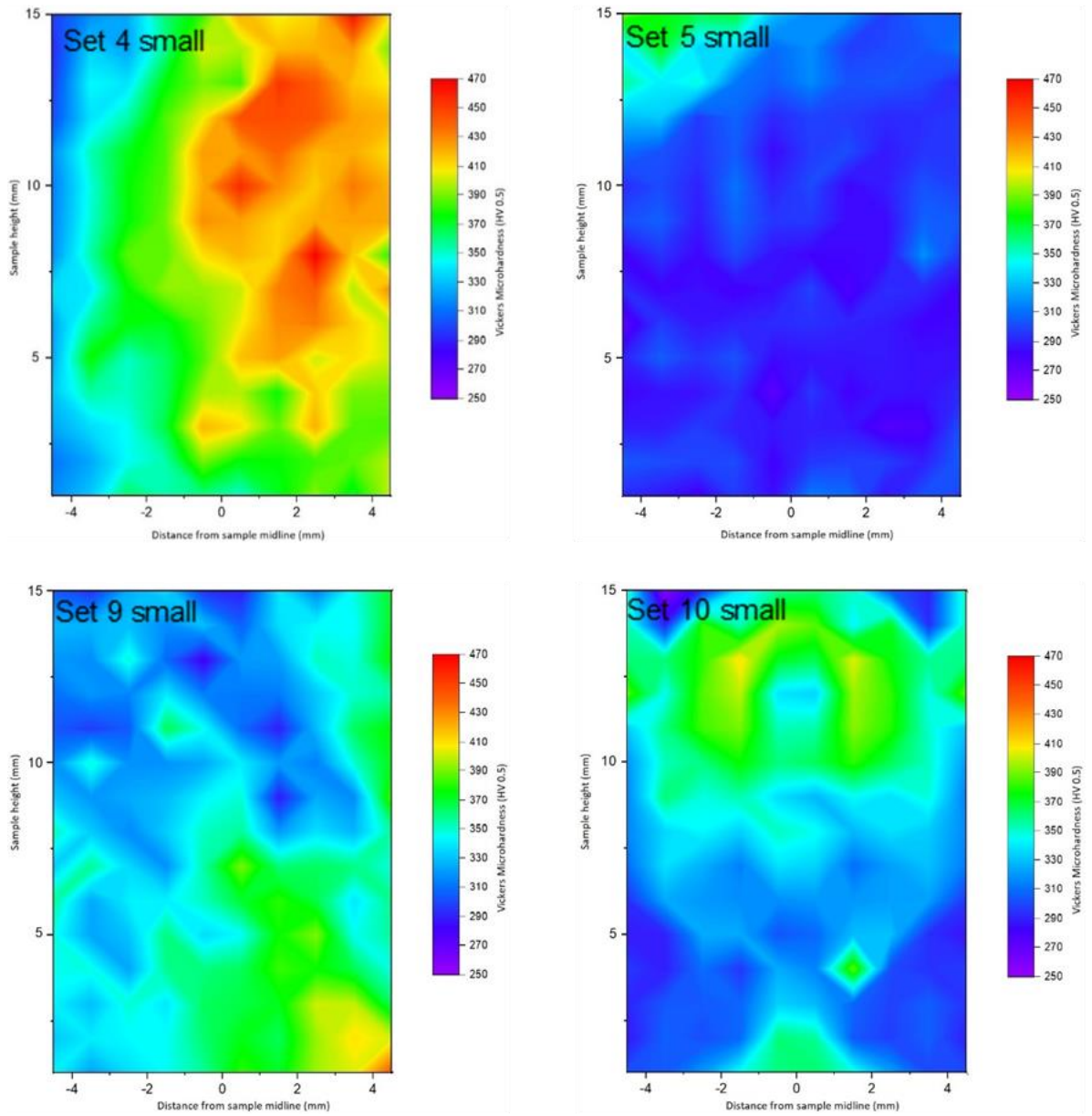


Figure 91: Microhardness maps plotted for each of the small blocks (cross section in the yz-plane).

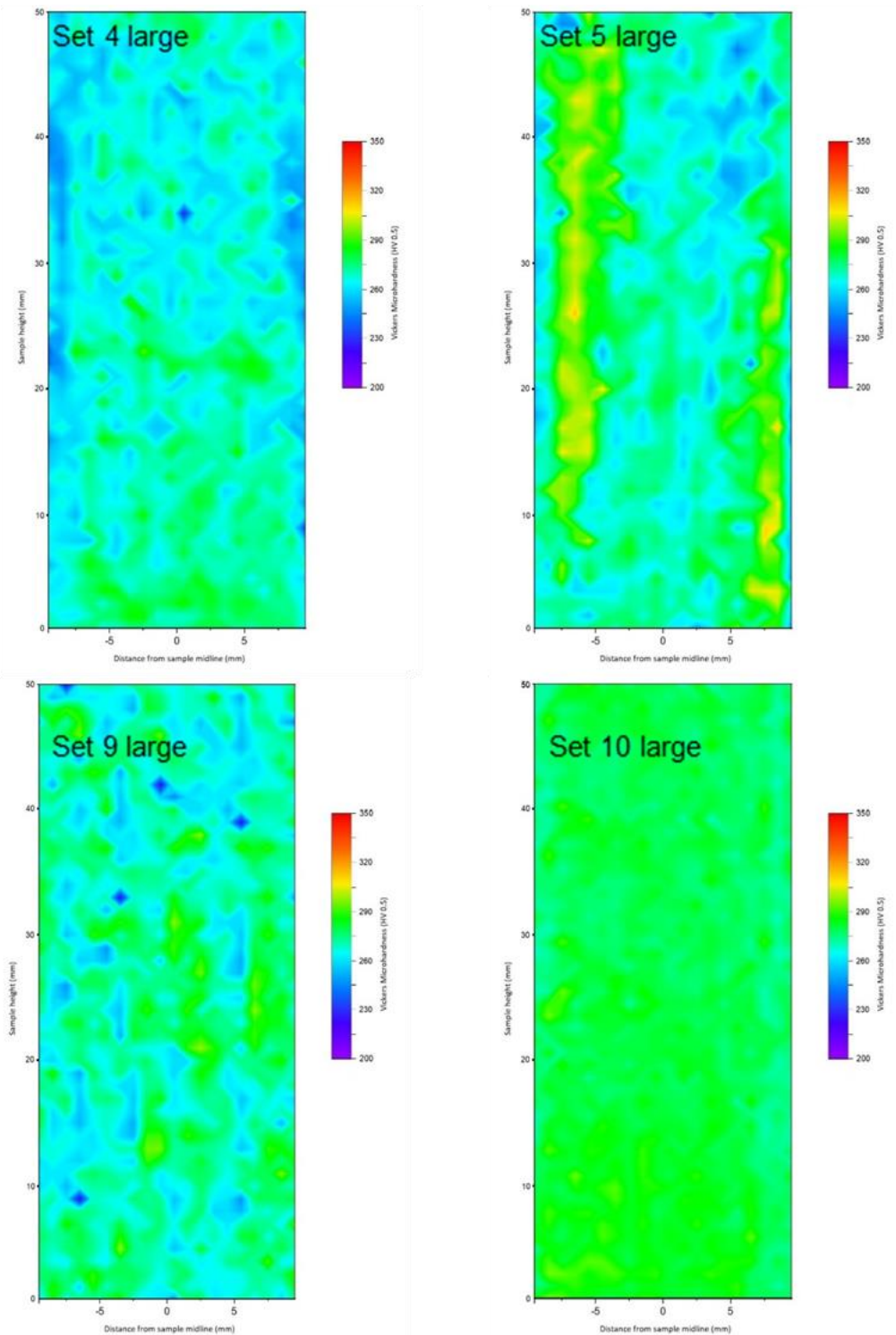


Figure 92: Microhardness maps plotted for each of the large blocks (cross section in the yz-plane).

4.1.5 Powder capture efficiency

Average powder capture efficiency based on the time to build each large block and total scan path distance is shown in Table 35. Inconel 718 has a density of 8.19 g/cm³ (SAE International, 2016), therefore a fully dense block with the dimensions used within this stage of work should weigh 1.86 kg. The final weights obtained are all within 0.05 kg of this value.

| Set | Powder input (kg) - build time | Powder input (kg) - scan path distance | Large block weight (kg) | Process efficiency (%) |
|------------|---------------------------------------|---|--------------------------------|-------------------------------|
| 4 | 2.44 | 2.25 | 1.85 | 78.99 |
| 5 | 2.40 | 2.07 | 1.87 | 83.63 |
| 9 | 1.83 | 1.80 | 1.81 | 99.91 |
| 10 | 2.20 | 1.89 | 1.81 | 88.42 |

Table 35: Values obtained for powder input, block weight, and calculated process efficiency for each large block.

4.2 Stage 2 – Investigation into anisotropy within a single DED-L part

4.2.1 Optical Light Microscopy

Specimens displayed no visible evidence of cracks prior to etching. Porosity was measured to be 0.03% (standard deviation: 0.02%).

Figure 93 shows a 3 mm × 3 mm × 2.5 mm section of the sample. OLM revealed the microstructure to vary between the three planes.

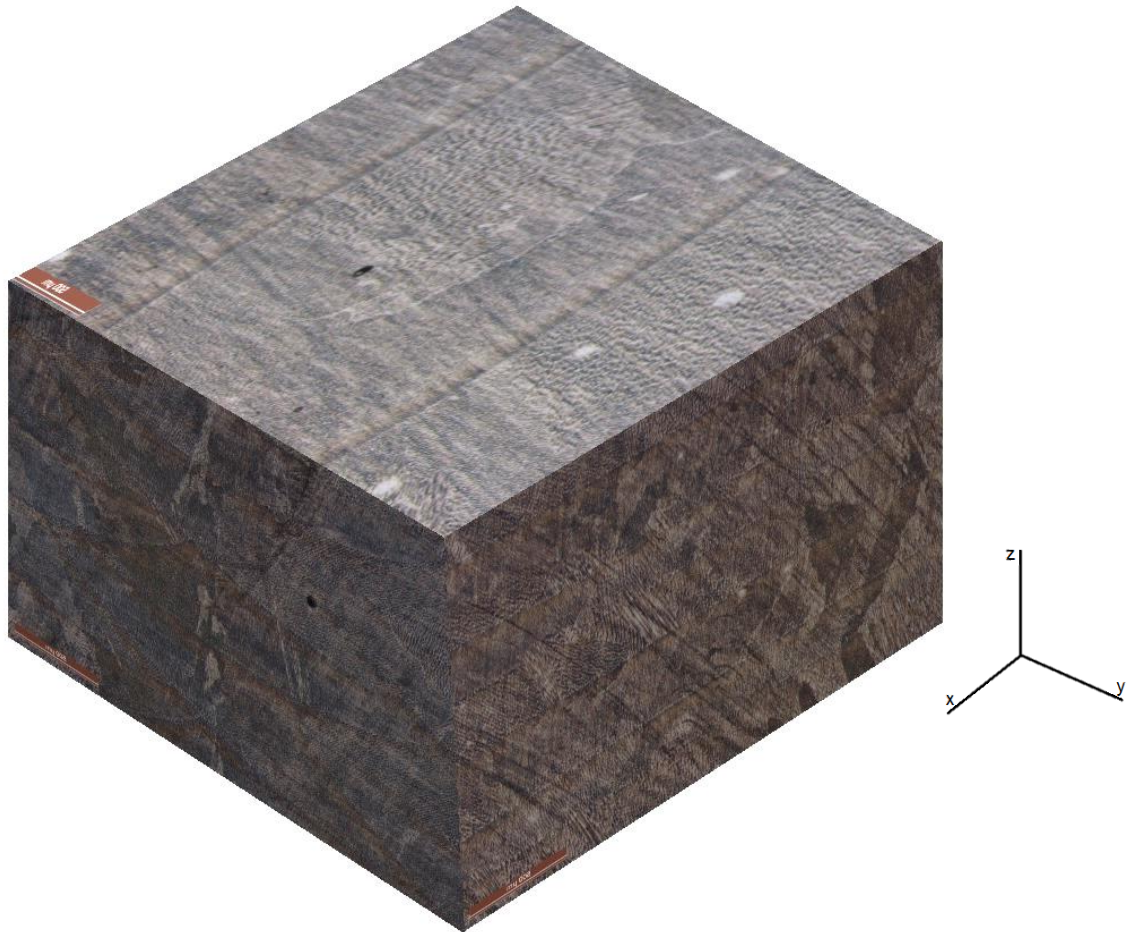


Figure 93: Optical micrograph of a 3-dimensional section of the sample. Differences between all three planes can be seen.

Individual deposited layers and tracks were visible in the etched sample, these are indicated by the yellow dashed lines on Figure 94. Columnar grains which had grown upwards towards the laser can also be observed, these are outlined in Figure 94 in blue.



Figure 94: Optical micrograph of the xz -plane where grains (outlined in blue) grew upwards through multiple layers (indicated by the yellow lines).

Some of the grains in the xz -plane could be seen to grow in a zig-zag pattern upwards (Figure 95), however this was not consistent through the sample and only occurred in certain regions. This is due to the x -direction which the material was deposited in alternating from the positive x -direction to the negative x -direction between layers.

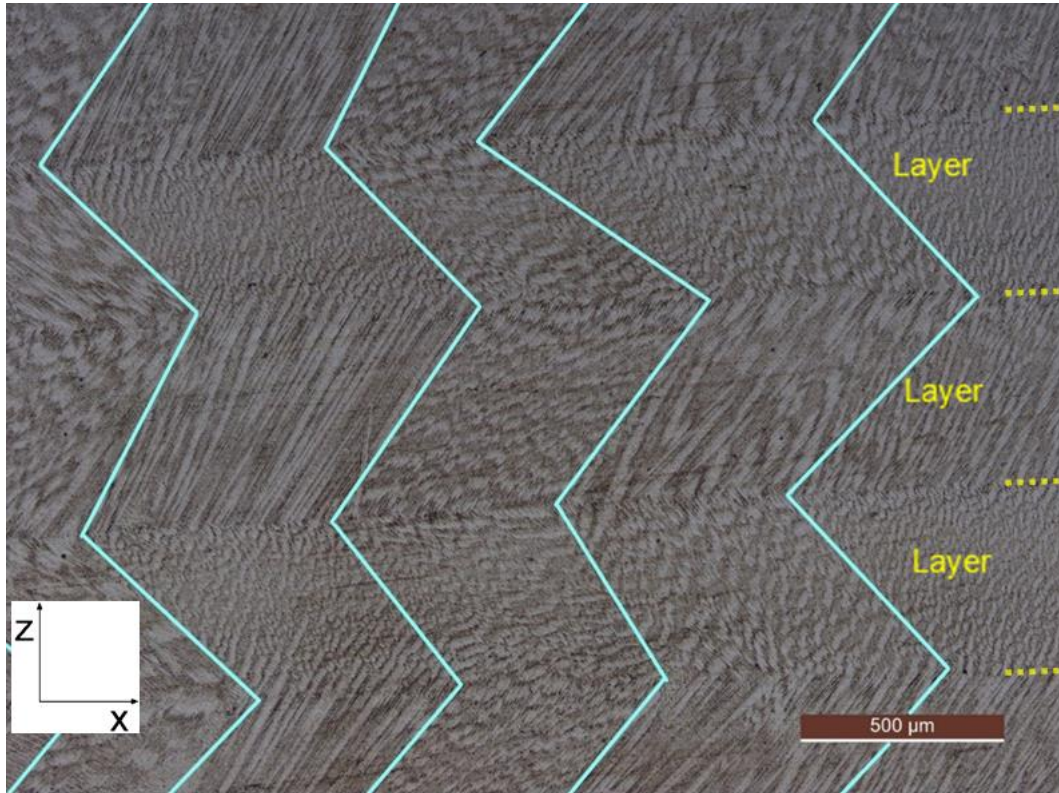


Figure 95: Optical micrograph of the xz -plane where grains (outlined in blue) grew upwards through multiple layers (indicated by the yellow lines) in a zig-zag pattern.

In the yz -plane the cross section of each deposited track could be seen (Figure 96) with grains extending across multiple layers and tracks. A difference in contrast is present in these images at the meeting point between adjacent tracks and layers. A variation in phase distribution can be observed at this meeting point, with a refinement in phases seen in heat-affected regions.

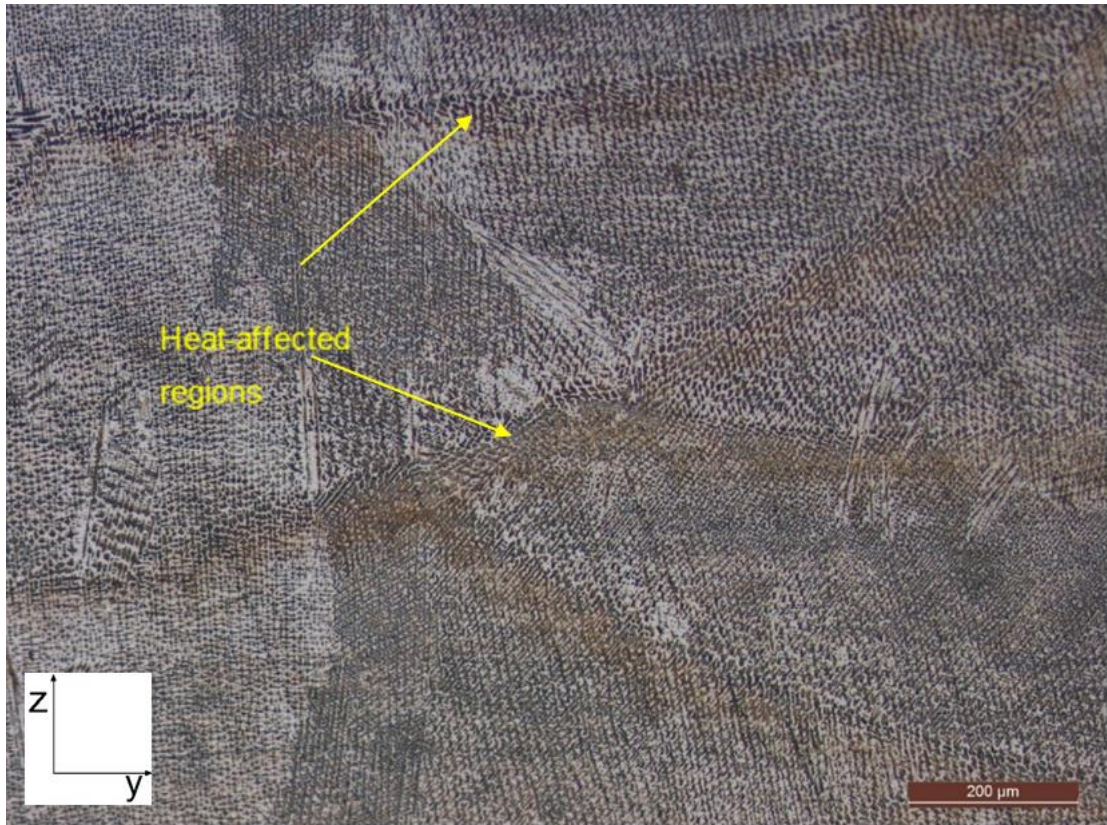


Figure 96: Optical micrograph of the yz -plane. Track meeting points can be seen. Heat-affected regions where phase refinement has occurred is shown.

Figure 97 highlights the change in microstructure from dendritic to refined to dendritic in the xz -plane at the interface between two layers. The refined region corresponds to the region which is heat-affected during the deposition of a subsequent layer. This heat-affected region measures $60\ \mu\text{m}$ in thickness (layer thickness is $450\ \mu\text{m}$, thus this region forms 13% of each layer). Comparison to images in Table 9 suggests that the light areas are most likely Ni-rich solid solution (γ -phase) and the dark areas precipitates such as primary and secondary carbides. Laves phase may be present within the dark areas, as Table 9 shows Laves phase to be surrounded by a dark region.

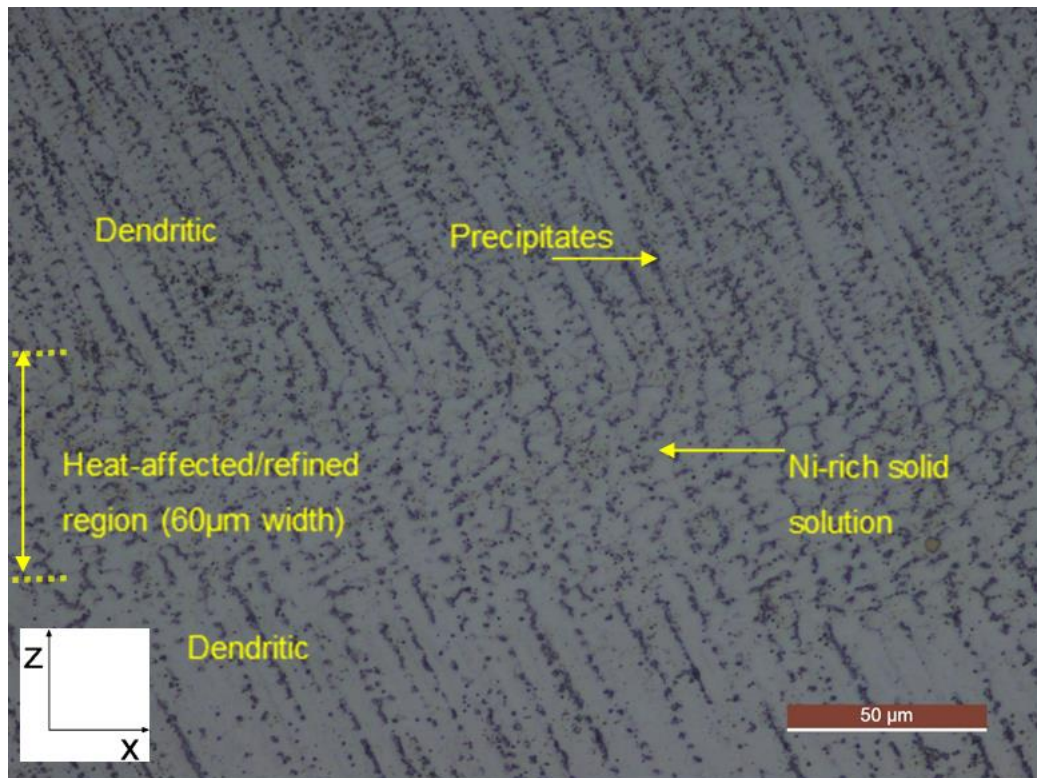


Figure 97: Higher magnification optical micrograph of the xz-plane. A variation in phase distribution can be seen moving across the heat-affected region. Possible phases – Ni-rich solid solution and precipitates – are indicated.

4.2.2 Scanning Electron Microscopy

Under the SEM a white phase was observed to form a discontinuous network through the samples (Figure 98). EDX point analysis found the white phase to be high in Nb, consistent with previous results. Small precipitates were also found. The corresponding EDX point analysis results are presented in Table 36.

| | Element Wt% | | | | | | |
|-------------------|-------------|-------|-------|------|------|------|------|
| | Ni | Fe | Cr | Nb | Mo | Ti | Al |
| Powder | 53.15 | 18.77 | 18.30 | 5.08 | 2.97 | 0.95 | 0.52 |
| Spectrum 1 | 51.1 | 19.8 | 18.8 | 2.8 | 2.3 | 1.0 | 0.5 |
| Spectrum 2 | 39.6 | 13.3 | 13.9 | 14.5 | 3.3 | 1.0 | - |
| Spectrum 3 | 41.4 | 16.1 | 16.0 | 5.2 | 2.3 | 4.5 | 5.3 |

Table 36: The EDX point analysis results for Figure 98.

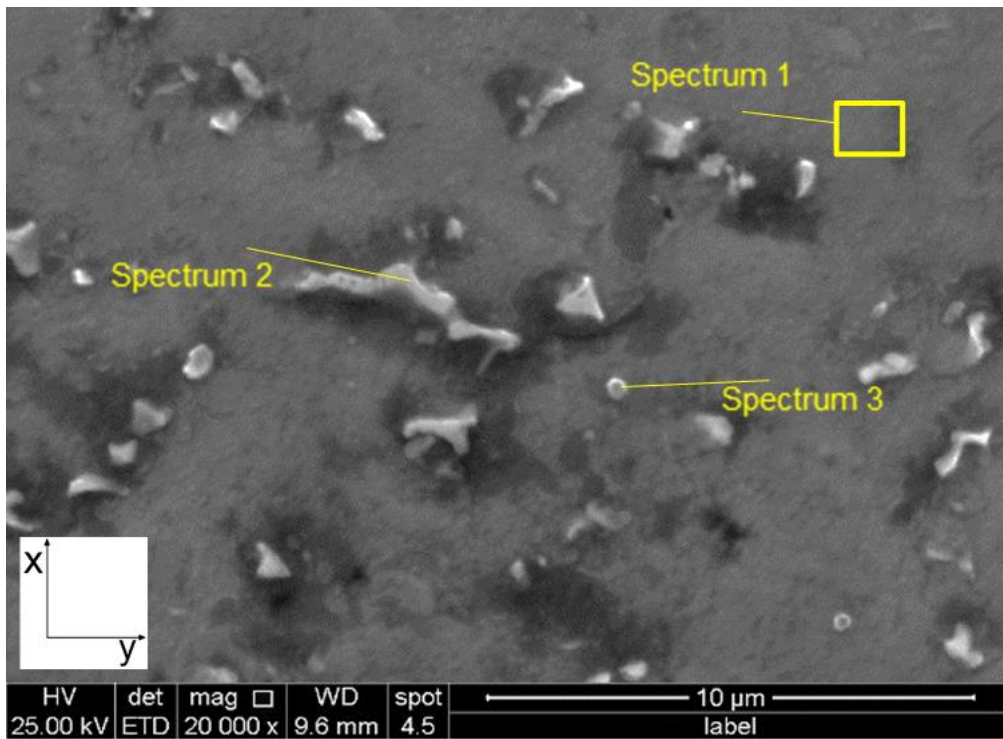


Figure 98: Secondary electron SEM image of the xy-plane showing the white phase and small precipitate.

An EDX map of a section of the yz-plane is shown, this shows elements to have segregated – predominantly Nb and Mo (Figure 99).

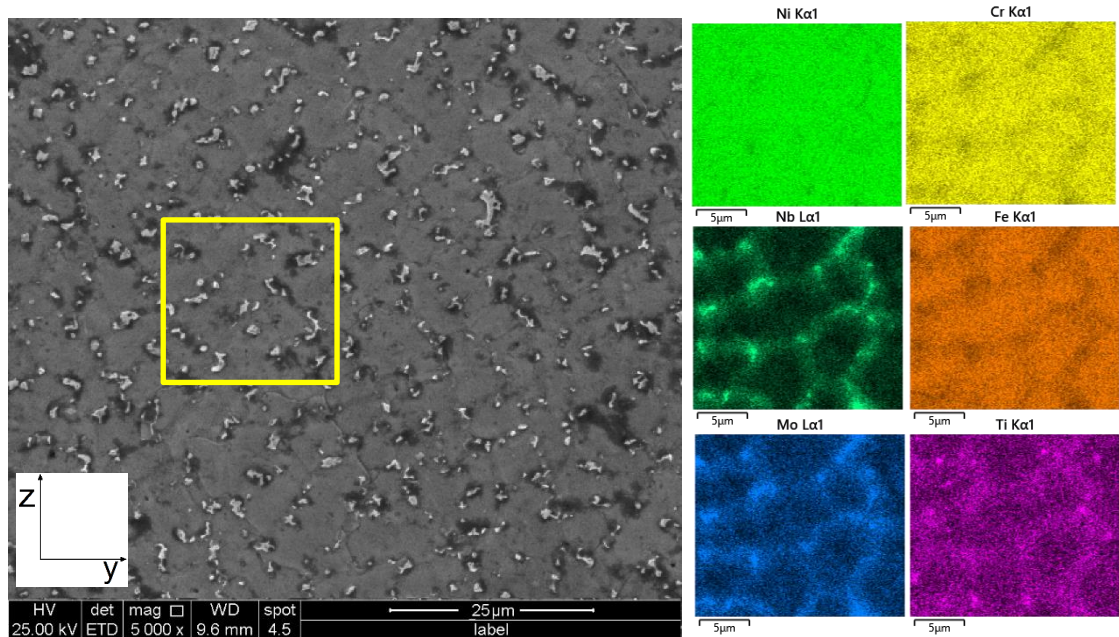


Figure 99: Secondary electron SEM image of the yz-plane where the white phase can be seen to have segregated. EDX maps of a smaller region of the image are shown.

4.2.3 Tensile Testing

The locations of tensile specimens taken relative to the laser and scan path direction are shown in Figure 100.

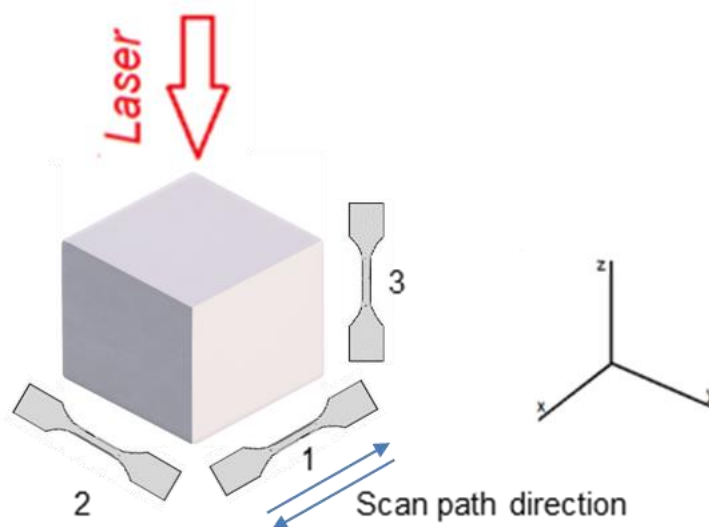


Figure 100: Schematic showing the locations of the tensile specimens with regards to the laser and scan path direction.

Tensile testing results are shown in Table 37, Figure 101, and Figure 102. All results are valid as they show small values of standard deviation. UTS and 0.2% proof stress of untreated Inconel 718 are shown for comparison. Sample 1 displayed the greatest tensile strength properties whilst sample 3 displayed the lowest. Values between samples differed significantly. Sample 3 had a significantly greater elongation value than samples 1 and 2, which were similar.

| Sample no. | 0.2% proof stress (MPa) | Std dev. | UTS (MPa) | Std dev. | Elongation (%) | Std dev. |
|------------|-------------------------|----------|-----------|----------|----------------|----------|
| 1 | 669 | 12.8 | 1013 | 18.7 | 18.8 | 1.9 |
| 2 | 601 | 35.5 | 831 | 17.6 | 17.9 | 2.4 |
| 3 | 535 | 7.3 | 781 | 1.1 | 33.2 | 0.3 |

Table 37: Mean values obtained from tensile testing. Values for standard deviation are shown.

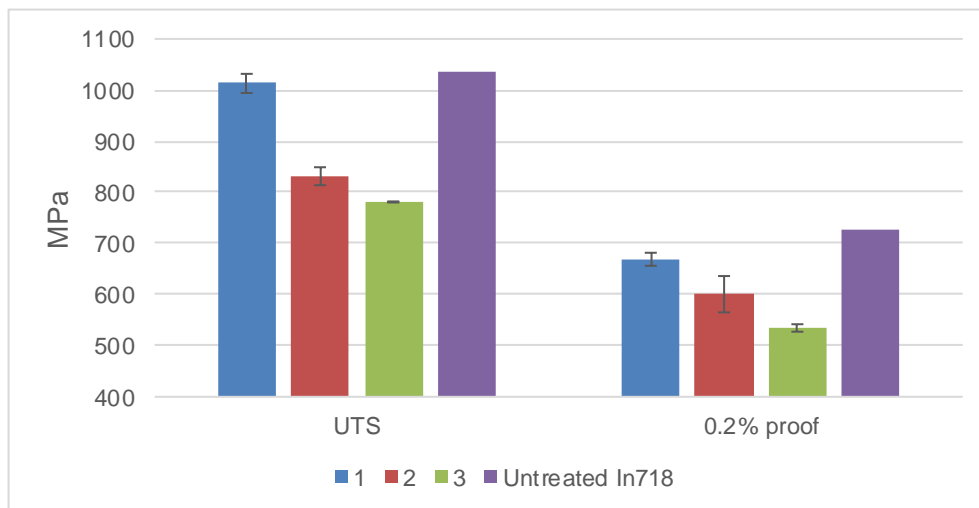


Figure 101: Graph displaying the mean results obtained for UTS and 0.2% proof stress. Standard deviation error bars are shown. Values for untreated wrought Inconel 718 are shown for comparison.

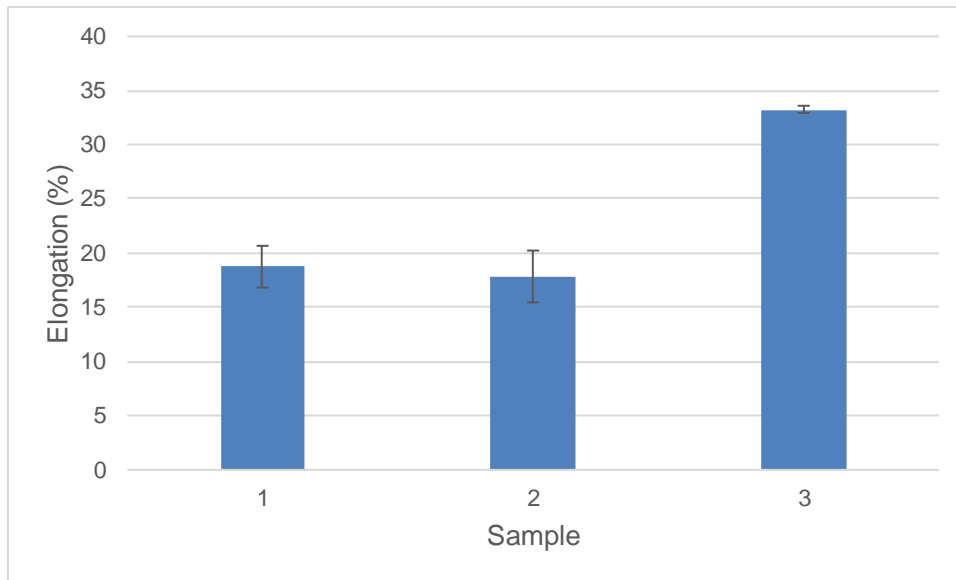


Figure 102: Graph showing mean elongation values obtained during tensile testing for samples.

4.2.3.1 Fractography

Visual examination of fracture faces for all tensile specimens found no presence of oxidation. Like the previous fractography results, cross sectional area of the tensile specimen decreased as the specimen gauge elongated. Again, plastic deformation was observable on the outside surface of the specimen and shear lips on the fracture surface could be seen.

At a lower magnification, the surface of specimens have a rough, jagged appearance displaying coarse intergranular regions with step-like features, and dimpled regions (Figure 103)

Under higher magnification features observed across the fracture face include step-like features, tearing ridges, microvoid coalescence, Al-oxide inclusions (confirmed by EDX analysis), cracks, and shear deformation (Figure 103, Figure 104, Figure 105).

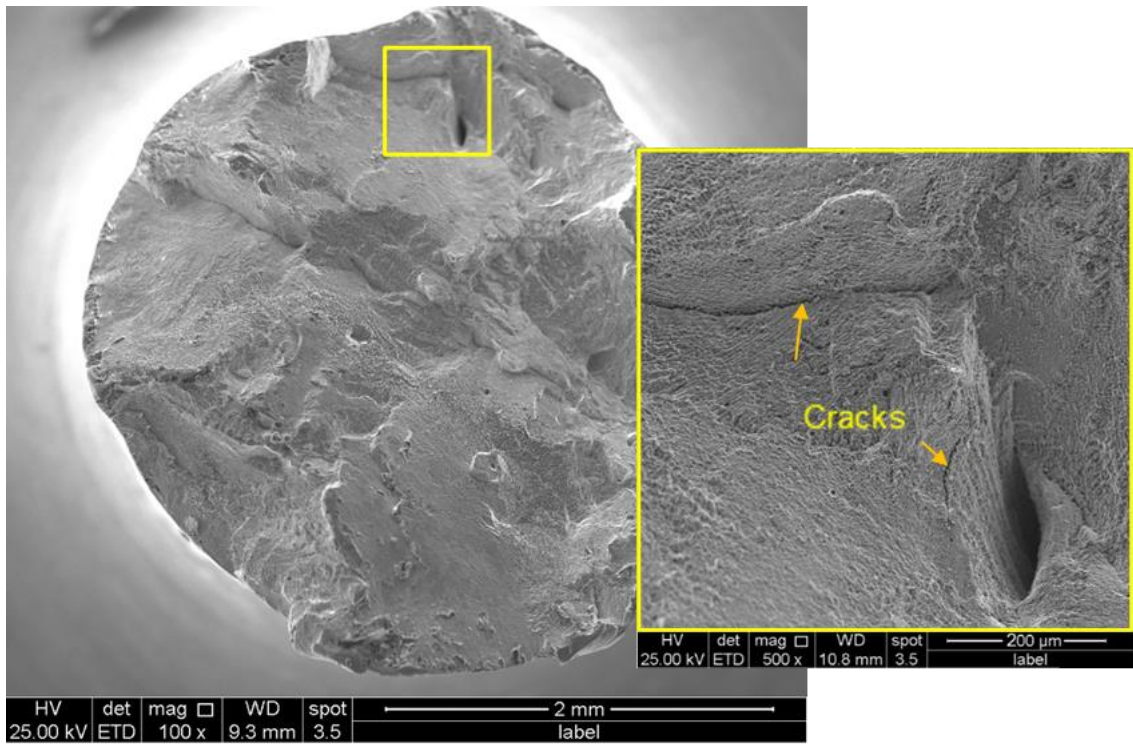


Figure 103: Secondary electron SEM image of a sample 1 fracture surface. and a higher magnification SEM image showing cracks in the sample surface.

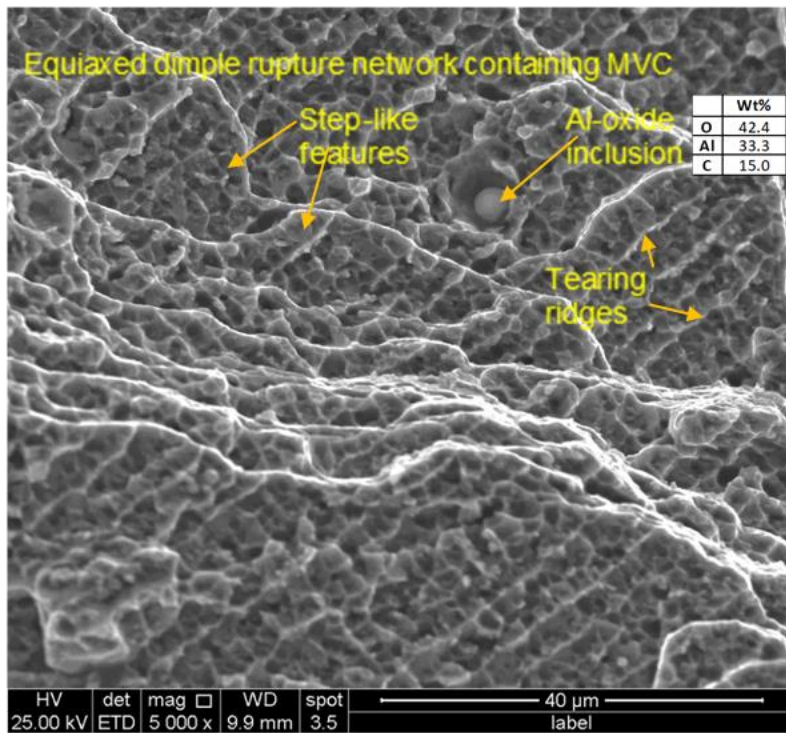


Figure 104: Higher magnification secondary electron SEM image of a sample 2 fracture surface. A network of equiaxed dimples containing microvoid coalescence is present. Step-like features, and tearing ridges (formed in uniform lines) are shown.

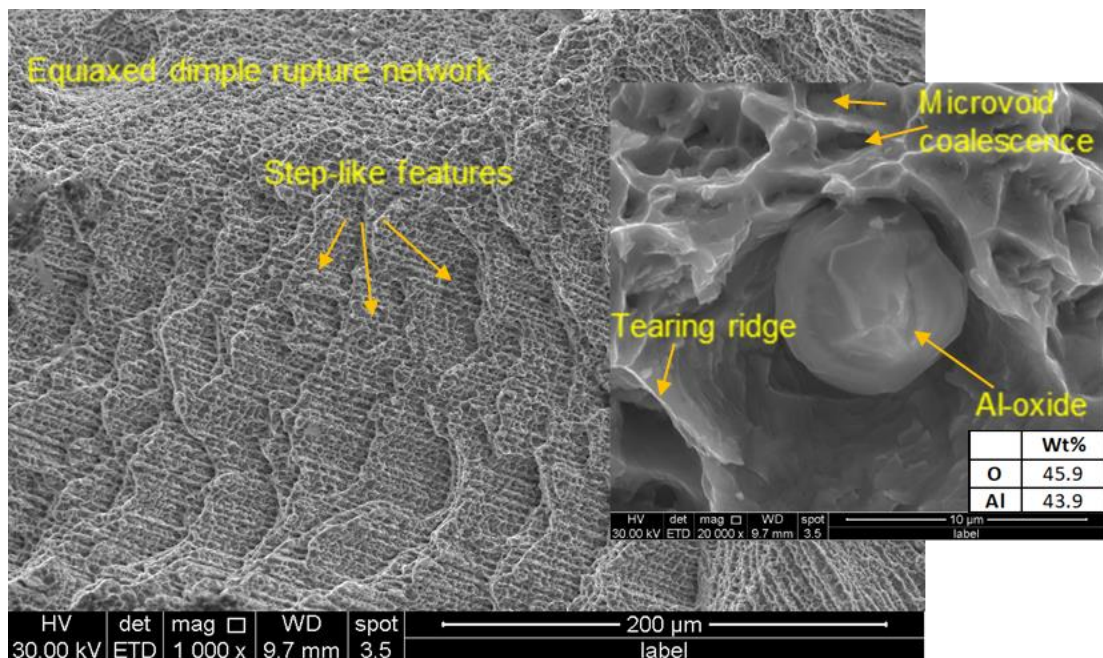


Figure 105: Higher magnification secondary electron SEM image of a sample 3 fracture surface. Step-like features can be seen on the left image. The right image shows microvoid coalescence, a tearing ridge, and an Al-oxide.

4.2.4 Vickers Hardness

The location for where Vickers macro/microhardness measurements were taken relative to the laser and scan path direction is shown in Figure 106.

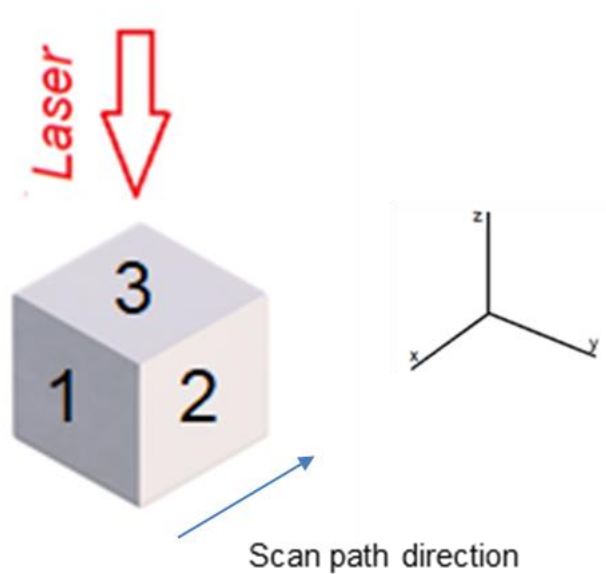


Figure 106: Schematic showing the location for where Vickers hardness measurements were taken from relative to the laser and scan path direction.

Vickers macrohardness and microhardness results are shown in Table 38 and Figure 107. All results are valid as they show small values of standard deviation. Samples 1, 2, and 3 did not differ significantly in macrohardness or microhardness values. Similar values were obtained for individual sample macro/microhardness. All values exceed standard Vickers Hardness for solution annealed Inconel 718 (246 HV) but are below solution annealed and aged Inconel 718 (385 HV).

| Sample no. | Macrohardness (HV ₁₀) | Std dev. | Microhardness (HV _{0.5}) | Std dev. |
|------------|-----------------------------------|----------|------------------------------------|----------|
| 1 | 271 | 11.6 | 279 | 10 |
| 2 | 262 | 5.5 | 267 | 8 |
| 3 | 262 | 5.8 | 264 | 9 |

Table 38: Mean values obtained for Vickers macro/microhardness. Standard deviation values are shown.

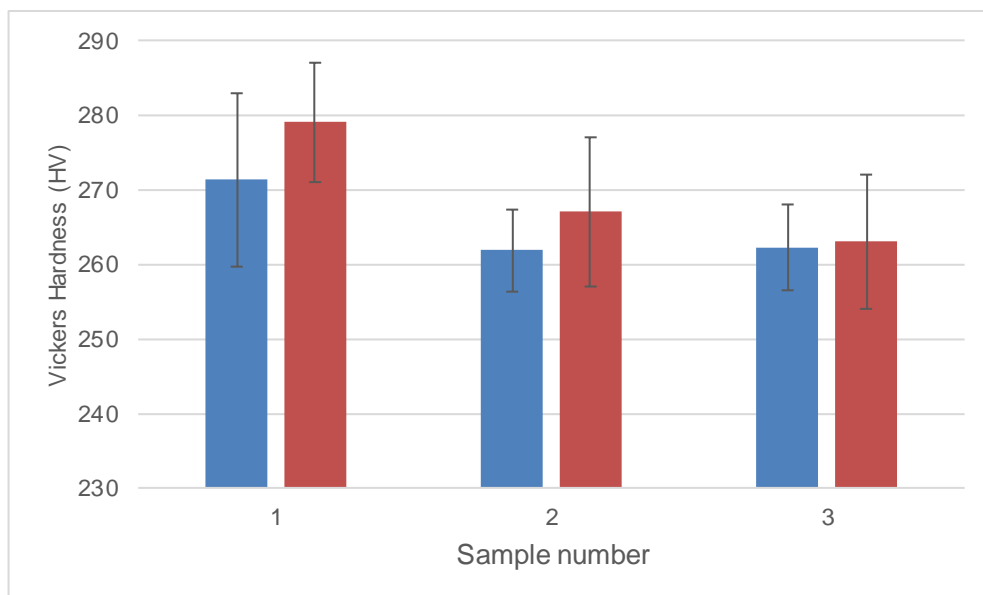


Figure 107: Graph showing the mean values obtained for Vickers macrohardness (HV₁₀) and microhardness (HV_{0.5}) testing. Standard deviation error bars are shown.

4.3 Stage 3 – Investigation into the effect of build direction on metallurgical and mechanical properties

4.3.1 Optical Light Microscopy

Specimens displayed no visible evidence of cracks prior to etching. Porosity was measured to be 0.30% (standard deviation: 0.21%) for horizontal specimens and 0.13% (standard deviation: 0.10%) for vertical specimens. Pore size and shape was consistent between the horizontal (H) and vertical (V) specimens.

Figure 108 and Figure 109 show 3-dimensional sections of the vertical (3 mm × 3 mm × 2.5 mm) and horizontal (2.5 mm × 3 mm × 2.5 mm) samples.

Differences were present between all three planes for horizontal samples. Due to 90° rotations between subsequent layers the vertical test specimen yz-plane and xz-plane are comparable microstructurally, but differ to the xy-plane.



Figure 108: Optical micrograph of a 3-dimensional section of the vertical sample. Differences between the xy-plane and the other two planes (xz and yz) can be seen.



Figure 109: Optical micrograph of a 3-dimensional section of the horizontal sample. Differences between all three planes can be observed.

Deposited layers and tracks were visible in the etched samples, these are indicated by the yellow dashed lines on Figure 110 and Figure 111. OLM revealed columnar grains which elongated upwards in the direction of the laser for both sample build directions, these are outlined in Figure 110 and Figure 111 in blue. Grains can be observed to extend across multiple layers and

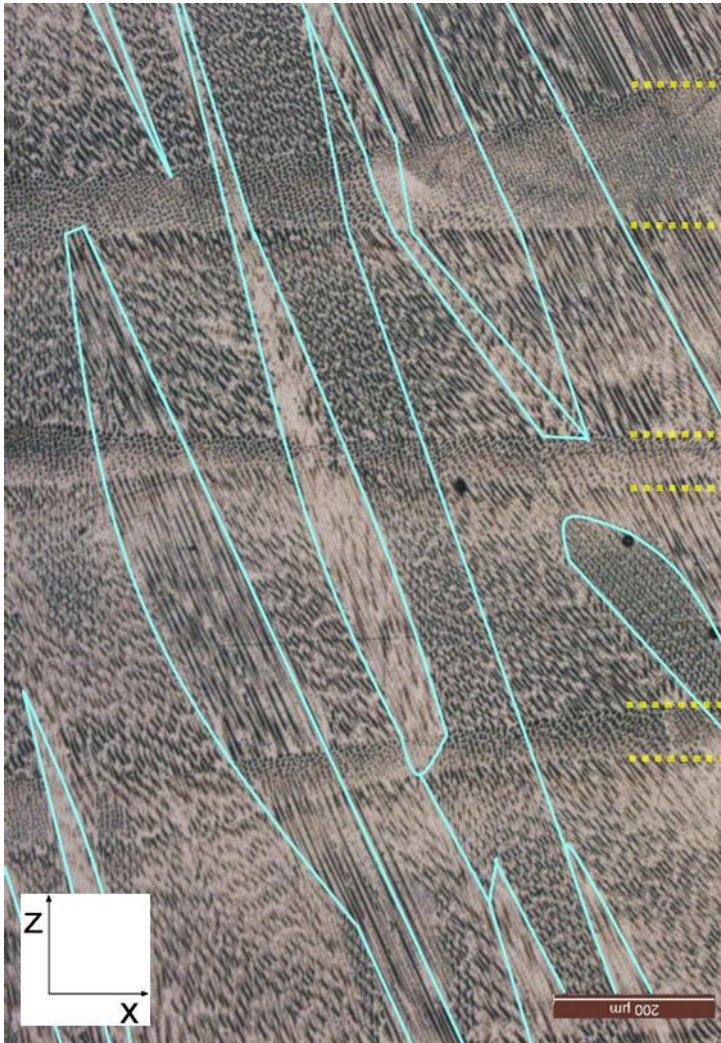


Figure 110: Optical micrograph of the horizontal sample xz-plane. Deposited layers are visible and indicated by yellow lines. Grains are outlined in blue and extend through multiple layers.

tracks.

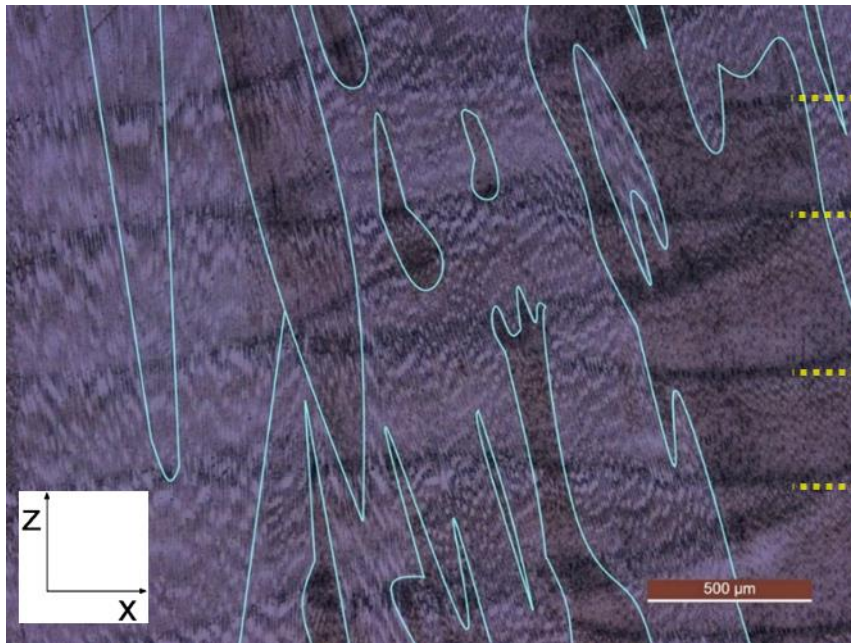


Figure 111: Optical micrograph of the vertical sample yz-plane (comparable to xz-plane). Deposited layers are visible and indicated by yellow lines. Grains are outlined in blue and extend through multiple layers and across tracks.

In the xy-plane a change in structure was observed in the region where adjacent tracks overlapped. This can be seen in Figure 112 which shows the horizontal test specimen xy-plane where a much darker region is present in the area of the previously deposited, this corresponds to the area of the previous track which has been heat-affected and possibly undergone partial remelting. The structure changes from dendritic to a more refined region of phases in the heat-affected area before changing back to dendritic in the subsequent track.

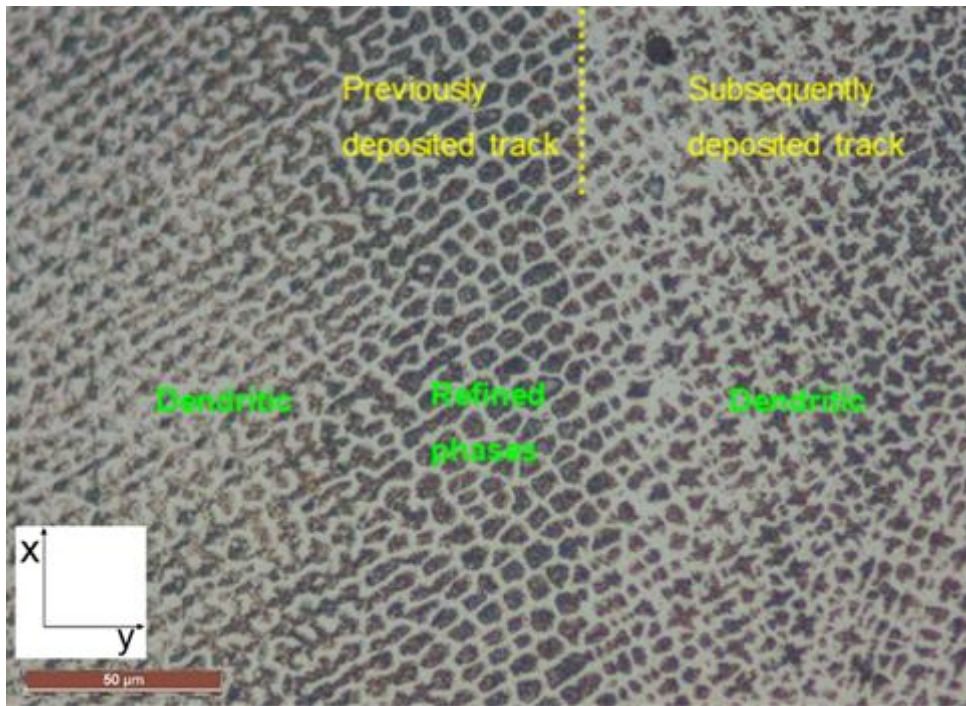


Figure 112: Optical micrograph of the horizontal sample xy -plane where two tracks overlap (indicated in yellow). A darker region containing refined phases can be seen in the heat-affected region.

Figure 113 shows the sample vertical test specimen yz -plane under higher magnification, where a dendritic structure can be seen.



Figure 113: Optical micrograph of the vertical sample yz -plane (comparable to xz -plane). Tracks can be clearly differentiated. A dendritic structure can be seen. Layers are indicated in yellow.

Investigation under higher magnification showed horizontal samples to have a more homogeneous microstructure compared to vertical samples which were more heterogenous (Figure 114, Figure 115). Dendritic structures were observed in both horizontal and vertical, with refinement of phases within the grain clearly present in the heat-affected areas. Comparison of these images to those in Table 9 indicates that, as previously stated, the light areas are most likely Ni-rich solid solution and the dark areas precipitates. It is possible that within the dark areas Laves phase is present, as Table 9 shows Laves phase to be surrounded by a dark region.

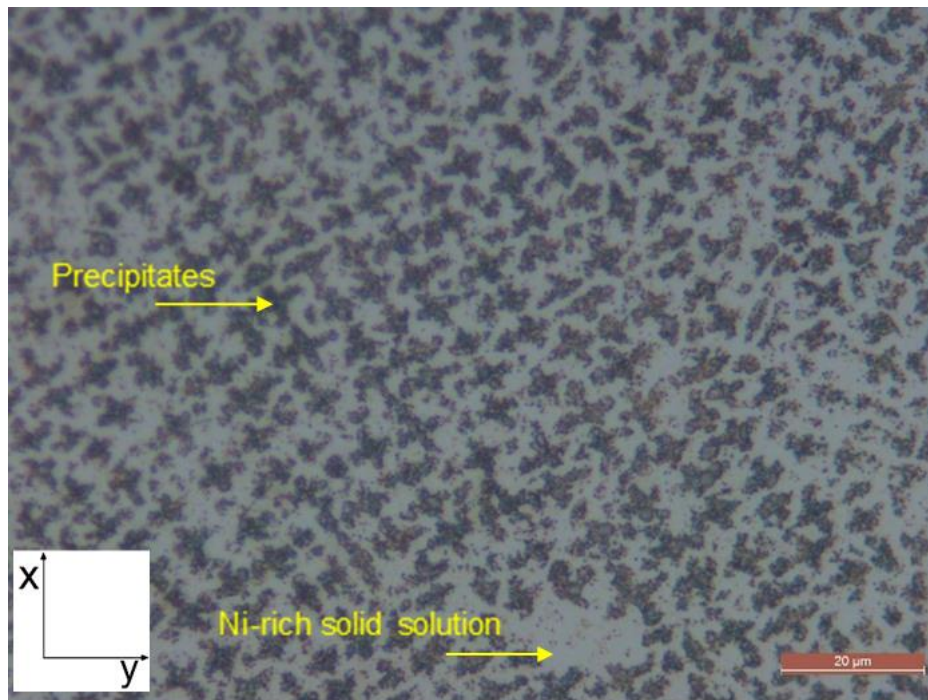


Figure 114: Optical micrograph of the horizontal xy -plane. A dendritic structure can be seen. Possible phases are indicated – Ni-rich solid solution and precipitates.

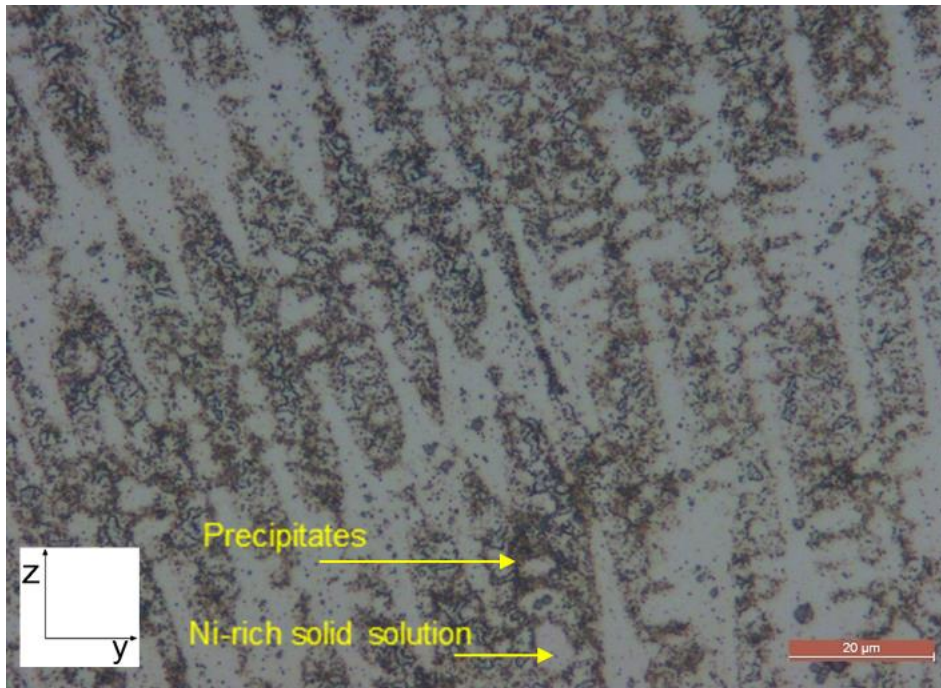


Figure 115: Optical micrograph of the vertical yz -plane. A dendritic structure can be seen. Possible phases are indicated – Ni-rich solid solution and precipitates.

4.3.2 Scanning Electron Microscopy

SEM investigation found an irregular shaped phase to be present in both horizontal and vertical samples. This was mainly observable as a discontinuous network of the white phase in the horizontal xz -plane (Figure 116). In vertical samples continuous networks of these formed (Figure 117). This phase corresponded to the phase observed in previous SEM result sections. Table 39 contains the compositions obtained from the EDX point analysis'.

| | Element Wt% | | | | | | |
|-------------------|-------------|--------|------|------|------|------|------|
| | Ni | Fe | Cr | Nb | Mo | Ti | Al |
| Powder | 53.15 | 18.767 | 18.3 | 5.08 | 2.97 | 0.95 | 0.52 |
| Spectrum 1 | 46.0 | 16.6 | 16.3 | 16.0 | 3.8 | 1.4 | - |
| Spectrum 2 | 45.4 | 16.3 | 16.5 | 16.7 | 3.7 | 1.4 | - |
| Spectrum 3 | 43.3 | 13.4 | 14.2 | 15.7 | 4.0 | 1.4 | - |
| Spectrum 4 | 43.1 | 14.6 | 15.6 | 11.7 | 3.8 | 1.1 | - |
| Spectrum 5 | 50.2 | 18.9 | 19.0 | 3.2 | 2.7 | 0.9 | 0.4 |

Table 39: The EDX point analysis results for the following figures of SEM images.

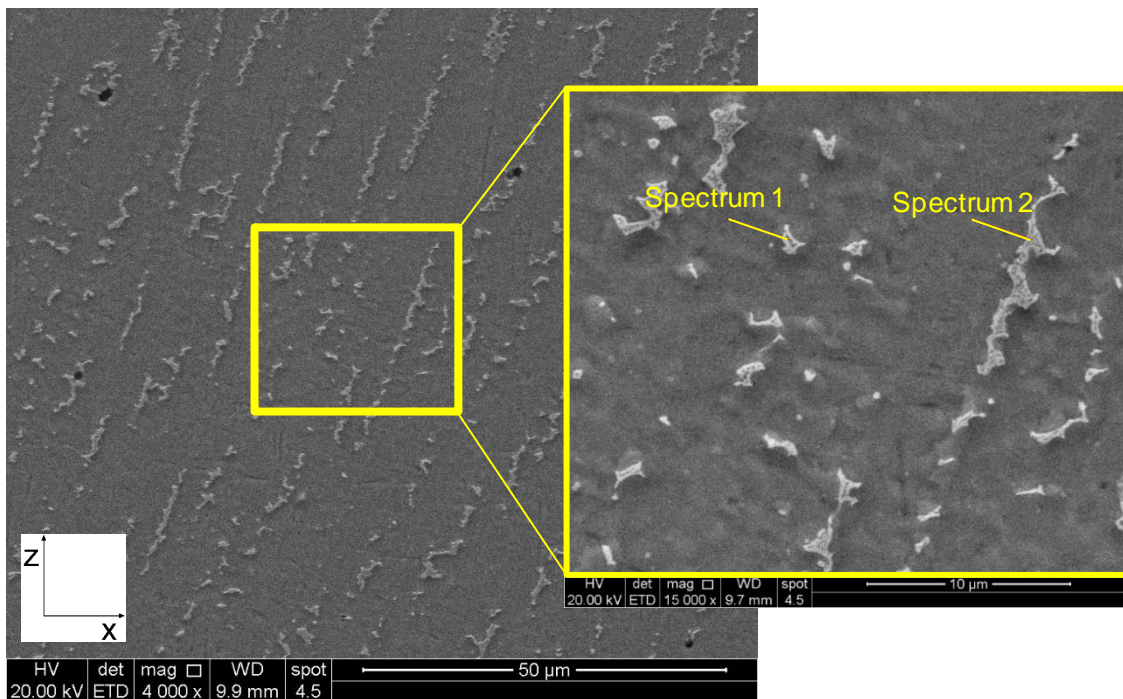


Figure 116: Secondary electron SEM image of horizontal xz-plane showing the discontinuous network of the bright phase. Spectrums of this phase were taken.

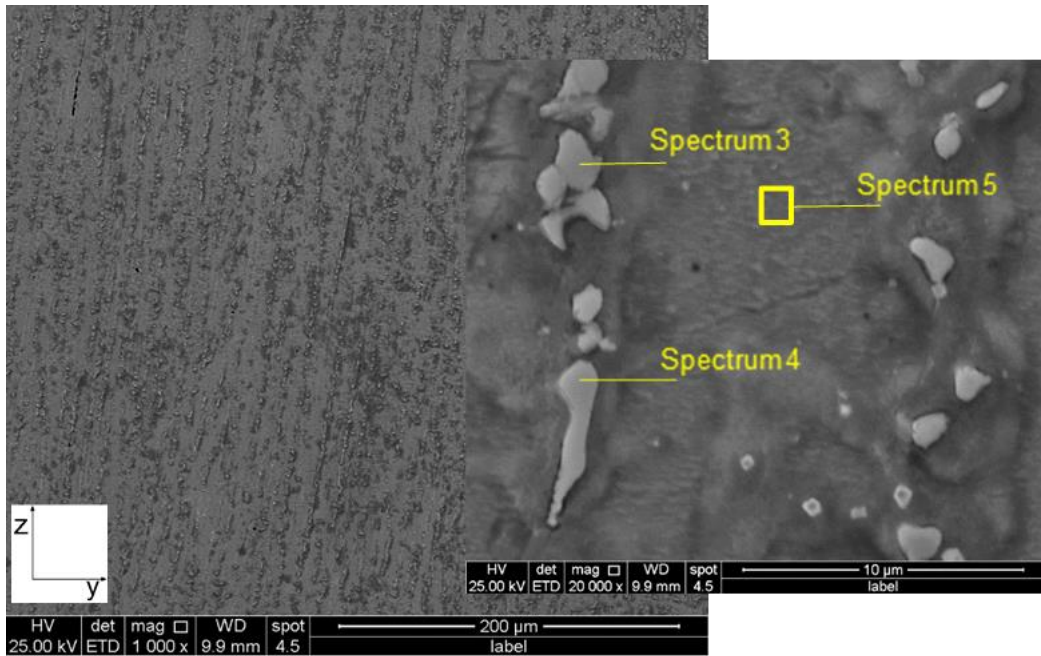


Figure 117: Secondary electron SEM image of vertical yz-plane showing the continuous network of the bright phase. Spectrums of this phase and the matrix were taken.

EDX maps of the vertical xy-plane are shown (Figure 118). Several phases can be seen, as in previous stages of work. Nb, Mo, and Ti have segregated to interdendritic regions, corresponding to the regions containing the white phase hand the immediate surrounding area.

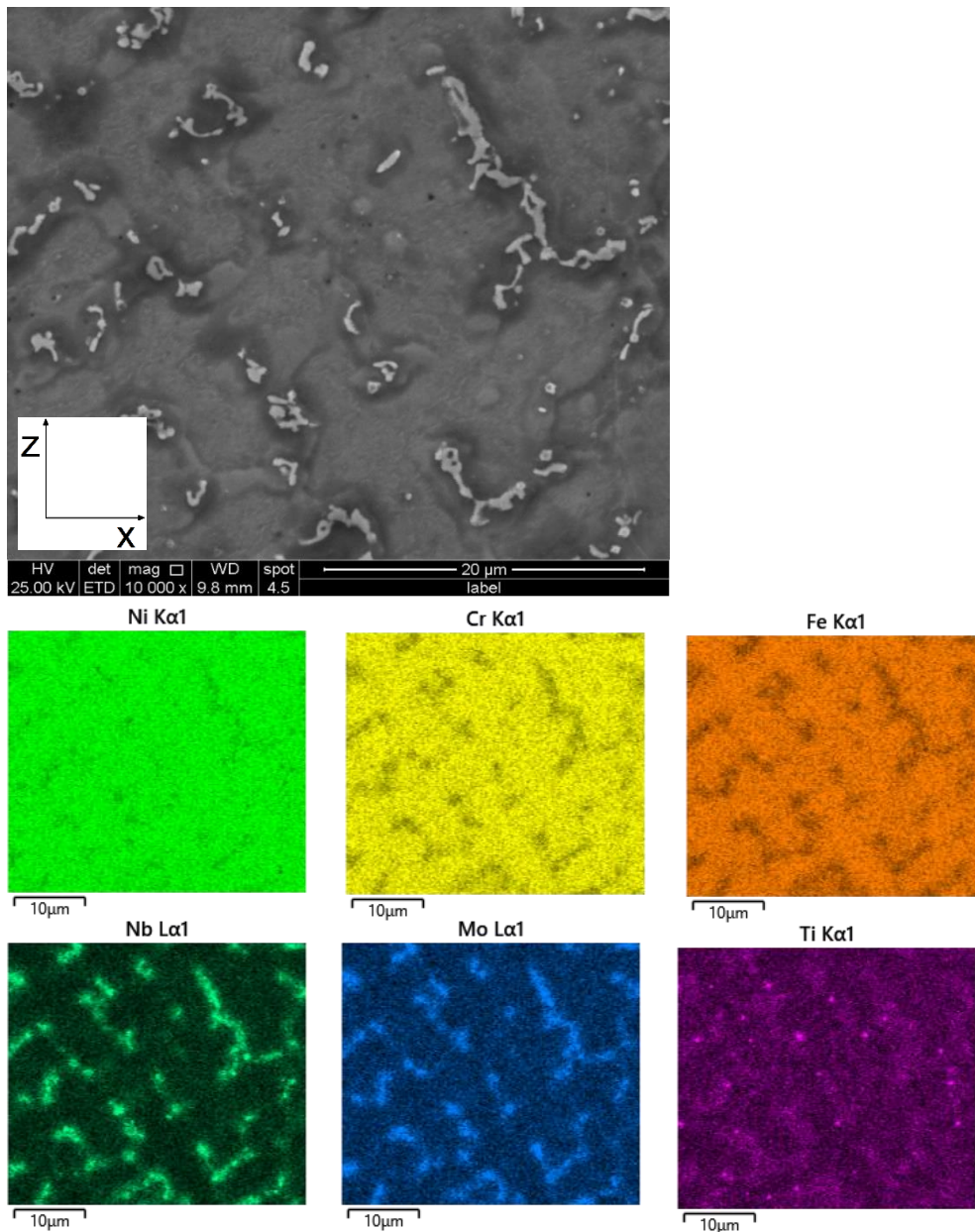


Figure 118: Secondary electron SEM image of a region within the vertical xz-plane (comparable to yz-plane) used for EDX mapping and the corresponding EDX maps obtained.

4.3.3 Tensile Testing

Tensile testing results are shown in Table 40, Figure 119, and Figure 120. All results are valid as they show small values of standard deviation. 0.2% proof stress values did not vary significantly between test specimens, however horizontal test specimens had a significantly greater UTS than vertical test specimens. Elongation was significantly greater in vertical specimens than horizontal specimens.

| Sample | 0.2% proof stress (MPa) | Std dev. | UTS (MPa) | Std dev. | Elongation (%) | Std dev. |
|--------|-------------------------|----------|-----------|----------|----------------|----------|
| H | 682 | 34.2 | 1024 | 37.9 | 20.0 | 3.4 |
| V | 648 | 3.3 | 916 | 8.7 | 30.9 | 037 |

Table 40: Mean values obtained from tensile testing. Standard deviation is shown.

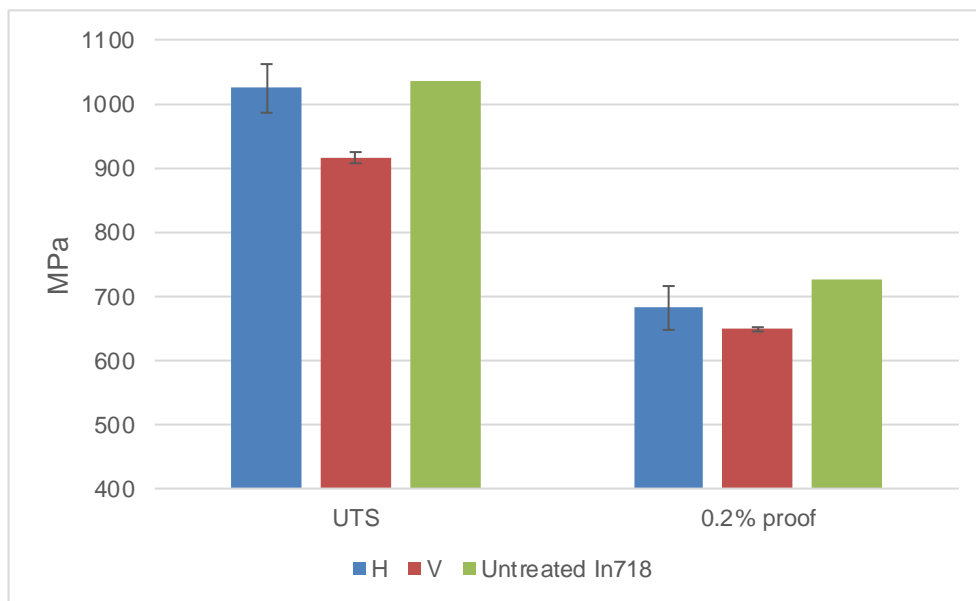


Figure 119: Graph showing the mean values obtained for UTS and 0.2% proof stress. Standard deviation error bars are shown. Values for untreated wrought Inconel 718 are shown for comparison.

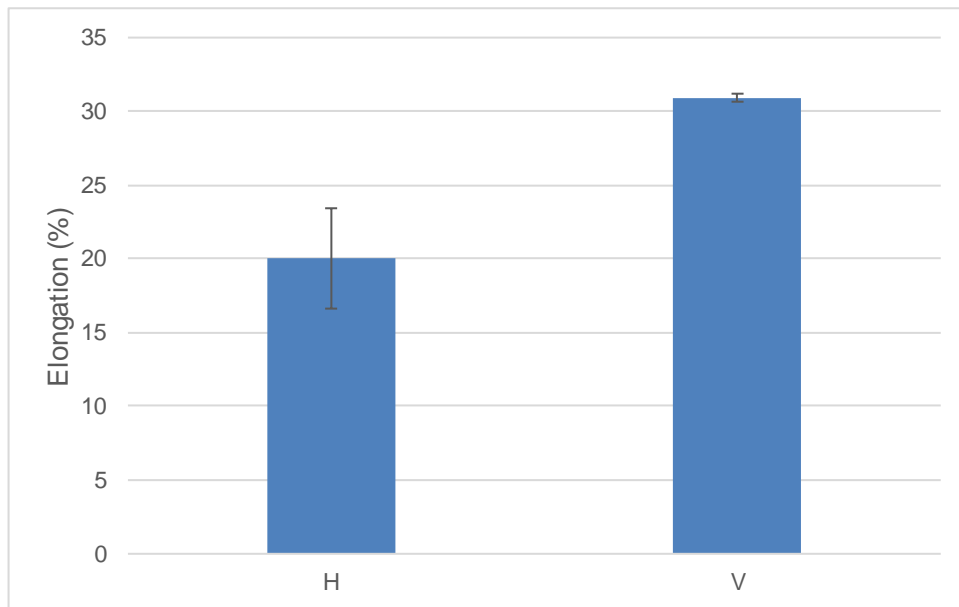


Figure 120: Graph showing the mean values obtained for elongation. Standard deviation error bars are shown.

4.3.3.1 Fractography

Visual examination of fracture faces for tensile specimens found no presence of oxidation. Cross sectional area of the fractured specimens decreased as gauge length elongated, with plastic deformation observable on the outside surface of the specimens.

At a lower magnification, the surfaces of the specimens have a rough, jagged appearance displaying coarse intergranular regions with step-like features, and dimpled regions (Figure 121, Figure 122). Shear lips on the fracture surface can be seen. Some regions of the fractured specimen faces experienced external contamination following tensile testing. Figure 122 shows this under higher magnification.

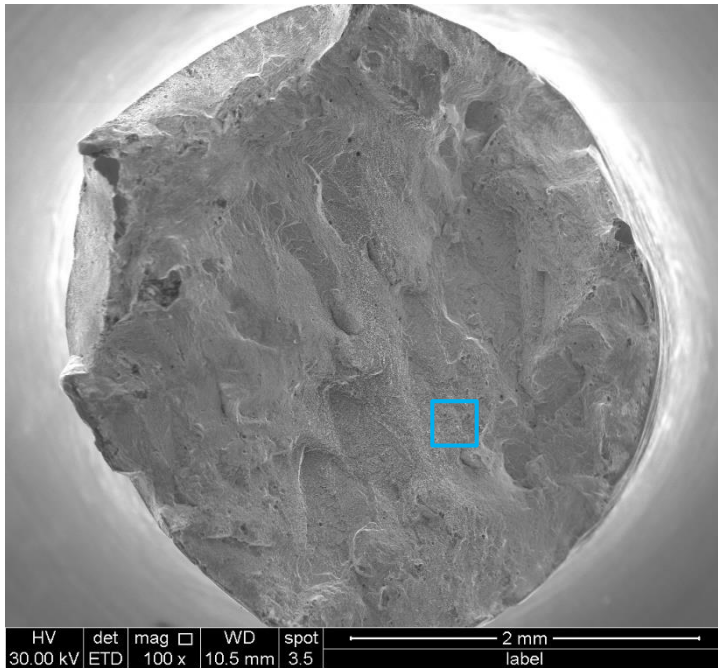


Figure 121: Secondary electron SEM image of a fracture surface of a horizontal tensile specimen.

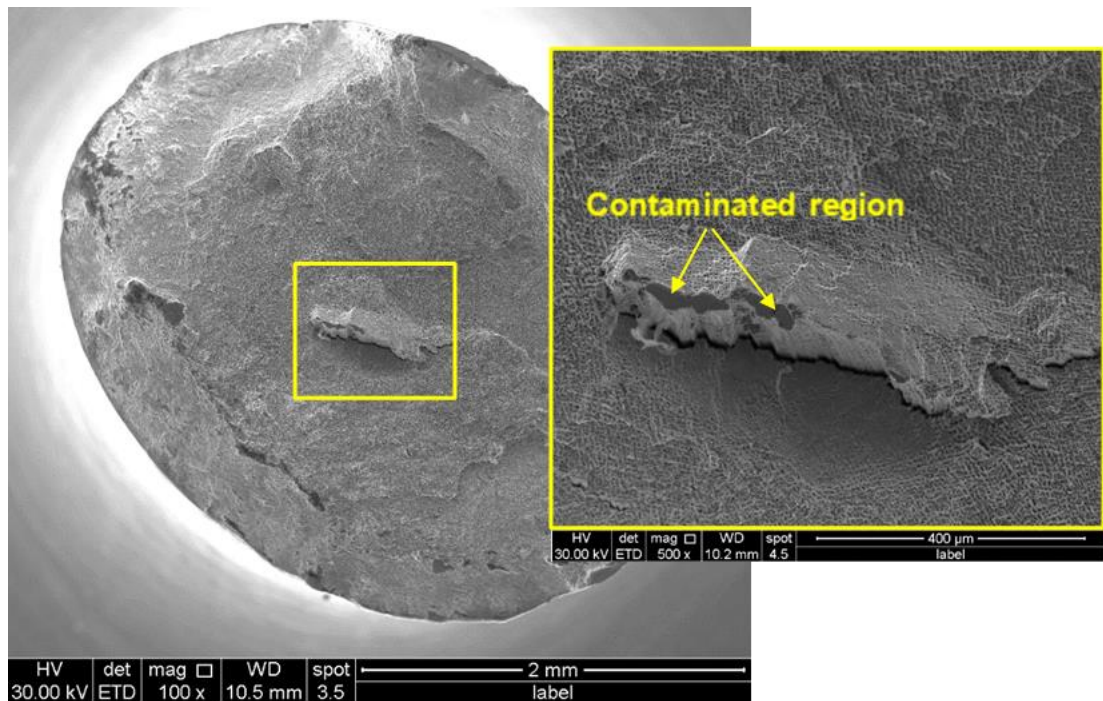


Figure 122: Secondary electron SEM image of a fracture surface of a vertical tensile specimen. A region where external contamination following fracture occurred is shown.

Under higher magnification features observed across the fracture face included step-like features, tearing ridges, microvoid coalescence, Al-oxide inclusions (confirmed by EDX analysis), cracks, shear deformation, and fragments of Laves phase (Figure 123, Figure 124).

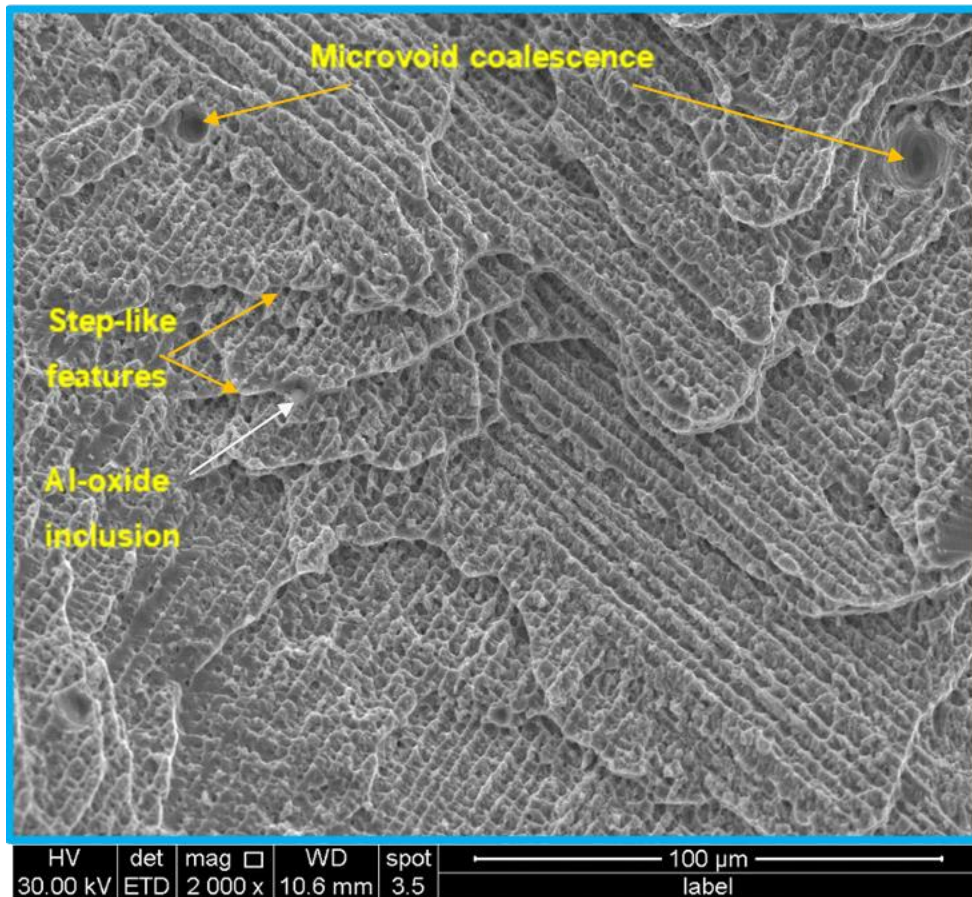


Figure 123: A higher magnification secondary electron SEM of the fracture surface of a horizontal tensile specimen. Examples of microvoid coalescence, step-like features and Al-oxide inclusion are indicated. Tearing ridges can be seen to have formed uniform lines.

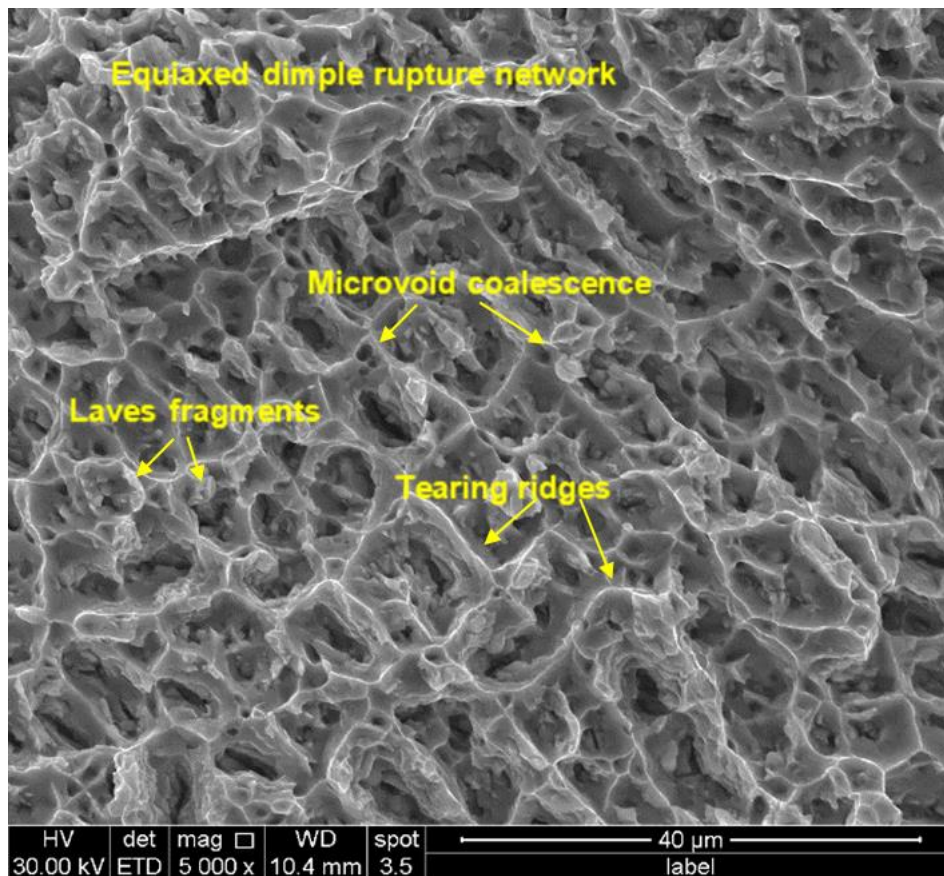


Figure 124: A higher magnification secondary electron SEM of the fracture surface of a vertical tensile specimen. An equiaxed dimple rupture network can be seen. Examples of microvoid coalescence, tearing ridges (formed randomly), and fragments of Laves are indicated.

4.3.4 Vickers Hardness

Macrohardness and microhardness results are shown in Table 41 and Figure 125. All results are valid as they show small values of standard deviation. Macro/microhardness did not vary significantly between the three horizontal planes, however a significant difference was present between vertical planes. V2 and V3 samples displayed the greatest macro/microhardness values and were significantly greater than the other planes. Macro/microhardness values for individual sample numbers were similar in value. All values exceed standard Vickers Hardness for solution annealed Inconel 718 (246 HV) but are below solution annealed and aged Inconel 718 (385 HV).

| Sample | Macrohardness | | | | Microhardness | | | |
|--------------|---------------|----------|-----|----------|---------------|----------|-----|----------|
| | H | Std dev. | V | Std dev. | H | Std dev. | V | Std dev. |
| 1 (xy-plane) | 266 | 8.8 | 249 | 6.8 | 266 | 7.1 | 255 | 6.6 |
| 2 (yz-plane) | 284 | 8.7 | 316 | 10.0 | 279 | 7.0 | 314 | 11.8 |
| 3 (xz-plane) | 276 | 6.3 | 312 | 5.0 | 268 | 4.3 | 313 | 11.3 |

Table 41: Mean values obtained for Vickers macro/microhardness for each plane of the horizontal and vertical samples are shown. Standard deviation values are shown.

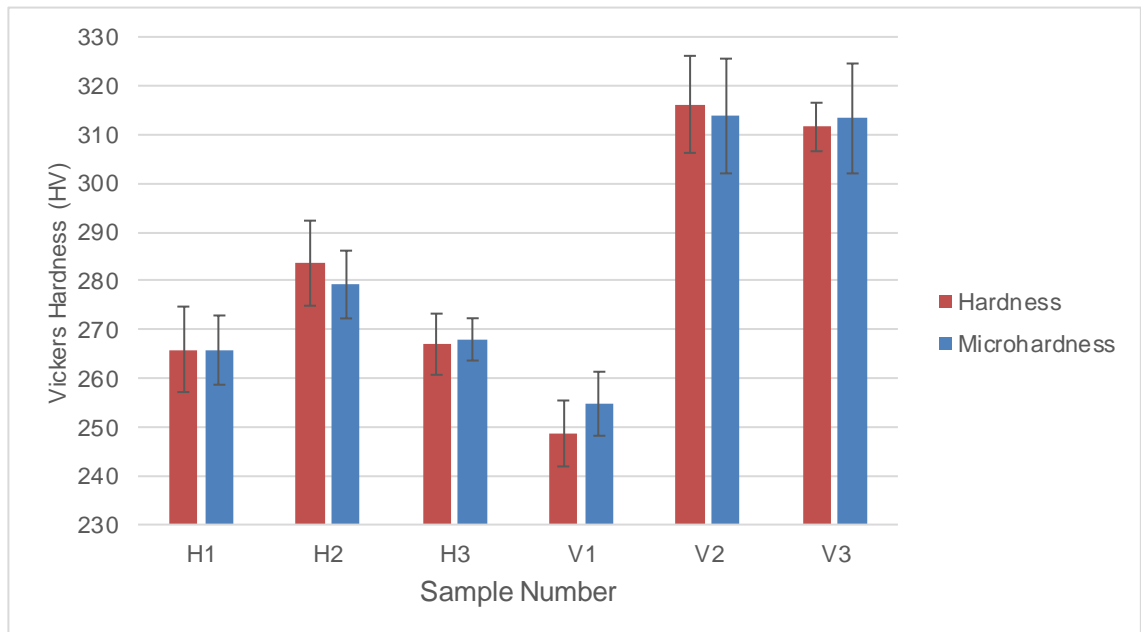


Figure 125: Graph displaying the mean Vickers macrohardness (HV₁₀) and microhardness (HV_{0.5}) values for each plane of the horizontal and vertical samples. Standard deviation error bars are shown.

4.4 Stage 4 – Investigation into the effect of an interface using multiple build directions on metallurgical and mechanical properties

4.4.1 Optical Light Microscopy

Specimens displayed no visible evidence of segregation prior to etching. Porosity was measured to be 0.06% (standard deviation: 0.01%) at the interface.

The interface between the build directions was clearly visible when subject to OLM (Figure 126). Layers and tracks are observable. Grains propagated from direction 1, extending through direction 2 layers. A crack was observed in direction 1 material reaching to the interface (Figure 127). A more homogenous microstructure is present in direction 1 compared to direction 2. Dendritic structures were observed in both directions of deposition.



Figure 126: Optical micrograph of the interface between build direction 1 and build direction 2. The deposited layers and tracks can be distinguished.

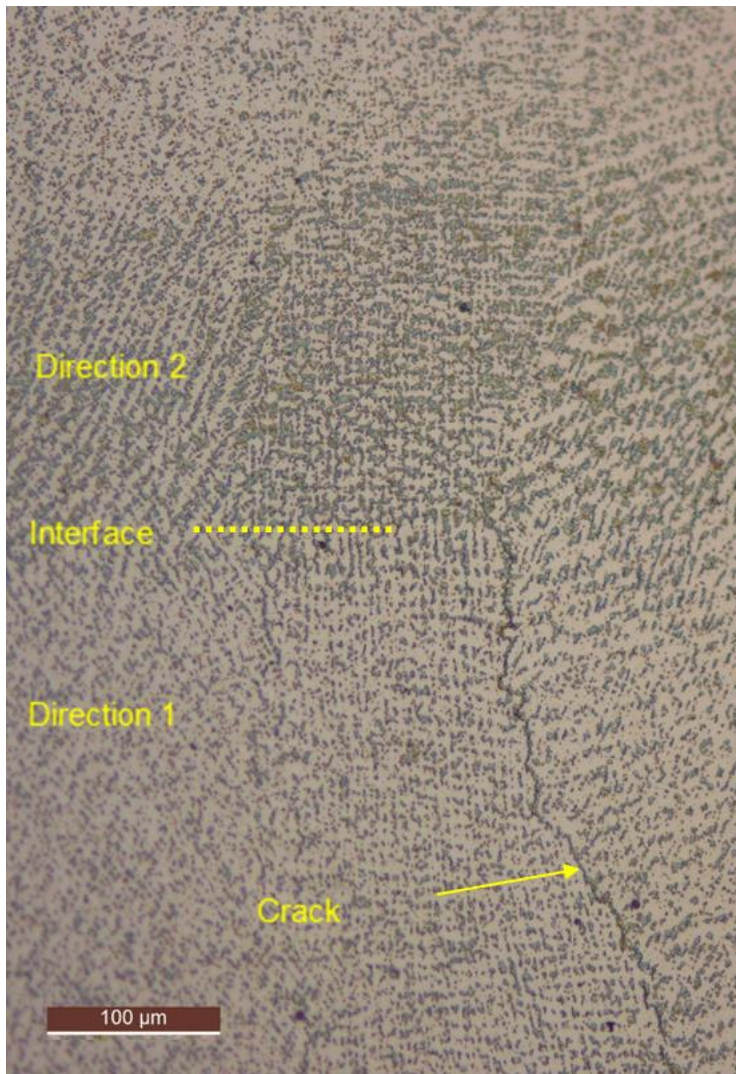


Figure 127: A higher magnification optical micrograph of the interface between build direction 1 and build direction 2. A crack can be observed to extend to the interface from direction 1 deposited material.

4.4.2 Scanning Electron Microscopy

Investigation under the SEM found the two directions to differ. Networks of the bright phase are observed as in previous samples, appearing more homogeneously spread in build direction 1. This can be seen in Figure 128. Figure 129 shows a high magnification image of the bright phase.

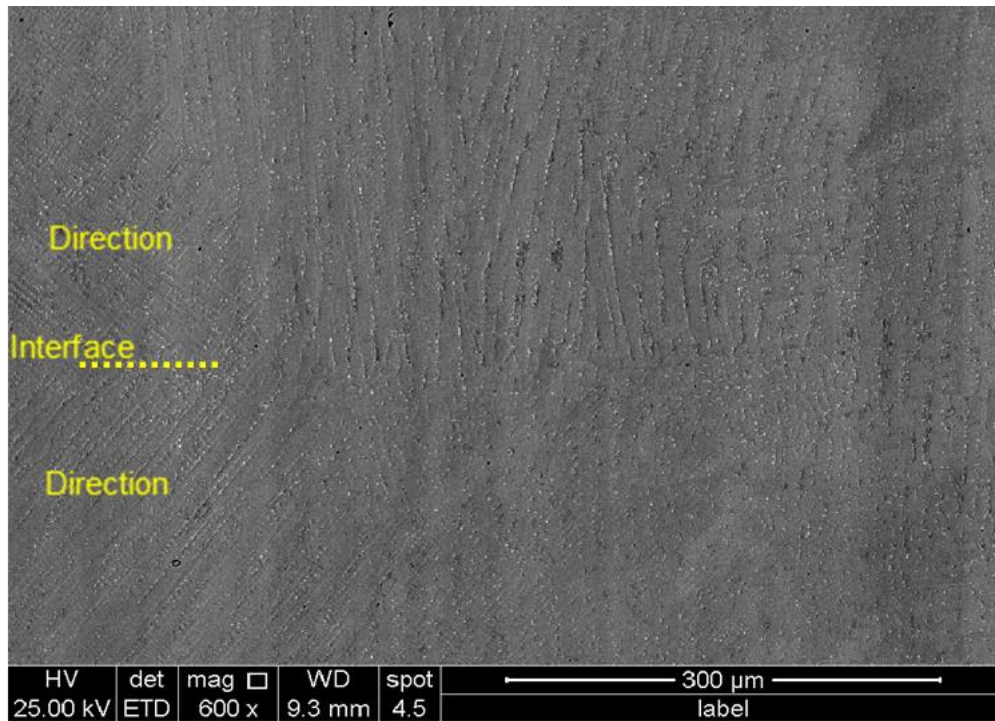


Figure 128: Secondary electron SEM image of the interface between build direction 1 and build direction 2. A bright phase can be seen to form a continuous network in build direction 2, whilst being more homogenously spread in build direction 1.



Figure 129: A high magnification secondary electron SEM image of the bright phase present within the sample.

4.4.3 Tensile Testing

Tensile testing results are shown in Table 42 and Figure 130. These results will be compared to the tensile testing results in section 4.3.3. All results are valid as they show small values of standard deviation.

| | 0.2% proof stress (MPa) | Std dev. | UTS (MPa) | Std dev. | Elongation (%) | Std dev. |
|------------------|--------------------------------|-----------------|------------------|-----------------|-----------------------|-----------------|
| Interface | 637 | 9.4 | 914 | 18.4 | 20.2 | 2.1 |

Table 42: Mean values obtained for tensile testing, including standard deviation values.

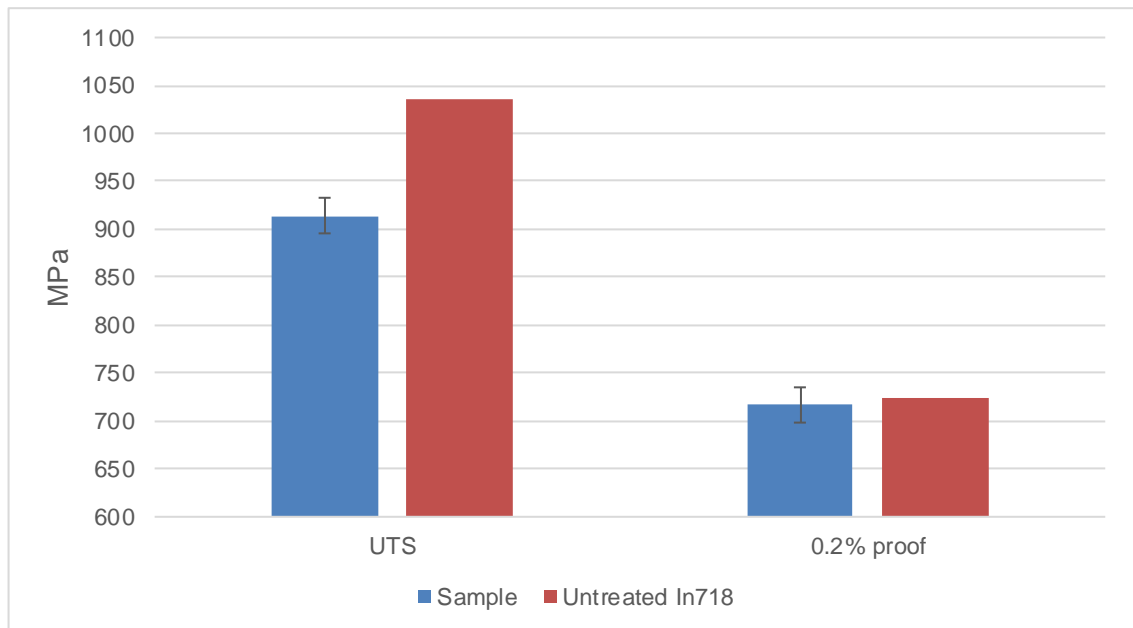


Figure 130: Graph displaying the mean UTS and 0.2% proof stress values obtained from tensile testing. Standard deviation error bars are shown. Untreated wrought Inconel 718 values are shown for comparison.

4.4.3.1 Fractography

All tensile specimens fractured in the half which corresponded to the second direction of the laser, showing this region to be weaker than the first build direction. This is demonstrated in Figure 131.

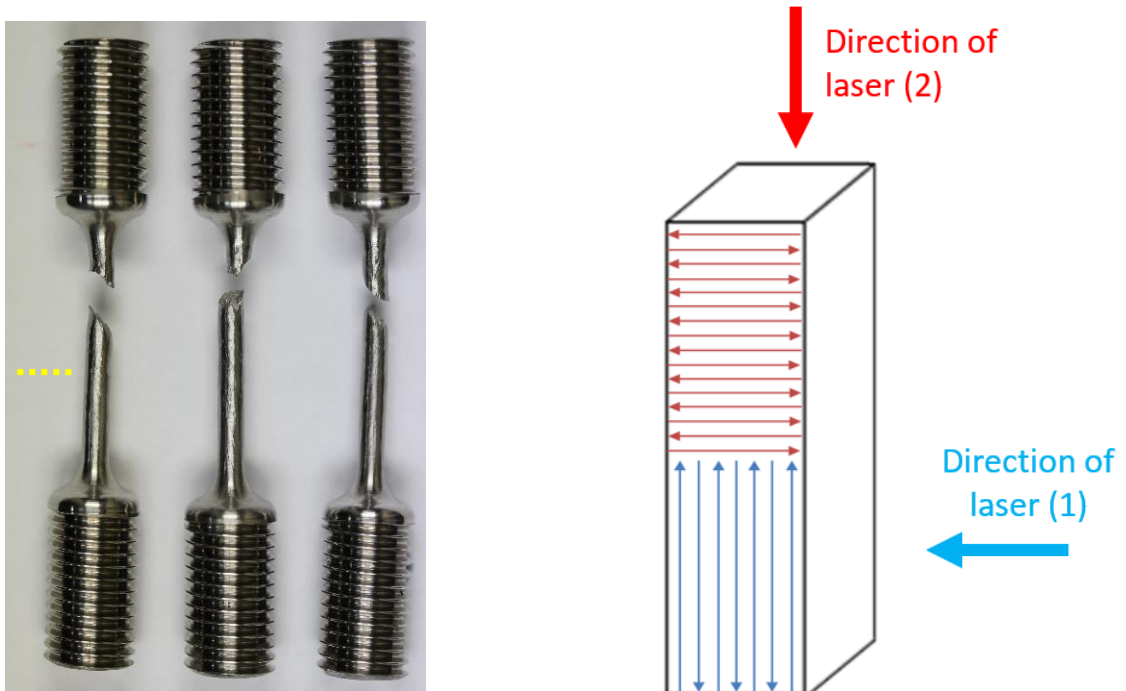


Figure 131: The fractured tensile specimens. The interface was aligned to fall at the midpoint of the specimen gage.

As for previously tested tensile specimens, visual examination of fracture faces found no presence of oxidation, and plastic deformation was observable on the outside surface of the specimen. Shear lips on the fracture surface could be seen.

At a lower magnification, the surface of the specimen has a rough, jagged appearance displaying coarse intergranular regions with step-like features, and dimpled regions (Figure 132). Under higher magnification, features observed across the fracture face included tearing ridges, microvoid coalescence, and cracks (Figure 133).

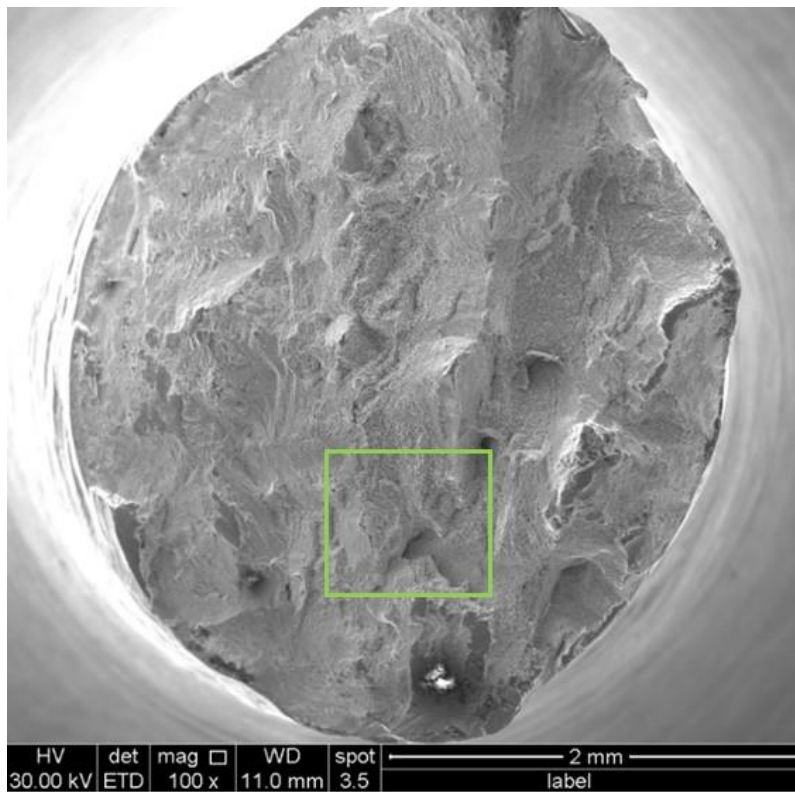


Figure 132: Secondary electron SEM image of a fracture surface of one of the tensile specimens.

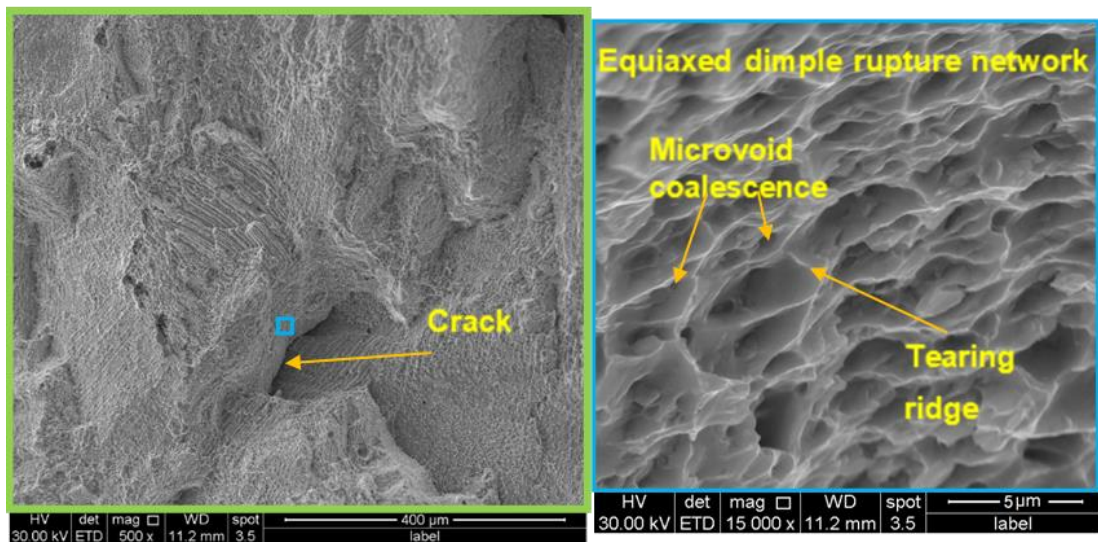


Figure 133: Higher magnification secondary electron SEM images of the fracture surface. The yellow boxed image on the left corresponds to the box in the previous figure. The blue boxed image on the right corresponds to the blue box in the image on the left. Examples of observable features are indicated on the images.

4.4.4 Vickers Hardness

Results for macrohardness are shown in Table 43 and Figure 134. All results are valid as they show small values of standard deviation. All values exceed standard Vickers Hardness for solution annealed Inconel 718 (246 HV) but are below solution annealed and aged Inconel 718 (385 HV).

| | Hardness (HV₁₀) | Std dev. |
|--------------------------|-----------------------------------|-----------------|
| Build direction 1 | 271 | 7.1 |
| Interface | 268 | 7.2 |
| Build direction 2 | 275 | 9.0 |

Table 43: Mean values obtained for Vickers macrohardness testing, including standard deviation values.

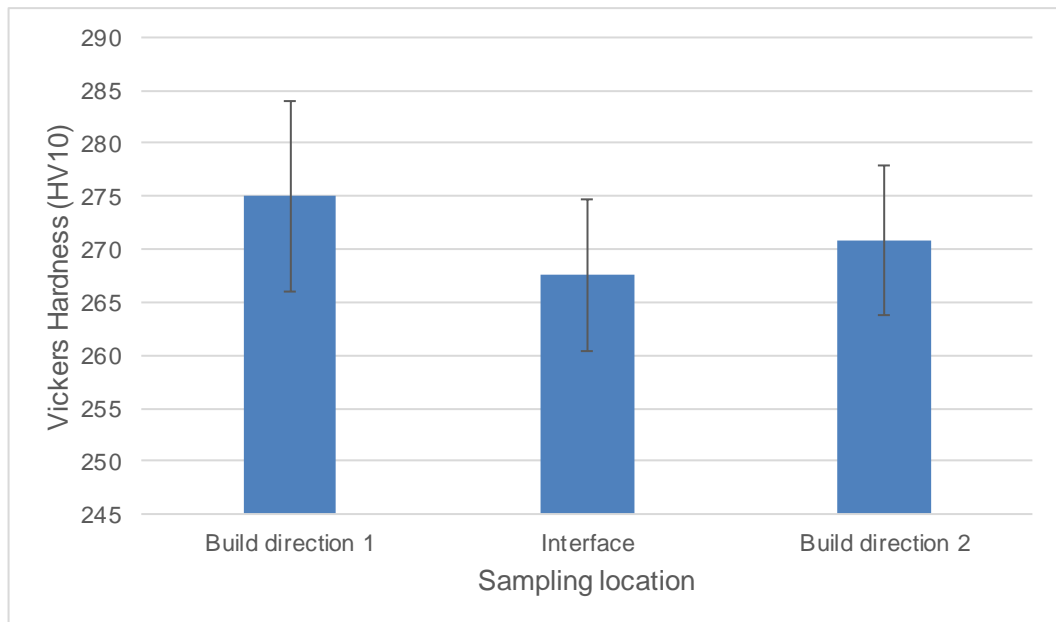


Figure 134: Graph displaying mean Vickers macrohardness (HV₁₀) values obtained. Standard deviation error bars are shown.

Average microhardness results moving across the interface are plotted as a graph in Figure 135. Standard deviation is shown. The visible line where build

directions meet in Figure 126 is defined as the interface (0 mm) in this graph. Microhardness values do not vary significantly moving across the interface although a minor decrease in $HV_{0.5}$ can be seen in average values on the graph at 0 mm. Figure 136 shows a microhardness indent which was directly on the interface (at 0 mm; sample was etched post-test).

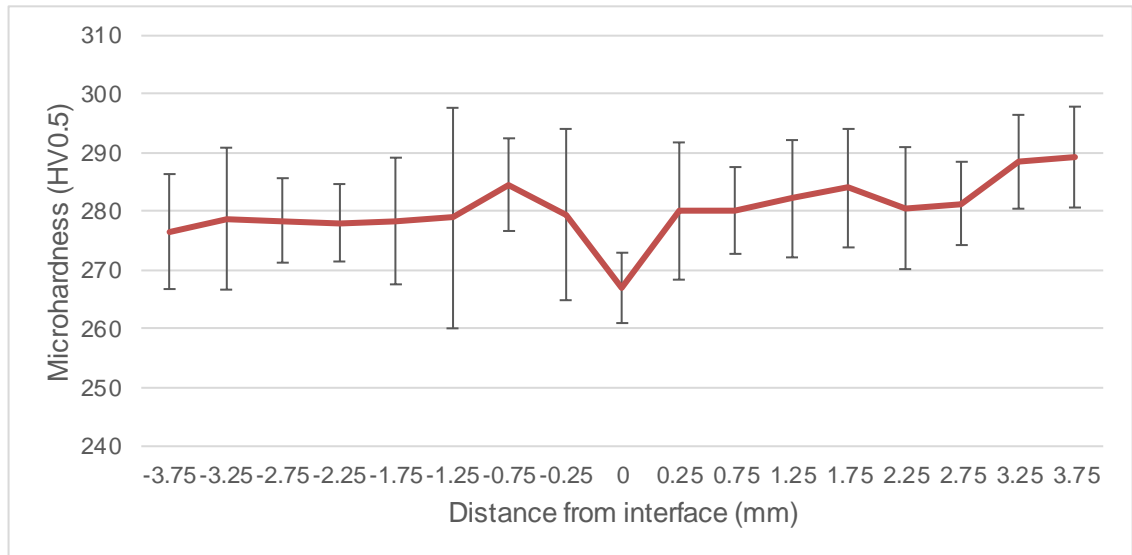


Figure 135: Graph showing average microhardness moving across the interface. The interface is at 0 mm. Standard deviation error bars are shown.

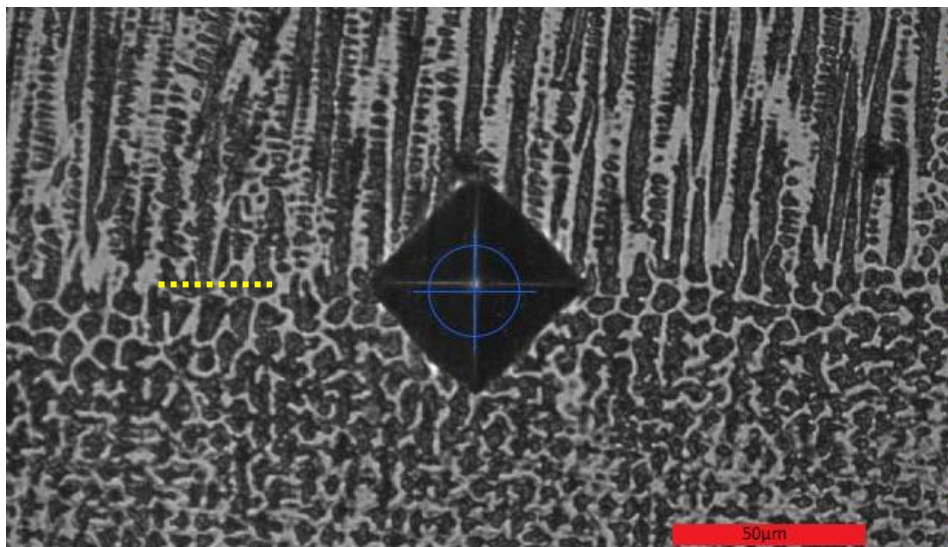


Figure 136: Optical micrograph showing a microhardness indent directly on the interface (at 0 mm).

4.5 Stage 5 – Investigation into the effect of a heat-treatment on metallurgical properties and Vickers Hardness

4.5.1 Optical Light Microscopy

OLM revealed grain boundaries, a light region most likely to be γ -phase, and darker regions of precipitates. These are indicated in Figure 137. The strong dendritic structure observed within previous stages of work was absent, with sample appearance comparable to Table 9 OLM images for solution treated and wrought Inconel 718.

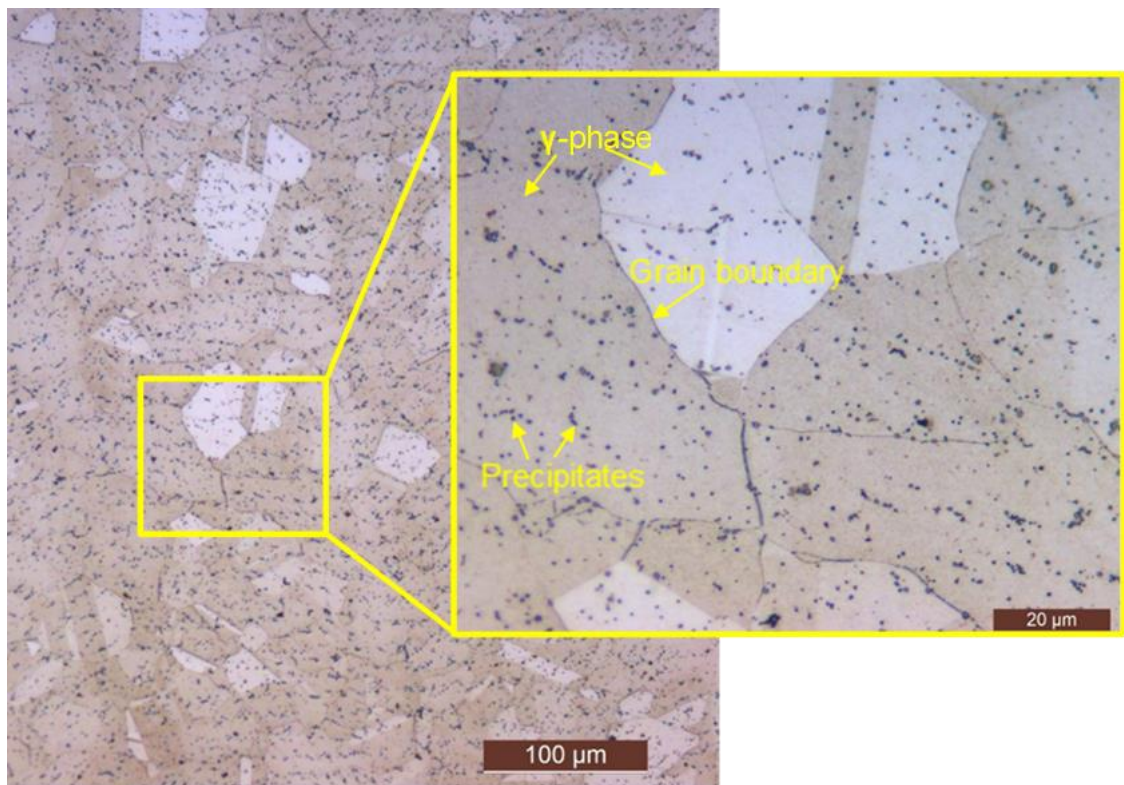


Figure 137: Optical micrograph of Stage 1 set 4 large block, showing examples of grain boundaries, γ -phase and precipitates.

4.5.2 Scanning Electron Microscopy

SEM found the bright phase to be considerably reduced following heat-treatment (Figure 138), with some particles still remaining. Under higher magnification (Figure 139) these had a similar structure as before, but were smaller in size, with EDX analysis confirming similar elemental composition (Table 44).

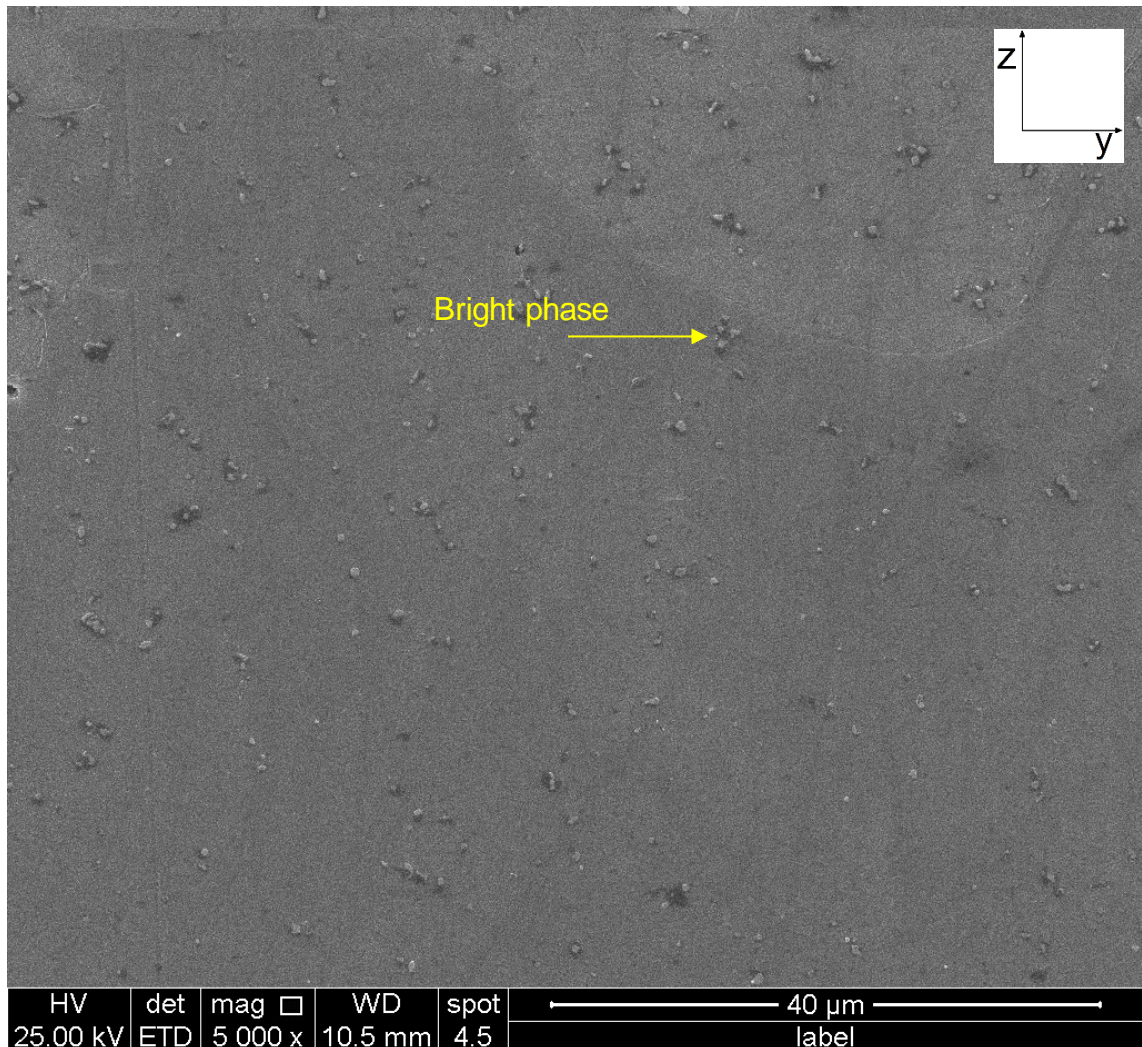


Figure 138: Secondary electron SEM image of heat-treated large block 4 yz-plane. The bright phase which was previously present within Stage 1 untreated samples is indicated.

| | Element Wt% | | | | | | |
|-------------------|-------------|--------|------|------|------|------|------|
| | Ni | Fe | Cr | Nb | Mo | Ti | Al |
| Powder | 53.15 | 18.767 | 18.3 | 5.08 | 2.97 | 0.95 | 0.52 |
| Spectrum 1 | 50.9 | 18.5 | 19.8 | 5.6 | 3.7 | 0.7 | 0.8 |
| Spectrum 2 | 47.7 | 16.6 | 18.0 | 14.7 | 1.0 | 2.0 | - |
| Spectrum 3 | 44.7 | 17.3 | 17.2 | 15.5 | 3.6 | 1.6 | 0.2 |
| Spectrum 4 | 36.8 | 11.7 | 15.2 | 32.8 | - | 3.4 | - |

Table 44: Table containing the element wt% for the powder pre-DED-L, and for the EDX analysis performed.

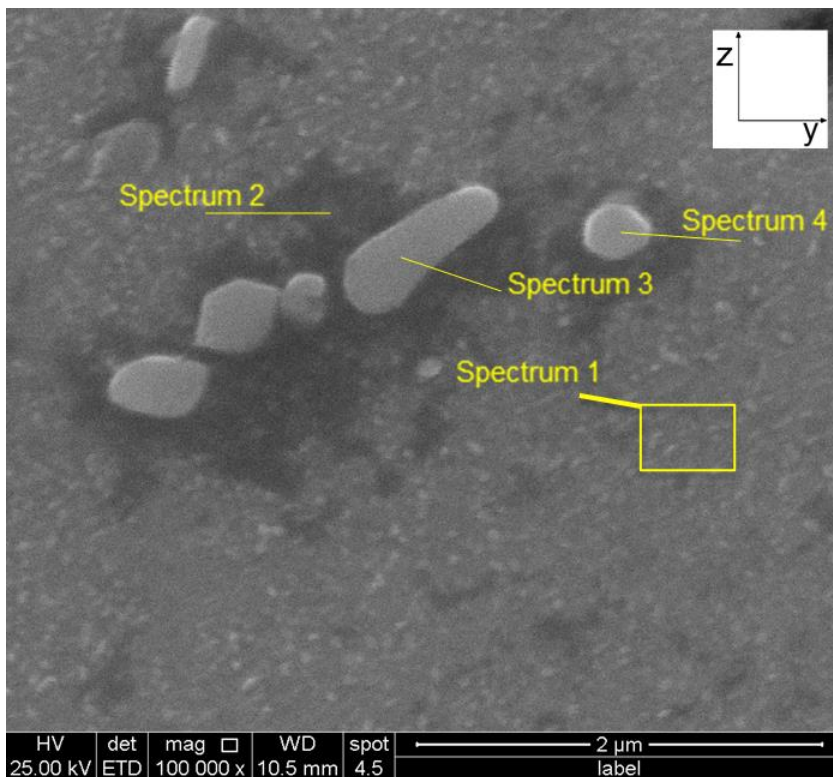


Figure 139: Higher magnification Secondary electron SEM image of the bright phase in heat-treated large block 4 yz-plane.

4.5.3 Vickers Hardness

Vickers macrohardness and microhardness for the heat-treated samples are shown in Table 45. All results are valid as they show small values of standard deviation. Values are plotted in Figure 140 alongside the values for the corresponding untreated material samples (see Table 31) for comparison. A significant increase of over 100 HV₁₀/HV_{0.5} can be seen following application of the heat-treatment described in Table 21. Variation between parameter sets which was seen in Stage 1 large block macro/microhardness also eliminated. All values exceed standard Vickers Hardness solution annealed and aged Inconel 718 (385 HV).

| | Heat- treated sections cut from Stage 1 large block | | | |
|------------|--|-----------------|---|-----------------|
| Set | Macrohardness (HV₁₀) | Std dev. | Microhardness (HV_{0.5}) | Std dev. |
| 4 | 452 | 1.5 | 404 | 8.1 |
| 5 | 448 | 2.4 | 413 | 7.1 |
| 9 | 449 | 2.8 | 402 | 18.3 |
| 10 | 451 | 2.1 | 412 | 9.8 |

Table 45: Mean values obtained for Vickers macro/microhardness of heat-treated samples. Standard deviation is shown.

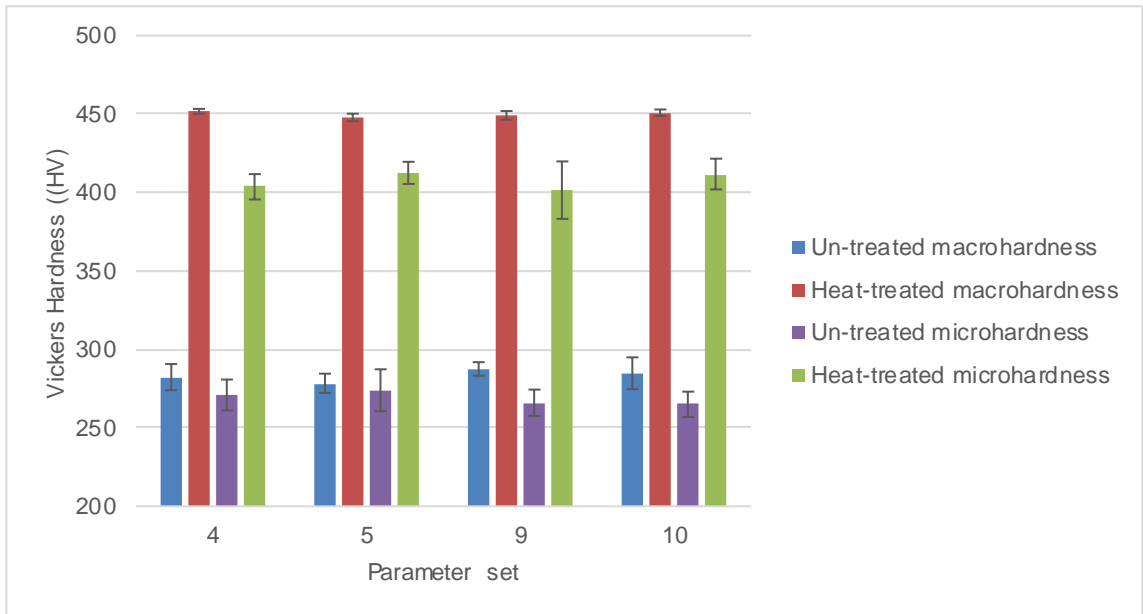


Figure 140: Graph displaying mean values for Vickers macrohardness (HV_{10}) and microhardness ($HV_{0.5}$) of heat-treated samples. Results from Stage 1 large blocks are shown to enable a comparison. Standard deviation is shown.

Chapter 5 – Discussion

This chapter discusses the results obtained during this study. The results are examined as a collective, and unique findings from each stage of work presented.

5.1 Using a Taguchi DOE for the DED-L process

Issues, such as the deposited tracks being unsuitable (insufficient width/height) for building larger thick walled blocks, sample burns (Figure 58), spattering and damage to/from the laser, were encountered during the manufacture of several samples for Stage 1 using the process parameter sets from the Taguchi DOE. This makes it evident that despite choosing a range of process parameter values which were successfully used in the past, building all the combinations generated by the DOE software was not feasible in practice. This shows that this DOE approach is not suitable for the DED-L process when using a wider range of process parameters, and that it should only be used when narrow ranges of process parameter values are being investigated. This may apply to other DOE methods, requiring their exploratory process parameter ranges to be narrowed or adapted to yield combinations which are achievable to fabricate using DED-L.

Due to the the high costs of raw material, and time required for building each specimen, the tests were not repeated using a narrower range of process parameters.

This orthogonal approach was used successfully by Sreekanth et al. (2021) for varying laser power, scanning speed, and powder feed rate at three levels. However their work focused on single tracks of Inconel 718, and they did not determine whether these parameter combinations could be used to build multi-layer/multi-track deposits successfully.

Three process parameters at three levels/values were used for this Taguchi DOE. This creates a “cube” structure of parameter level points, where only certain points are tested within the Taguchi DOE. As some of the process parameter sets within Stage 1 were unsuccessful, this indicates that within this “cube” structure there is a smaller group of process parameter sets which are successful for building multi-layer/multi-track deposits.

As not every process parameter set was suitable for building, this signifies that there are interactions present between the laser power, scan speed, and powder feed rate – meaning that each process parameter value strongly depends upon the values of the other two process parameters. For example, set 7 and set 10 use the same laser power and powder feed rate, however set 7 cannot be built due to its low scan speed whereas set 10 can. This shows that the scan speed value must be increased when depositing larger blocks using these laser power and powder feed rate values.

If the Taguchi DOE been successful, and all process parameter sets could have been built, the results would have been subject to Analysis of Variance to determine the significance of the DOE findings. Following this, the most influential process parameter - from laser power, scan speed, and powder feed rate – could have been identified. However, as only three of the nine Taguchi generated process parameter combinations could be built, further statistical analysis was not performed.

5.1.1 Determining process parameters for stage 2, 3, and 4

The following four process parameter sets were successful in building both sizes of blocks within Stage 1 (Table 46). These were used as a basis for choosing the process parameters for the subsequent three stages of work.

| Set | Laser power at workpiece (W) | Scan speed (mm/min) | Powder feed rate (g/min) | Energy density (J/mm³) | Mass density (x 10⁻³) (g/mm³) | Specific energy density (x 10⁴) (J/g) |
|----------------|-------------------------------------|----------------------------|---------------------------------|--|--|---|
| 4 | 1050 | 500 | 2.9 | 55.2 | 2.5 | 2.2 |
| 5 | 1050 | 750 | 4.0 | 45.1 | 2.9 | 1.6 |
| 9 | 1300 | 1000 | 2.9 | 33.4 | 1.2 | 2.7 |
| 10 | 1300 | 1000 | 4.0 | 30.7 | 1.6 | 2.0 |
| Stages | | | | | | |
| 2, 3, 4 | 995 | 675 | 3.0 | 28.2 | 1.4 | 2.0 |

Table 46: The four process parameter sets which were successful in building, and the values used to fabricate specimens for stages 2, 3 and 4. Energy density, mass density and specific energy density are shown.

- Due to the low hardness values obtained for Stage 1 set 5, process parameters which resulted in similar energy density, mass density, and specific energy density were avoided.
- Greater laser powers increase the probability of spatter and laser damage, thus it was decided to use a lower laser power value of 995 W moving forward.
- To minimise powder lost during the process a powder feed rate of 3.0 g/min was chosen.
- A scan speed which generated a lower energy density than the process parameter sets displayed (Table 24) and a mass density value lying mid-way between set 9 and set 10 was chosen. This was 675 mm/min. The

lower energy density may aid in reducing heat input, producing a more favourable microstructure.

5.2 Sample defects

Consistently low porosity values were noted within samples for all stages of work, with average porosity values ranging from 0.03% to 0.30%. This shows that the DED-L process parameters used throughout this work are efficient in melting the Inconel 718 powder. As the powder used is produced through APA™, a powder production method which minimises pores within the powder, the porosity is highly likely to have been induced by the DED-L process itself. The spherical shaped pores are gaseous pores, whilst the more irregular shaped pores are formed due to solidification shrinkage (Figure 59). This porosity could be eliminated through further optimisation of the process and parameters. Alternatively it could be removed through using HIP following fabrication (Kobryn & Semiatin, 2003).

Process parameters were kept constant during the building of each sample, thus there is high confidence that the values obtained are an accurate representation of the entire sample. As spherical and irregular internal inclusions could not be differentiated from pores using ImageJ, these will have been included in porosity measurements. Thus true porosity can be assumed to be the value obtained or lower. GE Additive suggest that porosity values below 0.5% do not influence the mechanical properties of the part, rendering them suitable for use within industry (GE Additive, 2021). Thus as all porosity values within this work are below 0.5%, porosity should not affect the mechanical properties.

Cracks were absent from most of the OLM examined samples. A prominent crack was present in a Stage 4 sample at the interface between the two build directions (Figure 127). This may have propagated at this interface, extending back into the first part of the sample (build direction 1), and could have formed during the cooling time between the two building directions. Alternatively, it may

have been introduced when the second build direction was used to deposit material onto the cooled material. As no other cracks were noted at this interface within the examined sample it is likely that this occurrence was not related to changing build directions during fabrication.

5.3 Sample microstructure

Etching of the samples revealed microstructures comprised of columnar grains containing dendritic structures. Certain regions contained more refined phases, as seen in Figure 97 and Figure 112.

Under OLM the microstructure was observed to vary in grain size, grain morphology, and phase distribution between the three planes (xy, xz, and yz) (Figure 93; Figure 109). This occurred within all samples except for those which used a 90° rotation of track deposition direction between subsequent layers (Stage 3 vertical samples (Figure 108) and Stage 4 build direction 2). A difference between the three planes is expected when a 90° rotation is not used due to the variation in how the deposition path relates to each plane. The incorporation of a 90° rotation of track deposition direction between layers results in a similar microstructure in the two planes which are parallel to the direction of the laser beam (xz and yz). A similar microstructure cannot be achieved in the third plane (xy) of a part due to the variation in deposition path caused by the directionality of the laser beam – the deposited track is always perpendicular to the laser beam.

Microstructural variation was observable within a single plane (xy, xz, or yz). This is attributed to the heterogenous environment that DED-L creates during deposition. Solidification is key in determining microstructure, and varies throughout the DED-L process, with several factors affecting it. This includes the difference in temperature between the material being deposited and the already solidified material. Heat dissipation also varies throughout the building period as the energy input during building causes heat to accumulate and increase as more layers are deposited. This reduces the temperature gradient

between the already deposited material and the newly deposited material, meaning that solidification of the initial layers occurs at a greater rate than successive layers. It is likely, as Kim et al. (2017) and Bennett et al. (2018) suggest, that during building these samples the cooling rate will have decreased as more layers were deposited until a certain cooling rate was reached, where it will have then stayed relatively constant for the remaining duration of building of the sample.

In addition to the heterogeneity of solidification during building samples, regions of material have undergone re-melting and re-solidification several times during the process, altering the microstructure each time. Re-melting occurs where tracks and layers meet – these regions are clearly highlighted following etching. This signifies that the structure within these regions differs to others, and that the arrangement of phases and degree of elemental segregation varies. Where re-melting takes place the material in proximity is exposed to increases in temperature and undergoes partial re-melting.

5.3.1 Grain morphology

Columnar grain growth was observed through the samples, growing in the direction towards the laser and forming elongated grains (Figure 60; Figure 62; Figure 94; Figure 95; Figure 110; Figure 111). This agrees with previous work (Yang, Du, & Chang, 2018; Mostafa, Rubio, Brailovski, Jahazi, & Medraj, 2017) that grain growth occurs in the direction perpendicular to the largest thermal gradient. In this case the largest thermal gradient is between the molten material and adjacent material/atmosphere.

These grains are visible in the xz-plane and yz-plane of samples. As the xy-plane is orientated perpendicular to the direction of grain growth, this plane contains cross sections of the columnar grains, meaning that examination of the xy-plane alone does not reveal any indication of columnar grain growth (Figure 64).

The columnar grains were observed to extend across multiple tracks and layers. This indicates that as new material is deposited, the upper portion of the grains within the previously deposited layer are re-melted. This provides an opportunity for the grains to grow, extending through into the most recently deposited layer, forming the elongated grains observed. This columnar growth is promoted by the repetitive heat cycling, which promotes grain coarsening (Kim, Cong, Zhang, & Liu, 2017). Grain coarsening can be reduced by incorporating a dwell time between depositing subsequent layers. This allows the deposited material to cool, increasing the temperature gradient between the solidified material and newly deposited molten material, thus increasing the solidification rate. This promotes the formation of finer grains and reduces the opportunity for grain growth (Bontha, Klingbeil, Kobryn, & Fraser, 2006; Everton, Hirsch, Stravroulakis, Leach, & Clare, 2016; Mao, et al., 2002).

Some grains may have extended the full length of the DED-L part, agreeing with Li et al. (2018), that columnar grains can grow the full length of an DED-L part. Grains are most likely to have extended the full length in Stage 3 vertical samples, as these have the smallest area per layer, hence heat build-up is quicker and less cooling can occur between subsequent layers.

In some cases, grains could be seen to develop at a slight angle, aligning towards the horizontal direction that the laser is travelling in for that layer. This occurs due to the thermal gradients from the top of the build downwards and across the newly deposited material and melt-pool as the laser progresses along its toolpath. This can result in a zig-zag pattern (Figure 95) when the track deposition direction alternates between the positive x-direction and the negative x-direction. This trend is less common than the upward grain growth and varies according to the area that the sample has been taken from with regards to track and layer overlap location. If all tracks and layers were deposited in the same x-direction (e.g. all moving in the positive x-direction), the grains would be expected to grow in a continuous diagonal upwards direction, with the diagonal orientated as demonstrated in Figure 141.

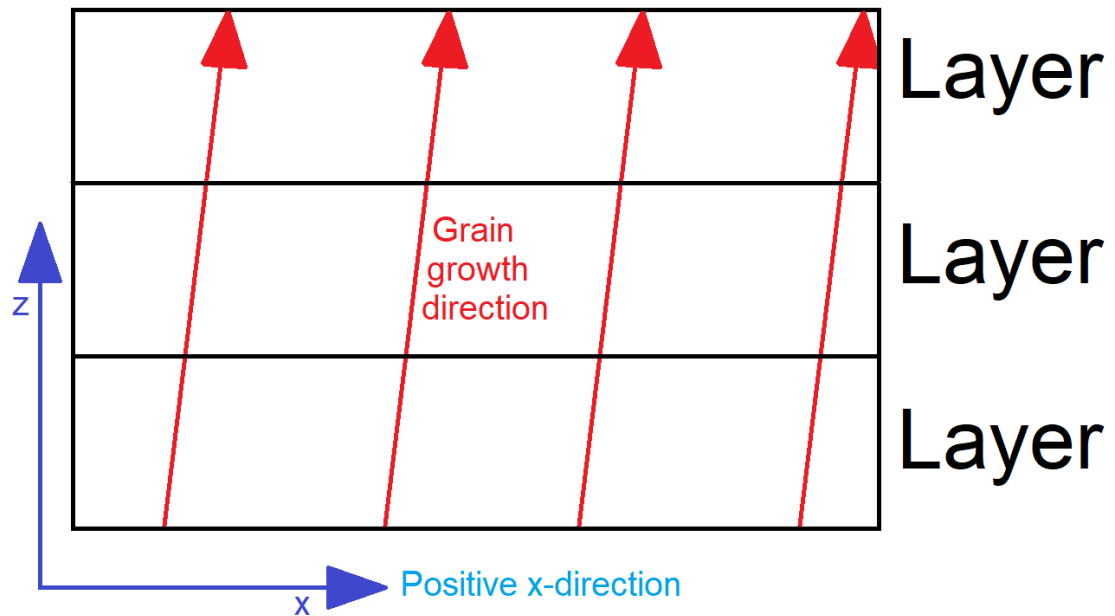


Figure 141: Schematic showing how grain-growth would form in a continuous diagonal direction if the same x-direction (in this case the positive x-direction) was used for all layers.

5.3.2 Microstructural phases

Several phases were observed within the microstructure. These were common to all samples, although the volume fraction of each phase varied between them. As the laser re-melts some of the previously solidified material during the deposition process, there will have been multiple opportunities for precipitates to form and the composition of the re-melted material to change – during the initial cooling of the material, and then again during cooling following any re-melting of material.

When applied to Inconel 718, Kalling's No. 2 etchant readily attacks and corrodes the γ -matrix and intermetallic phases, leaving precipitates such as carbides and Laves phase visible under the microscope. This results in the contrast seen in OLM images (such as Figure 60, Figure 97, Figure 112, Figure 114).

Through comparison of OLM images to ASM Handbook Inconel 718 images (ASM Committee on Metallography, 1972), including those in Table 9, it can be deduced that the light regions seen within the OLM images contain Ni-rich solid solution, in this case the γ -matrix. Darker regions are noted within the interdendritic regions of these images. These consist of possibly carbides and/or Laves phase. Based on previous literature these would be expected to be Nb-rich MC carbides as this is the predominant carbide phase to form in Inconel 718 (Sundararaman, Mukhopadhyay, & Banerjee, 1997).

Under the SEM, phases were further distinguishable from one-another, with five possible phases identified in backscatter electron imaging. Figure 73 (SEM) and Figure 74 (BSE) show these phases. These are the γ -matrix, a white phase (Laves), a phase surrounding the white phase (γ''), a phase within the white phase (γ'''), and a dark phase (carbides). Spherical precipitates measuring $<1 \mu\text{m}$ were also found within samples (Al-oxides) (Figure 71 spectrum 5; Figure 72 spectrum 8; Figure 98 spectrum 3).

EDX mapping indicates that a significant amount of elemental segregation took place during the DED-L process, most likely to have occurred during solidification as opposed to during powder melting. This segregation is influenced by the repetitive heat-cycling, as this provides multiple opportunities for elements to segregate. EDX maps were comparable between samples, finding interdendritic areas to be enriched with Nb, Mo, and Ti. These are the areas which solidify last during solidification (Figure 75; Figure 99; Figure 118). Greatest enrichment of these elements corresponded with the regions containing the white phase and its immediately adjacent material.

5.3.2.1 The γ -matrix

The γ -matrix forms the bulk of samples, taking on a similar composition to the Inconel 718 powder used for building. The dominant presence of γ -phase is expected based on the solidification stages of Inconel 718 (Table 8), γ -phase forms first. Temperature was not monitored for the deposition of these samples.

However the initial cooling of the deposited material can be assumed to reduce the temperature to below 871°C. Thus according to the TTT-diagram (Figure 26), the deposited material remains below the γ -curve, minimising the opportunity for other phases to form as building continues.

5.3.2.2 Laves phase

The white globular phase was seen in all samples under the SEM. The morphology of this phase (Figure 73; Figure 98; Figure 117; Figure 129; Figure 139) resembles SEM images of Laves phase within previous literature, as shown in Table 9 and Figure 27 (as-deposited). EDX point analysis (Table 30 spectrum 2, 3, 4, and 7; Table 36 spectrum 2; Table 39 spectrum 1, 2, 3, and 4; Table 44 spectrum 3 and 4) of this phase found it to contain greater Nb and less Ni, Fe, and Cr than the surrounding matrix and the powder used for fabricating the samples. These EDX results align with previous EDX of Laves phase shown in Table 11. This indicates that the white globular phase is Laves phase, forming in the final stages of solidification and consuming Nb, reducing available Nb for forming hardening phases/precipitates (Carlson & Radavich, 1989; Darolia, Lahrman, Field, & Sisson, 1988).

As previously stated, this phase is detrimental to Inconel 718 mechanical properties as it reduces strengthening phases such as γ from being formed (Witzel, Stannard, Gasser, & Kelbassa, 2011; Zhang Q. , Zhang, Zhuang, Lu, & Yao, 2020). As Laves formation is promoted by increased Nb and Mo segregation, this can be reduced by using a dwell time between depositing adjacent tracks and subsequent layers. This increases cooling rates, reducing Nb and Mo segregation, and hence Laves formation (Bambach, Sizova, Silze, & Schnick, 2018; Shi, Duan, Yang, Gua, & Gua, 2018). Alternatively a suitable heat-treatment can be applied following deposition – these have already been proved to reduce Laves proportions (Cao, Bai, Liu, Hou, & Guo, 2020; Fayed, et al., 2021; Liu, Lyu, Liu, Lin, & Huang, 2020; Sreekanth, Hurtig, Joshi, & Andersson, 2021).

5.3.2.3 γ'' -phase

A phase can be seen to surround the Laves phase (Figure 73 (3); Figure 74 (3)). Li et al. (2020) and Stevens et al. (2017) observed this phenomenon, suggesting that the phase could consist of γ' and γ'' , or γ'' alone. Sui et al. (2017) also observed γ'' to precipitate around Laves phase. Thus, these surrounding regions may consist of a combination of γ , γ' and γ'' , or solely γ'' . As Nb segregates during solidification it can act as a nucleation site for γ'' -phase, which takes the form Ni_3Nb . The EDX maps support the likelihood of these regions containing γ'' as they show the regions surrounding Laves to contain greater proportions of Nb than the matrix (Figure 75).

The fourth phase labelled in Figure 73 and Figure 74 may be the same as the phase noted to surround the Laves phase – a combination of γ , γ' , and γ'' or solely γ'' . Again the EDX maps support the possibility that this phase is γ'' due to the greater Nb content observed.

5.3.2.4 Al-oxide inclusions

The EDX point analysis performed on the $<1 \mu m$ spherical precipitates (Figure 71 spectrum 5; Figure 72 spectrum 8; Figure 98 spectrum 3) found them to contain greater Al than the surrounding material and the original powder. Inclusions found within Inconel 718 are typically oxides (Dupont, Lippold, & Kiser, 2009; Kistler, Nassar, Reutzel, Corbin, & Beese, 2017), suggesting that this inclusion is an Al-oxide. Ti was also observed to increase at this point. In Inconel 718 Yu et al. (2019) observed Ti/Nb carbides to precipitate on the surface of Al-oxide (Al_2O_3) particles, creating a core-shell composite. This may have occurred within these samples. The formation of these oxides suggests that the shielding gas rate was not sufficient to entirely protect the melt-pool from oxidation.

Alternatively, micron-sized Al-oxides have been previously noted in virgin plasma atomised Inconel 718 powder (Gruber, Luchian, Hryha, & Nyborg, 2020;

Sadeghi, et al., 2020), meaning that the observed <1um Al-oxides seen within these samples possibly formed during powder manufacture.

5.3.2.5 Carbides

Evidence of carbides was noted under the OLM, precipitating within interdendritic regions. Examination under the SEM found further evidence of carbides, appearing as small dark precipitates (Figure 73 (5); Figure 74 (5)) which corresponded with the carbides shown in the BSE image in Table 9.

As Sreekanth et al. (2021) suggest, further carbides may form amongst the observed Laves phase, rendering the carbides effectively indistinguishable under the OLM and SEM.

From these observations it can be concluded that the final microstructure formed consists of dendritic γ -matrix, and interdendritic Laves phase, γ'' -phase, and carbides.

5.3.2.6 Phase distribution

As all OLM images show, these phases are not distributed uniformly through the sample. Instead, dendritic segregation was observed in all of the samples. Dendritic segregation is the preferential distribution of alloying elements in the dendritic growth of a solid-solution phase from a melt. As a general principle, the element with a higher melting temperature solidifies preferentially from the parent melt, which progressively results in the remaining melt to become increasingly enriched with lower melting temperature elements. In this case, the interdendritic regions were found to be enriched in elements other than Ni. This non-uniform segregation is expected due to the variation in track cooling rates, solidification, and repetitive re-melting and re-solidifying cycles – as each time material undergoes re-melting there is an opportunity for elements to segregate and phases to change.

As re-melting of the solidified tracks and layers occurs during the DED-L process, material adjacent or below the re-melted material is affected by heat – resulting in a heat-affected region and possibly causing some partial melting of material, this is illustrated in Figure 142. In this heat-affected region, phases are altered and may change in distribution – thus the DED-L process is essentially acting to heat-treat these areas of material. In this case the region affected by heat can be seen to contain a more refined structure of phases as compared to the more typical dendritic structure seen through the samples. In Figure 97, this is clearly shown – changing from dendritic to refined and then back to dendritic. These heat-affected regions occur at the meeting points of tracks and layers, making them clearly visible under OLM, and will alter how the material behaves in these regions. This contributes to the variation in material properties throughout a component, with the refined region likely to possess greater hardness and tensile strength due to its more homogenous phase distribution.

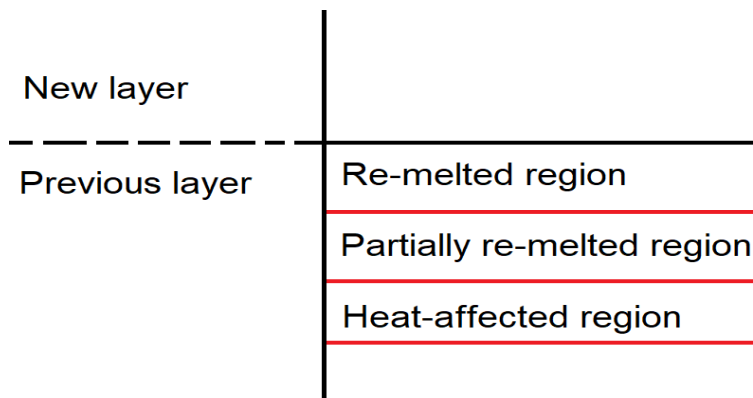


Figure 142: Schematic of the re-melted and heat-affected regions induced when a new layer is deposited onto a previous layer. Diagram is not to scale.

5.3.3 Track (yz-plane) and layer (xz-plane) microstructure

This visibility of tracks and layers is due to heterogenous elemental segregation and phase distribution when moving through the track cross section or layer. In this case the lighter regions contain γ -phase, whilst the dark consists of Laves,

carbides, and possibly some γ'' -phase. This occurs consistently across tracks and layers.

In Figure 62, Figure 96, and Figure 111 (yz-plane) overlapping track edges can be seen. Moving from the centre of a deposited track towards the meeting point of adjacent tracks an increase in Laves and carbide phases can be seen, with a clear line of these where the tracks meet.

Similarly, in Figure 60, Figure 94, Figure 95, and Figure 110 (xz-plane) individual layers can be seen. Moving upwards through a layer, from the lower region to the upper region, an increase in Laves and carbide phases, and decrease in γ -phase can be seen under the OLM. This is followed by a visible line of Laves and carbides where the initial layer meets the subsequent layer that has been deposited on top of it. Again, the lower region of this subsequent layer contains greater γ -phase than its upper constituent.

These observations occur consistently across tracks and layers throughout the samples. The variation in phase volumes are caused by the different solidification rates of the upper, middle, and lower regions of the deposited track. This results in segregation within the track, as different phases and precipitates form at different temperatures once cooling commences. As outlined in Table 8, γ -phase forms first from the molten liquid during solidification, whilst Nb and C start to segregate. This results in the greater γ -phase seen towards the bottom of the track/layer, which solidifies first (Figure 61). Carbides and Laves form after this, promoted by the segregation of Nb and C, hence resulting in their increased proportions towards the upper region of the track/layer which solidifies last.

Elemental segregation also varies between the regions. When a successive track or layer is deposited, a portion of the previous track or layer is re-melted. Previously solidified phases enter solution, and elements segregate and re-distribute during this re-melting; this is influenced by the dissolution temperatures of different phases and precipitates. This means that phases with

a lower dissolution temperature enter solution prior to others, altering the molten material composition. As the re-melted region solidifies, its composition, and phase distribution differs from what it was prior to being re-melted.

5.3.4 Stage 1 – comparison of parameter sets

OLM images did not reveal any key differences in microstructure between the different parameter sets. Examination under the SEM found Laves phase to be present within all of the large and small blocks, however it varied in distribution, shape, and hence appearance between parameter sets (Figure 68; Figure 69).

Comparison of small block SEM images found Laves to form in networks, appearing chain-like, extending towards the direction of the laser. These are most prominent within small block 10, whilst within small block 4 the phase is more evenly distributed, appearing as a discontinuous network. Long interconnected chains of Laves phase are reported to be more detrimental to mechanical properties than separate particles due to the brittleness of the phase (Radhakrishna, Prasad Rao, & Srivivas, 1995; Janaki Ram, Venugopal Reddy, Prasad Rao, & Madhusudhana Reddy, 2004).

In the large blocks, block 5 Laves phase is uniformly spread throughout the sample. Large block 9 also shows Laves phase to spread more uniformly, whilst the other large blocks (4 and 10) exhibit more tendency towards Laves phase forming in a continuous network.

5.3.4.1 Nb-rich phase

Values for the proportions of Nb-rich phase (Table 29) were similar between the small blocks (within a range of 2.05%) , and similar between the large blocks (within a range of 4.86%) except for set 9 which was much greater. Although the white globular phase has been identified as Laves phase, some NbC may be included within this white fraction if present within the sample. Sreekanth et al. (2021) suggest NbC and Laves phase possibly coexist within eutectic

regions, with differentiation difficult due to increased volumes of Nb noted by EDX analysis.

Small block 4 and 10 contain greater volumes of Nb-rich phase than the other two small blocks, whilst large block 9 Nb-rich phase was substantially greater than values for the other large blocks. This indicates that any effect induced by the selected combination of process parameters used is not consistent between the two sizes of block. The observations made for Nb-rich phase do not correlate to variations within energy density, mass density, specific energy density, SDAS, or Vickers Hardness.

5.3.4.2 Secondary Dendrite Arm Spacing

Significant differences were present for SDAS between small blocks 4 and 9, and between small blocks 5 and 9 (Table 28). SDAS increases through small blocks from 9, to 10, to 4, to 5. This corresponds to increasing mass density values (Table 24), suggesting that mass density may play a role in determining SDAS. It also corresponds to decreasing specific energy density. Powder feed rate is used to calculate mass density and specific energy density, suggesting that powder feed rate is key in regulating SDAS.

Previous work has linked SDAS to decrease as cooling rate is increased (Vandersluis & Ravindran, 2017; Chen & Mazumber, 2017). Set 5 had the greatest mass density and lowest specific energy density values, meaning that heat build-up will have been lowest within small block 5 compared to the other small blocks. This low value of specific energy density would aid in increasing the cooling rate, hence it would be expected for small block 5 to have smaller SDAS than the other small blocks, however this was not observed. Total time spent building and fully cooling could have been a factor altering cooling rate, however based on large block sample build times (Table 25) set 5 small block will have taken less time to build than set 4 and set 9 small blocks. This indicates that the total time spent building and fully cooling does not impact SDAS values as small block 5 SDAS exceeded small block 4 and 9 SDAS. As

previously stated, powder feed rate could be key in regulating SDAS. Thus the powder feed rate used for set 5 blocks may have not been suitable in conjunction with the laser power and/or scan speed, with specific energy density too low, or mass density too high to obtain the finer SDAS that would be expected.

No significant difference was present between large block SDAS. This could link to the greater build time required for large blocks, promoting heat accumulation, and increasing the time spent at high temperature, eliminating the differences seen between small block SDAS process parameter sets.

5.3.5 Stage 1 – comparison of built sample size

The difference in block size will have resulted in different solidification/cooling rates. This is influenced by several factors.

- Total layer area is smaller for small blocks as compared to large, this could increase heat build-up due to less time between depositing subsequent layers, and thus less cooling time, in turn decreasing cooling rates. Although there was less time between depositing subsequent layers for small blocks the total area of the layer to cool was smaller.
- Block height is less for small blocks, meaning that the heat conduction into the substrate during building played a role in aiding cooling for a greater proportion of the total deposited material for the small blocks. Heat accumulation increases with each deposited layer in the DED-L process to a certain point. Thus heat accumulation during building is unlikely to reach the same levels as large blocks.
- Total build time was less for small blocks, reducing the time spent at higher temperatures and thus time for heat accumulation, aiding cooling.

Due to these differences it is presumed that small blocks will have had greater cooling rates than the large blocks.

OLM did not provide a good representation of whether the block size affected microstructure. SEM found Laves to form networks within both small and large blocks (Figure 68; Figure 69).

5.3.5.1 Nb-rich phase

The proportion of Nb-rich phase, and hence Laves, was consistently less in small blocks compared to their large counterpart (Table 29). This links to the differences in cooling rates with small blocks having greater cooling rates. Slower cooling rates increase the time period for Nb to segregate, as well as time spent at Laves precipitation temperature (Table 8), increasing its volume. These findings agree with previous work which observed Laves phase to decrease when cooling rate is increased (Bambach, Sizova, Silze, & Schnick, 2018).

5.3.5.2 Secondary Dendrite Arm Spacing

SDAS varied significantly between the small and large blocks except for parameter set 5 (Table 28). Smaller SDAS is associated with increased cooling rates (Vandersluis & Ravindran, 2017; Chen & Mazumber, 2017). This agrees with these findings – it would be expected for smaller SDAS for the small blocks as cooling rates are greater.

This exception seen for parameter set 5, finding small block SDAS to lay close to large block SDAS, is unexpected. As previously discussed, the powder feed rate used for set 5 blocks may have not been suitable in conjunction with the laser power and/or scan speed, with specific energy density too low, or mass density too high to obtain the finer SDAS that would be expected.

5.3.6 Stage 2 – microstructure anisotropy within a single part

The block built clearly displays the anisotropy expected for an as-deposited DED-L part, this includes the columnar grains and segregation of phases

(Kobryn & Semiatin, 2003; Mostafa, Rubio, Brailovski, Jahazi, & Medraj, 2017; Shamsaei, Yadollahi, Bian, & Thompson, 2015). Each plane (xy, xz, and yz) consists of a distinctive microstructure (Figure 93), uniquely formed according to its orientation regarding the laser beam and laser scan path. This anisotropy will occur within all as-deposited DED-L parts and can be removed through heat-treating as demonstrated by Zhong et al. (2016).

5.3.7 Stage 3 – effect of build direction on microstructure

Microstructures differed between horizontal and vertical samples – individual vertical sample planes were more heterogeneous in terms of microstructure and phase distribution (Figure 114; Figure 115). These discrepancies can be attributed to variations in thermal cycling and heat build-up during the process. Vertical samples were greater in height than horizontal samples, and had a smaller area per layer, hence shorter cooling time between depositing subsequent layers. This combination resulted in quicker cooling rates and lesser heat build-up within horizontal samples.

Whilst building the vertical samples, previously deposited layers were observed to glow orange as further layers were deposited – when the final layer was deposited on the vertical sample approximately one third of the height below this layer was incandescent. This was not seen in any other samples within this work, indicating that the material deposited during building the vertical samples remained at greater temperatures than the other samples for longer. This temperature was not measured, but is significantly greater than 525°C (the temperature which solid materials glow visibly (Wilkie & Weidlich, 2011)). Based on previous work on the Trumpf 505 DMD system where temperature was monitored, it is presumed to have lain between 650°C – 800°C. If this temperature was greater than 700°C then ageing will have occurred within the incandescent material as building progressed, promoting the transformation of γ -phase to γ' and γ'' according to the TTT diagram (Figure 26). It will have also significantly reduced the cooling rate of the material for each layer, again altering the microstructure. A slower cooling rate increases Nb and Mo

segregation during solidification, promoting Laves phase and carbide formation (Shi, Duan, Yang, Gua, & Gua, 2018; Bambach, Sizova, Silze, & Schnick, 2018).

The finer homogenous dendritic structure observed in horizontal samples (Figure 114) compared to vertical samples (Figure 115), which contained larger columnar dendrites, can be attributed to the longer cooling time between subsequent horizontal layers. The variation in heat build-up between the two build directions will have also influenced this, with the increased heat build-up in vertical samples increasing the probability of the columnar grains growing through the entire length of the vertical samples (Li, et al., 2018).

Another source of the microstructural variation between the two build directions was the 90° rotation in track deposition direction used between subsequent layers for vertical samples.

Differences were also noted under the SEM. Laves phase formed in long chains extending upwards through vertical samples (Figure 117), parallel to the laser. In horizontal samples this phase was more evenly distributed (Figure 116). This agrees with previous work (Xiao, Li, Han, Mazumder, & Song, 2017) that greater cooling rates decrease the tendency for chain-like formation. This can be attributed to the greater accumulation of heat within vertical samples.

Previous work has observed Laves phase to decrease when cooling rate is increased (Bambach, Sizova, Silze, & Schnick, 2018), thus based on individual layer area of horizontal and vertical samples this means that horizontal samples would be expected to contain less Laves phase.

5.3.8 Stage 4 – effect of an interface on microstructure

In Stage 4, despite the cooling time between switching build directions, grains continued to extend through the interface (Figure 126). This indicates that the grains observed in the initial layers of the second build direction originated from those grains formed in the first deposited section despite the difference in

orientation and cooling. This is due to the re-melting of the previously cooled material, and thus grains, that occurred during the deposition of the first layer using the second build direction.

SEM examination found the sample to differ between the two build directions (Figure 128), containing similar structures to those observed in previous stages of work, notably Stage 3 (Figure 116; Figure 117). This is due to the toolpath and process parameters used for building the first section (build direction) of the sample being the same as for building the horizontal samples in Stage 3, whilst the second section (build direction 2) was built in the same way as Stage 3 vertical samples. This resulted in the microstructures within the two different build directions to correspond to Stage 3 horizontal and vertical samples accordingly.

The differences observed between the two different build direction sections can be attributed to the differences in thermal cycling and heat build-up that were experienced, as different deposition scan strategies were used. Laves phase can be seen throughout the sample; more evenly distributed in build direction 1, whilst forming a continuous network in build direction 2, with Laves extending parallel to the laser and build direction (Figure 128). This corresponds to that observed for Stage 3 horizontal and vertical samples. The transition point of Laves phase structure between the two directions is evident and appears to be immediate.

5.3.9 Stage 5 – effect of a heat-treatment on microstructure

The microstructure was altered considerably following heat-treatment (Figure 137). The as-deposited columnar dendritic structure was refined to an equiaxed structure during heat-treating, reducing the microstructural anisotropy seen throughout individual samples, and corresponding to previous observations (Zhong, Gasser, Kittel, Wissenbach, & Poprawe, 2016; Yuan, et al., 2018).

Laves phase was reduced in volume (Figure 138), dissolved by the heat-treatment, and prevented from re-precipitating. This released the Nb previously held within the Laves phase, making it available to form the hardening phases γ' and γ'' (Ma, Wang, & Zeng, 2015; Parimi, Ravi, Clark, & Attallah, 2014; Zhong, Gasser, Kittel, Wissenbach, & Poprawe, 2016; Manikandan, Sivakumar, & Kamaraj, 2019; Radhakrishna & Prasad Rao, 1997). This corresponds to the observations made by Sreekanth et al. (2021) regarding heat-treatments and Laves.

No δ was observed following Stage 5 heat-treatment. According to the TTT diagram (Figure 26) Stage 5 solution anneal temperature (980°C/1hr) lies just left of the δ curve, preventing its formation during this time. During cooling from this temperature there was insufficient time for δ precipitation ($\gamma \rightarrow \delta$), resulting in its absence from samples.

5.4 Tensile properties

All samples within this study displayed lower tensile strengths than the standard for untreated wrought Inconel 718 (Table 6, 0.2% proof stress 725 MPa, UTS 1035 MPa). This reduced strength is attributed to the columnar grain structure which formed in samples during building, and the Nb segregation observed using EDX analysis. Nb segregation is already known to have a detrimental effect on Inconel 718 properties as it promotes Laves phase formation, reducing or preventing strengthening phases from being formed and lowering mechanical properties (Witzel, Stannard, Gasser, & Kelbassa, 2011; Zhang Q. , Zhang, Zhuang, Lu, & Yao, 2020).

Stage 1 set 4 0.2% proof stress (Table 31, 700 MPa), Stage 2 set 1 UTS (Table 37, 1013 MPa) and Stage 3 horizontal UTS (Table 40, 1024 MPa) results are close to the standard value for untreated wrought Inconel 718 (0.2% proof stress 725 MPa, UTS 1035 MPa). This suggests that as-deposited DED-L components may have the potential to meet or exceed the standard value for untreated wrought Inconel 718 following further process parameter optimisation.

As previously stated, SDAS is the microstructural feature within dendritic microstructures which can be related to material strength and hardness (Vandersluis & Ravindran, 2017; Chen & Mazumber, 2017). However, as Figure 143 shows, there was no correlation found between SDAS and the tensile properties in this work.

Similarly when plotted against grain width (Figure 144) – which can be related to tensile strength using the Hall-Petch equation (Equation 2) – no correlation can be observed.

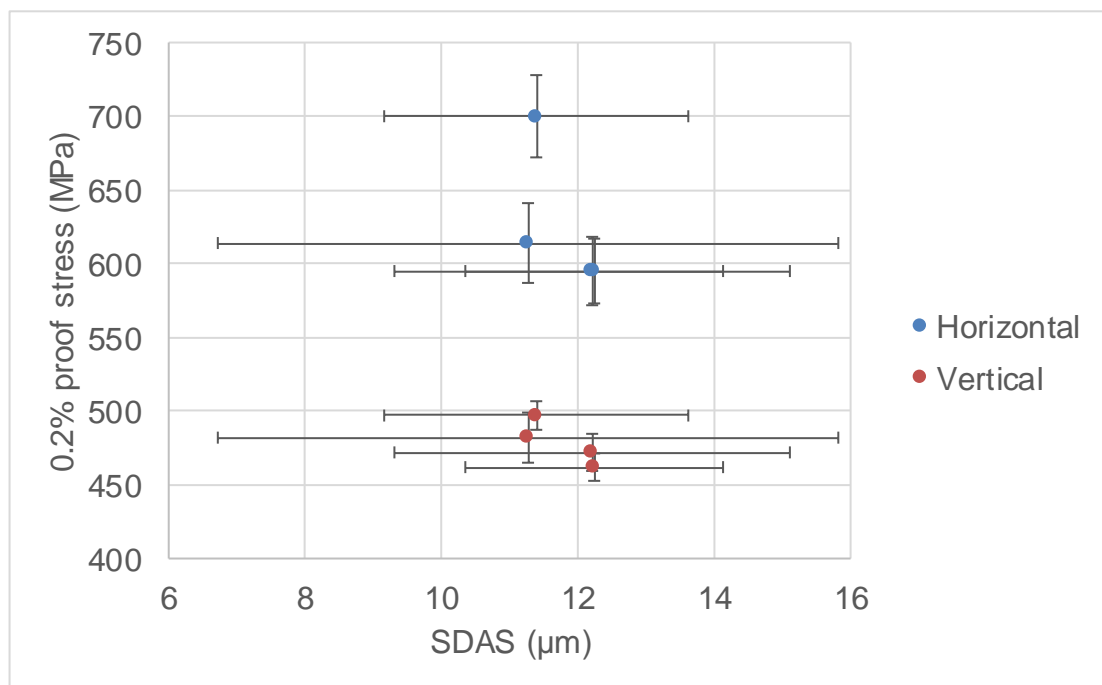


Figure 143: Graph displaying SDAS plotted against 0.2% proof stress for the Stage 1 tensile samples. Standard deviation is shown.

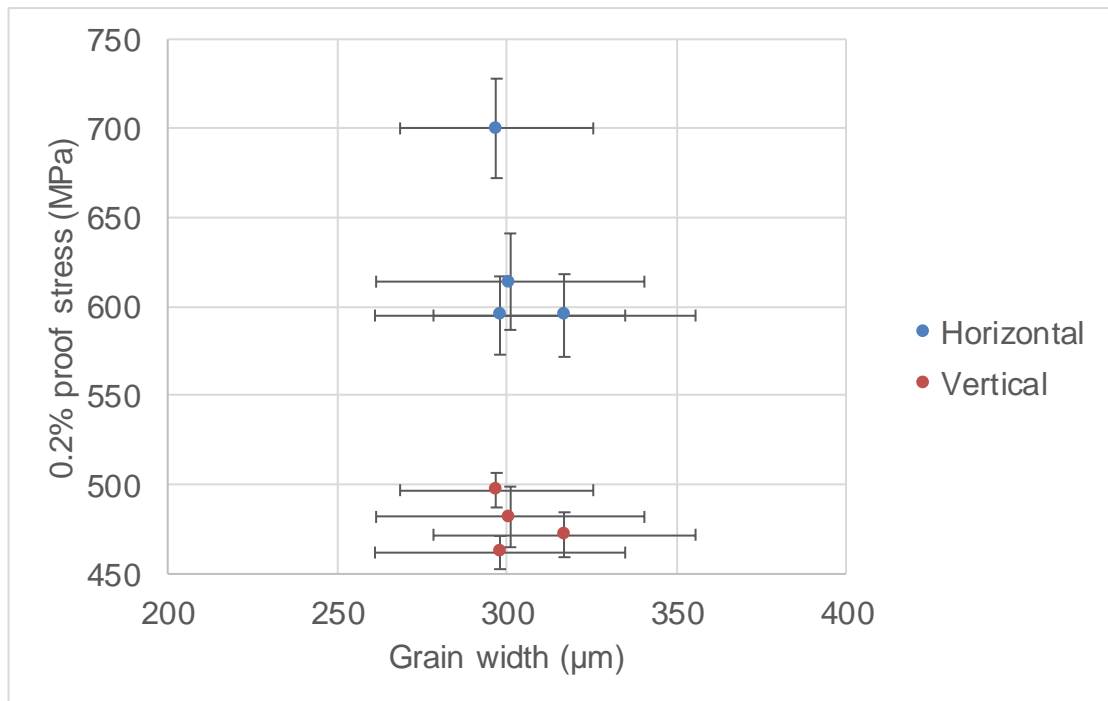


Figure 144: Graph showing average grain width plotted against 0.2% proof stress for Stage 1 samples. Standard deviation is shown.

Laves volume, energy density, mass density, and specific energy density were also plotted against 0.2% proof stress to examine for any correlation present, however none was found. This suggests that another factor is involved in influencing the tensile properties of the samples, altering the usual relationships present between SDAS and tensile strength, and grain width and tensile strength.

DED-L results in a complex microstructure containing multiple interfaces between tracks and layers. These could affect the relationship between SDAS/grain width and tensile strength, with interfaces acting as a boundary-type feature, altering how the material behaves in this region.

This could occur due to the following:

- 1) Track deposition direction alternates between adjacent tracks and subsequent layers, changing the direction that solidification of molten material occurs. This causes dendrite orientation, and phase

alignment and orientation, to change at the meeting point of adjacent tracks and subsequent layers.

- 2) The meeting points of tracks and layers contain more Laves and carbides as compared to a tracks central region. As grains extend across multiple tracks and layer, this results in non-uniform phase distribution throughout an individual grain, with regions containing greater Laves and carbides behaving differently.

As this work varied the geometry of builds and process parameters, the effect of the track and layer interfaces could not be determined.

Tensile specimens orientated parallel to the direction of grain growth (referred to as vertical specimens) consistently displayed lower UTS and 0.2% proof stress than tensile specimens orientated perpendicular to the direction of grain growth (referred to as horizontal specimens). Figure 145 shows how grains lay within a horizontal and a vertical tensile specimen.

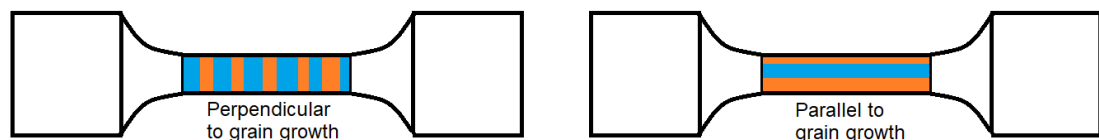


Figure 145: Schematic of how grains lay within tensile specimens taken perpendicular to (left: horizontal), and specimens taken parallel to (right: vertical), grain growth. Grains are indicated by blue and orange and are not to scale.

These observations for tensile properties go against what would be expected due to the orientation of the columnar grains. Their orientation means that in the vertical specimens the grain widths perpendicular to the applied tensile force applied are smaller, as compared to the grain widths which are perpendicular to the applied tensile force in the horizontal specimens. This would typically increase strength (Selcuk, 2011; Whang, 2011).

The differences in tensile properties according to a specimens orientation with regards to the build direction/columnar grain growth have been previously observed in laser-powder AM (Kok, et al., 2018; Sames W. , List, Pannala,

Dehoff, & Babu, 2016), with vertical tensile specimens predominantly noted to have lower yield strength and UTS compared to horizontal specimens.

Explanations for these differences are limited within DED-L. The reasoning behind these observations using Laser Powder Bed Fusion largely focuses on the number and orientation of layers (Rafi, Starr, & Stucker, 2013; Strößner, Terock, & Glatzel, 2015), and may apply to DED-L. Vertical specimens contain more layers as compared to horizontal. These align perpendicular to the tensile force in vertical samples, and parallel to the tensile force in horizontal samples. As layers are deposited, fabrication defects can form between the previous and subsequent layer. These align perpendicular to the applied tensile force in vertical specimens, opening at a lower stress level when the force is applied, increasing void nucleation and coalescence at these layer-layer interfaces. The greater number of layers also provides more opportunity for this to occur. However in horizontal specimens the defects align parallel to the applied tensile force, making them more difficult to open (Rafi, Starr, & Stucker, 2013).

Another explanation uses the number of layer-layer interfaces perpendicular to the applied tensile force, and the microstructure heterogeneity and non-uniform γ distribution to explain the variation in tensile properties. Nb was revealed to segregate at the layer-layer interfaces, suggested to create weak points within specimens, increasing susceptibility to fracture. Vertical specimens contain more of these Nb-rich regions due to their increased number of layers (Strößner, Terock, & Glatzel, 2015), these lie perpendicular to the applied tensile force, increasing fracture susceptibility.

Both of these explanations ignore the interfaces which form between adjacent tracks, which are also susceptible to fabrication defects and Nb segregation, thus would impact tensile properties.

Based on these suggestions, layer thickness (obtained using the z-increment) – which relates to the number of layers within a sample – was plotted against the 0.2% proof stress values (Figure 146). No correlation was found. However, this

is not conclusive as different geometries and process parameters were used within this work. Therefore it is possible that the orientation of tensile sample with regard to layers, and thus number of layer-layer interfaces, could affect tensile properties.

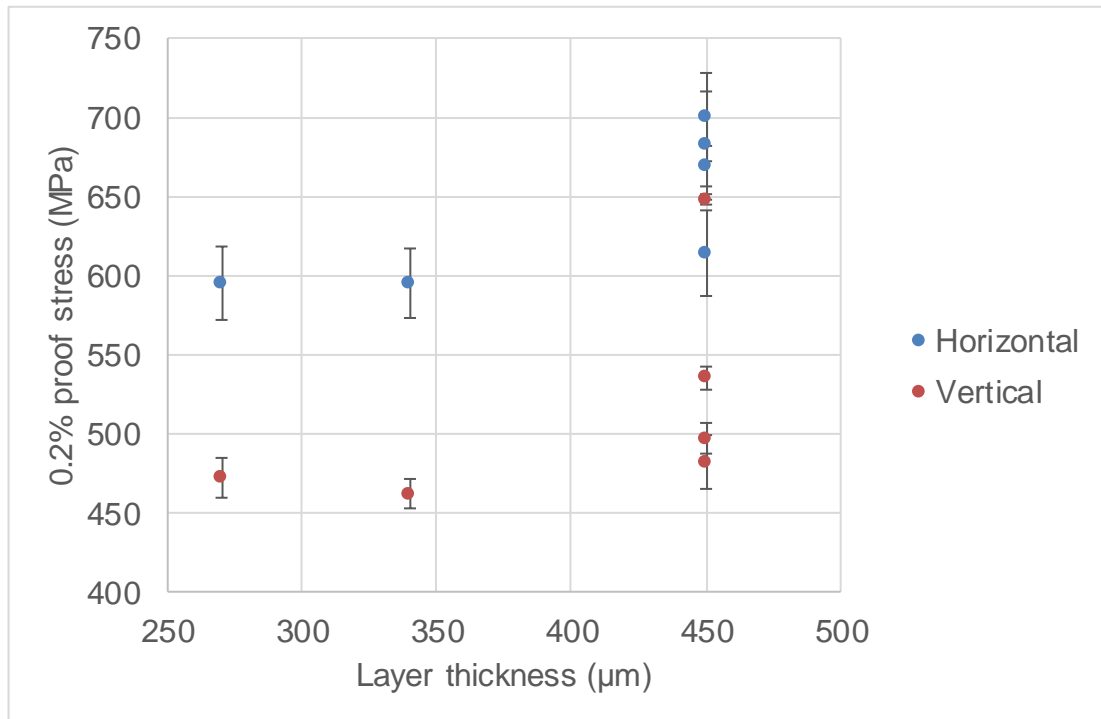


Figure 146: Plot of layer thickness against 0.2% proof stress (MPa) for Stage 1, 2, and 3 samples. Standard deviation is shown.

Similar to Strößner, Terock, & Glatzel, (2015) this work observed microstructure heterogeneity, non-uniform γ'' distribution, and Nb segregation (within Laves and carbides) at the layer-layer interfaces. This heterogenous phase distribution across layers and tracks will have influenced tensile properties according to their orientation with regards to the tensile specimen. Tensile specimens aligned parallel to the laser run upwards through multiple layers, crossing many layer-layer interfaces. This means that they cross, and contain, more track/layer upper regions, which contained greater proportions of Laves and carbides as compared to the lower regions. Thus vertical tensile specimens will contain greater Laves volume than horizontal. This has been suggested to increase the opportunity for cracks or failure to initiate (Schirra, Caless, & Hatala, 1991; Darolia, Lahrman, Field, & Sisson, 1988). However, under the SEM

precipitation hardening phase γ'' was observed around the periphery of Laves. This will impede dislocation movement, whilst carbides are known to cause pinning, further hindering dislocation movement (Song K. , 2008).

The networks of Laves phase align in a chain-like manner, parallel to the laser and grain growth in samples, hence Laves orientation regarding tensile testing direction differs between the horizontal and vertical tensile specimens. As Laves is associated with γ'' around its periphery, γ'' orientation with regard to the tensile specimens also differs. The different orientations of these phases will affect tensile properties.

The differences between horizontal and vertical tensile specimens may also link to the previous discussion regarding the track and layer interfaces acting as boundary-type features, affecting dislocation movement through the sample and altering the expected relationship between columnar grain orientations and tensile strength.

As Figure 95 shows, grains may form a zig-zag pattern, growing neither preferentially in the positive or negative x-direction, developing upward through the sample as tracks are deposited alternately in the positive x-direction and the negative x-direction. This potentially increases the tensile properties of a tensile specimen aligned in the x-direction as compared to a sample which has been deposited using a single x-direction (positive or negative). This is due to the effect that alternating the deposition direction has on the angle of grain boundaries. With regards to the tensile specimen, it ensures grains extend parallel to the laser, and perpendicular to the tensile specimen and force applied. Using a single x-direction for deposition causes grains to grow orientated at an angle towards the x-direction used for deposition (Figure 141), altering tensile properties along this direction.

Elongation, and thus ductility, was greater in the tensile specimens which were aligned parallel to the direction of grain growth. This correlates with the observations for 0.2% proof stress and UTS.

5.4.1 Stage 1 – comparison of parameter sets

Few significant differences were present between the tensile properties of the four process parameter sets (Figure 76; Figure 77; Figure 78). Notably the 0.2% proof stress results for set 4 horizontal tensile specimens were greater than the other sets (Table 31; 700 MPa). Despite this, set 4 vertical 0.2% proof stress was not significantly greater than the others (Table 30; 497 MPa).

The 0.2% proof stress mean values obtained for all parameter sets were within a range of 106 MPa for horizontal samples and 36 MPa for vertical samples. UTS mean values were within a range of 40 MPa (horizontal samples) and 55 MPa (vertical samples) (Table 31). The narrow range for these values indicates that the differences noted between the microstructures of the different parameter sets were not sufficient to have significantly impacted the tensile properties of the samples, and are therefore unlikely to be significant.

Set 4 and set 10 horizontal tensile specimen elongation was observed to significantly vary from other horizontal sets, with set 4 elongation (Table 32; 11.3%) significantly lower than other values and set 10 (Table 32; 31.3%) significantly greater (Figure 78). No significant differences were present between vertical tensile specimen elongation. Elongation for tensile specimens typically correlates with tensile strength – greater tensile strength is associated with reduced elongation. This was not consistent within the horizontal tensile specimens. Despite set 10 horizontal tensile specimen having similar 0.2% proof stress to horizontal sets 5 and 9, and similar UTS to horizontal sets 4, 5 and 9, a significantly greater elongation value was seen. This links to the low porosity observed in set 10 (large block) (Table 26). This lower porosity increases the material cross sectional area, reducing the opportunity for cracks to form and increasing elongation.

5.4.2 Stage 1 – comparison of tensile specimen location

When the change in 0.2% proof stress and UTS were plotted moving across and moving downward through the large blocks, only one consistent difference was observed (Figure 79; Figure 80). The 0.2% proof stress of the horizontal tensile specimen taken from the bottom of the blocks was greater than the other horizontal tensile specimen locations. This lowest region experienced different cooling rates due to the accumulation of heat during the fabrication process, the bottom region of the sample experiences greater cooling rates than the upper part of the sample. This is aided by heat conduction into the substrate. The lower region of the sample experienced elevated temperatures for the longest time period due to continuous heat conduction from newly deposited material. These factors possibly altered phase fractions here compared to the middle and upper regions of the block, contributing to the slightly greater 0.2% proof stress observed.

No trend in changing (increasing or decreasing) 0.2% proof stress was observed for vertical tensile specimens, and no trend in changing UTS for horizontal or vertical tensile specimens was observed either. This indicates that for a DED-L build of this size, 0.2% proof stress and UTS reside within a narrow range of values throughout the entire sample. This could be linked to the heat that builds up within the sample. There is little time for the material to cool prior to the subsequent track/layer being deposited. Following deposition of the initial layers heat dissipation decreases, causing the sample to retain heat. This is due to the limited area for it to disperse to from the sample, and the low thermal conductivity of Inconel 718 (Careri, et al., 2021). Except for the initially deposited layers, very outer edges of the block and upper layers – most of the deposited material for the block experiences similar thermal cycling and temperatures. This results in a similar microstructure for tracks and layers moving across and moving downward through the large blocks, and thus consistent tensile properties.

This may not be true for larger sized, or more complex geometry DED-L builds. An increase in size will alter the cooling rates, and changes in geometry will alter these and possibly also cause variation in cooling rates across a part. These alterations and variation will affect the microstructure, potentially resulting in different microstructures across a component and thus influencing tensile properties.

5.4.3 Stage 2 – comparison of tensile specimen orientation

Tensile testing observed significant differences in tensile properties (Figure 101; Figure 102). The specimens taken running parallel to the deposited tracks (set 1) had the greatest 0.2% proof stress and UTS (699 MPa, 1013 MPa) whilst the specimens parallel to the laser beam (set 3) had the lowest (535 MPa, 781 MPa). Set 2 results reside between the values of sets 1 and 3, with an average closer to the average result of set 3.

Due to their different orientations within the block, small variations in phase volumes, and their arrangement, were present between the three tensile specimens. This will have affected the movement of dislocations through the sample, and hence tensile properties.

It could be presumed that set 1 and set 2 would have similar values for strength due to their orientation with regards to the grains and layers – they are perpendicular to the grains. However, this was not the case with average values for 0.2% proof stress differing by 68 MPa and UTS by 182 MPa. This indicates that the orientation of tensile specimen with regards to the direction of track deposition alters tensile properties. Set 1 specimens aligned to the direction that the tracks were deposited in, whilst set 2 specimens were perpendicular to these, running across numerous tracks.

Set 2 tensile specimens will have contained more track-track interfaces moving along the length of the tensile specimens. Laves and carbides were noted to increase towards the edges of the track, at the track-track interface, therefore

the tensile specimens will have crossed more regions containing these phases. This increases the opportunity for cracks or failure to initiate, decreasing tensile strength (Schirra, Caless, & Hatala, 1991; Darolia, Lahrman, Field, & Sisson, 1988).

5.4.4 Stage 3 – effect of build direction on tensile strength

Horizontal tensile specimens displayed greater tensile strength than the vertical tensile specimens, and lower elongation, indicating decreased ductility (Figure 119; Figure 120). This is as expected based on Stage 1 and 2 results which have shown the vertically aligned tensile specimens to possess lower strength than the horizontal.

Despite Stage 3 vertical samples displaying lower tensile strength than horizontal samples, values are greater than all Stage 1 and Stage 2 vertically aligned tensile specimens, and Stage 1 horizontal tensile specimens (except set 4). This indicates that the perpendicular tensile strength within Stage 3 vertical samples will exceed that of all the horizontal tensile samples within this work. This increased strength is attributed to Stage 3 vertical samples containing greater volumes of hardening phases γ' and γ'' , formed due to ageing of γ within the incandescent material as building progressed.

5.4.5 Stage 4 – effect of an interface on tensile strength

All tensile specimens fractured in the half which corresponded to the second build direction (Figure 131), with 0.2% proof stress (637 MPa) and UTS values (914 MPa) similar to the values for Stage 3 vertical samples (Figure 130; 648 MPa, 916 MPa).

This value and location of fracture were expected based on Stage 3 tensile testing results (Figure 119). Stage 3 vertical samples displayed lower tensile strength properties compared to horizontal, thus it is expected that the samples built using the combination of the two build directions would fail in the second

section (build direction 2), which corresponded to the vertical sample build strategy.

This result could also indicate that the interlayer bonding at the interface between the two build orientations is stronger than the interlayer bonding between adjacent layers in the build direction 2, however it cannot be determined whether the interlayer bonding at the interface is stronger than the bonding within the section built using build direction 1.

Despite UTS corresponding to Stage 3 vertical samples, elongation results for the tensile specimens (20.2%) were akin to Stage 3 horizontal samples (20.0%), not Stage 3 vertical samples. This suggests that the section built using the first build direction, which used the same toolpath and process parameters as for Stage 3 horizontal samples, will have similar mechanical properties to these horizontal samples. It also indicates that the elongation, and hence ductility, of the samples built using two build directions was limited by the microstructure formed within the first build direction section. Thus, despite the interface itself not being seen to have had a detrimental effect on tensile properties, the specimen displays the lesser values for both strength and elongation that were observed in Stage 3. This suggests that when force is applied to a section of a component built using multiple build directions, it will have mechanical properties which correspond to the lowest values of tensile strength and elongation within that section.

5.4.6 Fracture mode

Common features were observed between the tensile specimen fracture surfaces, indicating that they failed through the same mechanisms.

The decrease in cross sectional area of the fractured specimens, the deformation observed on the outside surface of the specimen, and the presence of shear lips on the fracture surface are indications of ductile failure. However, fracture faces did not display typical “cup and cone” ductile failure mechanism.

Instead a coarse rocky-like fracture is present – this links to the inferior plasticity and low elongation values observed during tensile testing. Coarse intergranular regions with step-like features and dimpled regions are present. These are shown on the images of the fracture surfaces in the previous results section and are indicative of ductile failure mechanism.

The features noted under higher magnification also support a predominantly ductile failure mechanism, with shear deformation present within all samples. The visible step-like features indicate that the intergranular region probably propagated first, fracturing along grain boundaries (Figure 85; Figure 86; Figure 87; Figure 104; Figure 105; Figure 122; Figure 123). Propagation of the intergranular region may have been facilitated by the elemental segregation seen during SEM and EDX analysis of corresponding samples, potentially resulting in weaker areas and hence a preferential fracture path. Once the remaining ligament holding a tensile specimen together was small enough, the specimen was torn apart in a ductile manner. Microvoids initiated at the interface between Laves phase and the matrix, resulting in tearing ridges and the strong equiaxed dimple morphology observed (Figure 85; Figure 86; Figure 88; Figure 104; Figure 105; Figure 123; Figure 124; Figure 133).

Although features were common between fracture surfaces, some differences were noted in the prevalence, structure, and morphology of features between the specimens orientated perpendicular to the columnar grains (Stage 1 (horizontal), Stage 2 (1 and 2), and Stage 3 (horizontal)) and the specimens orientated parallel to these grains (Stage 1 (vertical), Stage 2 (3), and Stage 3 (vertical)). These differences relate to the variation in tensile properties observed between these two tensile specimen orientations – perpendicular displayed greater 0.2% proof stress and UTS than parallel.

In specimens perpendicular to the columnar grains, voids were shallower and narrower (Figure 123) than those observed on the parallel specimen fracture surfaces which were wider and deeper (Figure 124). They also took on a more uniform distribution, with void tearing ridges appearing in structured lines

(Figure 104; Figure 123), whilst those on the parallel specimen fracture surfaces appeared to be more randomly distributed, with fragments of Laves phase more frequently seen on the tearing ridges (Figure 124).

This variation in the tearing ridges occurs due to the orientation of fracture with regards to the networks of Laves formed throughout samples. Under SEM, Laves was observed to form in networks, elongating upwards towards the laser, appearing as lines or chains, parallel to the direction of grain growth. In perpendicular specimens, fracture occurs parallel to these lines, resulting in the uniform distribution of voids and tearing ridges along this network of lines. In parallel specimens, fracture occurs perpendicular to the network of Laves lines/chains, resulting in a random distribution as fracture occurs across a cross section of the preferentially upwards orientated network of Laves.

Step-like features were more abundant in the perpendicular specimens, causing their more jagged appearance (Figure 83; Figure 103).

These observations indicate that the failure mechanism of parallel specimens was more ductile than perpendicular specimens, where brittle fracture played a greater role.

In some cases, cracks were observed (Figure 86; Figure 87; Figure 89; Figure 103; Figure 133). At the location of these shear deformation can be seen to have occurred during their propagation. These may have originated at a discontinuity or fault within the specimen, for example at a pore, inclusion, or an un-melted powder particle, subsequently initiating fracture.

Al-oxides were noted at the face of some fractured specimens (Figure 85; Figure 86; Figure 88; Figure 89; Figure 104; Figure 105; Figure 123). These Al-oxide inclusions did not appear to have initiated fracture; however they could have formed a weak point within the specimen. These Al-oxides were significantly larger than the Al-oxide inclusion noted in polished and etched samples the SEM ($<1 \mu\text{m}$ (Figure 71 spectrum 5; Figure 72 spectrum 8; Figure 98 spectrum 3)), measuring at approximately $10 \mu\text{m}$ in diameter, and EDX did

not indicate any presence of Ti. This difference in size suggests that they formed during a different stage of powder manufacture or the DED-L process to the $<1\ \mu\text{m}$ Al-oxides. Based on the size and sphericity of the particles it is most likely these were present within the powder prior to DED-L fabrication, forming during the plasma atomisation process. This is supported by the findings of Popovich et al. (2017), who observed partially melted Al-oxide particles which originated from the powder within tensile fracture surfaces.

5.5 Vickers Hardness

Several observations were made regarding Vickers Hardness (macro and micro) during the stages of this study. Macrohardness and microhardness were similar in value for all samples except for Stage 1 small block samples. This shows that although DED-L is a process which can result in variation at a microscopic level it has not had a significant effect on the hardness of samples within this work.

5.5.1 Stage 1 – comparison of parameter sets

Large block hardness did not vary significantly between parameter sets (Figure 90). This indicates that similar microstructures and phase volumes formed between the four large blocks. This correlates with the lack of variation between large block SDAS (Figure 66).

Greater variation was noted between small block hardness, however these variations were not always significant. No significant variation in macrohardness was present between small block sets 4, 9, and 10. However the values for these three sets were all significantly greater than set 5 small block. For small block microhardness the only significant difference was present between parameter set 4 and parameter set 5.

Although not noted as significantly different, SDAS for set 5 small block was greater than sets 4, 9, and 10 small block SDAS. Correlation between greater

SDAS and lower hardness has previously been observed by Vandersluis and Ravindran (2017), and Amine, Newkirk and Liou (2014), thus this may relate to the lower observed hardness.

Another possible cause of this difference is the values for specific energy density – parameter set 5 specific energy density was 4000 J/g lower than the next lowest specific energy density for the four sets (Table 24). This reduced energy per unit of powder may have reduced hardness through altering the volume fraction of phases within the sample, less precipitation hardening γ'' -phase may have formed. No correlation was present between small block hardness and Laves phase present within binarised SEM images.

The plotted microhardness maps do not indicate any discernible difference between process parameter sets (Figure 91; Figure 92), although some variation can be seen within individual plotted maps. This variation differs across each cross section and shows that microhardness does not specifically increase or decrease from the centre outwards, or moving upwards, through the test specimen. The maps also indicate that although phase distribution varied across the tracks and layers, these variations did not have a significant effect on hardness.

5.5.2 Stage 1 – comparison of built sample sizes

Except for set 5, small blocks exhibited greater hardness than their corresponding large block (Figure 90). This difference was more evident in measured microhardness. This variation can be linked to the SDAS (Figure 66), with lower SDAS contributing to the greater hardness observed in small samples.

The exception seen for small block 5 is due to its SDAS. SDAS was greater in small block 5 as compared to small blocks 4, 9, and 10. This increase in SDAS subsequently decreases hardness, resulting in a hardness value which is closer to the values for set 5 large block.

The difference in microstructure between small and large blocks also contributes to the different hardness observed. Less of the white/Nb-rich phase – identified to predominantly consist of Laves – was present within small samples (Table 29). However, this does not account for why the hardness of set 5 small block was lower than the other small blocks. Laves is a brittle, hard phase, thus a lower volume of this, such as within the small blocks, would be expected to decrease hardness. However this was not the case, suggesting that SDAS has a greater effect on hardness than Laves volume, or that the phase observed to surround Laves – which is suggested to consist entirely or partly of precipitation hardening phase γ'' – alters the hardness values between samples. As less Laves phase formed within small blocks there will have been more Nb available for forming γ'' , increasing the volume of this hardening phase able to form within small blocks, in turn increasing hardness. This may not have occurred within set 5 small block due to the low specific energy density – more energy per unit of powder may have been required to facilitate greater formation of γ'' .

The greater heat build-up during building the large blocks may have affected hardness. Additionally the prolonged time the large blocks were at a higher temperature, due to longer build times, may have decreased hardness. These conditions alter the phase fractions and distribution as the deposition process progresses. These alterations would have occurred until a particular composition of phases – similar across all of the large blocks – was reached, causing the hardness values of the large blocks to lie within a small range of one another.

The microhardness maps plotted for the cross sections of the small and large blocks show that the small blocks, except set 5, contain more variation in microhardness values than the large blocks (Figure 91; Figure 92). This may be caused by the difference in heat build-up and time experienced at a high temperature. Large blocks were held at higher temperature for a longer time. This may have caused any variation which was once present to reduce as the build continued.

Based on the relationship present between hardness and tensile properties (Pavlina & Tyne, 2008; ASTM International, 2020), the differences observed between small block and large block hardness indicate that the small blocks (except set 5) would possess greater yield strength and UTS than the large blocks.

5.5.3 Stage 2 – comparison of individual planes

Vickers Hardness values varied slightly between the three planes, with greatest values observed for the zy-plane, however differences were not significant (Figure 107). There is a possibility this small difference in values for planes could be attributed to the variation in grain size and orientation with regards to the direction of testing. However, these results are not definitive, essentially indicating consistent hardness between the three planes of the sample. Despite hardness typically relating to tensile properties (Pavlina & Tyne, 2008; ASTM International, 2020), no correlation was seen between the hardness values and tensile properties for this block.

5.5.4 Stage 3 – effect of build direction on Vickers Hardness

Significant differences were observed between the horizontal and vertical samples for hardness (Figure 125). Vertical sample yz-plane (V2) and xz-plane (V3) hardness values were significantly greater than all three horizontal sample planes (xy, xz, and yz). However, microhardness of the vertical xy-plane (V1) was over 55 HV_{0.5} lower than the xz-plane (V2) and yz-plane (V3), and lower than all three horizontal sample planes (Table 41).

Hardness has been shown to correlate to tensile properties (Pavlina & Tyne, 2008; ASTM International, 2020). In this stage of work the hardness values which are perpendicular to the tensile specimen length (Table 41; horizontal yz-plane/H2 (284 HV₁₀, 266 HV_{0.5}) and vertical xy-plane/V1 (249 HV₁₀, 255 HV_{0.5}) appear to correlate to the tensile properties observed (Table 40; horizontal 682 MPa (0.2% proof stress), 1024 MPa (UTS) and vertical 648 MPa (0.2% proof

stress), 916 MPa (UTS)). This indicates that the hardness testing load must be applied 180° to the direction of the applied tensile testing force to relate these properties for the samples.

Based on the hardness values for the other planes of vertical samples (yz-plane/V2 (316 HV₁₀, 314 HV_{0.5}), xz-plane/V3 (313 HV₁₀, 312 HV_{0.5})) it would be expected that tensile strength in this orientation – perpendicular to the elongated grains – would exceed that of horizontal samples.

The increased hardness seen in vertical yz-plane/V2 and xz-plane/V3 links to the incandescence seen during building. As discussed, this results in ageing of the incandescent material, and the transformation of γ -phase to hardening phases γ' and γ'' .

The 90° rotation used between depositing subsequent layers may also contribute to increasing hardness. Without a 90° rotation between layers all track-track interfaces run in the same direction. By incorporating a 90° rotation between layers a more complex structure of layer-layer and track-track interfaces are formed, the arrangement of phases within tracks and layers means that this increases the complexity of phase distribution. This aids in reducing dislocations movement through the sample – increasing hardness.

The differences present between the horizontal and vertical samples also link to the different heat build-up and cooling rates experienced by the samples. These result in different SDAS and volume of Nb-rich phase in the different build directions, altering sample hardness and resulting in the variation observed. Based on Stage 1 SDAS findings it was suggested that horizontal samples would have lower SDAS than vertical samples, this does not correlate to the greater hardness values observed for the vertical xz-plane and yz-plane (V2 and V3) compared to horizontal sample hardness. This indicates that there is another factor contributing to the increased hardness, such as the previously discussed 90° rotation between layers.

5.5.5 Stage 4 – effect of an interface on Vickers Hardness

The interface formed between the two build directions was not seen to have a significant effect on Vickers Hardness when plotted moving across the interface (Figure 134; Figure 135). The incorporation of a second build direction creates a micro-feature between build directions; thus its effect would be expected to be noted in microhardness results rather than macrohardness results.

A minor decrease in average hardness occurred at 0 mm, directly on the interface, however this value did not significantly differ from other values. Values obtained were akin to those previously observed in this study, indicating that incorporating an interface into the build has not had a detrimental effect to the microstructure, and hence Vickers Hardness.

5.5.6 Stage 5 – effect of a heat-treatment on Vickers Hardness

The heat-treatment can be seen to significantly improve the Vickers Hardness of samples, with increases exceeding 100 HV₁₀/HV_{0.5} noted (). Based on the observations under OLM and SEM, and previous literature, this is due to the heat-treatment dissolving and reducing the volume of detrimental phases present, increasing the volume of hardening phases present, and eliminating the microstructural anisotropy previously seen between sample planes.

Based on this increase in Vickers Hardness, it is likely that the heat-treatment would have also increased 0.2% proof stress and UTS (Pavlina & Tyne, 2008; ASTM International, 2020) which were not tested in this work.

5.6 Powder capture efficiency

The results obtained for powder capture efficiency (Table 35) show that all the large blocks built were within 0.05 kg of what a fully dense block with the specified large block greater than the expected weight – this is caused by

excess deposited powder melting and sticking to the outside of the block. Both set 4 and set 5 had greater powder inputs (based on build time and scan path distance) and weighed more than set 9 and set 10 blocks. This indicates that the excess powder input increases the likelihood for the block to meet the expected weight. However powder capture efficiency is substantially reduced (set 4, 78.99%; set 5, 83.63%).

Set 9 and set 10 blocks weigh less than a fully dense Inconel 718 block of the specified dimensions, this is as expected for set 9 as the powder input calculated using both build time and scan path distance was less than 1.86 kg. Both sets also show better powder capture efficiency (set 9, 99.91%; set 10, 88.42%). Powder feed rate changes between set 9 and set 10, increasing from 2.9 g/min to 4 g/min, however block final weights are the same. This indicates that the increase in powder feed rate for set 10 is redundant, acting to increase powder wasted.

These results suggest that the expected density of a component to be built using DED-L should be calculated prior to building. This value can then be used to aid in determining a suitable powder feed rate and scanning speed to avoid excessive powder being wasted during fabrication.

5.7 Energy density, mass density, and specific energy density

The three process parameters under investigation were linked using the equations previously presented (Equation 4; Equation 5; Equation 6).

Individual examination of energy density, mass density and specific energy density, and comparison of parameter set ranks for these to the sets which were able to be built (Table 24) indicates that mass density and specific energy density are key in understanding whether a set of process parameters will work.

Energy density (J/mm^3) did not appear to be as crucial. Set 7 and set 8, which resulted in spattering and damage to the laser, were ranked at 8 and 6 respectively for energy density, laying between the sets which were successful in building – sets 4, 5, 9, and 10, ranked 4, 7, 9, and 10 respectively. This suggests that energy density itself should not be relied on as an indicator for whether a set of process parameters will work.

Inspection of mass density (g/mm^3) ranks found that the parameter set (set 3) with the highest mass density correlated with the deposited track which did not fuse to the substrate (and hence could not be used for further building), whilst the lowest mass density corresponded with the process parameter set (set 8) which resulted in damage to the laser. This indicates that mass density could be useful in determining suitable parameter sets. However mass density for parameter set 7, which was deemed unsuitable for building, fell between sets 4 and 5, and sets 9 and 10, which were successful. This indicates that another factor, possibly laser power, should also be considered in determining parameter set suitability.

The lowest specific energy density (J/g) was noted for set 3, which did not fuse with the substrate. Set 8, which was also unsuccessful, had the highest specific energy density. Again this indicates that specific energy density could be useful in determining suitable parameter sets – although it should be noted that parameter set 7 which was deemed unsuitable had the same specific energy density value as set 10 which was successful.

To examine all three process parameters together visually, the equation connecting two of the process parameters can be plotted against the third parameter (e.g. plotting specific energy density – obtained using laser power and powder feed rate – against scan speed). Through doing this it may then be possible to determine where a process window or working envelope of useful process parameters lay. An example of how this is shown in Figure 147, where the sets from this study, and previously used parameter sets for the Trumpf 505 DMD system, have been plotted and working envelope shown. The parameter

sets plotted were proved to be definitively successful or unsuccessful – parameter sets which were only used to deposit a single track in previous work have been excluded. A successful parameter set refers to builds which display good fusion, low porosity, and builds evenly. An unsuccessful parameter set consists of builds which display poor fusion, sample burns, spattering, or uneven building. Within this working envelope it is likely that a smaller region exists which produces more desirable material properties in the as-deposited material – such as greatest volume fraction of hardening phases, greatest tensile strength, or greatest hardness. More sets and testing are required to establish if this is the case or not.

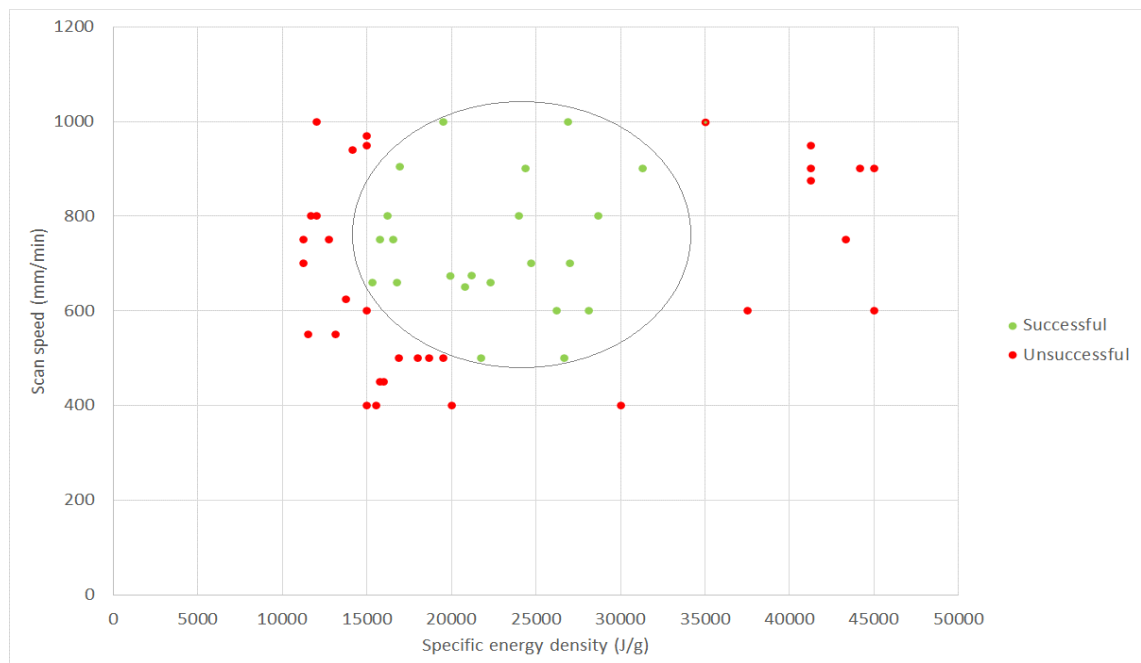


Figure 147: Graph displaying specific energy density plotted against scan speed to show where a working envelope of successful parameter sets lies for the Trumpf 505 DMD system for Inconel 718 (those from previous work are shown in Appendix 2).

Equation 11 presents this working envelope empirically, and thus the ranges that x (specific energy density) and y (scan speed) values reside in.

$$0 \leq \frac{(x - 24157)^2}{10056^2} + \frac{(y - 760)^2}{279^2} \leq 1$$

$$14101 \leq x \leq 34213$$

$$491 \leq y \leq 1039$$

Equation 11: Empirical formula for the working envelope presented in Figure 147, and thus the range for x and y values.

Chapter 6 – Conclusions

This chapter concludes the findings from this work, and addresses its limitations, prior to making recommendations for future work.

6.1 Findings

This research set out to investigate DED-L process parameters using a Trumpf 505 DMD system, aiming to determine the effect of altering specific process parameters on the metallurgical and mechanical properties of Inconel 718.

The following conclusions were made from the results.

6.1.1 Process parameter optimisation

Using either the highest laser power (1300 W), lowest scan speed (500 mm/min), or lowest powder feed rate (1.8 g/min) resulted in spattering and sample burns if suitable values were not used for the other two process parameters.

Using either the lowest laser power (800 W), highest scan speed (1000 mm/min), or highest powder feed rate (4.0 g/min) resulted in insufficient powder melting and poor or no fusion if inappropriate values are used for the other two process parameters.

Porosity was consistently below 0.30% showing that the process parameters used were sufficient in melting the Inconel 718 powder.

A laser power of 995 W, scan speed of 675 mm/min, and powder feed rate of 3 g/min were identified to be optimal for fabricating thick wall Inconel 718 builds on the Trumpf 505 DMD system.

An empirical working envelope of laser power, scan speed, and powder feed rate was established for depositing Inconel 718 using a Trumpf 505 DMD system. This working envelope is as follows:

$$0 \leq \frac{(x - 24157)^2}{10056^2} + \frac{(y - 760)^2}{279^2} \leq 1$$

Specific energy density (J/g): $14101 \leq x \leq 34213$

Scan speed (mm/min): $491 \leq y \leq 1039$

Equation 12: Empirical working envelope formula, and thus the range for specific energy density (x) and scan speed (y) values.

6.1.2 Microstructure

All untreated samples exhibited a unidirectional microstructure, comprising of dendritic Ni-base γ -matrix and interdendritic Laves phase, γ'' -phase and carbides. Columnar grains grew across consecutive tracks and layers in the direction of the laser, contributing to the anisotropy observed.

The interfaces formed between consecutive tracks and layers also contributed to the anisotropy noted in samples. Typical relationships between SDAS and tensile properties, and grain width and tensile properties, were absent from samples, altered by these interfaces.

6.1.2.1 Laser power, scan speed, and powder feed rate

Altering laser power, scan speed, and powder feed rate significantly affected small block SDAS. Increases in both laser power and scan speed decreased SDAS.

Increasing powder feed rate from 2.9 g/min to 4.0 g/min (at 1300 W, 1000 mm/min) increased SDAS by 23%.

6.1.2.2 Build geometry

The change in build geometry between small blocks and large blocks significantly altered SDAS and Laves volume. Small block SDAS (minimum 6.58 μm , maximum 9.83 μm) and Laves proportion (minimum 1.21%, maximum 3.26%) were lower than for their corresponding large block (SDAS: minimum 11.27 μm , maximum 12.24 μm . Laves: minimum 5.34%, maximum 10.20%).

6.1.2.3 Incorporating an interface

Using two different build directions to form an interface created a distinct boundary where a change in grain orientation was visible. Grains extended from the first build direction, across the interface and into the second build direction.

6.1.2.4 Heat-treatment

The use of heat-treatment following manufacture of the build eliminated the columnar dendritic grain structure, and reduced the volume of Laves phase present.

6.1.3 Mechanical properties

No process parameter set met the minimum tensile properties for untreated wrought Inconel 718 according to AMS 5597 (SAE International, 2016). All values for the untreated samples exceed standard Vickers Hardness for solution annealed Inconel 718, but are below solution annealed and aged Inconel 718 according to AMS 5662 (SAE International, 2016).

6.1.3.1 Laser power, scan speed, and powder feed rate

Changing laser power, scan speed, and powder feed rate did not significantly affect the mechanical properties of the large block. 0.2% proof stress values resided between 595 MPa and 700 MPa for horizontal specimens, and 462 MPa and 497 MPa for vertical. Macrohardness between 278 HV₁₀ and 288 HV₁₀, and microhardness between 265 HV_{0.5} and 274 HV_{0.5}.

6.1.3.2 Build geometry

Small block hardness (microhardness minimum 299 HV_{0.5}, maximum 285 HV_{0.5}) was significantly greater than large block hardness (microhardness minimum 265 HV_{0.5}, maximum 274 HV_{0.5}).

Process parameters are not interchangeable between geometries. Individually built small test samples should not be used as a representation of the material properties for a larger component built using the same set of process parameters.

6.1.3.3 Incorporating an interface

The interface itself had no significant effect on hardness, and did not fail at the interface during tensile testing.

The two sections deposited using the different build directions possess different tensile properties, resulting in the sample adopting the weaker tensile strength and lower elongation values of the two sections.

6.1.2.4 Heat-treatment

Heat treatment increased Vickers Hardness by an average of 55%, to 450 HV₁₀ and 408 HV_{0.5}. This exceeded the standard for minimum Vickers Hardness solution annealed and aged Inconel 718 (385 HV) (SAE International, 2016).

6.2 Limitations

Not every DOE generated combination of process parameters could be built within this work. This reduced the number of samples available for analysis, restricting the total understanding of how laser power, scan speed, and powder feed rate affected the materials properties across the full range of parameter values. However, to ensure all combinations of process parameters were successful in building both block sizes, a narrow range of values would have been required, potentially eliminating the observed effects of the process

parameters due to decreased variation in cooling rates and/or heat build-up between samples.

The cooling rates and heat build-up that occurred during building the samples in this work were not measured. By monitoring the temperature of each sample during building using thermo-couples or a microbolometer camera, a precise representation of how heat build-up varied, and to what extent, between the individual samples could have been obtained.

6.3 Future work

To progress this work further, the following recommendations have been made.

6.3.1 Residual stress analysis

Residual stress was not analysed within this study, however the repetitive thermal cycling of DED-L means that its presence is inevitable. Due to the differing energy density, specific energy density, and thus heat input of the process parameter sets investigated in Stage 1, residual stress is likely to have varied between samples. Its presence will have also influenced the mechanical properties observed within this study. By performing residual stress analysis on the small and large blocks, the effect of the different process parameter sets can be expanded.

6.3.2 Process parameter optimisation

This study highlights the importance of considering process parameters together rather than independently. To continue examining the optimisation of process parameters, further consideration of linking process parameters mathematically should be made.

Figure 147 shows a possible working envelope of successful process parameter combinations. To develop this and determine whether there is a working envelope of parameter combinations which produce more desirable material

properties and maximise powder capture efficiency, further building and testing should be performed.

6.3.3 Geometrical variation

Further work should be done into building small test samples, mimicking the conditions which would occur in a larger component such as heat build-up and cooling rates. Considerations for building the small test sample could include incorporation of dwell time between subsequent layers or holding the sample at a higher temperature whilst building.

To determine the point that variation in material properties is eliminated, sets of samples with small increments in dimensions should be built using the same process parameters. These should undergo metallurgical and mechanical analysis to determine what causes the reduced variation, at what point, and whether it occurs gradually or if there is a set point at which properties change substantially.

6.3.4 Heat-treatments

One heat-treatment was examined in this study and tensile testing was not performed on the heat-treated samples. To develop this, large samples should be built, heat-treated, and then tensile tested. This will enable a comparison of untreated and heat-treated tensile strength and determine whether the heat-treatment improves the tensile strength enough to match, or exceed, its relevant industry standard requirement.

Other heat-treatments, such as those outlined in Table 12, should be trialled, and the outcome compared to that within this work and with one another. This will establish which heat-treatment produces the most satisfactory material properties. Heat-treatments previously found successful for AM built parts in other literature and studies should also be considered for testing.

6.3.5 Layer and track interfaces

Further work should also focus on the interfaces between adjacent tracks and layers. These interfaces are clearly discernable under a microscope, but do not represent grain boundaries. Thus work should be carried out to determine what these interfaces represent in physical terms, in addition to their effect on material properties. To do this a technique such as Electron Back Scatter Diffraction could be used. This will enable direct characterisation of phase composition, chemical composition, and crystallographic orientation. This enables the preferred crystal orientation to be determined, and localised changes in texture to be studied.

References

- 3dexter. (2018). *Additive Manufacturing V/S Subtractive Manufacturing Process Adopted in 2018*. Retrieved from <https://3dexter.com/additive-manufacturing-vs-subtractive-manufacturing/>
- Ahsan, M., Pinkerton, A., Moat, R., & Shackleton, J. (2011). A comparative study of laser direct metal deposition characteristics using gas and plasma-atomized Ti-6Al-4V powders. *Materials Science and Engineering A*, 528, 7648-7657.
- Alcisto, J., Enriquez, H., Garcia, H., Hinkson, S., Steelman, T., Silverman, E., . . . Es-Said, O. (2011). Tensile properties and microstructures of Laser-formed Ti-6Al-4V. *Journal of materials engineering and performance*, 20(2), 203-212.
- Alhuzaim, A., Imbrogno, S., & Attallah, M. (2021). Controlling Microstructural and Mechanical Properties of Direct Laser Deposited Inconel 718 via Laser Power. *Journal of Alloys and Compounds*, 872, 159588.
- Alizadeh-Sh, M., Marashi, S., Renjbarnodeh, E., Shoja-Razavi, R., & Oliveira, J. (2020). Prediction of solidification cracking by an empirical-statistical analysis for laser cladding of Inconel 718 powder on a non-weldable substrate. *Optics & Laser Technology*, 128.
- American Machine Tools. (2012). *Heat Treatment of Metals*. Retrieved from http://americanmachinetools.com/heat_treating_metals.htm
- Amine, T., Newkirk, J., & Liou, F. (2014). An investigation of the effect of direct metal deposition parameters on the characteristics of the deposited layers. *Case studies in thermal engineering*, 3, 21-34.
- Anderson, M., & Whitcomb, P. (2000). Design of Experiments. *Kirk-Othermer encyclopedia of chemical technology*.

- Antonsson, T., & Fredriksson, H. (2005). The effect of cooling rate on the solidification of Inconel 718. *Metallurgical and Materials Transactions B*, 36, 85-96.
- Ardila, L., Garciandia, F., Gonzalez-Diaz, J., Alvarez, P., Petite, M., Deffley, R., & Ochoa, J. (2014). Effect of IN718 Recycled Powder Reuse on Properties of Parts Manufactured by Means of Selective Laser Melting. *Physics Procedia*, 56, 99-107.
- Arrizubieta, J., Ruiz, J., Martinez, S., Ukar, E., & Lamikiz, A. (2017). Intelligent nozzle design for the Laser Metal Deposition process in the Industry 4.0. *Manufacturing Engineering Society International conference, Vigo, Spain*.
- ASM Committee on Metallography. (1972). Microstructure of Nickel-Base and Cobalt-Base Heat Resistant Casting Alloys. In *Metals Handbook* (8 ed., Vol. 7, pp. 187-196). American Society for Metals.
- ASM International. (1987). Fractography: Nickel alloys: Atlas of Fractographs. *ASM Handbook*, 12, 396-397.
- ASM International. (1993). *An overview of joining processes: welding*.
- ASM International. (1999). *Hardness Testing* (2 ed.). Materials Park.
- ASTM International. (2009). *ASTM E6-09be1 Standard terminology relating to methods of mechanical testing*. ASTM.
- ASTM International. (2017). *ASTM E1097 - 12 Standard Guide for Determination of Various Elements by Direct Current Plasma Atomic Emission Spectrometry*.
- ASTM International. (2018). *ASTM E1019 - 18 Standard Test Methods for Determination of Carbon, Sulfur, Nitrogen, and Oxygen in Steel, Iron, Nickel, and Cobalt Alloys by Various Combustion and Inert Gas Fusion Techniques*.

- ASTM International. (2019). A240/A240 - 19 Standard Specification for Chromium and Chromium-Nickel Stainless Steel Plate, Sheet, and Strip for Pressure Vessels and for General Applications. *ASTM Compass*.
- ASTM International. (2020). *A370 - 20 Standard Test Methods and Definitions for Mechanical Testing of Steel Products*.
- Azadian, S., Wei, L., & Warren, R. (2004). Delta phase precipitation in Inconel 718. *Materials Characterization*, 53, 7-16.
- AZO Materials. (2008). *Nickel alloy Inconel 718 - Properties and applications by united performance metals*. Retrieved from <https://www.azom.com/article.aspx?ArticleID=4459>.
- Bambach, M., Sizova, I., Silze, F., & Schnick, M. (2018). Comparison of laser metal deposition of Inconel 718 from powder, hot and cold wire. *Procedia CIRP*, 74, 206-209.
- Bartolo, P., Lemos, A., Pereira, A., Mateus, A., Ramos, C., Santos, C., . . . Marques, T. (2013). High value manufacturing: Advanced research in virtual and rapid prototyping. *Proceedings of the 6th International conference on advanced research in virtual and rapid prototyping*, Leiria, Portugal, 1-5 October.
- Becker, W. (2002). Failure Analysis and Prevention: Mechanisms and Appearances of Ductile and Brittle Fracture in Metals. *ASM Handbook*, 11, 587-626.
- Bennett, J., Kafka, O., Liao, H., Wolff, S., Yu, C., Cheng, P., . . . Cao, J. (2018). Cooling rate effect on tensile strength of laser deposited Inconel 718. *Procedia Manufacturing*, 26, 912-919.
- Beuth, J., & Klingbeil, N. (2001). The role of process variables in laser-based direct metal. *Solid freeform fabrication symposium*.

- Bi, G., Gasser, A., Wissenbach, K., Drenker, A., & Popraw, R. (2006). Characterization of the process control for the direct laser metallic powder deposition. *Surface Coatings Technology*, 201, 2676-2683.
- Bian, L., Shamsaei, N., & Usher, J. (2017). *Laser-based additive manufacturing of metal parts: Modelling, optimization and control of mechanical properties*. CRC Press: Taylor & Francis Group.
- Bontha, S., Klingbeil, N., Kobryn, P., & Fraser, H. (2006). Thermal process maps for predicting solidification microstructure in laser fabrication of thin-wall structures. *Journal of materials processing technology*, 178(3), 135-142.
- Brueckner, F., Seidei, A., Lopez, E., & Willner, R. (2017). Enhanced manufacturing possibilities using multi-materials in laser metal deposition. *Journal of laser applications*, 30.
- Cao, Y., Bai, P., Liu, F., Hou, X., & Guo, Y. (2020). Effect of the Solution Temperature on the Precipitates and Grain Evolution on IN718 Fabricated by Laser Additive Manufacturing. *Materials*, 13, 340.
- Careri, F., Imbrogno, S., Umbrello, D., Attallah, M., Outeiro, J., & Batista, A. (2021). Machining and heat treatment as post-processing strategies for Ni-superalloys structures fabricated using direct energy deposition. *Journal of Manufacturing Processes*, 61, 236-244.
- Carlson, R., & Radavich, J. (1989). Microstructural characterisation of cast 718. *Superalloy 718-Metallurgy and Applications*, 79-95.
- Chen, B., & Mazumber, J. (2017). Role of process parameters during additive manufacturing by direct metal deposition of Inconel 718. *Rapid Prototyping Journal*, 23, 919-929.
- Chen, J., Lee, J., Jo, C., Choe, S., & Lee, Y. (1998). MC carbide formation in directionally solidified MAR-M247 LC superalloy. *Materials science and*

engineerings: Structural materials: Properties, microstructure and processing, 247(2), 113-125.

- Cortina, M., Arrizubieta, J., Ruiz, J., Lamikiz, A., & Ukar, E. (2018). Design and manufacturing of a protective nozzle for highly reactive materials processing via laser material deposition. *Procedia CRIP*, 68, 387-392.
- Costa, L., Vilar, R., Reto, T., & Deus, A. (2005). Rapid tooling by laser powder deposition: process simulation using finite element analysis. *Acta Materialia*, 53, 3987-3999.
- Darolia, R., Lahrman, D., Field, R., & Sisson, R. (1988). Formation of topologically closed packed phases in nickel base single crystal superalloys. *Superalloys*, 255-264.
- Dass, A., & Moridi, A. (2019). State of the Art in Directed Energy Deposition: From Additive Manufacturing to Materials Design. *Coatings*, 9(418).
- Dehoff, R., Tallman, C., Duty, C., & Blue, C. (2013). Case study: Additive manufacturing of aerospace brackets. *Advanced materials & processes*, 171(3), 19-22.
- Dempster, I., Forgings, W., & Wallis, R. (2016). Heat Treating of Nonferrous Alloys: Heat Treatment Metallurgy of Nickel-Base Alloys. *ASM Handbook*, 4E, 399-425.
- Dinda, G., K, D., & Mazumder, J. (2010). Laser aided direct metal deposition of Inconel 625 superalloy: microstructural evolution and thermal stability. *Materials science and engineering A*, 527, 7490-7497.
- Ding, R., Huang, Z., Li, H., Mitchell, I., Baxter, G., & Bowen, P. (2015). Electron microscopy study of direct laser deposited IN718. *Materials Characterisation*, 106, 324-337.
- Donachie, M., & Donachie, S. (2002). *Superalloys: A technical guide* (2nd ed.). USA: ASM International.

- Dunlap, M., & Adaskaveg, J. (1997). *Introduction to the Scanning Electron Microscope*. California: Imaging and Microscope Facility, University of California.
- Dupont, J., Lippold, J., & Kiser, S. (2009). *Welding Metallurgy and Weldability of Nickel-Base Alloys*. Hoboken, New Jersey: John Wiley and Sons.
- DuPont, J., Notis, M., Marder, A., Robino, C., & Michael, J. (1998). Solidification of Nb-bearing superalloys: Part I. Reaction sequences. *Metallurgical and Materials Transactions A*, 29, 2785-2796.
- Dye, S., Hunziker, O., & Reed, R. (2001). Numerical analysis of the weldability of superalloys. *Acta Materialia*, 49(4), 683-697.
- Egerton, R. (2005). *Physical Principles of Electron Microscopy*. USA: Springer.
- El-Bagoury, N., & Ramadan, M. (2012). Heat treatment effect on microstructure and mechanical properties of Re-containing Inconel 718 alloy. *Journal of minerals and materials characterisation and engineering*, 11, 924-930.
- Emmelmann, C., Herzog, D., & Kranz, J. (2017). Design for laser additive manufacturing. *Laser additive manufacturing*, 259-279.
- Emmelmann, C., Sander, P., Kranz, J., & Wycisk, E. (2011). Laser additive manufacturing and bionics: redefining lightweight design. *Proceedings of the International WLT-Conference on Lasers in Manufacturing*. Munich, Germany.
- Enomoto, Y. (2017). Steam turbine retrofitting for the life extension of power plants. In T. Tanuma, *Advances in Steam Turbines for Modern Power Plants* (pp. 397-436). Woodhead Publishing.
- Everton, S., Hirsch, M., Stravroulakis, P., Leach, R., & Clare, A. (2016). Review of in-situ process monitoring and in-situ metrology for metal additive manufacturing. *Materials & Design*, 95, 431-445.

- Fayed, E., Saadati, M., Shahriari, D., Brailovski, V., Jahazi, M., & Medraj, M. (2021). Effect of homogenization and solution treatments time on the elevated-temperature mechanical behavior of Inconel 718 fabricated by laser powder bed fusion. *Scientific Reports*, 11.
- Fotovvati, B., Wayne, S., Lewis, G., & Asadi, E. (2018). A review on melt-pool characteristics in laser welding of metals. *Advances in materials science and engineering*.
- Fraunhofer ILT. (2018). *VarioClad - Laser metal deposition with variable spot sizes*. Retrieved from <https://www.ilt.fraunhofer.de/en/media-center/brochures/brochure-Varioclad-Laser-Metal-Deposition-with-Variable-spot-sizes.html>
- Gabriel, B. (1987). Fractography: Principles and Practices: Scanning Electron Microscopy. *ASM Handbook*, 12, 166-178.
- Gaumann, M., Bezencon, C., Canalis, P., & Kurz, W. (2001). Single-crystal laser deposition of superalloys: processing - microstructure maps. *Acta Materialia*, 49(6), 1051-1062.
- GE Additive. (2017). *Advanced plasma atomization process*. Retrieved from GE Additive: <https://www.ge.com/additive/press-releases/advanced-plasma-atomization-process>
- GE Additive. (2021, March 10). *Get the Facts on... Porosity in Metal Additive Manufacturing*. Retrieved from <https://www.ge.com/additive/blog/get-facts-porosity-metal-additive-manufacturing>
- GE Aviation. (2013). *GE Aviation signs additive manufacturing cooperative agreement with Sigma Labs*. In-process inspection technology progresses additive production speeds. GE Aviation.
- Ghassemali, E., Riestra, M., Bogdanoff, T., Kumar, B., & Seifeddine, S. (2017). Hall-Petch equation in a hypoeutectic Al-Si cast alloy: grain size vs.

secondary dendrite arm spacing. *International Conference on the Technology of Plasticity*, (pp. 19-24). Cambridge, United Kingdom.

Gilbertson, L., & Zipp, R. (1981). *Fractography and Materials Science*. West Conshohocken: ASTM International.

Gleeson, B. (2008). High-temperature corrosion of metallic alloys and coatings. *Materials science and technology: A comprehensive treatment: Corrosion and environmental degradation*, 2, 173-228.

Goldston, R., & Rutherford, P. (1995). *Introduction to Plasma Physics*. CRC Press.

Goodfellow, A., Galindo-Nava, E., Christofidou, K., Jones, H., Boyer, C., Martin, T., . . . Stone, H. (2018). The effect of phase chemistry on the extent of strengthening mechanisms in model Ni-Cr-Al-Ti-Mo based superalloys. *Acta Materialia*, 153, 290-302.

Gregori, A., & Bertaso, D. (2007). Welding and deposition of Nickel superalloys 718, Waspaloy and single crystal alloy CNSZ-10. *Welding in the world*, 51(12), 34-47.

Gruber, H., Luchian, C., Hryha, E., & Nyborg, L. (2020). Effect of Powder Recycling on Defect Formation in Electron Beam Melted Alloy 718. *Metallurgical and Materials Transactions A*, 51, 2430-2443.

Gu, D. (2015). *Laser additive manufacturing of high-performance materials*. Springer.

Guévenoux, C., Hallais, S., Charles, A., & Charkaluk, E. (2020). Influence of interlayer dwell time on the microstructure of Inconel 718 Laser Cladded components. *Optics and Laser Technology*, 128.

Hashmi, S., Batalha, G., Tyne, C., & Yilbas, C. (2014). *Comprehensive materials processing*. Elsevier Ltd.

- High Temp Metals. (2015). *Inconel 718 technical data*. Retrieved from <http://www.hightempmetals.com/techdata/hitempInconel718data.php>
- Hiser, M., Schneider, A., Audrain, M., & Hull, A. (2020). Regulatory Research Perspective on Additive Manufacturing for Nuclear Component Applications. *Journal of Nuclear Materials*, 546, 152726.
- Hu, D., Mei, H., & Kovacevic, R. (2002). Improving solid freeform fabrication by laser-based additive manufacturing. *Journal of Engineering Manufacture*, 216, 1253-1264.
- Izabi, M., Farzaneh, A., Gibson, I., & Rolfe, B. (2017). The Effect of Process Parameters and Mechanical Properties of Direct Energy Deposited Stainless Steel 316. *Solid Freeform Fabrication 2017: Proceedings of the 28th Annual International* , 1058-1067.
- Janaki Ram, G., Venugopal Reddy, A., Prasad Rao, K., & Madhusudhana Reddy, G. (2004). Control of Laves phase in Inconel 718 GTA welds through the use of current pulsing. *Science and Technology of Welding and Joining*, 9.
- Jelvani, S., Razavi, R., Barekat, M., Dehnavi, M., & Erfanmanesh, M. (2019). Evaluation of solidification and microstructure in laser cladding Inconel 718 superalloy. *Optics and Laser Technology*.
- Jin, Y., He, Y., & Fu, J. (2013). An adaptive tool path generation for fused deposition modelling. *Advanced materials research*, 7-12.
- Jinoop, A., Paul, C., & Bindra, K. (2019). Laser assisted direct energy deposition of Hastelloy-X. *Optics and Laser Technology*, 109, 14-19.
- Kamara, A., Marimuthu, S., & Li, L. (2011). A numerical investigation into residual stress characteristics in laser deposited multiple layer waspaloy parts. *Journal of manufacturing, science and engineering*, 133(3).

- Kao, J., & Prinz, F. (1998). Optimal motion planning for deposition in layered manufacturing. *ASME Design engineering technical conferences*, 1-10.
- Katayama, S. (2013). *Handbook of laser welding technologies*. Woodhead publishing.
- Kerlins, V., & Phillips, A. (1987). Modes of Fracture. In A. H. Committee, *ASM Handbook, Volume 12: Fractography* (pp. 12-71).
- Kianian, B. (2017). *Wohlers Report 2017: 3D printing and additive manufacturing state of the industry, Annual worldwide progress report: The Middle East, and other countries* (22nd ed.). USE: Colorado: Fort Collings: Wohlers Associates Inc.
- Kim, H., Cong, W., Zhang, H., & Liu, Z. (2017). Laser Engineered Net Shaping of Nickel-Based Superalloy Inconel 718 Powders onto AISI 4140 Alloy Steel Substrates: Interface Bond and Fracture Failure Mechanism. *Materials*, 10.
- Kim, H., Cong, W., Zhang, H., & Liu, Z. (2017). Laser Engineered Net Shaping of Nickel-Based Superalloy Inconel 718 Powders onto AISI 4140 Alloy Steel Substrates: Interface Bond and Fracture Failure Mechanism. *Materials*, 10.
- Kinsella, M. (2008). *Additive manufacturing of superalloys for aerospace application*. Metals Branch: Metals, Ceramics and NDE Division.
- Kistler, N., Nassar, A., Reutzel, W., Corbin, D., & Beese, A. (2017). Effect of directed energy deposition processing parameters on laser deposited Inconel 718: Microstructure, fusion zone morphology, and hardness. *Journal of Laser Applications*, 29.
- Klimova-Korsmik, O., Turichin, G., Zemlyakov, E., K, B., Petrovsky, P., & Travynov, A. (2016). Technology of high-speed direct laser deposition

from Ni-based superalloys. *9th International conference on Photonic technology's: Physics Procedia*, 83, 716-722.

Knorovsky, G., Cieslak, M., Headley, T., Romig, A., & Hammett, W. (1989). Inconel 718: A solidification diagram. *Metallurgical Transactions A*, 20, 2149-2158.

Kobryn, P., & Semiatin, S. (2001). Mechanical properties of laser-deposited Ti-6Al-4V. *Solid freeform fabrication proceedings*, 179-186.

Kobryn, P., & Semiatin, S. (2003). Microstructure and texture evolution during solidification processing of Ti-6Al-4V. *Journal of Materials Processing Technology*, 135(3), 330-339.

Kok, Y., Tan, X., Wang, P., Nai, S., Loh, N., Liu, E., & Tor, S. (2018). Anisotropy and heterogeneity of microstructure and mechanical properties in metal additive manufacturing: A critical review. *Material & Design*, 139, 565-586.

Kou, S. (2003). *Welding Metallurgy* (2 ed.). Hoboken, New Jersey: John Wiley & Sons.

Kuhn, H., & Medlin, D. (2000). *Mechanical Testing and Evaluation* (Vol. 3). ASM International.

Lampman, S. (2002). Failure Analysis and Prevention: Intergranular Fracture. *ASM Handbook*, 11, 641-649.

Laserline Technical. (2010). *Laser welding*. Surrey: BOC.

Lawrence, J., & Waugh, D. (2014). *Laser surface engineering: processes and applications*. Elsevier.

Leal, R., Barreiros, F., Alves, L., Romeiro, F., Vasco, J., Santos, M., & Marto, C. (2017). Additive manufacturing tooling for the automotive industry.

International Journal of Advanced Manufacturing Technology, 92, 1671-1676.

- Lee, H. (2008). Effects of the cladding parameters on the deposition efficiency in pulsed Nd:YAG laser cladding. *Journals of Materials Processing Technology*, 202, 321-327.
- Li, C., Liu, Z., X, F., & Gua, Y. (2018). Residual stress in metal additive manufacturing. *Procedia CIRP*, 71, 348-353.
- Li, J., Luo, Z., Guan, X., Zhou, X., Brochu, M., & Zhao, Y. (2018). A novel microstructure simulation model for direct energy deposition process. *Solid Freeform Fabrication Symposium*, 1737-1750.
- Li, L., Gong, X., Ye, X., Teng, J., Nie, Y., Li, Y., & Lei, Q. (2018). Influence of Building Direction on the Oxidation Behavior of Inconel 718 Alloy Fabricated by Additive Manufacture of Electron Beam Melting. *Materials*, 11, 2549.
- Li, Z., Chen, J., Sui, S., Zhong, C., Lu, X., & Lin, X. (2020). The microstructure evolution and tensile properties of Inconel 718 fabricated by high-deposition-rate laser directed energy deposition. *Additive Manufacturing*, 31.
- Lindemann, C., & Jahnke, U. (2017). Modelling of laser additive manufactured product lifecycle costs. *Laser Additive Manufacturing: Materials, Design, Technologies and Applications*, 281-316.
- Liscic, B., Tensi, H., Canale, L., & Totten, G. (2010). *Quenching theory and technology*. Boca Raton: CRC Press.
- Liu, F., Lyu, F., Liu, F., Lin, X., & Huang, C. (2020). Laves phase control of inconel 718 superalloy fabricated by laser direct energy deposition via δ aging and solution treatment. *Journal of Materials Research and Technology*, 9, 9753-9765.

- Liu, Z., Li, T., Ning, F., Cong, W., Kim, H., Jiang, Q., & Zhang, H. (2019). Effects of deposition variables on molten pool temperature during laser engineered net shaping of Inconel 718 superalloy. *The International Journal of Advanced Manufacturing Technology*, 102, 969-976.
- Long, Y., Nie, P., Li, Z., Huang, J., Li, X., & Xu, X. (2016). Segregation of niobium in laser cladding Inconel 718 superalloy. *Transactions of Nonferrous Metals Society of China*, 431-436.
- Ludovico, A., Angelastro, A., & Campanelli, S. (2010). Experimental Analysis of the Direct Laser Metal Deposition Process. *New Trends in Technologies: Devices, Computer, Communication and Industrial Systems*, 253-272.
- Ma, M., Wang, Z., & Zeng, X. (2015). Effect of energy input on microstructural evolution of direct laser fabricated IN718 alloy. *Materials Characterisation*, 106, 420-427.
- Mahamood, R., & Akinlabi, E. (2014). Effect of laser power on surface finish during laser metal deposition process. *World congress on engineering and computer science 2014: October 22-24: San Francisco: USA*.
- Mahamood, R., & Akinlabi, E. (2015). Processing parameters optimization for material deposition efficiency in laser metal deposited titanium alloy. *Lasers in manufacturing and materials processing*, 3, 9-21.
- Mahamood, R., Akinlabi, E., & Owolabi, M. (2017). Effect of laser power and powder flow rate on dilution rate and surface finish produced during laser metal deposition of Titanium alloy. *8th international conference on mechanical and intelligent manufacturing technologies*.
- Mahamood, R., Akinlabi, E., Shukla, M., & Pityana, S. (2014). Characterising the effect of processing parameters on the porosity of laser deposited titanium alloy powder. *Proceedings of the international multiconference of engineers and computer scientists*, 2.

- Mandal, P., Lalvani, H., Watt, K., Conway, A., & Tuffs, M. (2020). A Study on Microstructural Evolution in Cold Rotary Forged Nickel Superalloys: C263 and Inconel 718. *Procedia Manufacturing*, 1403-1409.
- Manikandan, S., Sivakumar, D., & Kamaraj, M. (2019). *Welding the Inconel 718 Superalloy*. Elsevier.
- Manikandan, S., Sivakumar, D., Rao, K., & Kamaraj, M. (2015). Laves phase in alloy 718 fusion zone - microscopic and calorimetric studies. *Material Characterisation*, 100, 192-206.
- Mantri, S., Dasari, S., Sharma, A., Alam, T., Pantawane, M., Pole, M., . . . Banerjee, S. (2021). Effect of micro-segregation of alloying elements on the precipitation behaviour in laser surface engineered Alloy 718. *Acta Materialia*, 210, 116844.
- Mao, J., Chang, K., Yang, W., Furrer, D., Ray, K., & Vaze, S. (2002). Cooling precipitation and strengthening study in powder metallurgy superalloy Rene88DT. *Materials science and engineering A*, 332, 318-329.
Retrieved from <https://nptel.ac.in/courses/112107090/33>
- Matsunawa, A., Kim, J., Seto, N., & Mizuntani, M. (1998). Dynamics of keyhole and molten pool in laser welding. *Journal of laser applications*, 10(6), 941-947.
- Mazumder, J., Dutta, D., Kikuchi, N., & Ghosh, A. (2000). Closed loop direct metal deposition: art to part. *Optics and lasers in engineering*, 34(6), 397-414.
- Mazzucato, F., Forni, D., Valente, A., & Cadoni, E. (2021). Laser Metal Deposition of Inconel 718 Alloy and As-built Mechanical Properties Compared to Casting. *Materials*, 14, 437.
- Mercelis, P., & Kruth, J. (2006). Residual stresses in selective laser sintering and selective laser melting. *Rapid prototyping journal*, 12(5), 254-265.

- Milewski, J. (2017). *Additive manufacturing of metals*. Springer.
- Minitab, LLC. (2021). Retrieved from <https://www.minitab.com/en-us/>
- Mitchell, A. (2010). Primary Carbides in Alloy 718. *7th International Symposium on Superalloy 718 and Derivatives*, 161-167.
- Modin, H. (1968). *Metallurgical microscopy*. Butterworths.
- Montgomery, D. (1984). *Design and Analysis of Experiments* (Vol. 7). New York: Wiley.
- Mostafa, A., Rubio, I., Brailovski, V., Jahazi, M., & Medraj, M. (2017). Structure, Texture and Phases in 3D printed IN718 alloy subjected to homogenization and HIP treatments. *Metals*.
- NDT Resource Centre. (2018). *Solidification*. Retrieved from <https://www.nde-ed.org/EducationResources/CommunityCollege/Materials/Structure/solidification.htm>
- Ng, G., Jafors, A., Bi, G., & Zheng, H. (2009). Porosity formation and gas bubbles retention in laser metal deposition. *Applied physics*, 97(3), 641-649.
- Ngo, T., Kashani, A., Imbalzano, G., Nguyen, K., & Hui, D. (2018). Additive manufacturing (3D printing): A review of materials, methods, applications and challenges. *Composites Part B: Engineering*, 143, 172-196.
- Ocylok, S., Alexeev, E., Mann, S., Weisheit, A., Wissenback, K., & Kelbassa, I. (2014). Correlations of melt-pool geometry and process parameters during laser metal deposition by coaxial process monitoring. *Physics Procedia*, 56, 228-238.
- Optomec. (2016). *Lens materials FAQ*. Retrieved from https://www.optomec.com/wp-content/uploads/2014/02/LENS_MATERIALS_Datasheet_WEB2016.pdf

- Oradei-Basile, A., & Radavich, J. (1991). A Current T-T-T Diagram for Wrought Alloy 718. *Superalloys 718, 625 and Various Derivatives*, 325-335.
- Parimi, L., Ravi, G., Clark, D., & Attallah, M. (2014). Microstructural and texture development in direct laser fabricated IN718. *Material Characteristics*, 102-111.
- Park, G. (2007). Design of Experiments. *Analytic Methods for Design Practice*, 309-391.
- Paul, C., Ganesh, P., Mishra, S., Bhargava, P., Negi, J., & Nath, A. (2007). Investigating laser rapid manufacturing for Inconel 625 components. *Optics & Laser Technology*, 39, 800-805.
- Pavlina, E., & Tyne, C. (2008). Correlation of Yield Strength and Tensile Strength with Hardness for Steels. *Journal of Materials Engineering and Performance*, 17, 888-893.
- Petrat, T., Brunner-Schwer, C., Graf, B., & Rethmeier, M. (2019). Microstructure of Inconel 718 parts with constant mass energy input manufactured with direct energy deposition. *Procedia Manufacturing*, 36, 256-266.
- Pinkerton, A., & Li, L. (2004). Modelling the geometry of a moving laser melt pool and deposition track via energy and mass balances. *Journal of physics D: Applied physics*, 37(14), 1885-1895.
- Pirch, N., Niessen, M., Linnenbrink, S., Schopphoven, T., Gasser, A., Poprawe, R., . . . Schulz, W. (2018). Temperature field and residual stress distribution for laser metal deposition. *Journal of laser applications*, 30.
- Popovich, V., Borisov, E., Popovich, A., Sufiiarov, V., Masaylo, D., & Alzina, L. (2017). Functionally graded Inconel 718 process by additive manufacturing: Crystallographic texture, anisotropy of microstructure and mechanical properties. *Materials and Design*, 114, 441-449.

- Popvich, V., Borisov, E., Popovich, A., Sufiiarov, V., Masaylo, D., & Alzina, L. (2017). Impact of heat treatment on mechanical behaviour of Inconel 718 processed with tailored microstructure by selective laser melting. *Materials & Design*, 131, 12-22.
- Porter, D., & Easterling, K. (1991). *Phase transformations in metals and alloys* (3rd ed.). CRC Press.
- Qi, H., Azer, M., & Singh, P. (2010). Adaptive toolpath deposition method for laser net shape manufacturing and repair of turbine compressor airfoils. *The international journal of advanced manufacturing technology*, 48(4), 121-131.
- Radavich, J. (2004). The Physical Metallurgy of Cast and Wrought Alloy 718. *Superalloy 718 - Metallurgy and Applications*, 229-240.
- Radhakrishna, C., & Prasad Rao, K. (1997). The formation and control of Laves phase in superalloy 718 welds. *Journal of Materials Science*, 32, 1977-1984.
- Radhakrishna, C., Prasad Rao, K., & Srivivas, S. (1995). Laves phase in superalloy 718 weld metals. *Journal of Materials Science Letters*, 14, 1810-1812.
- Rafi, H., Starr, T., & Stucker, B. (2013). A comparison of the tensile, fatigue, and fracture behavior of Ti-6Al-4V and 15-5 PH stainless steel parts made by selective laser melting. *International Journal of Advanced Manufacturing Technology*, 69, 1299-1039.
- Ram, G., Reddy, A., Rao, K., Reddy, G., & Sundar, J. (2005). Microstructure and tensile properties of Inconel 718 pulsed Nd-YAG laser welds. *Journal of Materials Processing Technology*, 167, 73-82.
- Reed, R. (2006). *The superalloys - fundamentals and applications*. Cambridge University Press.

- Reimer, L. (1997). *Scanning Electron Microscopy: Physics of Image Formation and Microanalysis*. Springer.
- Reinforced Plastics. (2014). Reducing the weight of aircraft interiors. *Reinforced Plastics*, 58(4), 36-37.
- Routhu, S. (2010). 2-D path planning for direct laser deposition process. *ASME*, 415-423.
- Ruiz, J., Cortina, M., Arrizubieta, J., & Aitzol, L. (2018). Study of the influence of shielding gases on laser metal deposition of Inconel 718 superalloy. *Materials*, 11, 1388.
- Saboori, A., Gallo, D., Biamino, S., Fino, P., & Lombardi, M. (2017). An Overview of Additive Manufacturing of Titanium Components by Directed Energy Deposition: Microstructure and Mechanical Properties. *Applied Sciences*, 7.
- Sadeghi, E., Karimi, P., Israelsson, N., Shipley, J., Mansson, T., & Hansson, T. (2020). Inclusion-induced fatigue crack initiation in powder bed fusion of Alloy 718. *Additive Manufacturing*, 36.
- SAE International. (2016). Nickel Alloy, Corrosion and Heat Resistant, Sheet, Strip, and Plate, 52.5Ni - 19Cr - 3.0Mo - 5.1Cb (Nb) - 0.90Ti - 0.50Al - 18Fe, Consumable Electrode or Vacuum Induction Melted, 1950 °F (1066 °C) Solution Heat Treated AMS5597. *Aerospace Material Specification*.
- SAE International. (2016). Nickel Alloy, Corrosion and Heat-Resistant, Bars, Forgings, and Rings 52.5Ni - 19Cr - 3.0Mo - 5.1Cb (Nb) - 0.90Ti - 0.50Al - 18Fe Consumable Electrode or Vacuum Induction Melted 1775 °F (968 °C) Solution Heat Treated, Precipitation-Hardenable. *Aerospace Material Specification*.

- Saha, P. (2016). *Aerospace Manufacturing Processes*. Boca Raton: CRC Press.
- Sames, W., List, F., Pannala, R., Dehoff, R., & Babu, S. (2016). The metallurgy and processing science of metal additive manufacturing. *International Materials Reviews*, 61, 315-360.
- Sames, W., List, F., Pannala, S., Dehoff, R., & Babu, S. (2016). The Metallurgy and Processing Science of Metal Additive Manufacturing. *International Materials Reviews*, 61, 315-360.
- Sanchez Amaya, J., Amaya-Vazquez, M., & Botana, F. (2013). Laser welding of light metal alloys: aluminium and titanium alloys-8. *Handbook of laser welding technologies*, 215-254.
- Santos, E., Shiomi, M., Osakada, K., & Laoui, T. (2006). Rapid manufacturing of metal components by laser forming. *International journal of machine tools & manufacture*, 46, 1459-1468.
- Schirra, J., Caless, R., & Hatala, R. (1991). The effect of Laves phase on the mechanical properties of wrought and cast + HIP inconel 718. *Superalloys 718, 625 and Various Derivatives*, 375-389.
- Schwendner, K., Banerjee, R., Collins, P., Brice, P., & Fraser, H. (2001). Direct laser deposition of alloys from elemental powder blends. *Scripta Materialia*, 45, 1123-1129.
- Segerstark, A., Andersson, J., & Svensson, L. (2014). Review of laser deposited superalloys using powder as an additive. *8th International symposium on superalloy 718 and derivatives*, 393-408.
- Segerstark, A., Andersson, J., Svensson, L., & Ojo, O. (2018). Effect of process parameters on the crack formation in laser metal powder deposition of alloy 718. *Metallurgical and materials transactions A*, 49(10), 5042-5050.

- Selcuk, C. (2011). Laser metal deposition for powder metallurgy parts. *Powder metallurgy*, 54, 94-99.
- Shah, K., Pinkerton, A., Salman, A., & Li, L. (2010). Effects of melt pool variables and process parameters in laser direct metal deposition of aerospace alloys. *Materials and manufacturing processes*, 25(12), 1372-1380.
- Shamsaei, N., Yadollahi, A., Bian, L., & Thompson, S. (2015). An overview of Direct Laser Deposition for additive manufacturing; Part II: Mechanical behaviour, process parameter optimization and control. *Additive Manufacturing*, 8, 12-35.
- Shi, X., Duan, S., Yang, W., Gua, H., & Gua, J. (2018). Solidification and Segregation Behaviours of Superalloy IN718 at a Slow Cooling Rate. *Materials*, 11.
- Shiomi, M., Osakada, K., Nakamura, K., Yamashita, T., & Abe, F. (2004). Residual stress within metallic model made by selective laser melting process. *CIRP Annual of manufacturing technology*, 53(1), 195-198.
- Sims, C., Stoloff, N., & Hagel, W. (1987). *Superalloys 2, High-temperature materials for aerospace and industrial power*. John Wiley & Sons.
- Singh Handa, S. (2013). Precipitation of carbides in a Ni-based superalloy. *Division of manufacturing processes: Production engineering, human work sciences and ergonomics*.
- Smallman, R., & Ngan, A. (2014). *Modern physical metallurgy* (8 ed.). Oxford: Butterworth-Heinemann.
- Smallman, R., & Ngan, A. (2014). *Modern physical metallurgy* (8th ed.). UK: Oxford: Butterworth-Heinemann.
- Smith, D., Bicknell, J., Jorgensen, L., Patterson, B., Cordes, N., Tsukrov, I., & Knezevic, M. (2016). Microstructure and mechanical behaviour of direct

- metal laser sintered Inconel 718 alloy. *Materials Characterisation*, 113, 1-9.
- Song, K. (2008). Grain growth and particle pinning in a model Ni-based superalloy. *Materials science and engineering*, 479, 365-372.
- Song, L., Bagavath-Singh, V., Dutta, B., & Mazumder, J. (2021). Control of melt pool temperature and deposition height during direct metal deposition process. *International Journal of Advanced Manufacturing Technology*, 58, 247-256.
- Sreekanth, S., Hurtig, K., Joshi, S., & Andersson, J. (2021). Influence of Laser-Directed Energy Deposition Process Parameters and Thermal Post-Treatments on Nb-rich Secondary Phases in Single-Track Alloy 718 Specimens. *Journal of Laser Applications*, 33.
- Stevens, E., Toman, J., To, A., & Chmielus, M. (2017). Variation of hardness, microstructure, and Laves phase distribution in direct laser deposited alloy 718 cuboids. *Materials & Design*, 119, 188-198.
- Strößner, J., Terock, M., & Glatzel, U. (2015). Mechanical and Microstructural Investigation of Nickel-Based Superalloy IN718 Manufactured by Selective Laser Melting (SLM). *Advanced Engineering Materials*, 17, 1099-1105.
- Sui, S., Chen, J., Fan, E., Yang, H., Lin, X., & Huang, W. (2017). The Influence of Laves Phases on the High-Cycle Fatigue Behavior of Laser Additive Manufactured Inconel 718. *Materials Science and Engineering*, 695, 6-13.
- Sun, Y., & Hao, M. (2021). Statistical analysis and optimisation of process parameters in Ti6Al4V laser cladding using Nd:YAG laser. *Optics and Lasers in Engineering*, 50, 985-995.

- Sundararaman, M., Mukhopadhyay, P., & Banerjee, S. (1988). Precipitation of the δ -Ni₃Nb phase in two nickel base superalloys. *Metallurgical Transactions A*, 19, 453-465.
- Sundararaman, M., Mukhopadhyay, P., & Banerjee, S. (1997). Carbide precipitation in Nickel Base Superalloys 718 and 625 and their effect on mechanical properties. *Superalloys 718, 625, 706 and Various Derivatives*, 367-379.
- Sutton, B., Herderick, E., Thodla, R., Ahlfors, M., & Ramirez, A. (2019). Heat Treatment of Alloy 718 Made by Additive Manufacturing. *Additive Manufacturing: Validation and Control*, 71, 1134-1143.
- Thompson, S., Bian, L., Shamsaei, N., & Yadollahi, A. (2015). An overview of Direct Laser Deposition for additive manufacturing; Part I: Transport phenomena, modeling and diagnostics. *Additive Manufacturing*, 8, 36-62.
- Tian, Y., McAllister, D., Colijn, H., Mills, M., Farson, D., Nordin, M., & Babu, S. (2014). Rationalisation of Microstructure Heterogeneity in Inconel 718 Builds Made by the Direct Laser Additive Manufacturing Process. *Metallurgical and Materials Transactions A*, 45, 4470-4483.
- Totten, G. (2007). *Steel heat treatment: metallurgy and technologies*. Boca Raton: Taylor & Francis.
- Tucho, W., Cuviller, P., Sjolyst-Kverneland, A., & Hansen, V. (2017). Microstructure and Hardness studies of Inconel 718 Manufactured by Selective Laser Melting before and after Solution Heat Treatment. *Materials Science and Engineering A*, 689, 220-232.
- TWI Technology Centre. (2019). *Trumpf DMD 505 process parameters*. Yorkshire, United Kingdom.
- U.S Department of Energy. (2012). *Additive Manufacturing: pursuing the promise*. US Department of Energy: Advanced manufacturing office.

- Vander Voort, G. (1987). Fractography: Visual Examination and Light Microscopy. *ASM Handbook*, 12, 91-165.
- Vander Voort, G. (2004). Metallographic Techniques for Superalloys. *Microscopy and Microanalysis*, 10.
- Vander Voort, G. (2004). Metallography and Microstructures: Contrast Enhancement and Etching. *ASM Handbook*, 9, 294-312.
- Vander Voort, G. (2004). Metallography and Microstructures: Metallography and Microstructures of Nickel and Nickel-Copper Alloys. *ASM Handbook*, 9, 816-819.
- Vander Voort, G. (2004). Metallography and Microstructures: Tables of Chemicals and Etchants. *ASM Handbook*, 9, 1094-1114.
- Vandersluis, E., & Ravindran, C. (2017). Comparison of Measurement Methods for Secondary Dendrite Arm Spacing. *Metallography, Microstructure, and Analysis*, 6, 89-94.
- Versnyde, F., & Shank, M. (1970). The development of columnar grain and single crystal high temperature materials through directional solidification. *Material Science Engineering*, 6, 213-247.
- Vetter, P., Engel, T., & Fontaine, J. (1994). Laser cladding: the relevant parameters for process control. *Laser materials processing: Industrial and electronics applications*, 2207, 452-462.
- Vilar, R. (2001). Laser cladding. *Laser applications*, 11, 64-79.
- Wei, H., Knapp, G., Mukherjee, T., & DebRoy, T. (2019). Three-dimensional grain growth during multi-layer printing of a nickel based alloy Inconel 718. *Additive Manufacturing*, 48-459.
- Wei, H., Mazumber, J., & BedRoy, T. (2015). Evolution of solidification texture during additive manufacturing. *Scientific reports*, 5, 16446.

- Whang, S. (2011). Nanostructured Metals and Alloys. *Processing, Microstructure, Mechanical Properties and Applications*, 21-35.
- Wilkie, A., & Weidlich, A. (2011). A Physically Plausible Model for Light Emission from Glowing Solid Objects. *Eurographics Symposium on Rendering*, 4.
- Witzel, J., Stannard, S., Gasser, A., & Kelbassa, I. (2011). Characterization of micro/macrostructure of laser cladded inconel 718 with increased deposition rates as related to the mechanical properties. *30th International Congress on Applications of Lasers & Electro-Optics*, 560-566.
- Xiao, H., Li, S., Han, X., Mazumder, J., & Song, L. (2017). Laves phase control of Inconel 718 alloy using quasi-continuous-wave laser additive manufacturing. *Materials and Design*, 122, 330-339.
- Xiao, H., Li, S., Xiao, W., Li, Y., Cha, L., Mazumder, J., & Song, L. (2016). Effects of laser modes on Nb segregation and Laves phase formation during laser additive manufacturing of nickel-based superalloy. *Materials Letters*.
- Xu, X., Ding, J., Ganguly, S., & Williams, S. (2019). Investigation of process factors affecting mechanical properties of Inconel 718 superalloy in wire and arc additive manufacture process. *Journal of Materials Processing Technology*, 265, 201-209.
- Yang, S., Du, D., & Chang, B. (2018). Studies on the influence of beam profile and cooling conditions on the laser deposition of a directionally-solidified superalloy. *Materials*, 11.
- Yorserkani, E., Khajepour, A., & Corbin, S. (2005). *Laser Cladding*. Boca Raton, Florida: CRC Press.

- Yu, H., Hayashi, S., Kakehi, K., & Kua, Y. (2019). Study of Formed Oxides in IN718 Alloy during the Fabrication by Selective Laser Melting and Electron Beam Melting. *Metals*, 9.
- Yu, J., Lin, X., Ma, L., Wang, J., Fu, X., Chen, J., & Huang, W. (2011). Influence of laser deposition patterns on part distortion, interior quality and mechanical properties by laser solid forming (LSF). *Materials science and engineering: A*, 528(3), 1094-1104.
- Yuan, K., Guo, W., Li, P., Wang, J., Su, Y., Lin, X., & Li, Y. (2018). Influence of process parameters and heat treatments on the microstructures and dynamic mechanical behaviors of Inconel 718 superalloy manufactured by laser metal deposition. *Materials Science & Engineering A*, 721, 215-225.
- Yuan, K., Guo, W., Li, P., Wang, J., Su, Y., Lin, X., & Li, Y. (2018). Influence of Process Parameters and Heat Treatments on the Microstructures and Dynamic Mechanical Behaviors of Inconel 718 Superalloy Manufactured by Laser Metal Deposition. *Materials Science & Engineering A*, 721, 215-225.
- Yusuf, S., Cutler, S., & Gao, N. (2019). Review: The Impact of Metal Additive Manufacturing on the Aerospace Industry. *Metals*, 9, 1286.
- Zhang, J. (2004). Adaptive slicing for a multi-axis layer aided manufacturing process. *Journal of mechanical design*, 126, 254.
- Zhang, J., & Jung, Y. (2018). *Additive manufacturing: Materials, processes, quantifications and applications*. Butterworth-Heinemann.
- Zhang, K., Zhang, X., & Liu, W. (2012). Influences of processing parameters on dilution ratio of laser cladding layer during laser metal deposition shaping. *Advanced materials research*, 549, 785-789.

- Zhang, Q., Yao, J., & Jyoti, M. (2011). Laser Direct Metal Deposition Technology and Microstructure and Composition Segregation of Inconel 718 Superalloy. *Journal of Iron and Steel Research, International*, 18, 73-78.
- Zhang, Q., Zhang, J., Zhuang, Y., Lu, J., & Yao, J. (2020). Hot Corrosion and Mechanical Performance of Repaired Inconel 718 Components via Laser Additive Manufacturing. *Materials*, 13.
- Zhang, Y., Cao, X., Wanjara, P., & Medraj, M. (2013). Fiber laser deposition of Inconel 718 using powders. *Advanced materials, processes and applications for Additive Manufacturing*, 37-49.
- Zhang, Y., Li, Z., Nie, P., & Wu, Y. (2013). Effect of Precipitation on the Microhardness Distribution of Diode Laser Epitaxially Deposited IN718 Alloy Coating. *Journal of Materials Science & Technology*, 29, 349-352.
- Zhao, X., Chen, J., Lin, X., & Huang, W. (2008). Study on microstructure and mechanical properties of laser rapid forming Inconel 718. *Materials Science and Engineering: A*, 478, 119-124.
- Zheng, B., Zhou, Y. S., Schoenung, J., & Lavernia, E. (2008). Thermal behaviour and microstructure evolution during laser deposition with laser engineered net shaping: Part II. Experimental investigation and discussion. *Metallurgical materials transactions: A*, 39, 2237-2245.
- Zhong, C., Gasser, A., Kittel, J., Wissenbach, K., & Poprawe, R. (2016). Improvement of material performance of Inconel 718 formed by high deposition rate laser metal deposition. *Journal of Material Deposition*, 98, 128-134.
- Zhong, C., Kittel, J., Gasser, A., & Schleigenbau, J. (2019). Study of nickel-based superalloys Inconel 718 and Inconel 625 in high-deposition-rate laser metal deposition. *Optics and Laser technology*, 109, 352-360.

- Zhong, C., Pirch, N., Gasser, A., Poprawe, R., & Schleifenbaum, J. (2017). The influence of the powder stream on high-deposition rate laser metal deposition with Inconel 718. *Metals*, 7(443).
- Zhou, L., Mehta, A., McWilliams, B., Cho, K., & Sohn, Y. (2019). Microstructure, precipitates and mechanical properties of powder bed fused inconel 718 before and after heat treatment. *Journal of Materials Science & Technology*, 35, 1153-1164.
- Zhu, L., Xu, Z., & Gu, Y. (2018). Microstructural evolution of laser solid forming Inconel 718 superalloy under different laser power. *Materials Letters*, 217, 159-162.

Appendices

Appendix 1 – Stage 1 melt pool diameter, track separation and z-increment for each process parameter set.

| Parameter set | Melt-pool diameter (mm) | Track separation (mm) | z-increment (mm) |
|---------------|-------------------------|-----------------------|-------------------|
| 1 | 0.97 | N/A ¹ | N/A ¹ |
| 2 | 1.06 | N/A ¹ | N/A ¹ |
| 3 | 0.9 | N/A ¹ | N/A ¹ |
| 4 | 1.71 | 1.20 | 0.45 |
| 5 | 1.54 | 1.20 | 0.45 |
| 6 | 1.23 | 0.68 ² | 0.20 ² |
| 7 | 2.15 | 1.59 ² | 0.50 ² |
| 8 | 1.65 | 1.20 ³ | 0.25 ³ |
| 9 | 1.72 | 1.25 | 0.27 |
| 10 | 1.8 | 1.30 | 0.34 |

¹ parameter sets were not used past deposition of single track.

² values used for 2-layer, 6-track/5-track deposits. Parameter sets not used for depositing final blocks.

³ block was not completed.

Appendix 2 – Previous process parameter combinations on the Trumpf 505 DMD system.

| Laser power (W) | Scan speed (mm/min) | Powder feed rate (g/min) |
|-----------------|---------------------|--------------------------|
| 500 | 450 | 1.9 |
| 500 | 400 | 2 |
| 575 | 550 | 3 |
| 600 | 400 | 1.8 |
| 600 | 750 | 3.2 |
| 675 | 500 | 2.4 |
| 675 | 600 | 2.7 |
| 675 | 700 | 3.6 |
| 700 | 400 | 2.7 |
| 700 | 550 | 3.2 |
| 700 | 600 | 1.6 |
| 700 | 800 | 3.6 |
| 750 | 500 | 2.5 |
| 750 | 600 | 1.6 |
| 750 | 950 | 3 |
| 800 | 450 | 3 |

| | | |
|------|-----|-----|
| 800 | 800 | 4 |
| 825 | 875 | 1.2 |
| 825 | 625 | 3.6 |
| 840 | 500 | 2.7 |
| 850 | 940 | 3.6 |
| 850 | 750 | 4 |
| 900 | 600 | 1.2 |
| 900 | 700 | 2 |
| 1000 | 400 | 2 |
| 1000 | 600 | 1.6 |
| 1000 | 800 | 2.5 |
| 1000 | 970 | 4 |
| 1030 | 900 | 1.4 |
| 1050 | 900 | 1.4 |
| 1100 | 800 | 2.3 |
| 1100 | 900 | 1.6 |
| 1100 | 950 | 1.6 |
| 1200 | 900 | 2.3 |
| 1300 | 900 | 3.2 |

Appendix 3 – Raw grain boundary measurement data.

| | 1 | 2 | 3 | 4 | 5 | 6 | 7 | 8 | 9 | 10 |
|-------------------|-----|-----|-----|-----|-----|-----|-----|-----|-----|-----|
| Stage 1: 4 Large | 358 | 266 | 308 | 315 | 255 | 313 | 290 | 301 | 267 | 297 |
| Stage 1: 5 Large | 285 | 250 | 318 | 369 | 288 | 255 | 339 | 348 | 300 | 257 |
| Stage 1: 9 Large | 282 | 370 | 366 | 338 | 279 | 284 | 267 | 290 | 336 | 361 |
| Stage 1: 10 Large | 293 | 266 | 279 | 366 | 262 | 269 | 257 | 314 | 328 | 349 |

Appendix 4 – Raw SDAS data.

| | Length (μm) | No.arms | SDAS (μm) | Length (μm) | No.arms | SDAS (μm) | Length (μm) | No.arms | SDAS (μm) |
|-------------|-----------------------------|---------|---------------------------|-----------------------------|---------|---------------------------|-----------------------------|---------|---------------------------|
| Stage 1: 4 | 83.28 | 10 | 8.33 | 68.87 | 9 | 7.65 | 82.38 | 9 | 9.15 |
| Small | 52.53 | 6 | 8.75 | 56.80 | 7 | 8.11 | 79.50 | 10 | 7.95 |
| Stage 1: 5 | 70.65 | 8 | 8.83 | 101.11 | 9 | 11.23 | 66.38 | 6 | 11.06 |
| Small | 48.74 | 6 | 8.12 | 37.24 | 4 | 9.31 | 51.94 | 5 | 10.39 |
| Stage 1: 9 | 76.17 | 9 | 8.46 | 42.44 | 7 | 6.06 | 34.34 | 6 | 5.72 |
| Small | 50.12 | 8 | 6.27 | 51.17 | 8 | 6.40 | 46.06 | 7 | 6.58 |
| Stage 1: 10 | 77.58 | 9 | 8.62 | 81.50 | 9 | 9.06 | 35.33 | 5 | 7.07 |
| Small | 76.95 | 9 | 8.55 | 80.22 | 9 | 8.91 | 51.23 | 8 | 6.40 |
| Stage 1: 4 | 53.20 | 6 | 10.64 | 99.77 | 12 | 9.07 | 37.95 | 5 | 9.49 |
| Large | 52.26 | 6 | 10.45 | 92.05 | 7 | 15.34 | 93.54 | 8 | 13.36 |
| Stage 1: 5 | 59.25 | 8 | 8.46 | 48.65 | 4 | 16.22 | 37.20 | 3 | 18.60 |
| Large | 57.91 | 9 | 7.24 | 39.92 | 7 | 6.65 | 52.26 | 6 | 10.45 |
| Stage 1: 9 | 58.25 | 8 | 8.32 | 69.58 | 6 | 13.92 | 82.37 | 7 | 13.73 |
| Large | 69.79 | 6 | 13.96 | 45.91 | 4 | 15.30 | 40.04 | 6 | 8.01 |
| Stage 1: 10 | 58.18 | 7 | 9.70 | 78.85 | 6 | 15.77 | 57.43 | 6 | 11.49 |
| Large | 92.54 | 8 | 13.22 | 71.49 | 7 | 11.92 | 79.43 | 8 | 11.35 |

Appendix 5 – Raw tensile data.

| | Specimen 1 | | | Specimen 2 | | | Specimen 3 | | |
|------------------------|------------------|-----------|----------------|------------------|-----------|----------------|------------------|-----------|----------------|
| | 0.2% proof (MPa) | UTS (MPa) | Elongation (%) | 0.2% proof (MPa) | UTS (MPa) | Elongation (%) | 0.2% proof (MPa) | UTS (MPa) | Elongation (%) |
| Stage 1: 4 Horizontal | 668.0 | 874.8 | 10.9 | 695.4 | 1018.8 | 15.8 | 735.9 | 886.2 | 7.4 |
| Stage 1: 4 Vertical | 495.8 | 763.8 | 45.5 | 485.3 | 732.5 | 38.5 | 509.0 | 726.4 | 32.0 |
| Stage 1: 5 Horizontal | 598.2 | 943.0 | 19.5 | 591.1 | 951.8 | 26.8 | 651.7 | 982.9 | 21.5 |
| Stage 1: 5 Vertical | 490.5 | 776.2 | 32.1 | 458.7 | 781.5 | 38.4 | 498.0 | 799.2 | 36.1 |
| Stage 1: 9 Horizontal | 585.2 | 915.1 | 24.4 | 573.0 | 916.9 | 26.9 | 627.2 | 928.2 | 23.8 |
| Stage 1: 9 Vertical | 489.5 | 816.3 | 34.3 | 466.6 | 817.0 | 39.7 | 460.2 | 809.8 | 37.6 |
| Stage 1: 10 Horizontal | 591.7 | 958.3 | 35.4 | 569.2 | 932.9 | 28.8 | 622.8 | 978.8 | 29.8 |
| Stage 1: 10 Vertical | 450.9 | 799.4 | 43.1 | 460.0 | 808.6 | 38.1 | 473.6 | 803.4 | 38.5 |
| Stage 2: 1 | 661.0 | 1035.6 | 21.0 | 659.0 | 989.7 | 16.3 | 687.0 | 1013.5 | 18.9 |
| Stage 2: 2 | 645.0 | 819.3 | 15.8 | 599.0 | 818.6 | 16.5 | 558.0 | 856.3 | 21.2 |
| Stage 2: 3 | 545.0 | 779.7 | 33.6 | 529.0 | 781.2 | 32.8 | 530.0 | 782.3 | 33.4 |
| Stage 3: Horizontal | 730.0 | 1071.7 | 22.6 | 657.0 | 978.8 | 15.2 | 658.0 | 1022.6 | 22.3 |
| Stage 3: Vertical | 644.0 | 903.7 | 30.7 | 652.0 | 924.4 | 31.2 | 649.0 | 918.8 | 30.9 |
| Stage 4 | 651.0 | 897.9 | 19.2 | 611.0 | 940.2 | 23.1 | 649.0 | 904.6 | 18.3 |

Appendix 6 – Raw macrohardness data.

| | | Macrohardness (HV ₁₀) | | | | | | | | | | | | | | | | | | | | | | | |
|------------------------|-------|-----------------------------------|-------|-------|-------|-------|-------|-------|-------|-------|-------|-------|------------------------|-------|-------|-------|-------|-------|-------|-------|-------|-------|-------|-------|-------|
| Stage 1: 4 Small | 312.8 | 319.4 | 318.3 | 298.7 | 283.5 | 301.1 | 306.1 | 305.2 | 311.1 | 294 | 301.6 | 295.6 | Stage 1: 5 Small | 284.3 | 281.9 | 280.1 | 280.8 | 271.6 | 275.1 | 272.7 | 269.6 | 271.8 | 270.8 | 260.2 | 274 |
| Stage 1: 9 Small | 311.9 | 299.7 | 293.1 | 310.2 | 308.8 | 303.6 | 316.1 | 294.6 | 306.4 | 307.4 | 315.2 | 312.9 | Stage 1: 10 Small | 319.8 | 302.2 | 320.3 | 327.5 | 296.5 | 311.2 | 316 | 284.3 | 296.7 | 310.1 | 321.1 | 290 |
| Stage 1: 4 Large | 277.4 | 275.3 | 290.9 | 284.2 | 268.9 | 281.1 | 274 | 292.5 | 272.1 | 292.8 | 287.1 | 291.8 | Stage 1: 5 Large | 271.5 | 279.6 | 274.6 | 279.1 | 276.7 | 272.5 | 281.4 | 271.4 | 280.9 | 279.5 | 295.2 | 278.6 |
| Stage 1: 9 Large | 282.2 | 282.1 | 288.2 | 281.6 | 291.1 | 295.5 | 286.4 | 286.4 | 287.5 | 286.4 | 288.1 | 294.8 | Stage 1: 10 Large | 262.2 | 289.9 | 274.7 | 273.1 | 280.1 | 289.5 | 292.5 | 284.1 | 298.2 | 295 | 285.4 | 293.1 |
| Stage 2: 1 | 269.8 | 267.3 | 46.6 | 258.6 | 262.7 | 266.2 | 258.4 | 266.7 | 255.3 | 252.9 | 257.1 | 269.7 | Stage 2: 2 | 252.7 | 268.6 | 261.5 | 263.9 | 267.5 | 253.1 | 262.2 | 265.6 | 262.7 | 263.9 | 266.9 | 253.1 |
| Stage 2: 3 | 295.3 | 266.2 | 262 | 263.1 | 285.3 | 282.4 | 280.3 | 257 | 265 | 275.7 | 264 | 259.1 | Stage 3: Horizontal xy | 257.2 | 274.3 | 252.3 | 282.3 | 274.4 | 254.3 | 266.7 | 258.2 | 263.3 | 267.9 | 272.1 | 268.2 |
| Stage 3: Horizontal xz | 277.3 | 269.1 | 273.8 | 264.4 | 253.3 | 263.3 | 265.2 | 259.6 | 270.2 | 271.3 | 271.1 | 265.2 | Stage 3: Horizontal yz | 276.7 | 272.7 | 285 | 273.7 | 296.5 | 298.4 | 295.5 | 288 | 276.1 | 282.6 | 278.9 | 279.1 |
| Stage 3: Vertical xy | 258.3 | 255.6 | 247.3 | 249.2 | 238.1 | 254.8 | 248.3 | 240.5 | 244 | 257.1 | 251.7 | 239.3 | Stage 3: Vertical xz | 320.6 | 315.5 | 311.5 | 326.1 | 309.4 | 329.7 | 328.8 | 319.4 | 305.6 | 325.2 | 300.7 | 301.5 |
| Stage 3: Vertical yz | 309.5 | 312.5 | 305.8 | 312.6 | 311.9 | 304.8 | 308.4 | 321.1 | 311.7 | 320.3 | 313.6 | 306.1 | Stage 4: Build dir. 1 | 279 | 281.5 | 280 | 259.5 | | | | | | | | |
| Stage 4: Interface | 266.8 | 257.1 | 269.1 | 277.2 | | | | | | | | | Stage 4: Build dir. 2 | 263.7 | 264.9 | 281.1 | 273.7 | | | | | | | | |

Appendix 7 – Raw microhardness data.

| Stage 1: 4 Small Microhardness (HV_{0.5}) | | | | | | | | | |
|--|-----|-----|-----|-----|-----|-----|-----|-----|-----|
| 317 | 332 | 364 | 354 | 359 | 350 | 370 | 393 | 371 | 401 |
| 311 | 324 | 345 | 353 | 391 | 374 | 376 | 383 | 387 | 399 |
| 323 | 337 | 345 | 367 | 419 | 411 | 388 | 421 | 385 | 385 |
| 330 | 356 | 352 | 363 | 396 | 397 | 376 | 415 | 390 | 390 |
| 323 | 376 | 351 | 364 | 385 | 417 | 425 | 401 | 411 | 401 |
| 322 | 357 | 375 | 372 | 388 | 405 | 429 | 433 | 414 | 400 |
| 336 | 339 | 376 | 394 | 394 | 400 | 433 | 440 | 397 | 429 |
| 318 | 354 | 387 | 386 | 409 | 420 | 413 | 469 | 414 | 380 |
| 315 | 349 | 375 | 389 | 428 | 424 | 412 | 422 | 424 | 423 |
| 313 | 347 | 376 | 387 | 422 | 456 | 429 | 414 | 434 | 421 |
| 317 | 352 | 373 | 384 | 425 | 424 | 439 | 419 | 422 | 410 |
| 301 | 338 | 354 | 385 | 406 | 445 | 446 | 444 | 425 | 420 |
| 296 | 344 | 339 | 375 | 391 | 382 | 453 | 442 | 417 | 407 |
| 291 | 334 | 323 | 357 | 403 | 397 | 418 | 421 | 426 | 389 |
| 297 | 318 | 325 | 362 | 382 | 421 | 405 | 413 | 465 | 409 |

| Stage 1: 5 Small Microhardness (HV_{0.5}) | | | | | | | | | |
|--|-----|-----|-----|-----|-----|-----|-----|-----|-----|
| 292 | 287 | 279 | 296 | 284 | 313 | 309 | 286 | 302 | 298 |
| 304 | 301 | 299 | 300 | 281 | 295 | 298 | 297 | 290 | 305 |
| 288 | 288 | 297 | 289 | 287 | 289 | 287 | 276 | 278 | 302 |
| 283 | 286 | 286 | 294 | 272 | 296 | 281 | 287 | 285 | 292 |
| 290 | 305 | 295 | 303 | 284 | 286 | 287 | 288 | 285 | 286 |
| 272 | 297 | 287 | 291 | 292 | 294 | 291 | 288 | 282 | 284 |
| 292 | 282 | 285 | 280 | 285 | 299 | 277 | 293 | 291 | 281 |
| 281 | 294 | 283 | 300 | 286 | 282 | 283 | 284 | 318 | 294 |
| 301 | 306 | 288 | 307 | 295 | 296 | 284 | 284 | 306 | 304 |
| 293 | 300 | 290 | 311 | 290 | 300 | 283 | 289 | 303 | 297 |
| 309 | 302 | 295 | 305 | 284 | 297 | 301 | 288 | 295 | 296 |
| 329 | 333 | 296 | 307 | 292 | 298 | 296 | 292 | 293 | 297 |
| 358 | 341 | 348 | 312 | 305 | 316 | 302 | 304 | 300 | 290 |
| 339 | 373 | 335 | 337 | 309 | 317 | 297 | 300 | 303 | 311 |
| 387 | 375 | 367 | 369 | 329 | 317 | 317 | 298 | 307 | 306 |

| Stage 1: 9 Small Microhardness (HV_{0.5}) | | | | | | | | | |
|--|-----|-----|-----|-----|-----|-----|-----|-----|-----|
| 343 | 322 | 337 | 345 | 357 | 381 | 371 | 395 | 404 | 444 |
| 331 | 340 | 344 | 345 | 362 | 373 | 365 | 395 | 409 | 403 |
| 342 | 329 | 350 | 339 | 364 | 367 | 372 | 401 | 400 | 364 |
| 346 | 347 | 324 | 358 | 360 | 365 | 383 | 377 | 366 | 347 |
| 347 | 323 | 331 | 360 | 336 | 345 | 377 | 392 | 346 | 356 |
| 357 | 324 | 342 | 342 | 352 | 370 | 381 | 367 | 339 | 359 |
| 333 | 358 | 336 | 318 | 355 | 391 | 360 | 364 | 360 | 348 |
| 354 | 333 | 316 | 333 | 352 | 357 | 321 | 338 | 327 | 356 |
| 331 | 320 | 325 | 328 | 343 | 349 | 288 | 325 | 317 | 386 |
| 317 | 350 | 318 | 318 | 323 | 341 | 321 | 313 | 350 | 374 |
| 303 | 296 | 304 | 366 | 346 | 309 | 289 | 329 | 364 | 376 |
| 310 | 319 | 315 | 340 | 314 | 312 | 313 | 332 | 350 | 355 |
| 320 | 317 | 350 | 308 | 281 | 320 | 321 | 353 | 347 | 377 |
| 328 | 327 | 329 | 317 | 330 | 306 | 337 | 344 | 344 | 372 |
| 305 | 294 | 325 | 336 | 295 | 289 | 339 | 315 | 348 | 371 |

| Stage 1: 10 Small Microhardness (HV_{0.5}) | | | | | | | | | |
|---|-----|-----|-----|-----|-----|-----|-----|-----|-----|
| 301 | 304 | 320 | 346 | 360 | 362 | 348 | 322 | 300 | 299 |
| 287 | 306 | 301 | 308 | 361 | 357 | 304 | 297 | 299 | 289 |
| 291 | 304 | 304 | 307 | 334 | 328 | 301 | 298 | 306 | 294 |
| 296 | 289 | 310 | 296 | 325 | 315 | 286 | 300 | 294 | 297 |
| 288 | 289 | 325 | 324 | 303 | 308 | 329 | 330 | 293 | 286 |
| 293 | 324 | 320 | 318 | 318 | 320 | 320 | 322 | 322 | 295 |
| 309 | 338 | 326 | 314 | 338 | 334 | 310 | 322 | 330 | 312 |
| 315 | 336 | 344 | 334 | 352 | 346 | 328 | 338 | 332 | 316 |
| 315 | 362 | 348 | 355 | 337 | 327 | 345 | 338 | 349 | 313 |
| 319 | 353 | 360 | 376 | 360 | 365 | 381 | 365 | 352 | 321 |
| 332 | 360 | 383 | 391 | 353 | 355 | 393 | 385 | 359 | 335 |
| 386 | 346 | 386 | 399 | 338 | 334 | 395 | 382 | 347 | 387 |
| 361 | 361 | 380 | 410 | 372 | 366 | 404 | 374 | 358 | 359 |
| 353 | 290 | 383 | 352 | 396 | 386 | 342 | 373 | 292 | 355 |
| 351 | 254 | 293 | 340 | 357 | 362 | 345 | 298 | 260 | 354 |

